



HAL
open science

Numerical and experimental study on residual stresses in laser beam welding of dual phase DP600 steel plates

Shibo Liu

► **To cite this version:**

Shibo Liu. Numerical and experimental study on residual stresses in laser beam welding of dual phase DP600 steel plates. Mechanical engineering [physics.class-ph]. INSA de Rennes, 2017. English. NNT : 2017ISAR0003 . tel-01581004

HAL Id: tel-01581004

<https://theses.hal.science/tel-01581004>

Submitted on 4 Sep 2017

HAL is a multi-disciplinary open access archive for the deposit and dissemination of scientific research documents, whether they are published or not. The documents may come from teaching and research institutions in France or abroad, or from public or private research centers.

L'archive ouverte pluridisciplinaire **HAL**, est destinée au dépôt et à la diffusion de documents scientifiques de niveau recherche, publiés ou non, émanant des établissements d'enseignement et de recherche français ou étrangers, des laboratoires publics ou privés.

UNIVERSITÉ
BRETAGNE
LOIRE

THÈSE INSA Rennes
sous le sceau de l'Université Bretagne Loire
pour obtenir le titre de
DOCTEUR DE L'INSA RENNES
Spécialité: Génie Mécanique

présentée par

Shibo LIU

ÉCOLE DOCTORALE : SDLM
LABORATOIRE : LGCGM

Numerical and experimental study on residual stresses in laser beam welding of dual phase DP600 steel plates

Thèse soutenue le **08/06/2017**

devant le jury composé de :

Véronique FAVIER

Professeurs des Universités, Arts et Métiers ParisTech - Paris
/ *Présidente*

Laurent BARRALLIER

Professeurs des Universités, Arts et Métiers ParisTech - Centre
d'Aix-en-Provence / *Rapporteur*

Pierre-Yves MANACH

Professeurs des Universités, Université de Bretagne Sud /
Rapporteur

Guenaël GERMAIN

Maître de Conférences des Universités HDR, Arts et Métiers
ParisTech - Centre d'Angers / *Examineur*

Afia KOUADRI-HENNI

Maître de Conférence des Universités, INSA Rennes /
Co-encadrante de thèse

Adinel GAVRUS

Maître de Conférence des Universités HDR, INSA Rennes /
Directeur de thèse

Ionel NISTOR

Ingénieur Recherche Dr., EDF Lab Paris-Saclay / *Invité*

Numerical and experimental study on residual stresses in laser beam welding of dual phase DP600 steel plates

Shibo LIU



En partenariat avec



Remerciements

I want to thank my parents for their always encouragement and support. Without them, I would not achieve today's outcome. I also thank to China Scholarship Council for the financial support in these years.

I would like to express my sincere gratitude to my supervisor MCF HDR Dr. Adinel Gavrus and my co-supervisor MCF Dr. Afia Kouadri-Henni for the continuous support of my Ph.D study and research, for their patience, motivation, enthusiasm, and immense knowledge. Their guidance helped me a lot during research and writing of this thesis.

Besides my supervisor and co-supervisor, I would like to thank Pierre-Yves MANACH, Professor of Université de Bretagne Sud, and Laurent BARRALLIER, Professor of Arts et Métiers ParisTech - Centre d'Aix-en-Provence, for having accepted the work as reporters.

I also thank the rest of my thesis committee : Véronique FAVIER, Professeurs des Universités, Arts et Métiers ParisTech - Paris, and Guenael GERMAIN, Maître de Conférences des Universités HDR, Arts et Métiers ParisTech - Centre d'Angers for their work of examiners. Fulgence RAZAFIMAHERY, Maître de Conférences des Universités, Université de Rennes 1 and Ionel NISTOR Ingénieur Recherche Dr., EDF Lab Paris-Saclay for their encouragement, insightful comments, and great questions.

I also feel grateful to the Mecaproce Team of INSA de Rennes, LGCGM laboratory and to CEA of Saclay for the experimental measurements. They provide me great favor for my research work.

I also want to say thanks to my master supervisor Professor Dongjiang Wu for his scientific instructions and kindly help in my development.

I really thank my friends and my love who bring me wonderful times in France.

Finally to all the people who love me and who I love, thank you!

Table des figures

1.1	Schematic of Nd :YAG laser oscillator	24
1.2	Sketch of laser welding system	24
1.3	Three focusing positions of the laser beam	25
1.4	DP600 for automotive structural components	26
1.5	Microstructure of dual phase DP600 steel [1]	27
1.6	Three orders of residual stresses[2]	30
1.7	Thermal stress obtained by dilatation of a clamped bar	30
1.8	Inner and outer part of a material	31
1.9	Inner part geometry change in two dimension	32
1.10	Sketch of inner part geometry change during heating process	33
1.11	Sketch of outer part geometry change during heating process	33
1.12	The balance of inner and outer part at the end of heating process	34
1.13	The configuration of numerical model	36
1.14	The stress tensor and the strain tensor	37
1.15	Plasticity region	39
1.16	The surface normal vector direction definition in a cartesian coordinate system	42
2.1	The INSTRON tensile test machine (50KN)	57
2.2	Dimension of Specimen	58
2.3	The mark points of the tensile specimen	59
2.4	Tensile test of HSLA steel : (a) Force-displacement curve using LVDT sensor, (b) True stress-strain curve using camera measurements	59
2.5	True stress-strain curve of dual phase steel DP600 at room temperature and initial strain rate $8.33 \times 10^{-4} \text{s}^{-1}$	61
2.6	The plastic flow curve of dual phase steel DP600 at room temperature and initial strain rate $8.33 \times 10^{-4} \text{s}^{-1}$	61
2.7	Comparison of Ludwik model and experimental DP600 data	62
2.8	Comparison of Voce model and experimental DP600 data	63

2.9	Comparisons of rheological models and experimental DP600 data	65
2.10	Comparison of rheological models and experimental DP600 data	65
2.11	Temperature dependence of experiment data and simulation models	68
2.12	Temperature sensitivity of experiment data and simulation models	70
2.13	True stress-strain curves obtained at different strain rate at room temperature	71
2.14	The hardening model describing DP600 dual phase steel plastic behavior	71
2.15	Comparison between experimental data and simulation results of DP600 flow stress at room temperature 20°C	73
2.16	The plastic flow stress of DP600 dual phase steel at different temperatures and strain rates	73
2.17	The comparison between experimental data from literature [3] and simulation results of DP600 dual phase steel general constitutive model	75
2.18	Dimensions of specimen for tensile test	76
2.19	Yield surface predicted by Hill48 anisotropic model and Von Mises criterion	77
2.20	The computed results of residual stresses based on neutron diffraction method	79
3.1	A cell in analysis zone	82
3.2	The bulk and the mould wall of the weld	83
3.3	States of a growing grain	84
3.4	The growth direction angle θ	85
3.5	The direction of the grain	86
3.6	Parameters in a cell	86
3.7	basic iteration rule for each cell	87
3.8	Two types of neighborhood of Cellular Automaton	88
3.9	Rule for state change	89
3.10	Rule of grain growth	90
3.11	flowchart of the microstructure evolution model	91
3.12	Conical heat source with Gaussian distribution	92
3.13	Selected zone for calculating	93
3.14	The history temperature of node A	93
3.15	The schematic of distance weighting factor	94
3.16	The schematic of linear interpolation	95
3.17	Temperature distribution	96
3.18	The schematic of calculation of nucleation density [4]	97
3.19	The sketch of parameters used in solid fraction computation	99

3.20	Model of concentration in single cell	101
3.21	Schematic diagram of cells contact	103
3.22	Schematic diagram of cells contact	103
3.23	Growth velocity of the interface in a cell	106
3.24	The growth of equiaxed dendrite grain	108
3.25	The equiaxed dendrite grain of different directions	109
3.26	The growth of column dendrite grains	110
3.27	The growth of two dendrite grains	111
3.28	The equiaxed dendrite grain growth	113
3.29	Nucleation at the corner	114
3.30	Equiaxed grain competition growth of two directions	115
3.31	Grains with different growth direction growth at the same speed	116
3.32	Weld Microstructure Simulation of fine mesh	117
3.33	Weld Microstructure Simulation with coarse mesh	118
3.34	Dendrite morphology of 2D simulation and experimental SEM observation	119
3.35	Microstructure of FZ and HAZ of DP600 weld cross section	119
3.36	Microstructure of FZ and HAZ of DP600 weld upper surface	120
4.1	Linear material constitutive model of DP600 steel	124
4.2	The shape of heat source and Gauss heat distribution	125
4.3	The A geometry of welding simulation model	126
4.4	The B geometry of welding simulation model	127
4.5	Boundary conditions of thermal analysis model using B geometry	128
4.6	Boundary conditions of mechanical analysis model using B geometry	128
4.7	Hardening term of material constitutive model	130
4.8	Hardening models used in FEM laser welding simulation models	130
4.9	Temperature sensitivity term of material constitutive model	132
4.10	The 4 temperature sensitivity terms used in FEM laser welding simulation models	133
4.11	Temperature sensitivity term of material constitutive model	134
4.12	The strain rate sensitivity term under different temperatures	134
4.13	The specimens cut with different angles on dual phase steel DP600 plate	135
4.14	Rolling direction defined in numerical laser welding model	136
4.15	The CA simulation position in ABAQUS/FEM model	137
4.16	Temperature history data of 4 points	137
4.17	The flowchart of CA-FE model used to simulate residual stresses	138
4.18	Dendrite grains growth simulation obtained by the CA model	139

5.1	Rectangular type of mesh transition	144
5.2	Wedge type of mesh transition	144
5.3	Comparison of computation time between wedge type and rectangular type	146
5.4	Comparison of computation time of different element type model	146
5.5	Mesh of longitudinal direction	148
5.6	Residual stress distribution	149
5.7	Computation time of temperature and stress models	149
5.8	Numerical results of temperature range of melting pool heated by laser .	150
5.9	The maximal residual stress of models with different layers	150
5.10	Mesh transverse to weld	151
5.11	The comparison of computation time between Model-2x2 and Model-4x4	152
5.12	Residual stress distribution	153
5.13	Three lines fixed in thickness direction	153
5.14	Equivalent stress along weld longitudinal path	154
5.15	equivalent stress along transversal path	154
5.16	σ_{11} along weld longitudinal path	155
5.17	σ_{11} along transversal path	155
5.18	σ_{22} along weld longitudinal path	156
5.19	σ_{22} along transversal path	156
5.20	The distribution of equivalent residual stresses of welding simulation with different hardening models	157
5.21	The magnitude of equivalent residual stresses of welding simulation with different hardening models	158
5.22	The distribution of σ_{11} residual stresses of welding simulation with dif- ferent hardening models	159
5.23	The magnitude of σ_{11} residual stresses of welding simulation with dif- ferent hardening models	160
5.24	The distribution of σ_{22} residual stresses of welding simulation with dif- ferent hardening models	161
5.25	The magnitude of σ_{22} residual stresses of welding simulation with dif- ferent hardening models	161
5.26	The distribution of ϵ_{11}^e residual strains of welding simulation with dif- ferent hardening models	162
5.27	The magnitude of ϵ_{11}^e residual strains of welding simulation with different hardening models	162
5.28	The distribution of ϵ_{22}^e residual strains of welding simulation with dif- ferent hardening models	163

5.29	The magnitude of ϵ_{22}^e residual strains of welding simulation with different hardening models	164
5.30	The distribution of ϵ_{11}^p residual strains of welding simulation with different hardening models	165
5.31	The magnitude of ϵ_{11}^p residual strains of welding simulation with different hardening models	165
5.32	The distribution of ϵ_{22}^p residual strains of welding simulation with different hardening models	166
5.33	The magnitude of ϵ_{22}^p residual strains of welding simulation with different hardening models	166
5.34	The distribution of $\bar{\epsilon}^p$ residual strains of welding simulation with different hardening models	167
5.35	The magnitude of $\bar{\epsilon}^p$ residual strains of welding simulation with different hardening models	168
5.36	The distribution of equivalent residual stresses of welding simulation with 4 different temperature sensitivity terms	169
5.37	The magnitude of equivalent residual stresses of welding simulation models with 4 different temperature sensitivity terms	169
5.38	The distribution of σ_{11} residual stresses of welding simulation with 4 different temperature sensitivity terms	170
5.39	The magnitude of σ_{11} residual stresses of welding simulation models with 4 different temperature sensitivity terms	171
5.40	The distribution of σ_{22} residual stresses of welding simulation with 4 different temperature sensitivity terms	171
5.41	The magnitude of σ_{22} residual stresses of welding simulation models with 4 different temperature sensitivity terms	172
5.42	The distribution of ϵ_{11}^e elastic strains of welding simulation with 4 different temperature sensitivity terms	173
5.43	The magnitude of ϵ_{11}^e elastic strains of welding simulation models with 4 different temperature sensitivity terms	173
5.44	The distribution of ϵ_{22}^e elastic strains of welding simulation with 4 different temperature sensitivity terms	174
5.45	The magnitude of ϵ_{22}^e elastic strains of welding simulation models with 4 different temperature sensitivity terms	174
5.46	The distribution of ϵ_{11}^p plastic strains of welding simulation with 4 different temperature sensitivity terms	175
5.47	The magnitude of ϵ_{11}^p plastic strains of welding simulation models with 4 different temperature sensitivity terms	176
5.48	The distribution of ϵ_{22}^p plastic strains of welding simulation with 4 different temperature sensitivity terms	176

5.49	The magnitude of ϵ_{22}^p plastic strains of welding simulation models with 4 different temperature sensitivity terms	177
5.50	The distribution of $\bar{\epsilon}^p$ effective plastic strains of welding simulation with 4 different temperature sensitivity terms	178
5.51	The magnitude of $\bar{\epsilon}^p$ effective plastic strains of welding simulation models with 4 different temperature sensitivity terms	178
5.52	The distribution of equivalent residual stresses of welding simulation models with and without strain rate influence	179
5.53	The magnitude of equivalent residual stresses of welding simulation models with and without strain rate influence	179
5.54	The distribution of σ_{11} residual stresses of welding simulation models with and without strain rate influence	180
5.55	The magnitude of σ_{11} residual stresses of welding simulation models with and without strain rate influence	180
5.56	The distribution of σ_{22} residual stresses of welding simulation models with and without strain rate influence	181
5.57	The magnitude of σ_{22} residual stresses of welding simulation models with and without strain rate influence	181
5.58	The distribution of ϵ_{11}^e elastic strains of welding simulation models with and without strain rate influence	182
5.59	The magnitude of ϵ_{11}^e elastic strains of welding simulation models with and without strain rate influence	182
5.60	The distribution of ϵ_{22}^e elastic strains of welding simulation models with and without strain rate influence	183
5.61	The magnitude of ϵ_{22}^e elastic strains of welding simulation models with and without strain rate influence	183
5.62	The distribution of ϵ_{11}^p plastic strains of welding simulation models with and without strain rate influence	184
5.63	The magnitude of ϵ_{11}^p plastic strains of welding simulation models with and without strain rate influence	184
5.64	The distribution of ϵ_{22}^p plastic strains of welding simulation models with and without strain rate influence	185
5.65	The magnitude of ϵ_{22}^p plastic strains of welding simulation models with and without strain rate influence	185
5.66	The distribution of $\bar{\epsilon}^p$ effective plastic strains of welding simulation models with and without strain rate influence	186
5.67	The magnitude of $\bar{\epsilon}^p$ effective plastic strains of welding simulation models with and without strain rate influence	186

5.68	The distribution of equivalent residual stresses of welding simulation models with material anisotropy of $\theta = 0^\circ, 30^\circ, 45^\circ, 60^\circ, 90^\circ$ and isotropic material	187
5.69	The magnitude of equivalent residual stresses of welding simulation models with material anisotropy of $\theta = 0^\circ, 30^\circ, 45^\circ, 60^\circ, 90^\circ$ and isotropic material	188
5.70	Contour of residual stresses with different material rolling orientations .	189
5.71	Numerical welding residual stresses obtained from different rolling orientations	189
5.72	The distribution of equivalent residual stresses of welding simulation models with material anisotropy of $\theta = 0^\circ, 30^\circ, 45^\circ, 60^\circ, 90^\circ$ and isotropic material	190
5.73	The magnitude of equivalent residual stresses of welding simulation models with material anisotropy of $\theta = 0^\circ, 30^\circ, 45^\circ, 60^\circ, 90^\circ$ and isotropic material	191
5.74	The distribution of equivalent residual stresses of welding simulation models with all DP600 base metal and with weld material orientations along welding direction and obtained by CA model	192
5.75	The magnitude of equivalent residual stresses of welding simulation models with all DP600 base metal and with weld material orientations along welding direction and obtained by CA model	192
5.76	The distribution of equivalent residual stresses of welding simulation models with all DP600 base metal and with weld material orientations along welding direction and obtained by CA model	193
5.77	The magnitude of equivalent residual stresses of welding simulation models with all DP600 base metal and with weld material orientations along welding direction and obtained by CA model	194
5.78	Comparison between the experimental and the numerical residual stresses	195
5.79	The magnitude of equivalent residual stresses of welding simulation considering martensite volume fraction w change	202
6.1	Figure de l'évolution du matériau lors du processus de soudage	204
6.2	La courbe plastique de l'acier dual phase DP600 à température ambiante et la vitesse de déformation initiale de $8.33 \times 10^{-4} \text{s}^{-1}$	205
6.3	Comparaison des modèles rhéologiques et des données expérimentales DP600	206
6.4	Dépendance à la température des données expérimentales et des modèles de simulation	207
6.5	Les courbes plastique de l'acier dual phase DP600 à température différentes et la vitesse de déformation différentes	207

6.6	Surface de fluage prédite par le modèle anisotropique Hill48 et le critère Von Mises	208
6.7	The flowchart of CA-FE model used to simulate residual stresses	209
6.8	Ordinogramme du modèle d'évolution de la microstructure	210
6.9	Simulations numériques de la microstructure par modèle CA	211
6.10	Microstructure de FZ et HAZ de la section de soudure DP600 et de la surface supérieure	211
6.11	La répartition des contraintes résiduelles équivalent de simulation de soudage avec 5 modèles de ecrouissage différents	213
6.12	La répartition des contraintes résiduelles équivalent des modèles de simulation de soudage avec 4 termes de sensibilité à la température différents	214
6.13	La répartition des contraintes résiduelles équivalent des modèles de simulation de soudage avec et sans influence de la vitesse de contrainte	215
6.14	La répartition des contraintes résiduelles équivalentes des modèles de simulation de soudage avec une anisotropie matérielle de $\theta = 0^\circ, 30^\circ, 45^\circ, 60^\circ, 90^\circ$ et matériel isotrope	216
6.15	La répartition des contraintes résiduelles équivalentes des modèles de simulation de soudage avec tous les métaux de base DP600 et avec des orientations de matériau de soudure le long de la direction de soudage et obtenues par le modèle CA	217
6.16	Comparaison entre les contraintes résiduelles expérimentales et numériques	217
6.17	Les contraintes résiduelles équivalentes de la simulation de soudage en tenant compte de la changement de fraction de martensite volumique	220

Table des matières

Remerciements	1
Table des figures	3
Table des matières	11
Introduction générale	19
Introduction	23
1.1 Laser welding	23
1.1.1 Nd :YAG Laser	23
1.1.2 Sketch of laser welding system	24
1.1.3 Laser welding parameters	25
1.1.3.1 The power	25
1.1.3.2 The welding speed	25
1.1.3.3 The focusing position	25
1.1.3.4 The cover gas	26
1.2 Dual phase steel DP600	26
1.2.1 General information of DP600	26
1.2.2 Applications of DP600	26
1.2.3 Properties of DP600	27
1.2.3.1 Chemical composition of DP600 steel	27
1.2.3.2 Mechanical properties of DP600 steel	27
1.2.4 Laser welding DP600 development	28
1.3 Residual stresses	29
1.3.1 The first, second and third order of residual stress	29
1.3.2 Purpose of research residual stresses	29
1.3.3 The production mechanism of residual stress in welding	29

1.4	Continuum mechanics description	35
1.4.1	From physical world to mathematical conception	35
1.4.2	Von Mises effective stress and effective strain	38
1.4.3	Yield criteria	38
1.4.4	Elasticity	40
1.4.4.1	Isotropic linear elasticity	40
1.4.4.2	Orthotropic linear elasticity	41
1.4.5	Plasticity	45
1.4.5.1	Plastic flow	45
1.4.5.2	Anisotropic plastic flow	46
1.4.5.3	Defining anisotropic yield behavior on the basis of strain ratios (Lankford's r-values)	47
1.4.6	Material constitutive models	50
1.4.6.1	Hardening	51
1.4.6.2	Temperature sensitivity	53
1.4.6.3	Strain rate sensitivity	54
2	Experimental data concerning thermo-mechanical behavior of DP600	57
2.1	Experiment information	57
2.1.1	Equipment introduction	57
2.1.2	Material specimens of tensile tests	58
2.1.3	Uniaxial tensile testing	58
2.1.4	Rigidity of Machine during tensile tests	59
2.2	Material thermo-mechanical constitutive model of DP600	60
2.2.1	Hardening term	60
2.2.1.1	Ludwik model	61
2.2.1.2	Voce model	62
2.2.1.3	Proposed synthesis model	63
2.2.1.4	Synthesis hardening models parameters	66
2.2.2	Temperature sensitivity	66
2.2.2.1	Temperature sensitivity of a high strength steel	66
2.2.2.2	Temperature sensitivity of dual phase steel DP600	69
2.2.2.3	Synthesis of DP600 temperature sensitivity models	70
2.2.3	Strain rate sensitivity	70
2.2.3.1	The hardening term for hot rolled DP600 steel	70
2.2.3.2	Identification of the strain rate sensitivity based on hot-rolled DP600 dual phase steel	72

2.2.3.3	Use of experimental data from literature [3] to identify a larger zone of strain rate sensitivity	73
2.2.3.4	Strain rate sensitivity of DP600 dual phase steel	74
2.2.4	Planar anisotropy defined by Hill theory	74
2.3	Neutron diffraction observation	78
3	Cellular Automaton Model	81
3.1	Development of Cellular Automaton model	81
3.2	Cell	82
3.3	States	82
3.3.1	Bulk, mould and base metal	83
3.3.2	Liquid, growing or solid	83
3.3.3	Direction Index	84
3.4	Parameters	85
3.4.1	Parameters of the 2D CA model	87
3.5	Operation of update parameters	87
3.6	Neighbourhood	88
3.7	Rules of CA model	89
3.7.1	Melting rule	89
3.7.2	Grain growth rule	89
3.8	Mathematical description of the solidification model	90
3.9	Microstructure simulation of weld solidification	91
3.9.1	Read temperature database	91
3.9.2	Temperature	93
3.9.3	Distance weighting factor for cell temperature computation	94
3.9.4	Linear Interpolation for cell temperature estimation	95
3.10	Nucleation	96
3.10.1	The number of the nucleation	96
3.10.2	The position of the nucleation	98
3.11	Solid fraction	98
3.11.1	Interface Curvature	98
3.12	Interface Concentration	100
3.13	Surface tension anisotropy	101
3.14	Diffusion Equation	101
3.14.1	Equation widely accepted	101
3.14.2	Revised Equation	103
3.15	Growth velocity of the interface	105

3.15.1	Fick's laws of diffusion	105
3.16	Conservation equation	105
3.17	Time increment	106
3.18	Simulation results	107
3.18.1	Equiaxed dendrite grain growth	107
3.18.2	Equiaxed dendrite grain of 48 directions	108
3.18.3	Column dendrite grain growth	109
3.18.4	Two equiaxed dendrite grain growth	110
3.18.5	Corner Nucleation Growth	112
3.18.6	The final solidification of the liquid	113
3.18.7	Dendrite grain growth of two directions	114
3.18.8	Equiaxed dendrite grain 12 different directions	115
3.18.9	Microstructure simulation of weld	116
3.19	Cellular Automaton Simulation validation	118
3.19.1	Equiaxed dendrite	118
3.19.2	Microstructure of laser welding	119
3.19.2.1	Weld cross section	119
3.19.2.2	Weld upper surface	120
4	Finite Element Model and FEM-CA coupling for numerical simulation of residual stresses	121
4.1	Model Information	121
4.2	Basic material properties	122
4.2.1	Unit system used in ABAQUS/FEM	122
4.2.2	Conductivity	122
4.2.3	Density	123
4.2.4	Specific Heat	123
4.2.5	Elastic property	123
4.2.6	Plastic property	124
4.2.7	Expansion	124
4.2.8	Heat souce model	124
4.3	Model geometry	126
4.3.1	A geometry	126
4.3.2	B geometry and mesh method	126
4.4	Boundary conditions	127
4.4.1	Thermal boundary conditions	127
4.4.2	Mechanical boundary conditions	128

4.5	Analysis steps	129
4.6	FEM Models with different hardening terms	129
4.7	FEM Models with different temperature sensitivity terms	132
4.8	FEM Models with different strain rate sensitivity terms	133
4.9	FEM Models with different material anisotropy properties	135
4.10	Cellular Automaton - Finite Element coupling	136
4.10.1	Base metal elasticity	136
4.10.2	Weld material elasticity	136
5	Numerical simulation results, experimental analysis and discussions	143
5.1	Mesh type	143
5.1.1	Rectangular type of mesh transition	143
5.1.2	Wedge type of mesh transition	143
5.1.3	Computation time	145
5.1.3.1	Comparison between rectangular type and wedge type	145
5.2	Mesh density	147
5.2.1	Mesh of longitudinal direction	147
5.2.2	Mesh of thickness direction	151
5.2.2.1	Thickness section of weld	151
5.2.2.2	CPU time	151
5.2.2.3	Residual stress distribution	152
5.3	Boundary condition	153
5.3.1	Constrain position	153
5.3.2	Simulation results	154
5.3.2.1	Equivalent residual stress	154
5.3.2.2	Weld longitudinal direction residual stress	155
5.3.2.3	Weld transversal direction residual stress	156
5.4	Hardening analysis of DP600	157
5.4.1	Simulation results of equivalent residual stresses	157
5.4.2	Simulation results of σ_{11} residual stresses	159
5.4.3	Simulation results of σ_{22} residual stresses	160
5.4.4	Simulation results of ϵ_{11}^e residual elastic strains	161
5.4.5	Simulation results of ϵ_{22}^e residual elastic strains	163
5.4.6	Simulation results of ϵ_{11}^p residual plastic strains	164
5.4.7	Simulation results of ϵ_{22}^p residual plastic strains	165
5.4.8	Simulation results of $\bar{\epsilon}^p$ residual equivalent plastic strains	167
5.5	Temperature sensitivity analysis of DP600	168

5.5.1	Simulation results of equivalent residual stresses	168
5.5.2	Simulation results of σ_{11} residual stresses	170
5.5.3	Simulation results of σ_{22} residual stresses	171
5.5.4	Simulation results of ϵ_{11}^e residual elastic strains	172
5.5.5	Simulation results of ϵ_{22}^e residual elastic strains	173
5.5.6	Simulation results of ϵ_{11}^p residual plastic strains	175
5.5.7	Simulation results of ϵ_{22}^p residual plastic strains	176
5.5.8	Simulation results of $\bar{\epsilon}^p$ equivalent residual strains	177
5.6	Strain rate sensitivity analysis of DP600	179
5.6.1	Simulation results of equivalent residual stresses	179
5.6.2	Simulation results of σ_{11} residual stresses	180
5.6.3	Simulation results of σ_{22} residual stresses	181
5.6.4	Simulation results of ϵ_{11}^e residual elastic strains	182
5.6.5	Simulation results of ϵ_{22}^e residual elastic strains	183
5.6.6	Simulation results of ϵ_{11}^p residual plastic strains	184
5.6.7	Simulation results of ϵ_{22}^p residual plastic strains	185
5.6.8	Simulation results of $\bar{\epsilon}^p$ equivalent plastic strains	186
5.7	Plastic planar anisotropy analysis using Hill coefficients	187
5.7.1	Simulation results of equivalent residual stresses	187
5.7.2	Simulation results of σ_{11} and σ_{22} residual stresses	188
5.7.3	Simulation results of $\bar{\epsilon}^p$ residual equivalent plastic strains	189
5.8	Elastic orthotropic anisotropy analysis using cellular automaton	191
5.8.1	Simulation results of equivalent residual stresses	191
5.8.2	Simulation results of $\bar{\epsilon}^p$ residual equivalent plastic strains	192
5.9	Model validation by experimental analysis	193
	General Conclusions	197
6	Résumé détaillé - Étude numérique et expérimentale des contraintes résiduelles générées lors du soudage laser sur des plaques d'acier dual phase DP600	203
6.1	Introduction	203
6.2	Chapitre 2 : Données expérimentales concernant le comportement thermo- mécanique de DP600	204
6.2.1	Écrouissage	205
6.2.2	Sensibilité à la température	206
6.2.3	Sensibilité à la vitesse de déformation	207
6.2.4	L'anisotropie planaire définie par la théorie de Hill	208

6.2.5	Analyse de l'anisotropie orthotrope élastique à l'aide de l'automate cellulaire	208
6.3	Chapitre 3 : Modèle d'automate cellulaire	210
6.4	Chapitre 4 et 5 : ABAQUS/FEM modèles, résultats de simulation et résultats expérimentaux	212
6.4.1	Informations sur le modèle	212
6.4.2	Résultats de simulation des modèles de soudage numérique	212
6.4.2.1	Ecrouissage	212
6.4.2.2	Sensibilité à la température	213
6.4.2.3	Sensibilité à la vitesse de déformation	214
6.4.2.4	L'anisotropie plastique	215
6.4.2.5	L'anisotropie élastique	216
6.4.2.6	Validation du modèle numérique	217
6.5	Conclusion	218
A	List of Publications	221
	Appendix 02	221
	Bibliographie	228

Introduction générale

La recherche de cette travail de thèse se concentre sur les contraintes résiduelles après soudage laser de l'acier dual phase DP600. Les travaux majeurs sont réalisés grâce à deux approches :

— L'approche de simulation numérique :

1. Des modèles incrementaux séquentiels thermo-mécanique type éléments finis (FEM) sont utilisés pour simuler le procédé du soudage laser sur l'acier DP600 dual phase.
2. Le modèle constitutif du matériau est considéré comme un facteur important dans la simulation FEM. Les effets de chaque terme d'érouissage, de la sensibilité à la température et à la vitesse de déformation, de l'anisotropie plastique et orthotropique élastique sur des contraintes résiduelles sont analysés.
3. Pour rechercher l'anisotropie orthotropique élastique, une modèle d'automate cellulaire 2D est programmé sous JAVA par l'auteur pour simuler le processus de solidification lors du soudage laser. Les résultats numériques de la microstructure et des orientations des grains sont utilisés pour intégrer les propriétés élastiques de la soudure DP600 dans la simulation FEM ainsi que la fraction volumique de l'orientation des grains.

— L'approche expérimentale :

1. Des expériences de soudage au laser sont effectuées en utilisant différentes puissances laser et directions de soudage par rapport au sens de laminage de la plaque d'acier de base DP600. Les meilleurs paramètres de soudage laser sont obtenus grâce aux observations expérimentales qualité microscopique, macroscopique et mécanique.
2. Des tests de tractions uniaxiales sont utilisés pour obtenir les courbes contrainte-déformation vraie de l'acier DP600 à dual phase. À l'aide de modèles classiques et d'un modèle proposé par l'auteur à partir des études précédentes issues de la littérature, le comportement de l'acier DP600 thermo-mécanique a été identifié pour différents conditions de sollicitation afin d'être implémenté dans les modèles éléments finis de simulation du soudage laser.
3. La diffraction des neutrons est réalisée pour mesurer la déformation des plaques d'acier soudées DP600. Les contraintes résiduelles correspondantes sont calculées et comparées aux résultats de simulations numériques.

Suivant cette méthodologie de travail, cette thèse est structurée en plusieurs parties :

D’abord une partie d’introduction générale synthétisant, les connaissances actuelles concernant les contraintes résiduelles lors d’un processus de soudage laser. Les théories pertinentes utilisées pour étudier le procédé de soudage par laser sont présentés en détail et décrites avec des éléments liés à l’analyse des contraintes résiduelles.

Dans le deuxième chapitre, en tant que facteurs clés dans la simulation des contraintes résiduelles du processus de soudage laser, le comportement élasto-thermo-plastique de l’acier dual phase DP600 est analysé en détail et identifié par des techniques de régression non-linéaire en partant des données expérimentales obtenu lors des essais de traction uniaxiales.

Dans le troisième chapitre, une modèle numérique d’Automate Cellulaire 2D (CA) programmé sous JAVA afin de pouvoir simuler la microstructure après soudage laser est étudié ainsi que l’influence de la microstructure sur l’anisotropie élastique orthotropique est présenté en détail.

Dans le quatrième chapitre, sur la base des modèles constitutifs du matériau identifiés au chapitre 2 et de l’élasticité orthotropique analysée au chapitre 3, les résultats des modèles FEM visant à analyser les influences de l’écrouissage, de la sensibilité à la température, de la sensibilité à la vitesse de déformation, de l’anisotropie plastique et de l’anisotropie orthotropique élastique sont effectuées.

Dans le cinquième chapitre, les résultats numériques correspondant aux modèles FEM du chapitre précédent sont analysés ensemble avec une synthèse de discussion concernant l’impact de modèles utilisés sur la simulation des contraintes résiduelles lors du soudage laser de DP600.

Les principaux résultats de cette thèse sont présentés ci-dessous :

1. L’analyse de l’influence de l’écrouissage prouve qu’un petit changement dans le modèle constitutif du matériau peut entraîner une grande différence sur les contraintes résiduelles. Les différents modèles constitutifs du matériau reproductible du comportement réel observé lors des essais de traction, présentent les mêmes influences sur la simulation des contraintes résiduelles.
2. La température a une influence importante sur les contraintes résiduelles équivalentes. Le modèle proposé et celui polynomial décrivent bien le comportement à la sensibilité à la température du DP600 et se révèlent avoir des résultats de simulations similaires.
3. La vitesse de la déformation présente une valeur maximale des contraintes résiduelles et de la déformation tandis que les modèles ne prenant pas en compte l’influence de la vitesse de la déformation présente des contraintes résiduelles de plus faibles valeurs aux bord de la zone de soudage et une courbe plutôt stable tout au long de la zone de soudage.
4. L’étude de l’angle entre la direction de laminage et la direction de soudure a mis également en évidence l’importance de l’orientation de la tôle. Lorsque l’angle est de 45° , les contraintes résiduelles autour de la soudure sont les plus élevées.

Lorsque l'angle entre le sens du laminage et de soudure est de 90° , les contraintes résiduelles autour de la soudure sont les plus faibles.

5. L'anisotropie élastique orthotropique qui prend en compte l'orientation des grains dont la fraction volumique, obtenue grâce au modèle numérique 2D CA, a peu d'influence sur les contraintes résiduelles. Ce résultat était attendu car la zone soudée est très peu texturée et présente une structure équiaxe.
6. Enfin, les résultats expérimentaux et ceux obtenus par le couplage des deux modèles CA/FEM ont montré de bonnes convergences et permet de confirmer la robustesse générale du modèle numérique de simulation du procédé de soudage laser pour estimer les contraintes résiduelles.

Introduction

1.1 Laser welding

Laser is short for “Light Amplification by Stimulated Emission of Radiation” It is an intensive light and is generated by exciting a specific material with large energy from light, discharge, and so on. Based on the material type, lasers are categorized into solid-state laser, liquid laser, gas laser and chemical laser.

The first ruby laser was built in 1960 by Theodore H. Maiman at Hughes Research Laboratories, based on theoretical work of Charles Hard Townes and Arthur Leonard Schawlow [5]. Shortly after that the diode laser was created in 1962 by two US groups of Robert N. Hall at the General Electric research center [6] and of Marshall Nathan at the IBM T.J. in Watson Research Center [7]. The Nd :YAG laser was first invented by J. E. Geusic et al. at Bell laboratories [8] and the CO₂ laser by C.K.N. Patel at Bell laboratories. The disk laser concept was proposed in the early 1990s with a first industrial product applied in 2003 [9]. Among these various types of lasers, the Nd :YAG laser is widely used in welding manufacturing process because of its good compatibility with optical fibers and high heat absorption coefficient with metal.

1.1.1 Nd :YAG Laser

Nd :YAG laser is a kind of solid-state laser. The production of Nd :YAG laser is illustrated in figure 1.1. A trivalent Nd ion, Nd³⁺ is doped in YAG material. This is because Nd³⁺ has a energy level structure for four-level model and because YAG crystal is so superior to other laser materials in term of the thermal conductivity.

The pumping and the oscillation wavelength of Nd :YAG laser are 808 nm and 1064 nm, respectively. Arranging a number of rod media in the axial direction of the resonator enables several tenth kW CW oscillation. In fact, a number of companies has realized products of several kW Nd :YAG laser to weld steel and aluminum alloy. The output of a typical Nd :YAG laser is, however, at most several hundreds W. The typical repetition rate of Nd :YAG pulsed laser is in the range between several Hz and several kHz. At Q-switching operation, a high power pulse (several hundreds mJ) of a duration of 10 ns to 50 ns has been generated.

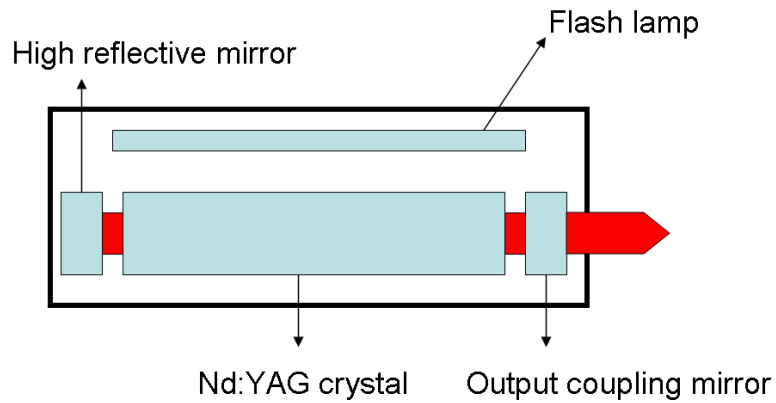


FIGURE 1.1 – Schematic of Nd :YAG laser oscillator

1.1.2 Sketch of laser welding system

As is seen in figure 1.2, a sketch is presented in a laser welding system. After generated in the oscillator, the laser is transported through fiber or lens to the desired place. Before use for welding process, the laser beam is focused by lens to get a focus point where the power density can be very high to melt, vaporise and even ionize any existing material.

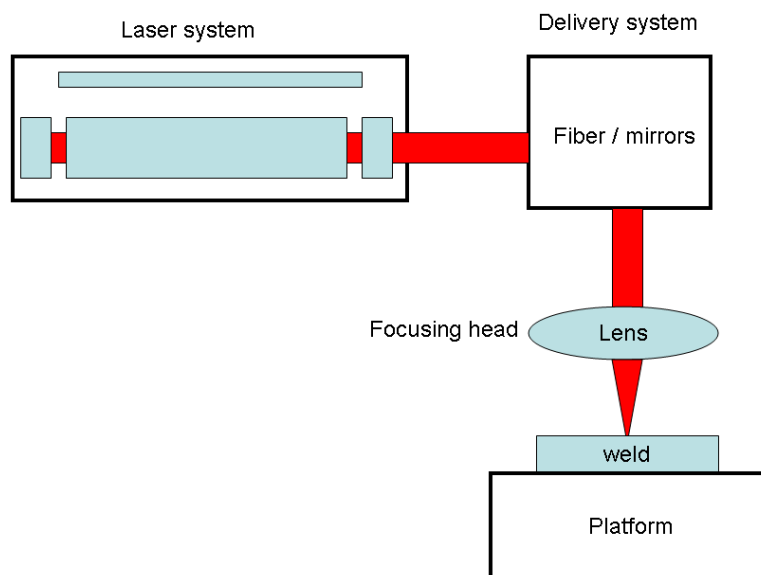


FIGURE 1.2 – Sketch of laser welding system

With different laser beam energy density applied on the material, there are two different forms of welding : heat conduction welding and deep penetration welding. When the laser beam have a low power density or a high welding speed, the heat

conduction welding occurs. When a high power density laser beam is applied to the material, absorbed energy can not fully transferred by heat conduction, a part of energy is to vaporise the material and a key hole is formed through which laser penetrate into the workpiece.

1.1.3 Laser welding parameters

1.1.3.1 The power

The welding power directly influences the specific energy input expressed per unit volume of base plate. It is one of the most important parameters of laser welding process. For a given welding condition, as the power of laser beam increases, the geometry of weld changes from shallow to deep and the welding mode from conduction welding to deep penetration welding. For deep penetration welding, the dimension of a weld will reach a threshold when the power of laser beam increase continuously, because energy input are absorbed by the plasma of on the keyhole.

1.1.3.2 The welding speed

The welding speeding influences the specific energy input of base plate. For a given laser power, high welding speed can decrease the input energy density applied on the base plate. In this way, the deep penetration welding can be changed into conduction welding. With a fixed rate of power input, a high speed will lead the weld to be shallow. Moreover, for a penetration welding, too high speed can result in unstable keyhole and a non-uniform penetration weld. If the welding speed is too low, large amount energy are lost by heat conduction to base metal. It is necessary to balance laser power and welding speed given process condition.

1.1.3.3 The focusing position

As is seen in figure 1.3, the focusing position can be expressed by the defocusing amount "D". When $D=0$, the focal point is at the plate surface. The interaction area of laser beam applied on the material surface is the smallest. When $D>0$ or $D<0$, the focal point is above or under the plate surface. The interaction area increases as the $|D|$ increase.

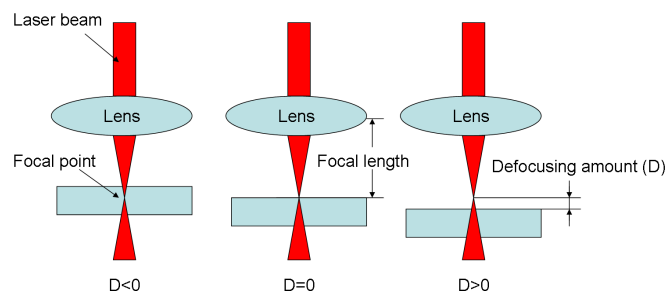


FIGURE 1.3 – Three focusing positions of the laser beam

1.1.3.4 The cover gas

Argon, helium or nitrogen inert gas are usually used as the cover gas. The cover gas is used to protect the weld from rapid oxidation. During welding, the cover gas is blasted on the surface of fusion zone with low pressure flow volume to shield the weld zone from room oxygen. Welds with cover gas are usually shiny and the mechanical properties are not affected. The flowing cover gas can take away some amount of heat during welding, thus reduce the temperature gradient and the thermal load of welding process.

1.2 Dual phase steel DP600

1.2.1 General information of DP600

To relieve energy crisis and environment problems, high strength material is applied in automotive industries in order to reduce the car weight [10]. As a type of AHSS (advanced high-strength steel), DP600 is widely used in automobile industries. DP means dual phase steel (martensite + ferrite) and 600 series means that the tensile strength is over 600 MPa. This steel is a low carbon steel with a soft ferrite matrix containing a hard second phase, mainly islands of martensite (3%-30%) [11]. The hard phase of martensite contributes to the high strength while soft ferrite helps to improve ductility [12, 13], which make a good combination of formability and high strength. Compared with traditional high-strength low-alloy (HSLA) steels, DP steel has no yield point elongation and has a higher strain-hardening rate [14]. The high strain-hardening rate enhance the absorption of energy when deformation is happened, which helps decrease of damage in car collision [15].

1.2.2 Applications of DP600

In figure 1.4, many automotive structural components are made in DP600, such as B-pillar, seat, shotgun, floor panel tunnel, front sub-frame package tray and engine cradle. These are all safety cage components that require sufficient strength with low weight.

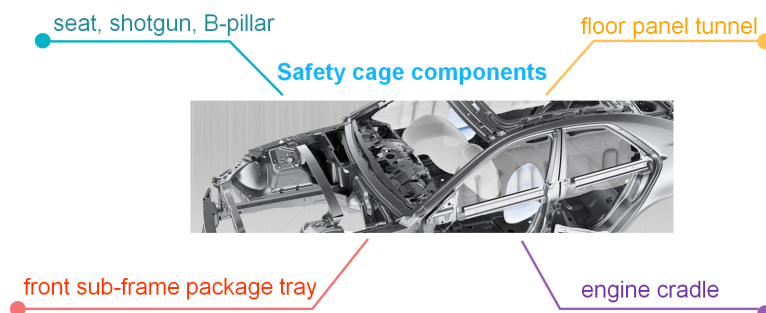


FIGURE 1.4 – DP600 for automotive structural components

1.2.3 Properties of DP600

The yield and tensile strength of DP 600 steel are primarily determined by the volume proportion of martensite in the softer ferritic matrix.

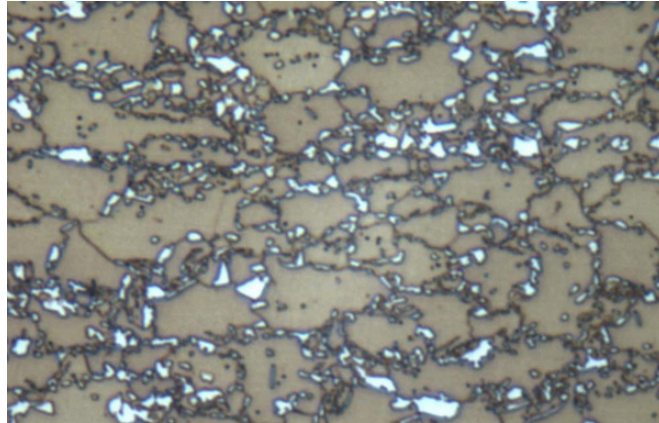


FIGURE 1.5 – Microstructure of dual phase DP600 steel [1]

1.2.3.1 Chemical composition of DP600 steel

The chemical composition of DP600 steel is shown in table 1.1.

TABLE 1.1 – Chemical composition of DP600 steel [16]

DP 600 steel [wt. %]							
C	Mn	Si	P	S	Al	N	Cr
max. 0.2	max. 2.00	max. 0.50	max. 0.090	max. 0.015	min. 0.02	max. 0.012	max. 1.00

1.2.3.2 Mechanical properties of DP600 steel

The general mechanical properties of DP600 steel is shown in table 1.2.

TABLE 1.2 – Mechanical properties of DP600 steel [16]

Mechanical properties of DP600 steel	
Yield strength $R_{p0.2}$ [MPa]	380-470
Strength R_m [MPa]	580-670
Maximum $R_{p0.2}/R_m$ proportion	0.70
Minimum ductility A_5 [%]	24

1.2.4 Laser welding DP600 development

In the year of 2016, G.C.C. Correard et al. [17] investigated the microstructure of DP600/DP600 weld and DP600/TRIP750 weld especially on heat affected zone (HAZ) by a fiber laser with 1300 W power and 50mm/s welding speed. Martensite is found in weld zone. In HAZ region, martensite and ferrite are observed. The tensile strength of different type of DP600 weld joints is about 400 MPa, ranges from 380MPa to 400MPa. Fatigue curves presented a limit at approximately 350 MPa for DP600 steels.

In 2012, Y. Song et al. [18] used Nd :YAG laser to weld DP600 and DX56D steel. The Vickers hardness are tested and based on the mixture rule, the relationship between the micro-Vickers hardness value and material parameters (i.e., the strain hardening exponent, the strength coefficient and Young's modulus) was quantitatively built. At the same year, M. Hazratinezhad et al. [19] researched the influence of Nd :YAG laser pattern on the after welding mechanical property of DP steel. The energy input pattern and effective peak power density is found to influence material strength and high pulse duration lead to coarse grain in HAZ (Heat Affected Zone).

At year 2010 and 2011, N.Farabi et al. [20, 21, 22] investigated diode laser welded on DP600/DP600 and DP600/DP980 steel joints. Microstructures, fatigue properties, microhardness profiles, tensile properties and work hardening characteristics of laser weld joints are studied. Several results are found in their throughout research :

- The welding resulted in a significant increase of hardness in the fusion zone (nearly full martensite is found of DP600/DP980 FZ), but also the formation of a soft zone in the outer heat-affected zone (HAZ). The degree of softening was found to be stronger in the DP980 welded joints than in the the DP600 welded joints and lead to a significant decrease in the fatigue limit of DP980 softening zone.
- For DP600 joint, while the ductility decreased after welding, the yield strength increased and the ultimate tensile strength remained almost unchanged.
- At higher stress amplitudes, the fatigue life of DP600 is almost the same between the base metal and welded joint. Tensile fracture and fatigue failure occurred at the outer HAZ. Fatigue crack initiation was from the specimen surface and crack propagation was characterized by their characteristics..

C. Dharmendra et al. [23] investigated laser welding-brazing DP600/AA6016 with CW Nd :YAG laser. The microstructure and composition analyses of the brazed joints were examined. The micro-hardness and tensile strength were measured. The laser welding parameters were optimized based on mechanical resistance and thickness of steel seam interface.

M. Xia et al. [24] investigated Nd :YAG laser heat input influence on heat affected zone (HAZ) of dual phase steels. Maximum HAZ softening was proportional to the martensite content, and the heat input controlled the completion of softening.

X. Li [25] advocated a technique to stabilize laser lap welding zinc coated DP600 : the technique is addition of a small amount of aluminum to the faying surface region, so that a liquid Al-Zn alloy of high boiling point is formed, thus lowering the Zn vapor

pressure. The comparison of weld surface profiles and weld interface microstructures, with and without Al foil, are presented to show the good quality of Al added on plate surface.

1.3 Residual stresses

Residual stresses are “self equilibrating internal stresses” existing in a free body with no external forces or constraints on its boundary.

1.3.1 The first, second and third order of residual stress

A distinction is made between first, second and third order residual stresses (Figure 1.6) [2] :

1. First order (σ^I , macro) : nearly homogeneous across large areas (several grains of the material). First order residual stresses, σ^I , extend over macroscopic areas and are averaged stresses over several crystallites.
2. Second order (σ^{II} , meso) : nearly homogeneous across smaller areas, of the order of some grains or phases of a material. Second order residual stresses, (σ^{II} , act between crystallites or crystallite subregions (size approx. 1-0.01 mm) and are averaged within these areas (for instance residual stresses around piled-up dislocations or secondary phases).
3. Third order (σ^{III} , micro) : inhomogeneous across submicroscopic areas of the material, several atomic distances within a grain. Third order residual stresses, σ^{III} , act between atomic areas (size approx. $10^{-2} - 10^{-6}$ mm ; for instance, the residual stresses around a single dislocation).

The macroscopic residual stresses are of particular relevance for engineering purposes. In this dissertation, the objective is focused on the first order of residual stresses.

1.3.2 Purpose of research residual stresses

1. Residual stresses superimpose to applied stresses during service life
2. Residual stresses can affect the mechanical behavior of a component
3. Residual stresses influence the corrosion behavior of the weld part.

Thus, the residual stress evaluation is fundamental to ensure the performance of a product.

1.3.3 The production mechanism of residual stress in welding

To better understand the complex welding residual stress, simple cases are analyzed. The production of thermal stress is shown in figure 1.7. A bar at 20°C, at 200°C without

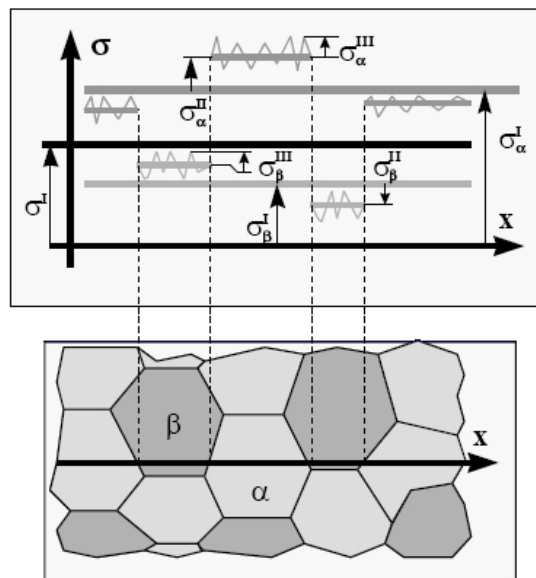


FIGURE 1.6 – Three orders of residual stresses[2]

constrain and at 200°C with constrain is presented. Generally the material increases its body volume due to temperature increase, which is usually called thermal expansion. For the bar at 20°C and at 200°C without constrain, the bar is at free state with no internal stress in the bar. For the bar at 200°C with constrain, the bar is at constrained state with internal stress in the bar. This internal stress is called thermal stress and its magnitude depend on temperature change and boundary conditions. In a macroscopic point of view, the thermal stress can be produced without strain due to the temperature change.

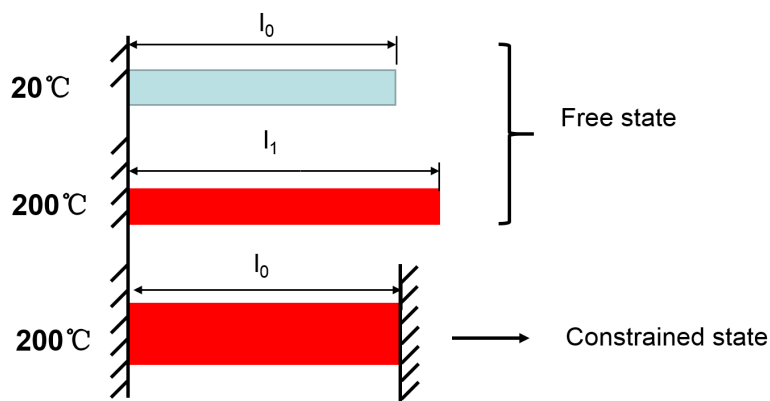


FIGURE 1.7 – Thermal stress obtained by dilatation of a clamped bar

The length at free state of 200°C is given by :

$$l_1 = l_0(1 + \alpha \Delta T) \quad (1.1)$$

Supposing only elastic behavior, the stress of constrained state at 200°C is written as :

$$\sigma_{thermal} \approx -E \left(\frac{l_1 - l_0}{l_0} \right) = -E\alpha\Delta T \quad (1.2)$$

Figure 1.8 shows the inner part and outer part of a material. At first, the temperature of the inner part and the outer part is the same. There are no interval and no stress between inner and outer part surface. When the temperature of inner part is increased while the temperature of outer remains the same, the inner part tends to expand while the outer part tends to remain the same. The conflict between the two part happens.

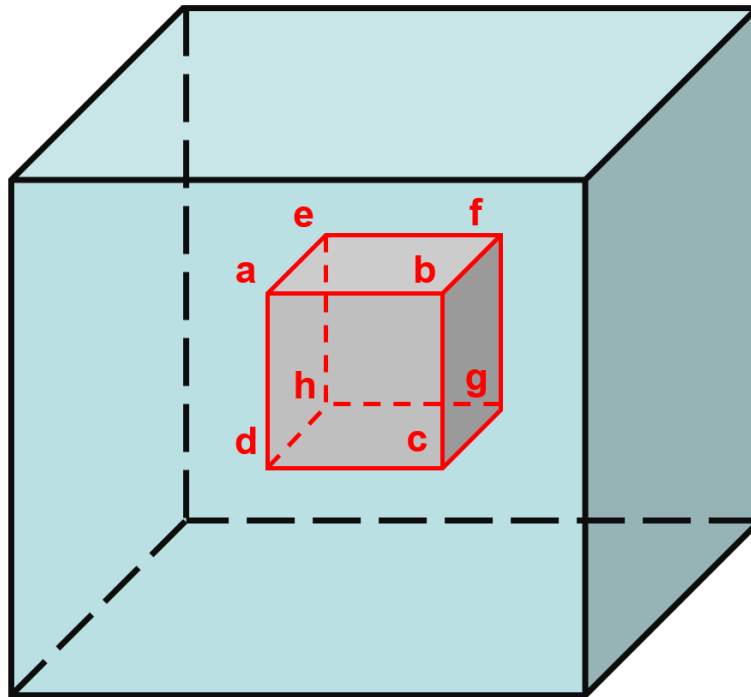


FIGURE 1.8 – Inner and outer part of a material

The inner and outer part is plotted in two dimension to sketch out the geometry change of inner part (the outer part is also changed but not marked in figure 1.9). In the figure, abcd stands for the geometry of inner part at cool state, a''b''c''d'' the geometry of inner part of hot state supposing no outer part constrained and a'b'c'd' the geometry of inner part of hot state considering the constrain of outer part.

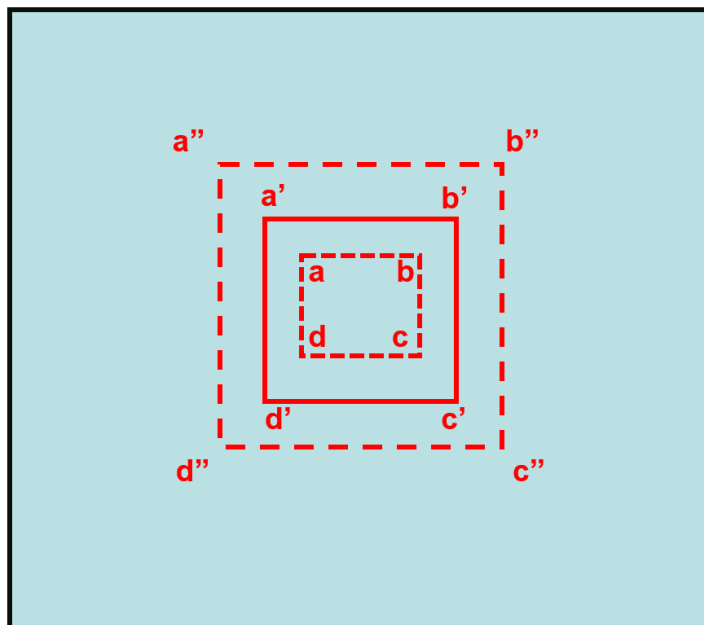


FIGURE 1.9 – Inner part geometry change in two dimension

To analyze the geometry change of inner part during heating process, the geometry of inner part at three states in figure 1.10 are plotted with the point d, d' and d'' at the same place to illustrate more clearly the volume change of the inner part. First, the geometry of inner part at cool state abcd is heated. If there is no constrain of outer part, abcd is imagined to expand to a hot state of a''b''c''d''. But in reality, the inner part is always constrained by a outer part. Thus, the inner part at cool state abcd expand to a constrained hot state a'b'c'd' , or the inner part at free heated state a''b''c''d'' is compressed to a constrained hot state a'b'c'd'.

During the imagined compressed process, the inner part must take into account an elastic and plastic deformation. Along an horizontal direction, the length change of inner part can be express as :

$$\Delta l = l_{d''c''} - l_{d'c'} = l_e + l_p \quad (1.3)$$

where Δl is the inner part length change when constrained by outer part at heated state, l_e is the elastic deformation length and l_p is the plastic deformation length of inner part.

Corresponding to the inner part, the outer part that has the boundary attached to the inner part is plotted in figure 1.11. Due to the expansion of inner part, the outer part is deformed from state ABCD to A'B'C'D'. If the outer part has no stiffness, the outer part may be pushed by inner part to the dotted shape. (The maximum volume of inner part at heated state without constrain).

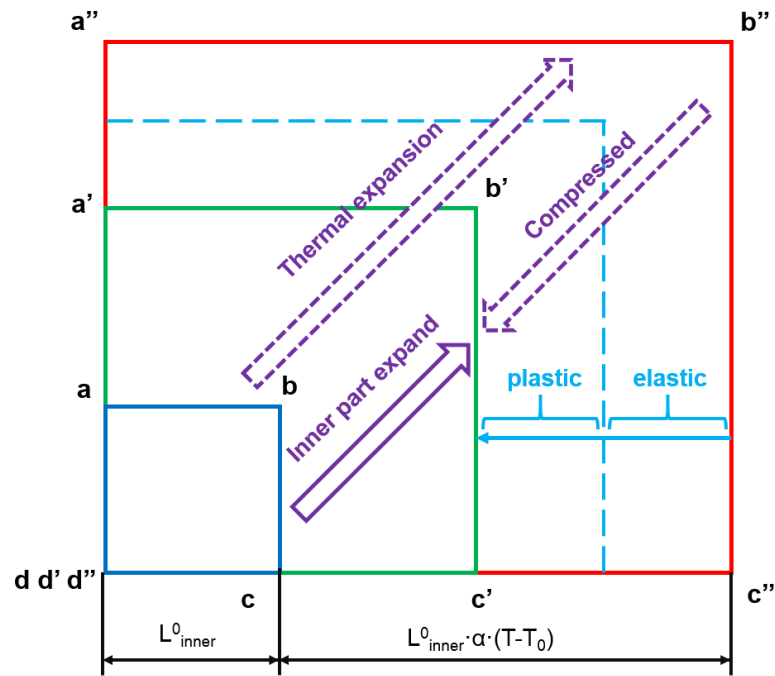


FIGURE 1.10 – Sketch of inner part geometry change during heating process

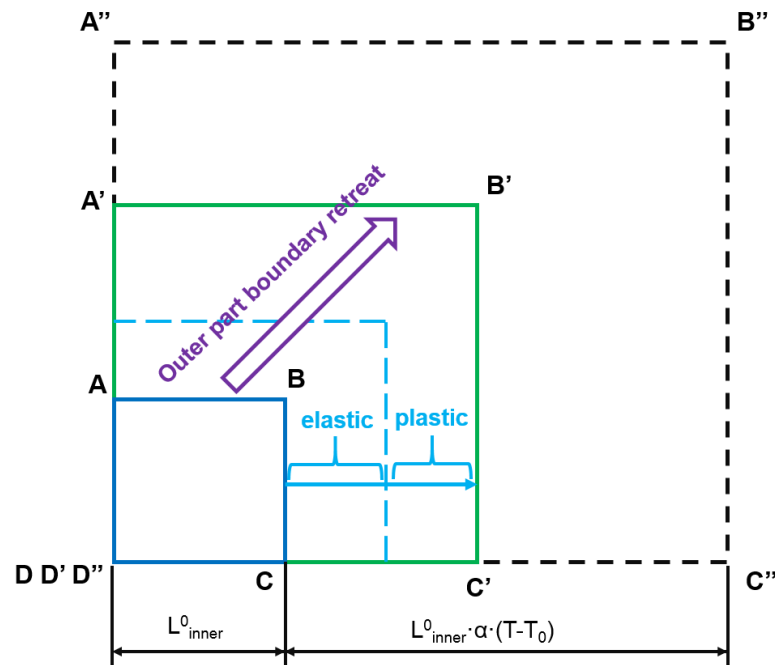


FIGURE 1.11 – Sketch of outer part geometry change during heating process

This deformation must contains an elastic deformation and may contains a plastic deformation. In horizontal direction, the length change of outer part can be express as :

$$\Delta L = l_{D'C'} - l_{DC} = L_e + L_p \quad (1.4)$$

where ΔL is the outer part length change when pushed by the inner part expansion, L_e is the elastic deformation length and L_p is the plastic deformation length of outer part.

In figure 1.10 and figure 1.11, the inner part is heated and the geometry of inner and outer part are sketched. During the heating process, both the inner and the outer are compressed due to the heating of inner part (though the inner part compression is imagined).

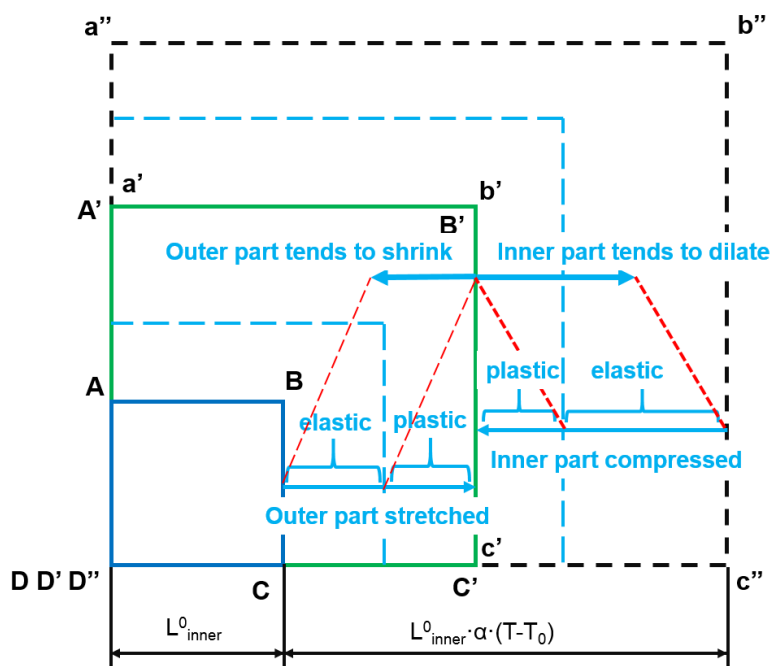


FIGURE 1.12 – The balance of inner and outer part at the end of heating process

When the inner part reaches the highest temperature, the inner and outer part reach a balance geometry of $a'b'c'd'$ and $A'B'C'D'$ in figure 1.12. At this moment in horizontal direction, the stress at the interface between inner and outer part can be expressed :

$$\sigma_{inner} = E_{inner} \cdot \varepsilon_{inner}^e \quad (1.5)$$

$$\sigma_{outer} = E_{outer} \cdot \varepsilon_{outer}^e \quad (1.6)$$

For laser welding, the heating process is followed by a cooling step. In this simple case, the heated inner part is cooled. In this cooling process, both inner and outer part tend to return to its original state. The plastic deformation during heating process is preserved and may be also produced during cooling process. The stress at the interface between a'b'c'd' and A'B'C'D' should be the same and can be computed considering the elastic and plastic deformation.

1.4 Continuum mechanics description

The material constitutive model is an important part of numerical mechanical simulation. It describes the essential relationship between the strains and the stresses, which is a linear relationship for elastic analyses and a complex nonlinear relationship for plastic analyses, involving plastic strain, temperature, strain rate and state variables describing mechanism of deformation at microscopic level.

The elasticity of a material is described in terms of a stress-strain relation. Typically, two types of relation are considered. The first type deals with materials that are elastic only for small strains. The second deals with materials that have large elastic strains. For small strains, the measure of the Cauchy stress is used while the measure of strain is an infinitesimal strain tensor; the resulting (predicted) material behavior is termed linear elasticity, which for metallic materials is called the generalized Hooke's law describing both isotropic and anisotropic elasticity.

In 1867 Tresca published his works [26, 27] on material yielding behavior under various stress states. He used the maximum shear stress as the yield criteria. His systematic experimental investigations on yielding became a theoretical basis for plasticity investigation. After Tresca's work, the Von Mises yield criteria [28] was proposed in 1913. In principal stress space, the yield surface of Tresca criteria is circumscribed by Von Mises's yield criteria. The effective Von Mises stress can be viewed as a proportion to the elastic distortional energy which makes Von Mises criteria a more reasonable criteria. Based on Von Mises, Rodney Hill developed several yield criteria [29, 30, 31, 32, 33] for anisotropic plastic deformations which are provided successful in predicting metals, polymers and certain composites. In this work, the Von Mises yield criteria and Hill yield law are used, so a brief description the plasticity including the Von Mises and Hill's criteria are introduced below.

1.4.1 From physical world to mathematical conception

To analysis the residual stresses after welding process, the solid dynamics of continuum mechanics are used through a Finite Element Method (FEM) used by the commercial software ABAQUS.

To describe the material mathematical formulations, several basic definitions are introduced according to the figure 1.13. For more detail informations, please refer to continuum mechanics theory.

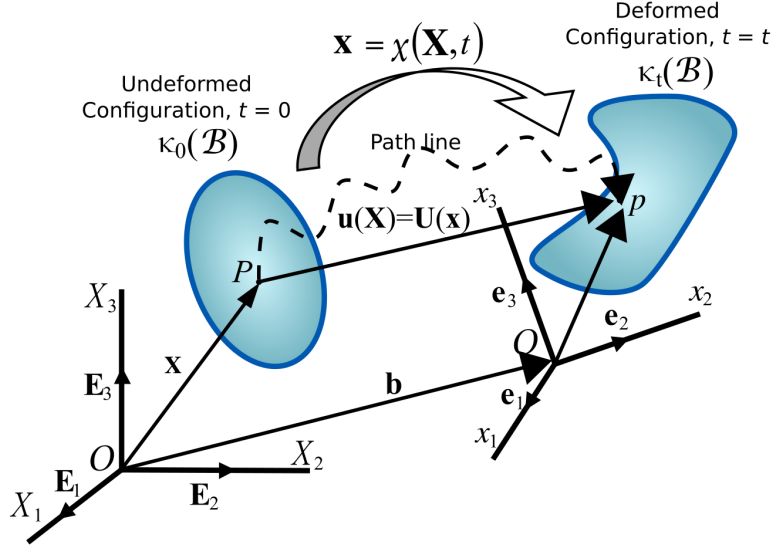


FIGURE 1.13 – The configuration of numerical model

For a material body \mathcal{B} , the region it takes up in 3D space at time t is the body's configuration and is labeled $\kappa_t(\mathcal{B})$. A particular particle of body \mathcal{B} in a particular configuration $\kappa_t(\mathcal{B})$ can be characterized by a position vector $\mathbf{x} = \sum_{i=1}^3 x_i \mathbf{e}_i$. For a particular time such as $t=0$, the vector \mathbf{x} can be written as the reference vector \mathbf{X} . For the material body \mathcal{B} , at time t the position vector \mathbf{x} can be written as a function of the reference vector \mathbf{X} with expression as $\mathbf{x} = \kappa_t(\mathbf{X})$.

The transformation gradient \mathbf{F} is the derivative of each component of deformed \mathbf{x} vector with respect to each component of the reference \mathbf{X} vector. The transformation gradient \mathbf{F} contains the information of the deformation of material body.

$$F_{ij} = x_{i,j} = \frac{\partial x_i}{\partial X_j} = \begin{bmatrix} \frac{\partial x_1}{\partial X_1} & \frac{\partial x_1}{\partial X_2} & \frac{\partial x_1}{\partial X_3} \\ \frac{\partial x_2}{\partial X_1} & \frac{\partial x_2}{\partial X_2} & \frac{\partial x_2}{\partial X_3} \\ \frac{\partial x_3}{\partial X_1} & \frac{\partial x_3}{\partial X_2} & \frac{\partial x_3}{\partial X_3} \end{bmatrix} \quad (1.7)$$

Derived from the transformation gradient \mathbf{F} , infinitesimal or small strain can be computed by :

$$d\boldsymbol{\varepsilon} = \frac{1}{2}(d\mathbf{F} + d\mathbf{F}^T) - \mathbf{I} \quad (1.8)$$

or

$$\boldsymbol{\varepsilon} = \frac{1}{2}(\mathbf{F} + \mathbf{F}^T) - \mathbf{I} \quad (1.9)$$

where $d\mathbf{F}$ define the increment transformation gradient in the case of use of an updated Lagrangian method.

The Lagrangian strain tensor (infinitesimal deformation) is given as follows :

$$\mathbf{E} = \frac{1}{2}(\mathbf{F} \cdot \mathbf{F}^T) - \mathbf{I} \quad (1.10)$$

For small material deformations, $\boldsymbol{\varepsilon} = \int d\boldsymbol{\varepsilon} \approx \mathbf{E}$. These equations are generally used for metallic materials to define a more consistent definition of large plastic deformations using the evaluation of incremental strain state tensor by $d\boldsymbol{\varepsilon} = d\boldsymbol{\varepsilon}^{el} + d\boldsymbol{\varepsilon}^{pl}$ and $\mathbf{F} = \mathbf{F}^{el} \mathbf{F}^{pl}$.

To fully describe the stress state of a material, the strain tensor is illustrated in figure 1.14 (a) and the stress tensor is illustrated in figure 1.14 (b) :

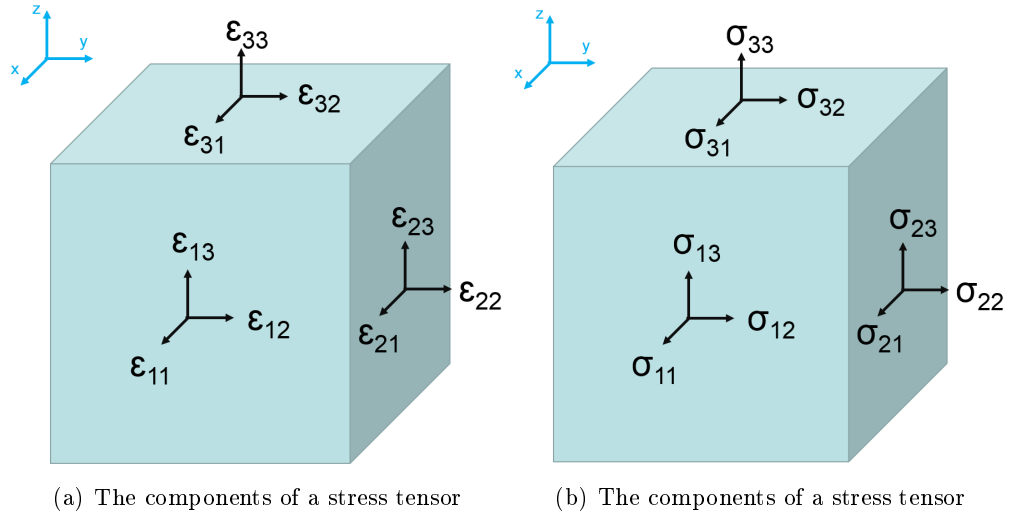


FIGURE 1.14 – The stress tensor and the strain tensor

Due to the inherent symmetries of $\varepsilon_{ij} = \varepsilon_{ji}$, the strain tensor can be written as follows :

$$\boldsymbol{\varepsilon} = \begin{bmatrix} \varepsilon_{11} & \varepsilon_{12} & \varepsilon_{13} \\ \varepsilon_{12} & \varepsilon_{22} & \varepsilon_{23} \\ \varepsilon_{13} & \varepsilon_{23} & \varepsilon_{33} \end{bmatrix} = \begin{bmatrix} \varepsilon_{11} & \varepsilon_{12} & \varepsilon_{13} \\ & \varepsilon_{22} & \varepsilon_{23} \\ \text{symm.} & & \varepsilon_{33} \end{bmatrix} \quad (1.11)$$

Due to the inherent symmetries of $\sigma_{ij} = \sigma_{ji}$, the stress tensor is given by :

$$\boldsymbol{\sigma} = \begin{bmatrix} \sigma_{11} & \sigma_{12} & \sigma_{13} \\ \sigma_{12} & \sigma_{22} & \sigma_{23} \\ \sigma_{13} & \sigma_{23} & \sigma_{33} \end{bmatrix} = \begin{bmatrix} \sigma_{11} & \sigma_{12} & \sigma_{13} \\ & \sigma_{22} & \sigma_{23} \\ \text{symm.} & & \sigma_{33} \end{bmatrix} \quad (1.12)$$

1.4.2 Von Mises effective stress and effective strain

Strain tensor in equation 1.11 and stress tensor in equation 1.12 each have 6 components of different values, respectively. These values provide the material mechanical state under certain circumstances.

To simplify the analysis, a lot of multiaxial yield laws are proposed and among them the most commonly used is the Von Mises criteria. The Von Mises effective stress or the equivalent stress is calculated as follows :

$$\begin{aligned}\sigma_e &= \sqrt{\frac{1}{2}[(\sigma_{11} - \sigma_{22})^2 + (\sigma_{22} - \sigma_{33})^2 + (\sigma_{33} - \sigma_{11})^2 + 6(\sigma_{23}^2 + \sigma_{31}^2 + \sigma_{12}^2)]} \\ &= \sqrt{\frac{3}{2}(s_{11}^2 + s_{22}^2 + s_{33}^2 + 2\sigma_{23}^2 + 2\sigma_{31}^2 + 2\sigma_{12}^2)}\end{aligned}\quad (1.13)$$

where s is the deviatoric stress term.

The Von Mises infinitesimal effective plastic strain or equivalent plastic strain is computed by :

$$d\varepsilon_e^p = \sqrt{\frac{2}{3}(d\varepsilon_{11}^p{}^2 + d\varepsilon_{22}^p{}^2 + d\varepsilon_{33}^p{}^2 + 2d\varepsilon_{23}^p{}^2 + 2d\varepsilon_{31}^p{}^2 + 2d\varepsilon_{12}^p{}^2)}\quad (1.14)$$

Notice that “e”, the subscript of σ_e and ε_e^p , means effective. Using Von Mises effective stress and strain definition, complex material stress and strain states with 6 values can be simplified into only one value, respectively. With this simplification, the uniaxial tensile test can be the reference for yield state for many complex material stress-strain states.

For steel material, an idealized uniaxial stress-strain curve showing elastic and plastic deformation regimes for the deformation theory of plasticity :

By definition, the elasticity is a solid material undergoing reversible changes of shape in response to applied forces while the plasticity is a solid material undergoing non-reversible changes of shape in response to applied forces. In figure 1.15, the material stress-strain state corresponding to the blue region means that the material is under elastic state. Under the elastic state, the material can return to its original shape when the applied forces are removed. The material stress-strain state corresponding to the red region means that the material is under plastic state. Under the plastic state, the material can not return to its original shape when the applied forces are removed. For steel material, the crystallographic slip and dislocations accumulate. This process is not reversible and when the process reach a certain extent, the fracture happens. The welding process is not involved with fracture in this study, so only elasticity and plasticity of DP600 material is focused on.

1.4.3 Yield criteria

Through a material uniaxial tensile test, the effective stress-strain curve are obtained such as that in figure 1.15. The curve in the figure can be expressed by :

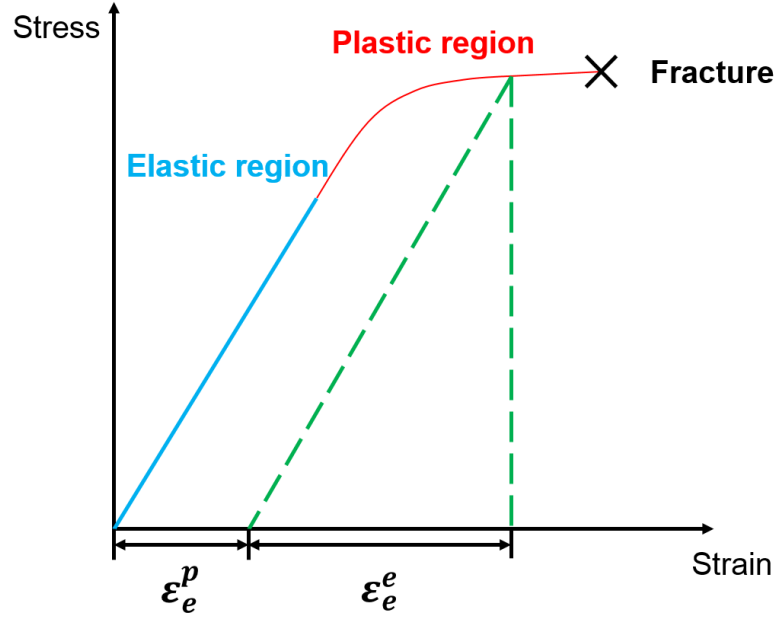


FIGURE 1.15 – Plasticity region

$$\sigma_e^{\text{yield}} = \text{Function}(\varepsilon_e^p) \quad (1.15)$$

The Von Mises effective plastic strain is noted as ε_e^p . The computation method is based on equation 1.14.

$$\varepsilon_e^p = \int d\varepsilon_e^p \quad (1.16)$$

According to the material constitutive model used by the numerical simulation and considering the deformation history, an effective plastic strain ε_e^p and corresponding effective stress σ_e are obtained. Then the computed effective stress σ_e and the yield effective stress σ_e^{yield} of material is compared using yield criteria f :

$$f = \sigma_e - \sigma_e^{\text{yield}} \quad (1.17)$$

Based on yield criteria f , the material can be determined to be yield or not in the simulation.

- If yield criteria f is less than 0, then the material is under elastic state, the material is deformed elastically.
- If yield criteria f is equal to 0, then the material is under plastic state, the material is deformed plastically.
- The yield criteria f should not be bigger than 0, the plastic flow will increase the effective plastic strain ε_e^p and then increase the yield effective stress σ_e^{yield} .

1.4.4 Elasticity

Based on some criteria, the material under elastic or plastic state is determined. When the material is under elastic state, the relationship between stress and strain matrix is given as :

$$\boldsymbol{\sigma} = \mathbf{C} \cdot \boldsymbol{\varepsilon} \quad (1.18)$$

Where \mathbf{C} is the stiffness tensor and can be expressed by a $3 \times 3 \times 3 \times 3$ matrix of 81 real numbers C_{ijkl} . Due to the inherent symmetries, the stresses and strains can be expressed as follows :

$$\begin{bmatrix} \sigma_{11} \\ \sigma_{22} \\ \sigma_{33} \\ \sigma_{12} \\ \sigma_{13} \\ \sigma_{23} \end{bmatrix} = \begin{bmatrix} D_{1111} & D_{1122} & D_{1133} & D_{1112} & D_{1113} & D_{1123} \\ & D_{2222} & D_{2233} & D_{2212} & D_{2213} & D_{2223} \\ & & D_{3333} & D_{3312} & D_{3313} & D_{3323} \\ & & & D_{1212} & D_{1213} & D_{1223} \\ & sym & & & D_{1313} & D_{1323} \\ & & & & & D_{2323} \end{bmatrix} \begin{bmatrix} \varepsilon_{11} \\ \varepsilon_{22} \\ \varepsilon_{33} \\ 2\varepsilon_{12} \\ 2\varepsilon_{13} \\ 2\varepsilon_{23} \end{bmatrix} \quad (1.19)$$

1.4.4.1 Isotropic linear elasticity

The simplest form of the elasticity is the isotropic linear elasticity. the stress-strain relationship is given by :

$$\begin{bmatrix} \sigma_{11} \\ \sigma_{22} \\ \sigma_{33} \\ \sigma_{12} \\ \sigma_{13} \\ \sigma_{23} \end{bmatrix} = \begin{bmatrix} \lambda + 2\mu & \lambda & \lambda & 0 & 0 & 0 \\ & \lambda + 2\mu & \lambda & 0 & 0 & 0 \\ & & \lambda + 2\mu & 0 & 0 & 0 \\ & & & \mu & 0 & 0 \\ & sym & & & \mu & 0 \\ & & & & & \mu \end{bmatrix} \begin{bmatrix} \varepsilon_{11} \\ \varepsilon_{22} \\ \varepsilon_{33} \\ 2\varepsilon_{12} \\ 2\varepsilon_{13} \\ 2\varepsilon_{23} \end{bmatrix} \quad (1.20)$$

where Lamé constants λ and μ are expressed by Young's modulus E and Poisson's ratio ν :

$$\lambda = \frac{E\nu}{(1+\nu)(1-2\nu)} \quad (1.21)$$

$$\mu = G = \frac{E}{2(1+\nu)} \quad (1.22)$$

In equation 1.22, G is the shear modulus, E the Young's modulus and ν Poisson coefficient. The value of Young's modulus E and Poisson's ratio ν are values in variation with temperature in the welding process.

The invert form of equation 1.20 is given by :

$$\begin{bmatrix} \varepsilon_{11} \\ \varepsilon_{22} \\ \varepsilon_{33} \\ 2\varepsilon_{12} \\ 2\varepsilon_{13} \\ 2\varepsilon_{23} \end{bmatrix} = \frac{1}{E} \begin{bmatrix} 1 & -\nu & -\nu & & & \\ -\nu & 1 & -\nu & & & \\ -\nu & -\nu & 1 & & & \\ & & & 2(1+\nu) & & \\ & & & & 2(1+\nu) & \\ & & & & & 2(1+\nu) \end{bmatrix} \begin{bmatrix} \sigma_{11} \\ \sigma_{22} \\ \sigma_{33} \\ \sigma_{12} \\ \sigma_{13} \\ \sigma_{23} \end{bmatrix} \quad (1.23)$$

The isotropic linear elasticity is used in numerical welding simulation except for the case of elastic orthotropic anisotropy analysis considering phase transformation, material phase mixture and especially grains orientations in the weld. The orthotropic elastic anisotropy analysis is introduced in the next section.

1.4.4.2 Orthotropic linear elasticity

A more complex elasticity is the orthotropic linear elasticity which is defined by three moduli E_1, E_2, E_3 , three Poisson's ratios $\nu_{12}, \nu_{13}, \nu_{23}$ and three shear moduli G_{12}, G_{13}, G_{23} associated with the material's principal directions.

$$\begin{bmatrix} \sigma_{11} \\ \sigma_{22} \\ \sigma_{33} \\ \sigma_{12} \\ \sigma_{13} \\ \sigma_{23} \end{bmatrix} = \begin{bmatrix} D_{1111} & D_{1122} & D_{1133} & 0 & 0 & 0 \\ & D_{2222} & D_{2233} & 0 & 0 & 0 \\ & & D_{3333} & 0 & 0 & 0 \\ & & & D_{1212} & 0 & 0 \\ & sym & & & D_{1313} & 0 \\ & & & & & D_{2323} \end{bmatrix} \begin{bmatrix} \varepsilon_{11} \\ \varepsilon_{22} \\ \varepsilon_{33} \\ 2\varepsilon_{12} \\ 2\varepsilon_{13} \\ 2\varepsilon_{23} \end{bmatrix} \quad (1.24)$$

where the constants define the D matrix is given by :

$$D_{1111} = E_1(1 - \nu_{23}\nu_{32})\gamma \quad (1.25)$$

$$D_{2222} = E_2(1 - \nu_{13}\nu_{31})\gamma \quad (1.26)$$

$$D_{3333} = E_3(1 - \nu_{12}\nu_{21})\gamma \quad (1.27)$$

$$D_{1122} = E_1(\nu_{21} + \nu_{31}\nu_{23})\gamma = E_2(\nu_{12} + \nu_{32}\nu_{13})\gamma \quad (1.28)$$

$$D_{1133} = E_1(\nu_{31} + \nu_{21}\nu_{32})\gamma = E_2(\nu_{13} + \nu_{12}\nu_{23})\gamma \quad (1.29)$$

$$D_{2233} = E_2(\nu_{32} + \nu_{12}\nu_{31})\gamma = E_3(\nu_{23} + \nu_{21}\nu_{13})\gamma \quad (1.30)$$

$$D_{1212} = G_{12} \quad (1.31)$$

$$D_{1313} = G_{13} \quad (1.32)$$

$$D_{2323} = G_{23} \quad (1.33)$$

where γ is expressed as :

$$\gamma = \frac{1}{1 - \nu_{12}\nu_{21} - \nu_{23}\nu_{32} - \nu_{31}\nu_{13} - 2\nu_{21}\nu_{32}\nu_{13}} \quad (1.34)$$

The invert form of equation 1.24 is given by :

$$\begin{bmatrix} \varepsilon_{11} \\ \varepsilon_{22} \\ \varepsilon_{33} \\ 2\varepsilon_{12} \\ 2\varepsilon_{13} \\ 2\varepsilon_{23} \end{bmatrix} = \begin{bmatrix} 1/E_1 & -\nu_{21}/E_2 & -\nu_{31}/E_3 & & & \\ -\nu_{12}/E_1 & 1/E_2 & -\nu_{32}/E_3 & & & \\ -\nu_{13}/E_1 & -\nu_{23}/E_2 & 1/E_3 & & & \\ & & & 1/G_{12} & & \\ & & & & 1/G_{13} & \\ & & & & & 1/G_{23} \end{bmatrix} \begin{bmatrix} \sigma_{11} \\ \sigma_{22} \\ \sigma_{33} \\ \sigma_{12} \\ \sigma_{13} \\ \sigma_{23} \end{bmatrix} \quad (1.35)$$

The orthotropic linear elasticity is defined not only with three moduli E_1 , E_2 , E_3 , three Poisson's ratios ν_{12} , ν_{13} , ν_{23} and three shear moduli G_{12} , G_{13} , G_{23} , but also by definition of the material's principal direction. When the principal direction changes and have angles with 11, 22 and 33 directions, the elastic stiffness is changed following formula based on change matrix [34] :

The direction cosine In figure 1.16, $\vec{on} \perp \triangle abc$. The angles between the vector \vec{on} and coordinate axes x, y and z are α , β and γ , respectively. It is defined that direction cosines (l_1 , m_1 , n_1) of \vec{on} with respect to axes x, y and z are :

$$l_1 = \cos\alpha, \quad m_1 = \cos\beta, \quad n_1 = \cos\gamma \quad (1.36)$$

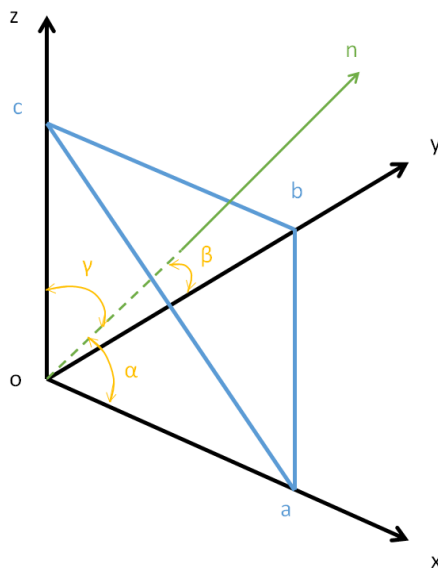


FIGURE 1.16 – The surface normal vector direction definition in a cartesian coordinate system

There are two cartesian coordinate systems, one is named $[S]$ with coordinates (1,2,3) and the other is $[K]$ with (x,y,z). Direction cosines between two coordinate axes are shown in table 1.3.

TABLE 1.3 – Direction cosines between two coordinate axes

	x	y	z
1	l_1	m_1	n_1
2	l_2	m_2	n_2
3	l_3	m_3	n_3

Transition of stresses in different coordinate systems Stresses $[\sigma_{ij}^{[S]}]$ in coordinate system $[S]$ and $[\sigma_{ij}^{[K]}]$ in $[K]$ can be written as :

$$[\sigma_{ij}^{[S]}] = \begin{bmatrix} \sigma_1 \\ \sigma_2 \\ \sigma_3 \\ \tau_{23} \\ \tau_{31} \\ \tau_{12} \end{bmatrix}, \quad [\sigma_{ij}^{[K]}] = \begin{bmatrix} \sigma_x \\ \sigma_y \\ \sigma_z \\ \tau_{yz} \\ \tau_{zx} \\ \tau_{xy} \end{bmatrix} \quad (1.37)$$

The relation between $[\sigma_{ij}^{[S]}]$ and $[\sigma_{ij}^{[K]}]$ can be written as :

$$[\sigma_{ij}^{[S]}] = [A_{ij}] [\sigma_{ij}^{[K]}] \quad (1.38)$$

where $[A_{ij}]^{-1}$ is written by :

$$[A_{ij}]^{-1} = \begin{bmatrix} l_1^2 & l_2^2 & l_3^2 & 2l_2l_3 & 2l_3l_1 & 2l_1l_2 \\ m_1^2 & m_2^2 & m_3^2 & 2m_2m_3 & 2m_3m_1 & 2m_1m_2 \\ n_1^2 & n_2^2 & n_3^2 & 2n_2n_3 & 2n_3n_1 & 2n_1n_2 \\ m_1n_1 & m_2n_2 & m_3n_3 & m_2n_3 + m_3n_2 & m_3n_1 + m_1n_3 & m_1n_2 + m_2n_1 \\ n_1l_1 & n_2l_2 & n_3l_3 & n_2l_3 + n_3l_2 & n_3l_1 + n_1l_3 & n_1l_2 + n_2l_1 \\ l_1m_1 & l_2m_2 & l_3m_3 & l_2m_3 + l_3m_2 & l_3m_1 + l_1m_3 & l_1m_2 + l_2m_1 \end{bmatrix} \quad (1.39)$$

Transition of strains in different coordinate systems Strains $[\varepsilon_{ij}^{[S]}]$ in coordinate system $[S]$ and $[\varepsilon_{ij}^{[K]}]$ in $[K]$ can be written as :

$$[\varepsilon_{ij}^{[S]}] = \begin{bmatrix} \varepsilon_1 \\ \varepsilon_2 \\ \varepsilon_3 \\ \gamma_{23} \\ \gamma_{31} \\ \gamma_{12} \end{bmatrix}, \quad [\varepsilon_{ij}^{[K]}] = \begin{bmatrix} \varepsilon_x \\ \varepsilon_y \\ \varepsilon_z \\ \gamma_{yz} \\ \gamma_{zx} \\ \gamma_{xy} \end{bmatrix} \quad (1.40)$$

The relation between $[\varepsilon_{ij}^{[S]}]$ and $[\varepsilon_{ij}^{[K]}]$ can be written as :

$$[\varepsilon_{ij}^{[S]}] = [B_{ij}] [\varepsilon_{ij}^{[K]}] \quad (1.41)$$

and $[B_{ij}]$ is written in the form :

$$[B_{ij}] = \begin{bmatrix} l_1^2 & m_1^2 & n_1^2 & m_1 n_1 & n_1 l_1 & l_1 m_1 \\ l_2^2 & m_2^2 & n_2^2 & m_2 n_2 & n_2 l_2 & l_2 m_2 \\ l_3^2 & m_3^2 & n_3^2 & m_3 n_3 & n_3 l_3 & l_3 m_3 \\ 2l_2 l_3 & 2m_2 m_3 & 2n_2 n_3 & m_2 n_3 + m_3 n_2 & n_2 l_3 + n_3 l_2 & l_2 m_3 + l_3 m_2 \\ 2l_3 l_1 & 2m_3 m_1 & 2n_3 n_1 & m_3 n_1 + m_1 n_3 & n_3 l_1 + n_1 l_3 & l_3 m_1 + l_1 m_3 \\ 2l_1 l_2 & 2m_1 m_2 & 2n_1 n_2 & m_1 n_2 + m_2 n_1 & n_1 l_2 + n_2 l_1 & l_1 m_2 + l_2 m_1 \end{bmatrix} \quad (1.42)$$

Elastic constants transition in different coordinate systems The relationship between $[\sigma_{ij}^{[S]}]$ and $[\varepsilon_{ij}^{[S]}]$ is :

$$[\sigma_{ij}^{[S]}] = [C_{ij}^{[S]}] [\varepsilon_{ij}^{[S]}] \quad (1.43)$$

Instead $[\sigma_{ij}^{[S]}]$ with equation 1.38 and $[\varepsilon_{ij}^{[S]}]$ with equation 1.41 :

$$[A_{ij}] [\sigma_{ij}^{[K]}] = [C_{ij}^{[S]}] [B_{ij}] [\varepsilon_{ij}^{[K]}] \quad (1.44)$$

Left multiply $[A_{ij}]^{-1}$ at both sides of equation 1.44 :

$$[\sigma_{ij}^{[K]}] = [A_{ij}]^{-1} [C_{ij}^{[S]}] [B_{ij}] [\varepsilon_{ij}^{[K]}] \quad (1.45)$$

Considering the relationship between $[\sigma_{ij}^{[K]}]$ and $[\varepsilon_{ij}^{[K]}]$:

$$[\sigma_{ij}^{[K]}] = [C_{ij}^{[K]}] [\varepsilon_{ij}^{[K]}] \quad (1.46)$$

so

$$[C_{ij}^{[K]}] = [A_{ij}]^{-1} [C_{ij}^{[S]}] [B_{ij}] \quad (1.47)$$

Calculation of elastic constants with 2D crystalline orientation If the original martensite is in [S] coordinate system and the rotated martensite (with orientation) is in [K] coordinate system, and the martensite is assumed to rotate in the plate plane with angle of θ , the direction cosines between [S] and [K] coordinate axes are :

With these values, the matrix of $[A_{ij}^{-1}]$ can be given by :

TABLE 1.4 – Direction cosines values in plane rotation with angle θ

	x	y	z
1	$l_1 = \cos\theta$	$m_1 = -\sin\theta$	$n_1 = 0$
2	$l_2 = \sin\theta$	$m_2 = \cos\theta$	$n_2 = 0$
3	$l_3 = 0$	$m_3 = 0$	$n_3 = 1$

$$[A_{ij}]^{-1} = \begin{bmatrix} \cos^2\theta & \sin^2\theta & 0 & 0 & 0 & 2\sin\theta\cos\theta \\ \sin^2\theta & \cos^2\theta & 0 & 0 & 0 & -2\sin\theta\cos\theta \\ 0 & 0 & 1 & 0 & 0 & 0 \\ 0 & 0 & 0 & \cos\theta & -\sin\theta & 0 \\ 0 & 0 & 0 & \sin\theta & \cos\theta & 0 \\ -\sin\theta\cos\theta & \sin\theta\cos\theta & 0 & 0 & 0 & \cos^2\theta - \sin^2\theta \end{bmatrix} \quad (1.48)$$

and $[B_{ij}]$ is :

$$[B_{ij}] = \begin{bmatrix} \cos^2\theta & \sin^2\theta & 0 & 0 & 0 & -\sin\theta\cos\theta \\ \sin^2\theta & \cos^2\theta & 0 & 0 & 0 & \sin\theta\cos\theta \\ 0 & 0 & 1 & 0 & 0 & 0 \\ 0 & 0 & 0 & \cos\theta & \sin\theta & 0 \\ 0 & 0 & 0 & -\sin\theta & \cos\theta & 0 \\ 2\sin\theta\cos\theta & -2\sin\theta\cos\theta & 0 & 0 & 0 & \cos^2\theta - \sin^2\theta \end{bmatrix} \quad (1.49)$$

By changing the elastic constants, the orthotropic linear elasticity are defined with principal directions. For welding simulation developed by the author, elastic constants are determined from the contents of ferrite and austenite. The principal orientation is determined by a Cellular Automaton method developed in this work.

1.4.5 Plasticity

1.4.5.1 Plastic flow

For the plasticity, the material behavior are first started by an assumption of normality of plasticity : the increment in the plastic strain tensor is in a direction which is normal to the tangent to the yield surface at the load point. When the plasticity happens, the increment of plastic flow can be expressed using Levy-Mises relationship :

$$\begin{bmatrix} d\varepsilon_{11}^p & d\varepsilon_{12}^p & d\varepsilon_{13}^p \\ d\varepsilon_{21}^p & d\varepsilon_{22}^p & d\varepsilon_{23}^p \\ d\varepsilon_{31}^p & d\varepsilon_{32}^p & d\varepsilon_{33}^p \end{bmatrix} = d\lambda \begin{bmatrix} \partial f / \partial \sigma_{11} & \partial f / \partial \sigma_{12} & \partial f / \partial \sigma_{13} \\ \partial f / \partial \sigma_{21} & \partial f / \partial \sigma_{22} & \partial f / \partial \sigma_{23} \\ \partial f / \partial \sigma_{31} & \partial f / \partial \sigma_{32} & \partial f / \partial \sigma_{33} \end{bmatrix} \quad (1.50)$$

When we use the Von Mises effective stress for computation, then yield criteria f in equation 1.50 can be expressed by :

$$f = \sigma_e - \sigma_e^{yield} = \sqrt{\frac{3}{2}(s_{11}^2 + s_{22}^2 + s_{33}^2 + 2\sigma_{23}^2 + 2\sigma_{31}^2 + 2\sigma_{12}^2)} - \sigma_e^{yield} \quad (1.51)$$

Substitute equation 1.51 into equation 1.50, the increment of plastic flow can be expressed by :

$$\begin{bmatrix} d\varepsilon_{11}^p & d\varepsilon_{12}^p & d\varepsilon_{13}^p \\ d\varepsilon_{21}^p & d\varepsilon_{22}^p & d\varepsilon_{23}^p \\ d\varepsilon_{31}^p & d\varepsilon_{32}^p & d\varepsilon_{33}^p \end{bmatrix} = \frac{3}{2\sigma_e} d\lambda \begin{bmatrix} \frac{2}{3}\sigma_{11} - \frac{1}{3}\sigma_{22} - \frac{1}{3}\sigma_{33} & \sigma_{12} & \sigma_{13} \\ \sigma_{12} & \frac{2}{3}\sigma_{22} - \frac{1}{3}\sigma_{11} - \frac{1}{3}\sigma_{33} & \sigma_{23} \\ \sigma_{13} & \sigma_{23} & \frac{2}{3}\sigma_{33} - \frac{1}{3}\sigma_{11} - \frac{1}{3}\sigma_{22} \end{bmatrix} \quad (1.52)$$

The equation 1.52 can be simplified using plastic strain $\boldsymbol{\varepsilon}^p$ and deviatoric stress $\boldsymbol{\sigma}'$:

$$d\boldsymbol{\varepsilon}^p = \frac{3}{2\sigma_e} d\lambda \boldsymbol{\sigma}' \quad (1.53)$$

In equation 1.50 and 1.52, the plastic multiplier $d\lambda$ determines the plastic flow amount so that when plastic deformation happens, yield criteria f is always 0.

To compute the plastic multiplier $d\lambda$, the yield effective stress σ_e^{yield} in equation 1.17 and equation 1.51 plays an important role. The value of the yield effective stress σ_e^{yield} is based on experiments with respect to plastic strain, temperature and plastic strain rate. The definition of σ_e^{yield} is introduced in detail in the later subsection 1.4.6.

1.4.5.2 Anisotropic plastic flow

Hill's potential function is a simple extension of the Mises function, which can be expressed in terms of rectangular Cartesian stress components as

$$f = \sqrt{F(\sigma_{22} - \sigma_{33})^2 + G(\sigma_{33} - \sigma_{11})^2 + H(\sigma_{11} - \sigma_{22})^2 + 2L\sigma_{23}^2 + 2M\sigma_{31}^2 + 2N\sigma_{12}^2} - \sigma_e = 0 \quad (1.54)$$

where F, G, H, L, M, and N are constants obtained by tests of the material in different orientations. They are defined as

$$F = \frac{(\sigma_e^{yield})^2}{2} \left(\frac{1}{\bar{\sigma}_{22}^2} + \frac{1}{\bar{\sigma}_{33}^2} - \frac{1}{\bar{\sigma}_{11}^2} \right) = \frac{1}{2} \left(\frac{1}{R_{22}^2} + \frac{1}{R_{33}^2} - \frac{1}{R_{11}^2} \right) \quad (1.55)$$

$$G = \frac{(\sigma_e^{yield})^2}{2} \left(\frac{1}{\bar{\sigma}_{33}^2} + \frac{1}{\bar{\sigma}_{11}^2} - \frac{1}{\bar{\sigma}_{22}^2} \right) = \frac{1}{2} \left(\frac{1}{R_{33}^2} + \frac{1}{R_{11}^2} - \frac{1}{R_{22}^2} \right) \quad (1.56)$$

$$H = \frac{(\sigma_e^{yield})^2}{2} \left(\frac{1}{\bar{\sigma}_{11}^2} + \frac{1}{\bar{\sigma}_{22}^2} - \frac{1}{\bar{\sigma}_{33}^2} \right) = \frac{1}{2} \left(\frac{1}{R_{11}^2} + \frac{1}{R_{22}^2} - \frac{1}{R_{33}^2} \right) \quad (1.57)$$

$$L = \frac{3}{2} \left(\frac{\tau_e^{yield}}{\bar{\sigma}_{23}} \right)^2 = \frac{3}{2R_{23}^2} \quad (1.58)$$

$$M = \frac{3}{2} \left(\frac{\tau_e^{yield}}{\bar{\sigma}_{13}} \right)^2 = \frac{3}{2R_{13}^2} \quad (1.59)$$

$$N = \frac{3}{2} \left(\frac{\tau_e^{yield}}{\bar{\sigma}_{12}} \right)^2 = \frac{3}{2R_{12}^2} \quad (1.60)$$

where each $\bar{\sigma}_{ij}$ is the measured yield stress value when σ_{ij} is applied as the only nonzero stress component; σ_e^{yield} is the user-defined reference yield stress specified for the metal plasticity definition; R_{11} , R_{22} , R_{33} , R_{12} , R_{13} , and R_{23} are anisotropic yield stress ratios; and $\tau_e^{yield} = \sigma_e^{yield} / \sqrt{3}$. The six yield stress ratios are, therefore, defined as follows (in the order in which you must provide them) :

$$\frac{\bar{\sigma}_{11}}{\sigma_e^{yield}}, \frac{\bar{\sigma}_{22}}{\sigma_e^{yield}}, \frac{\bar{\sigma}_{33}}{\sigma_e^{yield}}, \frac{\bar{\sigma}_{12}}{\tau_e^{yield}}, \frac{\bar{\sigma}_{13}}{\tau_e^{yield}}, \frac{\bar{\sigma}_{23}}{\tau_e^{yield}}$$

Because of the form of the yield function, all of these ratios must be positive. If all the constants F, G, and H are positive, the yield function is always well-defined. However, if one or more of these constants is negative, the yield function may be undefined for some stress states because the quantity under the square root is negative.

The flow rule is estimated by :

$$d\varepsilon^{pl} = d\lambda \frac{\partial f}{\partial \sigma} = \frac{d\lambda}{f} b \quad (1.61)$$

where, from the above definition of plastic criteria f above,

$$b = \begin{bmatrix} -G(\sigma_{33} - \sigma_{11}) + H(\sigma_{11} - \sigma_{22}) \\ F(\sigma_{22} - \sigma_{33}) - H(\sigma_{11} - \sigma_{22}) \\ -F(\sigma_{22} - \sigma_{33}) + G(\sigma_{33} - \sigma_{11}) \\ 2N\sigma_{12} \\ 2M\sigma_{31} \\ 2L\sigma_{23} \end{bmatrix} \quad (1.62)$$

1.4.5.3 Defining anisotropic yield behavior on the basis of strain ratios (Lankford's r-values)

In Abaqus [35], Hill's anisotropic plasticity potential is defined consisting of ratios of yield stress in different directions with respect to a reference stress. However, in some cases, such as sheet metal forming applications, it is common to find the anisotropic material data given in terms of ratios of width strain to thickness strain. Mathematical

relationships are then necessary to convert the strain ratios to stress ratios that can be input into Abaqus.

In sheet metal forming applications we are generally concerned with plane stress conditions. Consider x , y to be the longitudinal (rolling) and respectively transversal directions in the plane of the sheet where z is the thickness direction. From a design viewpoint, the type of anisotropy usually desired is that in which the sheet is isotropic in the plane and has an increased strength in the thickness direction, which is normally referred to as normal anisotropy. Another type of anisotropy is characterized by different strengths in different directions in the plane of the sheet, which is called planar anisotropy.

From a simple tensile test performed in the x -direction in the plane of the sheet, the flow rule for this potential (given above) defines the incremental strain ratios (assuming small elastic strains) as

$$d\varepsilon_{11} : d\varepsilon_{22} : d\varepsilon_{33} = G + H : -H : -G \quad (1.63)$$

Therefore, the ratio of width to thickness strain, often referred to as Lankford's r -value, is

$$r_x = \frac{d\varepsilon_{22}}{d\varepsilon_{33}} = \frac{H}{G} \quad (1.64)$$

Similarly, for a simple tension test performed in the y -direction in the plane of the sheet, the incremental strain ratios are

$$d\varepsilon_{11} : d\varepsilon_{22} : d\varepsilon_{33} = -H : F + H : -F \quad (1.65)$$

and

$$r_y = \frac{d\varepsilon_{11}}{d\varepsilon_{33}} = \frac{H}{F} \quad (1.66)$$

Normal anisotropy A normal anisotropic material is one where $r_x = r_y$. If we define σ^0 in the metal plasticity model to be equal to $\bar{\sigma}_{11}$,

$$R_{11} = R_{22} = 1 \quad (1.67)$$

and, using the relationships above,

$$R_{33} = \sqrt{\frac{r_x + 1}{2}} \quad (1.68)$$

If $r_x = 1$ (isotropic material), $R_{33} = 1$ and the Mises isotropic plasticity model is recovered.

Planar anisotropy In the case of planar anisotropy r_x and r_y are different and R_{11}, R_{22}, R_{33} will all be different. If we define σ^0 in the metal plasticity model to be equal to $\bar{\sigma}_{11}$,

$$R_{11} = 1 \quad (1.69)$$

and, using the relationships above, we obtain

$$R_{22} = \sqrt{\frac{r_y(r_x + 1)}{r_x(r_y + 1)}} \quad (1.70)$$

$$R_{33} = \sqrt{\frac{r_y(r_x + 1)}{r_x + r_y}} \quad (1.71)$$

Again, if $r_x = r_y = 1$, $R_{22} = R_{33} = 1$ and the Mises isotropic plasticity model is recovered.

General anisotropy Thus far, we have only considered loading applied along the axes of anisotropy. To derive a more general anisotropic model in plane stress, the sheet must be loaded in one other direction in its plane. Suppose we perform a simple tension test at an angle α_1 to the x-direction; then, from equilibrium considerations we can write the nonzero stress components as

$$\sigma_{11} = \sigma \cos^2 \alpha_1 \quad (1.72)$$

$$\sigma_{22} = \sigma \sin^2 \alpha_1 \quad (1.73)$$

$$\sigma_{12} = \sigma \sin \alpha_1 \cos \alpha_1 \quad (1.74)$$

where σ is the applied tensile stress. Substituting these values in the flow equations and assuming small elastic strains yields

$$d\varepsilon_{11} = [(G + H) \cos^2 \alpha_1 - H \sin^2 \alpha_1] \frac{\sigma}{f} d\lambda \quad (1.75)$$

$$d\varepsilon_{22} = [(F + H) \sin^2 \alpha_1 - H \cos^2 \alpha_1] \frac{\sigma}{f} d\lambda \quad (1.76)$$

$$d\varepsilon_{33} = -[F \sin^2 \alpha_1 + G \cos^2 \alpha_1] \frac{\sigma}{f} d\lambda \quad (1.77)$$

$$d\gamma_{12} = [N \sin \alpha_1 \cos \alpha_1] \frac{\sigma}{f} d\lambda \quad (1.78)$$

Assuming small geometrical changes, the width strain increment (the increment of strain at right angles to the direction of loading, α_1) is written as

$$d\varepsilon_{\alpha_1 + \frac{\pi}{2}} = d\varepsilon_{11} \sin^2 \alpha_1 + d\varepsilon_{22} \cos^2 \alpha_1 - 2d\gamma_{12} \sin \alpha_1 \cos \alpha_1 \quad (1.79)$$

and Lankford's r-value for loading at an angle α_1 is

$$r_{\alpha_1} = \frac{d\varepsilon_{\alpha_1 + \frac{\pi}{2}}}{d\varepsilon_{33}} = \frac{H + (2N - F - G - 4H) \sin^2 \alpha_1 \cos^2 \alpha_1}{F \sin^2 \alpha_1 + G \cos^2 \alpha_1} \quad (1.80)$$

One of the more commonly performed tests is that in which the loading direction is at 45° . In this case

$$r_{45} = \frac{2N - (F + G)}{2(F + G)} \text{ or } \frac{N}{G} = (r_{45} + \frac{1}{2})(1 + \frac{r_x}{r_y}) \quad (1.81)$$

If σ^0 is equal to σ_{11} in the metal plasticity model, $R_{11} = 1$. R_{22}, R_{33} are as defined before for transverse or planar anisotropy and, using the relationships above,

$$R_{12} = \sqrt{\frac{3(r_x + 1)r_y}{(2r_{45} + 1)(r_x + r_y)}} \quad (1.82)$$

1.4.6 Material constitutive models

Normally the equation 1.15 " $\sigma_e^{\text{yield}} = \text{Function}(\varepsilon_e^{\text{p}})$ " is in a general form :

$$\sigma_e^{\text{yield}} = \sigma_0 + F(\varepsilon_e^{\text{p}}) \quad (1.83)$$

$$\sigma_e^{\text{yield}} = \sigma_0(\dot{\varepsilon}^{\text{p}}, T) + F(\varepsilon_e^{\text{p}}, \dot{\varepsilon}^{\text{p}}, T) \quad (1.84)$$

where σ_0 is yield stress and $F(\varepsilon_e^{\text{p}})$ is the back stress in function of plastic strain ε_e^{p} . When the influence of strain rate and temperature is considered, the equation 1.83 can be more complex (equation 1.84). Based on the equation form, the general form under strain rate and temperature influence can be summarized by four categories [36] :

1. Only the yield stress is influenced by strain rate sensitivity and temperature sensitivity, such as the work of Zerilli-Armstrong model for BCC material [37].

$$\sigma_e^{\text{yield}} = A(\dot{\varepsilon}^{\text{p}}, T) \cdot \sigma_0 + F(\varepsilon_e^{\text{p}}) \quad (1.85)$$

2. Only the back stress is influenced by strain rate sensitivity and temperature sensitivity, such as the work of Zerilli-Armstrong model for FCC material [37].

$$\sigma_e^{\text{yield}} = \sigma_0 + A(\dot{\varepsilon}^{\text{p}}, T) \cdot F(\varepsilon_e^{\text{p}}) \quad (1.86)$$

3. Both the yield and the back stress are equally influenced by strain rate sensitivity and temperature sensitivity, such as the work of Cowper-Symonds model [38], Johnson-Cook model [39].

$$\sigma_e^{\text{yield}} = A (\dot{\varepsilon}^{\text{P}}, T) \cdot [\sigma_0 + F(\varepsilon_e^{\text{P}})] \quad (1.87)$$

4. The yield and the back stress are influenced differently by strain rate sensitivity and temperature sensitivity, such as the work of Zhao [40] and Khan-Liang [41].

$$\sigma_e^{\text{yield}} = A (\dot{\varepsilon}^{\text{P}}, T) \cdot \sigma_0 + B (\dot{\varepsilon}^{\text{P}}, T) \cdot F(\varepsilon_e^{\text{P}}) \quad (1.88)$$

General constitutive model A proposed constitutive law of A. Gavrus [42, 43, 44, 45] developed from physical mechanisms of dislocations kinetics, taking into account a mixture Avrami formulation and a material structure evolution at a mesoscopic scale, define in a more general way the constitutive behavior of a large class of metallic alloys, written the equivalent stress variation in the following general form :

$$\sigma_e^{\text{yield}}(\varepsilon_e^{\text{P}}, \dot{\varepsilon}, T) = H(\varepsilon_e^{\text{P}}) \cdot G(\dot{\varepsilon}) \cdot F(T) \quad (1.89)$$

where the hardening term is $H(\varepsilon_e^{\text{P}}) = \sigma_h(\varepsilon_e^{\text{P}}) \cdot (1 - \psi) + \sigma_s \cdot \psi$, strain rate sensitivity $G(\dot{\varepsilon})$ and temperature sensitivity $F(T)$.

The strain rate G and temperature F dependency functions have been also proposed in order to generalize classical Cowper-Symonds, Zerilli-Amstrong, Johnson-Cook, Norton-Hoff or Hirt formulations. Concerning this general mesoscopic law proposed by A. Gavrus [42, 43, 44, 45], the hardening term σ_h can be expressed by Ludwick, Voce or generalized Voce expressions and the material fraction ψ describing the dynamic softening phenomena such as : dynamic recovery, dynamic recrystallizations, twinning, respectively phase transition and dual-phase structure material mixture is written in the following form : $\psi = 1 - e^{-r \cdot \varepsilon_e^{\text{P}}}$ where r and s can have constant values or strain rate and temperature dependency [46, 42, 43, 44, 45]. The saturated term σ_s can be regarded generally as a constant value or in the case of dual-phase material as a variation with the plastic strain.

1.4.6.1 Hardening

Mixture model Based on theory of dislocations glides and starting from the mixture micro-structures formulations proposed by Avrami, the general constitutive rheological model of equation 1.89 describing the variation of equivalent yield stress σ_e^{yield} can be written for a dual-phase material in the following form :

$$H(\varepsilon_e^{\text{P}}) = \sigma_h(\varepsilon_e^{\text{P}}) \cdot w + \sigma_s(\varepsilon_e^{\text{P}}) \cdot (1 - w) \quad (1.90)$$

where ε_e^{P} is the cumulated effective plastic strain. In equation 1.90, $\sigma_h(\varepsilon_e^{\text{P}})$ represents the hardening component, $\sigma_s(\varepsilon_e^{\text{P}})$ the softening component and w the material fraction describing the mixture of the dual-phase material ($w=1-\psi$ is the hardening component fraction).

Ludwik model For a material phase such as the martensite one, the material flow stress σ_e^{yield} can be expressed by the Ludwik hardening model using a classical power form :

$$H(\varepsilon_e^p) = \sigma_0 + n_1(\varepsilon_e^p)^{n_2} \quad (1.91)$$

Ludwik model can be interpreted as a particular term of the general constitutive equation 1.89 defined by $\sigma_h(\varepsilon_p) = \sigma_0 + n_1\varepsilon_p^{n_2}$ and $\psi = 0$.

Voce model The Voce law is a good rheological formulation used to describe the material recovery (hardening with saturation plateaus) such as the plastic flow of the ferrite. The Voce model can be expressed in the following form :

$$H(\varepsilon_e^p) = \sigma_0 + n_1 \cdot \left[1 - e^{-n_2 \cdot \varepsilon_e^p} \right] \quad (1.92)$$

In Equation 1.92, $n_1 + \sigma_0$ is the saturation stress and σ_y is the initial yield stress. Voce model can be interpreted in term of equation 1.90 at the sum of $(n_1 + \sigma_0) \cdot \left[1 - e^{-n_2 \cdot \varepsilon_e^p} \right]$ and $\sigma_0 \cdot e^{-n_2 \cdot \varepsilon_e^p}$ define where $\sigma_S = n_1 + \sigma_0$, $\sigma_h = \sigma_0$ and $\psi = 1 - e^{-n_2 \cdot \varepsilon_e^p}$ is the dynamic recovery material fraction.

Sung-Kim-Wagoner model At the year 2010, Sung et al. [47] proposed a "H/V model" ("Hollomon/Voce" model) considering temperature as an influence parameter on Hardening term. The "H/V model" Hardening term is given by :

$$\begin{aligned} H(\varepsilon_e^p, T) &= p(T)f_H + (1 - p(T))f_V \\ p(T) &= p_1 - p_2(T - T_0) \\ f_H &= H_{HV}\varepsilon_p^{n_{HV}} \\ f_V &= V_{HV}(1 - A_{HV}e^{-B_{HV}\varepsilon_p}) \end{aligned} \quad (1.93)$$

where T_0 is a reference temperature, and p_1 , p_2 , H_{HV} , n_{HV} , V_{HV} , A_{HV} , and B_{HV} are material constants. This model is a particular case of the general constitutive model of equation 1.89 ($\psi = p(T)$).

A proposed hardening model According to the above considerations, only mathematical improvements of classical hardening laws to fit more accurately the experimental data are generally not physically based models. Since DP600 is a dual phase material containing both martensitic and ferritic phases, a proper and physical rheological hardening model should be defined. Based on equation 1.90, using a hardening term $H(\varepsilon_e^p)$ defined by a mixture Avrami formulation with a Voce model σ_s describing the ferritic recovery and the hardening influence σ_h of martensite and introducing the material fraction w to define the content of martensitic phase, the following synthesis model is proposed :

$$H(\varepsilon_e^p) = w \cdot \sigma_{h-martensite} + (1 - w) \cdot \sigma_{s-ferrite} \quad (1.94)$$

1.4.6.2 Temperature sensitivity

When a material is subjected to a high temperature, its strength tends to drop. In laser welding process, this phenomenon has a great effect on evaluation of elasto-plastic material behavior. In order to built a fine welding model and obtain good results of residual stresses, a proper material model taking into account the temperature sensitivity is investigated. Several temperature sensitivity models are taken into account and used to analysis the welding process. A lot of scientific works define the temperature sensitivity term $F(T)$ in function of the homologous temperature T^* . Generally the homologous temperature T^* can be defined as :

$$T^* = \frac{T - T_r}{T_{\text{melt}} - T_r} \quad (1.95)$$

T_{melt} , T , T_r are melting, current, and room temperature, respectively. For DP600 steel, T_{melt} is supposed to be 1803.15 K and the room temperature is 298.15 K.

Arrhenius model The temperature sensitivity of Arrhenius term ([48]) is expressed by :

$$F(T) = \exp\left(\frac{m'Q}{RT}\right) \quad (1.96)$$

Where R is the universal gas constant, m' is an adjustable parameter and Q the activation energy. Majority of thermo-mechanical plasticity applications consider a simplified expression using the thermal parameter $\beta = m'Q/R$.

Hirt model Similar to Arrhenius model, the Hirt model is defined as :

$$F(T) = \exp(-\beta' T) \quad (1.97)$$

Linear model The linear model can be viewed as an one order Taylor development of the exponential Hirt model :

$$F(T) = \exp(-\beta' T) = 1 - \beta' T + \dots \quad (1.98)$$

Using "m" for " β' " and " $T - T_r$ " to instead of " T " and avoid the rest, a simple linear model can be obtained.

The linear term of temperature sensitivity has been proposed by Hutchison ([49]) in 1960s. The material drops linearly with temperature increment.

$$F(T) = 1 - m \cdot (T - T_r) \quad (1.99)$$

Where m is a material coefficient and T_r is reference temperature. The linear model is simple in form but not suitable for rapid material strength drop.

Johnson-Cook model About twenty years later, based on many experimental tests and phenomenological analysis, Johnson-Cook ([39]) proposed a well-founded material model which is still widely used nowadays to describe dynamic forming process. The temperature sensitivity term of Johnson-Cook model can well predict the material temperature sensitivity below about $\frac{1}{2}T_m$ but not well above. For Johnson-Cook model, T_r is room temperature to define T^* in Equation 1.95.

$$F(T) = 1 - T^{*m} \quad (1.100)$$

Khan model A power function with respect to temperature T is proposed by Khan ([50]) as a temperature sensitivity model. For Khan model, T_r is reference temperature, so Khan temperature sensitivity model can use different parameters "m" with different temperature range. The use of different parameters enable the model to predict material temperature sensitivity at high temperature range.

$$F(T) = \left(\frac{T_m - T}{T_m - T_r} \right)^m \quad (1.101)$$

Chen model The Chen model ([51]) contains the temperature sensitivity term as the following form. The Taylor development of the Chen model is " $1 + n \cdot T^{*m} + \dots$ ", so when "n" is set to "-1" and the Chen model can be viewed as a first order approximation of Johnson-Cook model.

$$F(T) = \exp(n \cdot T^{*m}) \quad (1.102)$$

Proposed model The proposed model can be viewed as a more general form equation as Johnson-Cook temperature model ($k = n = 1$).

$$F(T) = (1 - k \cdot T^{*m})^n \quad (1.103)$$

1.4.6.3 Strain rate sensitivity

The power model The power model known as a Norton one [52] is suitable for low strain rates :

$$G(\dot{\varepsilon}) = \left(\frac{\dot{\varepsilon}}{\dot{\varepsilon}_0} \right)^m \quad (1.104)$$

where $\dot{\varepsilon}$ and $\dot{\varepsilon}_0$ are the current and reference strain rates, m is a material parameter.

The Cowper-Symonds model The Cowper-Symonds model [38] is used for small strain rates :

$$G(\dot{\varepsilon}) = \left(1 + \frac{\dot{\varepsilon}}{C} \right)^{1/m} \quad \text{or} \quad G(\dot{\varepsilon}) = 1 + \left(\frac{\dot{\varepsilon}}{C} \right)^{1/m} \quad (1.105)$$

where C and m are material parameters.

The Johnson-Cook model Johnson-Cook model [39] is used for high strain rates :

$$G(\dot{\varepsilon}) = 1 + m \cdot \ln \frac{\dot{\varepsilon}}{\dot{\varepsilon}_0} \quad (1.106)$$

As defined in the part of power law, $\dot{\varepsilon}$ and $\dot{\varepsilon}_0$ are the current and reference strain rates, m is a material parameter.

The general Arcsinus hyperbolic model Starting from the general strain rate sensitivity term proposed by A. Gavrus [42, 43, 44, 45], physically based on kinetics mechanisms of dislocations glides for both static and dynamic loadings, a sinus hyperbolic strain rate sensitivity is defined for describing material behavior for a wide range of strain rate (from small to very large value) :

$$G(\dot{\varepsilon}) = 1 + Ash \left[\frac{1}{2} (\dot{\varepsilon}/\dot{\varepsilon}_0)^D \right], T_0 < T < T_m \quad (1.107)$$

or

$$G(\dot{\varepsilon}) = Ash \left[\frac{e}{2} (\dot{\varepsilon}/\dot{\varepsilon}_0)^D \right], 0.3T_m < T < T_m \quad (1.108)$$

where $Ash(x)$ is the inverse function of $\sinh(x)$ and $Ash(x)$ is defined as :

$$Ash(x) = \ln \left(x + \sqrt{1 + x^2} \right) \quad (1.109)$$

It is shown in the work [42, 43, 44, 45] that this proposed law predict Norton power or Cowper-Symmonds form for small strain rate and Johnson-Cook form for high strain rate. For the welding simulation, the equation 1.107 is used to describe strain rate sensitivity from room temperature to melting temperature, taking into account gradients of strain rate between melted region and static solid boundary (BM-Base material).

Chapitre 2

Experimental data concerning thermo-mechanical behavior of DP600

2.1 Experiment information

2.1.1 Equipment introduction

The tensile test machine “Instron 3369 J9297” is presented in the figure 2.1. It is controlled by an INSTRON software in the computer. During the tensile test, the forces, displacement and corresponding time are recorded. The original experimental data are then analyzed so that force-displacement curves can be converted into true stress-strain ones. A camera is also used to observe the local deformation of the specimen during tensile loads.

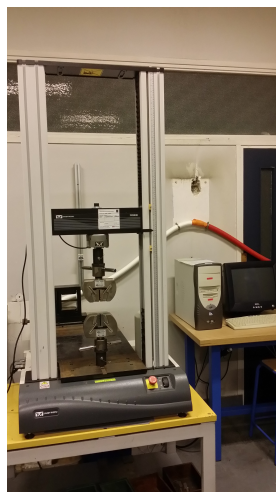


FIGURE 2.1 – The INSTRON tensile test machine (50KN)

2.1.2 Material specimens of tensile tests

A lot of specimens are cut out from a dual phase steel DP600 plate with a thickness of 1.25mm. The geometric dimensions are presented in Figure 2.2. The gauge length and width are 20mm and 10mm, respectively [53]. Compared with standard tensile test dimension, this tensile test specimen is relatively shorter [54] to obtained more precise measurements of the strain ratio (width strain/ thickness strain).

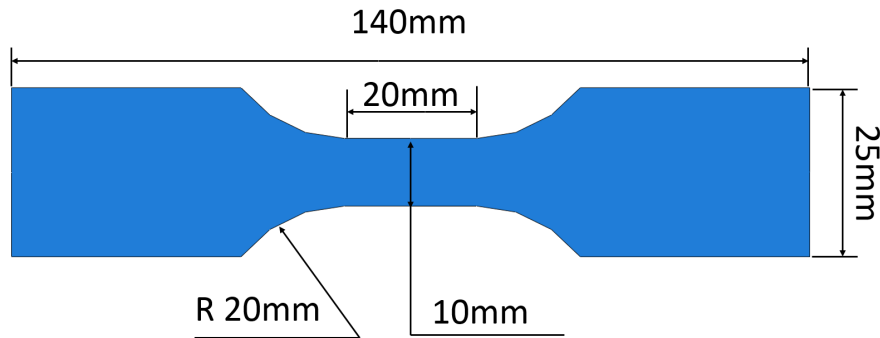


FIGURE 2.2 – Dimension of Specimen

2.1.3 Uniaxial tensile testing

Uniaxial tensile tests are operated according to previous work presented in [55]. According to a longitudinal load, the tensile direction is along the plate rolling direction (0°). For a middle diagonal load the tensile direction has 45° with the plate rolling direction. Along a transversal loading the tensile direction is perpendicular to the plate rolling direction (90°). The steps of uniaxial tensile testing are presented as below :

1. Cut of the specimen as described in the Figure 2.2.
2. Mark on the sample to remember initial length and width of sample
3. Conduct the uniaxial tensile test at the speed of 1mm/min [53] using a digital camera to record mark coordinates
4. Unload the specimen at the tensile strain of 15%
5. Measure variations of the length and width of specimen starting from measured marks
6. Calculate R_{11} , R_{22} , R_{33} , R_{12}
7. Reload the sample for tensile strength

In Figure 2.3, there are points marked along and transverse to stretching direction. The points are illuminated by a KL 1500 compact cold light source. The positions of points are observed by a digital camera. With the help of software Visonstage, the strains along longitudinal and transversal direction ε_x and ε_y are obtained.

The specimen is stretched on machine Instron 3369 with a speed of 1mm/min and all the tensile data are recorded and analyzed by the software Bluehill 2.



FIGURE 2.3 – The mark points of the tensile specimen

2.1.4 Rigidity of Machine during tensile tests

To calculate the rigidity, 6 formula below should be considered :

$$F_{total} = F_{machine} = F_{specimen} \quad (2.1)$$

$$F_{machine} = K_{machine} \cdot \Delta l_{machine} \quad (2.2)$$

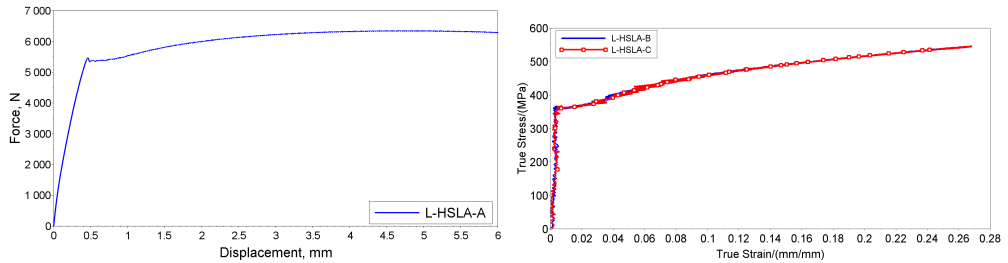
$$F_{specimen} = K_{specimen} \cdot \Delta l_{specimen} \quad (2.3)$$

$$F_{total} = K_{total} \cdot \Delta l_{total} \quad (2.4)$$

$$\Delta l_{total} = \Delta l_{machine} + \Delta l_{specimen} \quad (2.5)$$

$$K_{specimen} = \frac{E_{specimen} \cdot S_{specimen}}{l_{specimen}} \quad (2.6)$$

1. In figure 2.4, with the data detected from tensile test machine and camera, a reference high strength low steel (HSLA) with obvious point of elastic limit is used to compute the rigidity of machine :



(a) Force-displacement curve using LVDT sensor (b) true stress-strain curve using camera measurements

FIGURE 2.4 – Tensile test of HSLA steel : (a) Force-displacement curve using LVDT sensor, (b) True stress-strain curve using camera measurements

2. Based on data in figure 2.4, the Young's Modulus of specimen is calculated :

$$E_{\text{HLSA}} = \frac{\sigma}{\varepsilon} = \frac{328.90\text{MPa} - 29.17\text{MPa}}{0.0037 - 0.0022} = 199.82\text{GPa} \quad (2.7)$$

3. Since the length of specimen $L_{\text{speciman}} = 20\text{mm}$ and the cross-area of the specimen $S_{\text{speciman}} = 15\text{mm}^2$, the rigidity of specimen K_{specimen} can be get :

$$K_{\text{specimen}} = \frac{E_{\text{HLSA}} \cdot S_{\text{speciman}}}{L_{\text{speciman}}} = \frac{199.82\text{GPa} \times 15\text{mm}^2}{20\text{mm}} = 1.499 \times 10^5\text{N/mm} \quad (2.8)$$

4. The total rigidity K_{total} is :

$$K_{\text{total}} = F_{\text{total}} / \Delta L_{\text{total}} = \frac{5092\text{N}}{0.4005\text{mm}} = 1.271 \times 10^4\text{N/mm} \quad (2.9)$$

5. Use the equations from Equation 2.1 to Equation 2.6, the rigidity of machine is calculated :

$$K_{\text{machine}} = \frac{1}{\frac{1}{K_{\text{total}}} - \frac{1}{K_{\text{specimen}}}} = \frac{K_{\text{total}} \cdot K_{\text{specimen}}}{K_{\text{specimen}} - K_{\text{total}}} \quad (2.10)$$

$$= \frac{14.99 \times 1.271}{14.99 - 1.271} \times 10^4\text{N/mm} = 1.389 \times 10^4\text{N/mm}$$

For the tensile tests on dual phase DP600 steel, the same rigidity $1.389 \times 10^4\text{N/mm}$ is used for experimental data improvement supposing the machine rigidity do not varies with the change of test material from HSLA to DP600 steel.

2.2 Material thermo-mechanical constitutive model of DP600

2.2.1 Hardening term

A tensile test of cold rolled dual phase steel DP600 specimen is conducted at room temperature and initial strain rate $8.33 \times 10^{-4}\text{s}^{-1}$ along the longitudinal direction (0°) to obtained the reference true stress-strain curve. The result are presented in figure 2.5.

In FEM simulation of ABAQUS, the plastic flow of dual phase steel DP600 is input either by a pair of true stress - plastic true strains points or by a UHARD subroutine. The plastic part of true stress-plastic strain curve is presented in figure 6.2.

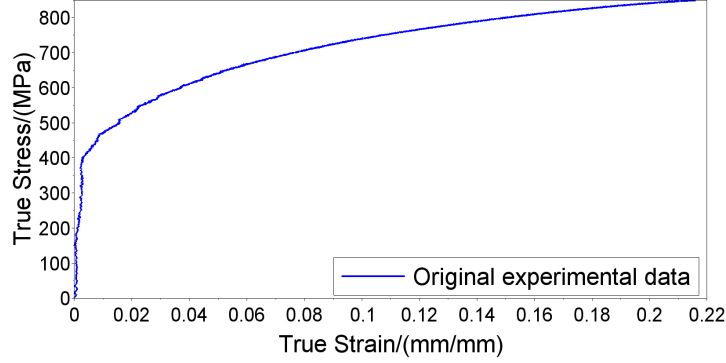


FIGURE 2.5 – True stress-strain curve of dual phase steel DP600 at room temperature and initial strain rate $8.33 \times 10^{-4} \text{s}^{-1}$

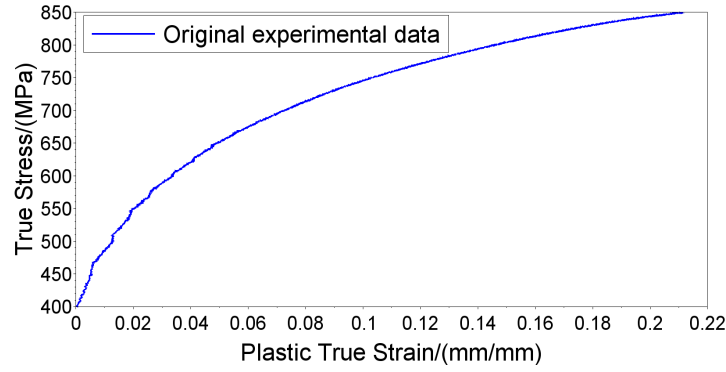


FIGURE 2.6 – The plastic flow curve of dual phase steel DP600 at room temperature and initial strain rate $8.33 \times 10^{-4} \text{s}^{-1}$

2.2.1.1 Ludwik model

Ludwik model is introduced in equation 1.91 of section 1.4.6.1 with the formula given by :

$$\sigma_e^{\text{yield}}(\varepsilon_p) = \sigma_0 + n_1 \varepsilon_p^{n_2}$$

Based on the experimental data of figure 6.2 and using a non-linear regression method, parameters are identified for the Ludwik model of dual phase steel DP600 at room temperature and initial strain rate 0.0005s^{-1} . The Ludwik model with identified parameters is named “Classical Ludwik model 01” and the formula is given by :

$$\sigma_e^{\text{yield}}(\varepsilon_p) = 400 + 980 \varepsilon_p^{0.48} \quad (2.11)$$

For the DP600 steel, the Ludwik model cannot fully fit all the original experimental curve, so a mathematically modified form of Ludwik model is proposed to represent the observed material behavior :

$$\sigma_e^{\text{yield}}(\varepsilon_p) = \sigma_y + n_1 \varepsilon_p^{n_2} + n_3 \varepsilon_p + n_4 \quad (2.12)$$

Based on the experimental data of figure 6.2, identified “Modified Ludwik model” has the form :

$$\sigma_e^{\text{yield}}(\varepsilon_p) = 400 + 1690\varepsilon_p^{0.5} - 1240\varepsilon_p - 65 \quad (2.13)$$

As can be seen in figure 2.7, “Classical Ludwik model 01” correspond to the classical form (equation 2.11) and “Modified Ludwik model” becomes only a mathematical improvement of the Ludwik one. It is important to note that the addition of the linear term “ $n_3\varepsilon_p + n_4$ ” in Equation 2.12 permits to fit more accurately the experimental data but has not any physical meaning. The straight line is used to corresponding to small plastic strain values of the obtained non-linear regression curve.

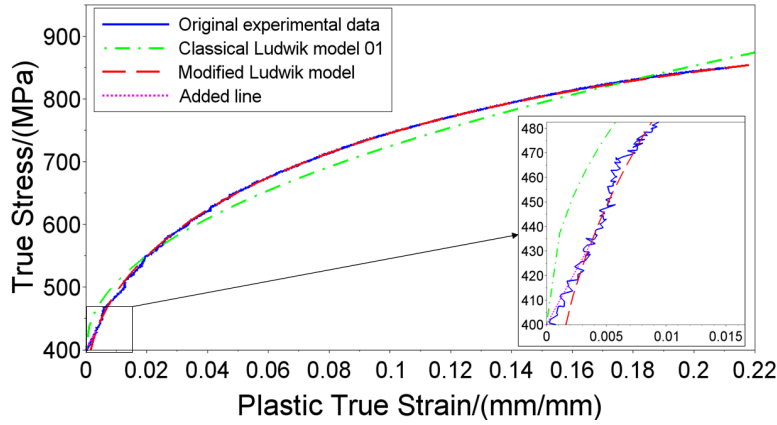


FIGURE 2.7 – Comparison of Ludwik model and experimental DP600 data

2.2.1.2 Voce model

The Voce law is a good rheological formulation used to describe material recovery (hardening with saturation plateaus) such as the plastic flow of the ferrite. The Voce model can be expressed in the following form [56] :

$$\sigma_e^{\text{yield}}(\varepsilon_p) = \sigma_y + n_1 \cdot [1 - \exp(-n_2\varepsilon_p)]$$

In the framework of equation 1.89, $n_1 + \sigma_y$ is the saturation stress σ_s and σ_y is the initial yield stress and $\psi = 1 - \exp(-n_2\varepsilon_p)$.

Based on the experimental data of figure 6.2, the identified “Classical Voce model 01” can be written by :

$$\sigma_e^{\text{yield}}(\varepsilon_p) = 400 + 555 \cdot [1 - \exp(-15.5\varepsilon_p)] \quad (2.14)$$

It can be seen that the plastic flow stress can not be perfectly fitted by the Voce equation, so a mathematically modified form is proposed in order to fit the experimental curve.

$$\sigma_e^{\text{yield}}(\varepsilon_p) = \sigma_y + n_1 \cdot [1 - \exp(-n_2\varepsilon_p)] + n_3\varepsilon_p \quad (2.15)$$

The identified “Modified Voce model” is given by :

$$\sigma_e^{yield}(\varepsilon_p) = 400 + 270 \cdot [1 - \exp(-30\varepsilon_p)] + 900\varepsilon_p \quad (2.16)$$

As is seen in figure 2.8, “Classical Voce model 01” is the original form of Voce law and “Modified Voce model” only a mathematical improvement form of the classical Voce equation. The addition of the linear term “ $n_3\varepsilon_p$ ” in equation 2.15 permits to obtain a best fit of the original experimental data. This mathematical improvement is not based on the physical mechanisms characterizing the material plasticity and of the real mechanical behavior of hardness martensite / softening ferrite mixture, but can be regarded as a first approximation if an equal repartition of two phases is considered.

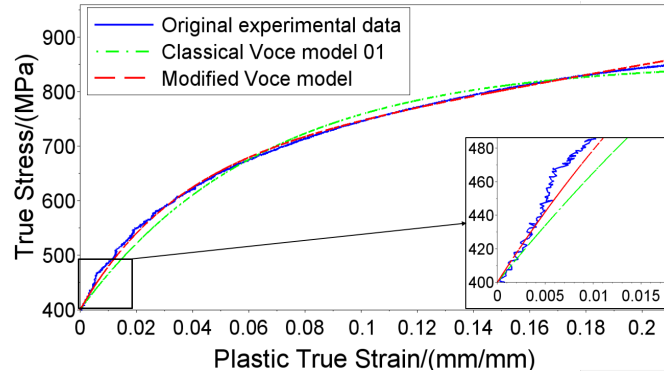


FIGURE 2.8 – Comparison of Voce model and experimental DP600 data

Regarding all these previous identified classical and improved law, it can be noted that a relatively poor accuracy is observed to describe behaviors for small plastic strain and more greater ones.

2.2.1.3 Proposed synthesis model

According to the above considerations, only mathematical improvements of classical hardening laws to fit more accurately the experimental data are generally not physically based on material microstructure or plastic phenomena. Since DP600 is a dual phase material containing both martensitic and ferritic phases, a proper and physical rheological hardening model should be defined. Starting from general constitutive model proposed by A. GAVRUS [43, 42, 44, 45], neglecting any phase transformation or dynamic phenomena (i.e. $\psi = 0$), using a hardening term σ_h defined by a mixture Avrami formulation with a classical Voce model describing the ferritic recovery and introducing the material fraction w to define Ludwik hardening of martensitic phase, a synthesis model is proposed as presented in section 1.4.6.1 (equation 1.94) to define the hardening function $H(\varepsilon_p)$ and to express the equivalent stress in the following form :

$$\sigma_e^{yield}(\varepsilon_p) = w \cdot (\sigma_{y_m} + n_1\varepsilon_p^{n_2}) + (1 - w) \cdot \{ \sigma_{y_f} + n_3 \cdot [1 - \exp(-n_4\varepsilon_p)] \} \quad (2.17)$$

During laser welding material the martensite volume fraction is changed, from experimental point of view, and it is difficult to estimate the volume fraction of martensite. Dual phase DP600 steel has generally a martensite volume fraction from 0.2 to 0.6. An average value of 0.4 has been considered in a first time. Furthermore, experimental tensile tests for DP600 steel with different martensite fraction must be used to identify σ_{ym} and σ_{yf} . Here $\sigma_y = \sigma_{ym} = \sigma_{yf}$.

Identification with martensite fraction of “w=0.40” A firstly rough identification for an average value of w equal to 0.4 concerning the martensitic fraction is obtained in the below equation :

$$\sigma_e^{yield}(\varepsilon_p) = 0.40 \cdot (400 + 1660\varepsilon_p^{0.63}) + 0.60 \cdot \{400 + 340 \cdot [1 - \exp(-27.5\varepsilon_p)]\} \quad (2.18)$$

This proposed synthesis model is a mixture of the “Classical Ludwik model 02” and the “Classical Voce model 02” defining respectively hardening of martensite and recovery of ferrite.

The “Classical Ludwik model 02” is given by :

$$\sigma_e^{yield}(\varepsilon_p) = 400 + 1660\varepsilon_p^{0.63} \quad (2.19)$$

The “Classical Voce model 02” is identified and written by :

$$\sigma_e^{yield}(\varepsilon_p) = 400 + 340 \cdot [1 - \exp(-27.5\varepsilon_p)] \quad (2.20)$$

The figure 2.9 plot the difference between the experimental data, the classical Ludwik model 02 and the classical Voce model 02 and the proposed synthesis model (identified in the plastic strain range of all experimental results i.e. [0, 0.2]). It can be seen the advantage of the proposed synthesis model to obtain a very good agreement with all experimental measurements describing the real elasto-plastic behavior of dual phase DP600 steel, both for plastic strain range [0, 0.05] and [0.05, 0.2] corresponding to a large class of welding process.

Identification with martensite fraction of “w=0.20” Based on a martensite fraction w=2.0 (close to the real value of studied DP600 steel), the parameters of proposed synthesis model are re-identified. The re-identified parameters of proposed synthesis model named as "Proposed synthesis model 02" is given by :

$$\sigma_e^{yield}(\varepsilon_p) = 0.20 \cdot (400 + 3411.28\varepsilon_p^{0.6014}) + 0.80 \cdot \{400 + 234.40 \cdot [1 - \exp(-27.1092\varepsilon_p)]\} \quad (2.21)$$

Proposed synthesis model 1 (w=1) is presented as :

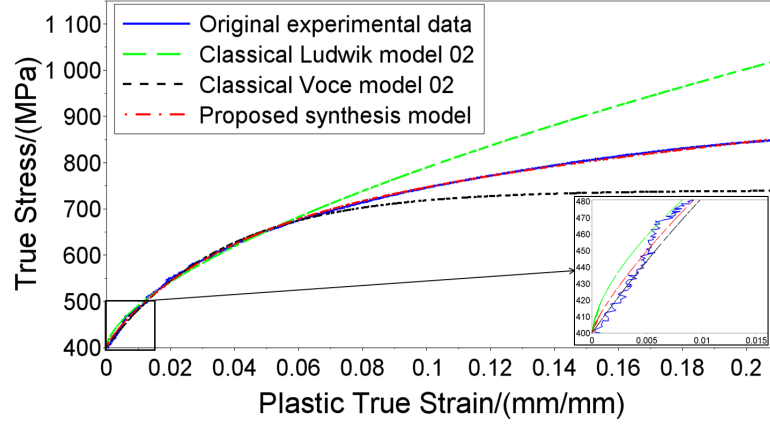


FIGURE 2.9 – Comparisons of rheological models and experimental DP600 data

$$\sigma_e^{\text{yield}}(\varepsilon_p) = 400 + 3411.28\varepsilon_p^{0.6014} \quad (2.22)$$

Proposed synthesis model 0 ($w=0$) is presented as :

$$\sigma_e^{\text{yield}}(\varepsilon_p) = 400 + 234.40 \cdot [1 - \exp(-27.1092\varepsilon_p)] \quad (2.23)$$

The "Proposed synthesis model 02", "Proposed synthesis model 0" and "Proposed synthesis model 1" are compared with original experimental data in figure 2.10 :

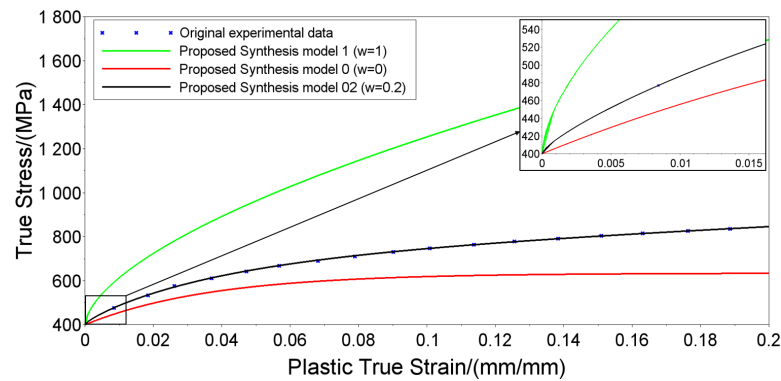


FIGURE 2.10 – Comparison of rheological models and experimental DP600 data

It can be noted in this case that equation 2.22 describes only the martensite phase hardening ($w=1$) and equation 2.23 describes the ferrite phase recovery ($w=0$).

2.2.1.4 Synthesis hardening models parameters

Table 2.1 presents all the rheological parameters of DP600 identified for different hardening models. The mathematical form of the hardening models are discussed in the following parts. It can be noted that the proposed synthesis model equation 2.17 describe with a high accuracy the real hardening behavior of the analyzed DP600 dual phase steel.

TABLE 2.1 – Rheological coefficients corresponding to different DP600 hardening models

	σ_y	n_1	n_2	n_3	n_4	w	Equation	Nonlinear regression ε_p range
Classical Ludwik model 01	400	980	0.48	-	-	-	(2.11)	[0, 0.2]
Classical Ludwik model 02	400	1660	0.63	-	-	-	(2.19)	[0, 0.05]
Modified Ludwik model	400	1690	0.5	-1240	-65	-	(2.13)	[0, 0.2]
Classical Voce model 01	400	555	15.5	-	-	-	(2.14)	[0, 0.2]
Classical Voce model 02	400	340	27.5	-	-	-	(2.20)	[0, 0.05]
Modified Voce model	400	270	30	900	-	-	(2.16)	[0, 0.2]
Proposed synthesis model (w=0.4)	400	1660	0.63	340	27.5	0.40	(2.17 et 2.18)	[0, 0.2]
Proposed synthesis model 02 (w=0.2)	400	3411.3	0.60	234.4	27.1	0.20	(2.17 et 2.21)	[0, 0.2]
Proposed synthesis model 1 (w=1)	400	3411.3	0.60	234.4	27.1	1	(2.17)	-

2.2.2 Temperature sensitivity

2.2.2.1 Temperature sensitivity of a high strength steel

The temperature sensitivity of a high strength steel described in the work of Chen [57] is presented in table 2.2. The thermal softening fraction is the ratio of the stress at elevated temperature to the value at room temperature. The thermal softening fraction is presented with different temperature sensitivity models by setting $F(T_{room}) = 1$.

Johnson-Cook temperature sensitivity model Several temperature sensitivity model are used to fit the experimental data above. Generally the homologous temperature T^* can be defined as equation 1.95 :

$$T^* = \frac{T - T_r}{T_{melt} - T_r}$$

T_{melt} , T , T_r are melting, current, and room temperature, respectively. For DP600 steel, T_{melt} is supposed to be 1803.15 K and the room temperature is 298.15 K.

For Johnson-Cook model [39], T_r is room temperature to define T^* in equation 1.100.

$$F(T) = 1 - T^{*m}$$

To fit the experimental data of table 2.2 obtained, $m=1.5$ are used. So the Johnson-Cook sensitivity model can be written as :

$$F(T) = 1 - T^{*1.5} \quad (2.24)$$

TABLE 2.2 – Temperature sensitivity at different temperatures and strains

Temperature, °C	$f_{0.2}=F(\varepsilon_{0.002})$	$f_{0.5}=F(\varepsilon_{0.005}^{total})$	$f_{1.5}=F(\varepsilon_{0.015}^{total})$	$f_{2.0}=F(\varepsilon_{0.020}^{total})$
22	1	1	1	1
60	0.95	0.96	0.96	0.96
120	0.94	0.94	0.96	0.96
150	0.96	0.95	0.98	0.99
180	0.92	0.92	0.97	0.97
240	0.89	0.89	0.99	1
300	0.89	0.9	0.975	0.985
410	0.87	0.87	0.94	0.94
460	0.8	0.81	0.85	0.84
540	0.75	0.75	0.76	0.74
600	0.6	0.61	0.56	0.59
660	0.43	0.44	0.43	0.42
720	0.21	0.21	0.22	0.22
770	0.14	0.14	0.15	0.14
830	0.08	0.08	0.08	0.09
940	0.05	0.05	0.05	0.05

Khan temperature sensitivity model A power function with respect to temperature T is proposed by Khan [50] as a temperature sensitivity model defined using equation 1.101.

$$F(T) = \left(\frac{T_m - T}{T_m - T_r} \right)^m$$

According to the above experimental data, $m=0.5$ are identified. So the Khan sensitivity model can be written as :

$$F(T) = \left(\frac{T_m - T}{T_m - T_r} \right)^{0.5} \quad (2.25)$$

Chen temperature sensitivity model The Chen model [51] temperature sensitivity term is written in equation 1.102 :

$$F(T) = \exp(n \cdot T^{*m})$$

The parameters $m=-28.418$ and $n=4.254$ are obtained from the fit of experimental data and the temperature sensitivity of Chen model is given by :

$$F(T) = \exp(4.254 \cdot T^{*-28.418}) \quad (2.26)$$

A proposed temperature sensitivity model The proposed model can be viewed as a more general form of Johnson-Cook temperature model ($k = n = 1$).

$$F(T) = (1 - k \cdot T^{*m})^n$$

For the high strength steel, parameters of $m=4.027$, $n=38.629$ and $k=0.699$ are obtained and the proposed temperature sensitivity model becomes :

$$F(T) = (1 - 0.699 \cdot T^{*4.027})^{38.629} \quad (2.27)$$

Polynomial temperature sensitivity model To precisely describe the temperature sensitivity model of high strength steel, two polynomial temperature functions are used with parameters of :

$$295.15K < T < 993.15K :$$

$$F(T) = 1.55 - 3.50 \times 10^{-3} \cdot T + 7.00 \times 10^{-6} \cdot T^2 - 4.82 \times 10^{-9} \cdot T^3 \quad (2.28)$$

$$993.15K < T < 1213.15K :$$

$$F(T) = 5.18 - 7.83 \times 10^{-3} \cdot T + 2.30 \times 10^{-6} \cdot T^2 + 5.35 \times 10^{-10} \cdot T^3 \quad (2.29)$$

Synthesis of DP600 temperature sensitivity models As is seen in figure 2.11, the thermal soften fraction is presented with different temperature sensitivity models by setting $F(T_{room}) = 1$. The Johnson-Cook model and the Khan model can be suitable from room temperature to about 800 K, but not appropriate above 800 K. The Chen model and the proposed model are near to experiment data except for the data around 1000 K. The proposed model and the polynomial expression describe precisely the experimental data.

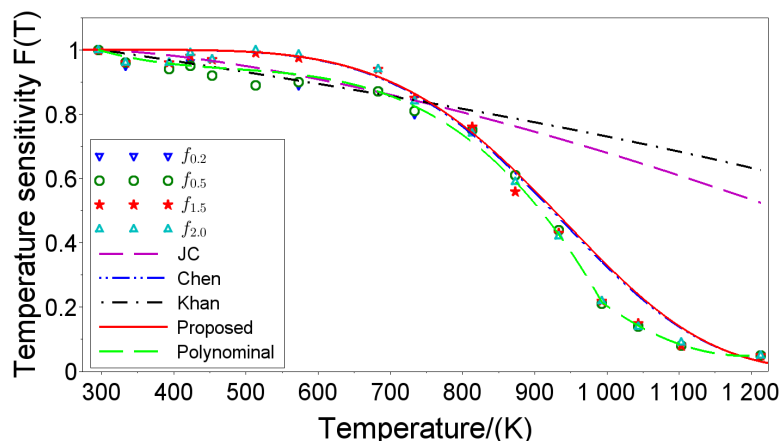


FIGURE 2.11 – Temperature dependence of experiment data and simulation models

2.2.2.2 Temperature sensitivity of dual phase steel DP600

According to the work of Aydemir et al. [58], the temperature influence on mechanical properties of DP600 are measured from 20°C to 800°C. The thermal softening fraction is the ratio of the stress at elevated temperature to that at room temperature. With the yield strength $R_{p0.2}$ and ultimate strength R_m of the work of Aydemir et al., the temperature sensitivity of DP600 plastic hardening model are calculated by :

$$F(T) = \frac{\sigma^T}{\sigma^{20^\circ\text{C}}} = \frac{R_{p0.2}^T + R_m^T}{R_{p0.2}^{20^\circ\text{C}} + R_m^{20^\circ\text{C}}} \quad (2.30)$$

TABLE 2.3 – The yield and ultimate strength from literature data [58] and the corresponding temperature sensitivity of DP600

Temperature (°C)	20	200	400	600	700	800
Yield strength $R_{p0.2}$ (MPa)	431	413	378	168	84	38
Ultimate strength R_m (MPa)	671	630	619	224	110	46
Temperature sensitivity $F(T)$	1	0.946	0.905	0.356	0.176	0.076

Based on the temperature sensitivity experimental data of Aydemir et al [58], the DP600 temperature sensitivity model are re-identified.

Johnson-Cook temperature sensitivity model The Johnson-Cook temperature sensitivity model with parameter $m=1.5$ is also suitable for the dual phase material DP600 :

$$F(T) = 1 - T^{*1.5} \quad (2.31)$$

Khan temperature sensitivity model The Khan temperature sensitivity model with parameter $m=0.5$ is also suitable for the dual phase material DP600 :

$$F(T) = \left(\frac{T_m - T}{T_m - T_r} \right)^{0.5} \quad (2.32)$$

Chen temperature sensitivity model The parameters $m=-51.61$ and $n=4.23$ are used to fit the experimental data and the temperature sensitivity of Chen model is given by :

$$F(T) = \exp(4.23 \cdot T^{*-51.61}) \quad (2.33)$$

A proposed temperature sensitivity model For dual phase steel DP600, the following temperature sensitivity model is obtained :

$$F(T) = (1 - 0.491 \cdot T^{*4.212})^{103.17} \quad (2.34)$$

Polynomial temperature sensitivity model To precisely describe the temperature sensitivity model of high strength steel, two polynomial temperature functions are used with parameters of :

$$20^{\circ}C < T < 400^{\circ}C :$$

$$y = 1.099792 - 0.0003741T + 0.0000001T^2 \quad (2.35)$$

$$400^{\circ}C < T < 800^{\circ}C :$$

$$y = 4.5386048 - 0.0074378T + 0.0000030T^2 \quad (2.36)$$

2.2.2.3 Synthesis of DP600 temperature sensitivity models

As is seen in Figure 2.12, the temperature sensitivity $F(T)$ computed by different models are presented. The linear model, Johnson-Cook model and Khan model can be suitable from room temperature to about 700 K, but not appropriate above 700 K. The proposed model and Chen model are near to experiment data from room temperature up to 1100 K.

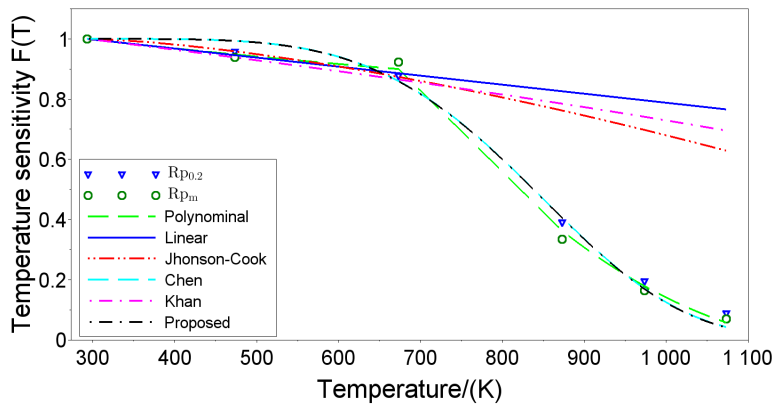


FIGURE 2.12 – Temperature sensitivity of experiment data and simulation models

2.2.3 Strain rate sensitivity

2.2.3.1 The hardening term for hot rolled DP600 steel

In figure 2.13, the true stress-strain curves obtained at different initial strain rate of $0.2s^{-1}$, $0.02s^{-1}$, $0.002s^{-1}$ and $0.0002s^{-1}$ at room temperature are presented. It is shown

in figure 2.13 that with the increase of strain rate, the flow stress increases. According to

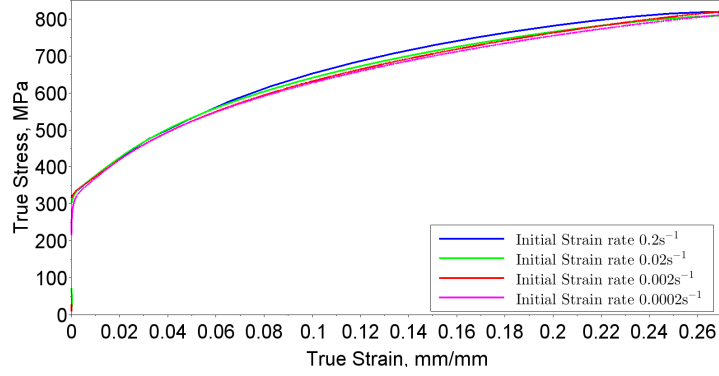


FIGURE 2.13 – True stress-strain curves obtained at different strain rate at room temperature

the experimental data of DP600 at initial strain rate 0.002 s^{-1} in figure 2.13, parameters of the proposed hardening model of hot-rolled DP600 dual phase steel are identified using nonlinear regression method. The identification results are given in following equation.

$$\begin{aligned}
 H(\varepsilon_p) = & 0.2 \times (2772.93 \times \varepsilon_p^{0.5765} + 331.74) \\
 & + 0.8 \times (289.34 \times [1 - \exp(-11.5505 \times \varepsilon_p)] \\
 & + 331.74)
 \end{aligned} \tag{2.37}$$

According to equation 2.37, the simulation flow stress curve of DP600 are plotted and compared with experimental DP600 steel flow stress data obtained from uniaxial tensile test. The comparison are presented in figure 2.14

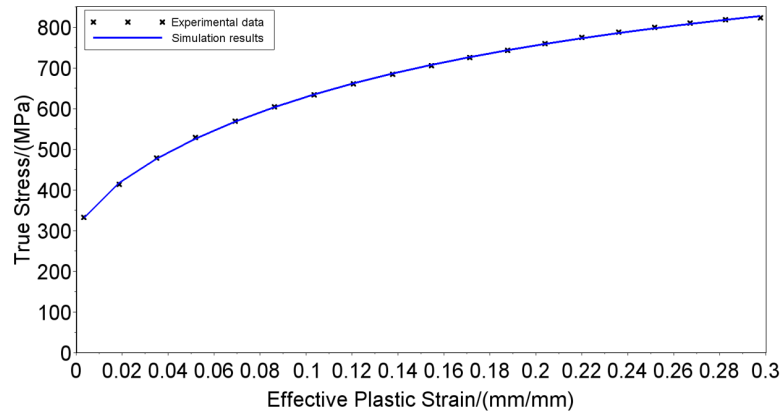


FIGURE 2.14 – The hardening model describing DP600 dual phase steel plastic behavior

It is shown that the hardening model described by equation 2.37 can well predict the flow stress of DP600 dual phase steel at room temperature and initial strain rate $0.0002s^{-1}$ for all range of plastic strain $[0,0.3]$.

2.2.3.2 Identification of the strain rate sensitivity based on hot-rolled DP600 dual phase steel

The hardening term can only predict the material behavior of DP600 at particular strain rate. For material behavior of DP600 at other strain rate, the strain rate sensitivity are used to predict the flow stress change with respect to strain rate change. Based on the hot-rolled DP600 dual phase steel hardening term, the strain rate sensitivity model proposed by A. Gavrus [43, 42] is identified. The temperature sensitivity under room temperature is set to 1. The reference strain rate for the Hardening term is based on the flow stress curve at initial strain rate $0.0002s^{-1}$. The obtained reference strain rate is 0.997, so approximation $\bar{\epsilon}_0 \approx 1$ is used. The result is given in equation 2.38 by :

$$G(\dot{\bar{\epsilon}}) = 0.7022851 \times \left[1 + Ash \left(\frac{1}{2} \dot{\bar{\epsilon}}^{0.0160537} \right) \right] \quad (2.38)$$

Combine the hardening, temperature sensitivity and strain rate sensitivity, the DP600 flow stress model considering strain, temperature and strain rate are written in equation 2.39.

$$\begin{aligned} \sigma(\epsilon_p, T, \dot{\bar{\epsilon}}) = & \{ 0.2 \times (2772.93 \times \epsilon_p^{0.5765} + 331.74) + 0.8 \times [289.34 \\ & \times (1 - e^{-11.5505 \times \epsilon_p}) + 331.74] \} \times (1 - 0.49 \times T^{*4.21})^{103.17} \\ & \times 0.7022851 \times \left[1 + Ash(0.5 \cdot \dot{\bar{\epsilon}}^{0.0160537}) \right] \end{aligned} \quad (2.39)$$

According to equation 2.39 that the simulation flow stress curves are plotted and compared with experimental data obtained from uniaxial tensile tests. The comparisons are presented in figure 2.15.

It is shown from figure 2.15, the material plasticity model for DP600 dual phase steel predicts the plastic flow stress at different strain rate very well for the room temperature.

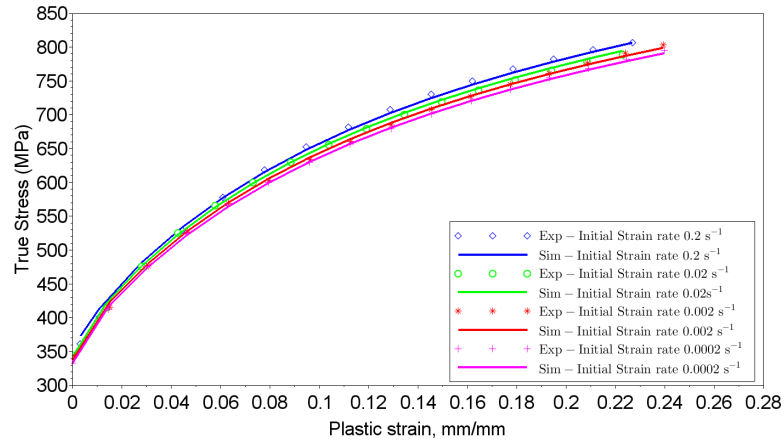


FIGURE 2.15 – Comparison between experimental data and simulation results of DP600 flow stress at room temperature 20°C

2.2.3.3 Use of experimental data from literature [3] to identify a larger zone of strain rate sensitivity

After the investigation of strain rate sensitivity at room temperature for the DP600 dual phase steel, the strain rate sensitivity at higher temperatures are investigated based on literature data obtained by S. Curtze et al. [3]. The plastic flow stress from tensile experiments and from literature [3] are presented in figure 6.5.

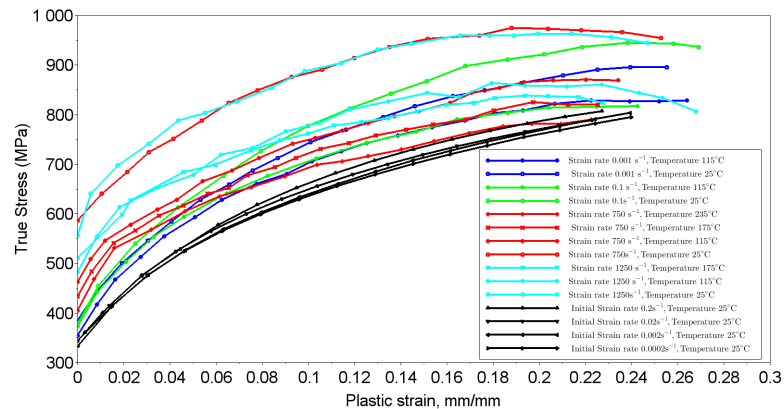


FIGURE 2.16 – The plastic flow stress of DP600 dual phase steel at different temperatures and strain rates

From figure 6.5, it is observed that at various conditions with different temperatures and strain rates, the flow stresses of literature [3] are higher than our experimental data, but the shapes of flow stress-strain curves are similar. Based on the identified hardening

term at room temperature of the authors' experimental data, the strain rate sensitivity are identified and discussed below.

2.2.3.4 Strain rate sensitivity of DP600 dual phase steel

Based on all the above data, the following strain rate sensitivity term based on the plastic flow curves of figure 6.5 is obtained :

$$G(\dot{\varepsilon}) = 0.8042232 \times \left[1 + Ash \left(\frac{1}{2} \left(\frac{\dot{\varepsilon}}{96.077} \right)^{0.0005410 \times T - 0.1443611} \right) \right] \quad (2.40)$$

Using the hardening, the temperature sensitivity and the strain rate sensitivity, the DP600 flow stress model finally written by :

$$\begin{aligned} \sigma(\varepsilon_p, T, \dot{\varepsilon}) = & \{ 0.2 \times (2772.93 \times \varepsilon_p^{0.5765} + 331.74) + 0.8 \times [289.34 \\ & \times (1 - e^{-11.5505 \times \varepsilon_p}) + 331.74] \} \times (1 - 0.49 \times T^{*4.21})^{103.17} \\ & \times 0.8042232 \times \left[1 + Ash \left(\frac{1}{2} \left(\frac{\dot{\varepsilon}}{96.077} \right)^{0.0005410 \times T - 0.1443611} \right) \right] \end{aligned} \quad (2.41)$$

The flow stress simulation results from the DP600 dual phase steel material model using the strain rate sensitivity model of equation 2.40 is presented in figure 2.17.

Though the flow stresses of DP600 dual phase steel at temperature of 25°C, 115°C and 175°C with different strain rate of 0.2s⁻¹, 0.02s⁻¹, 0.002s⁻¹ and 0.0002s⁻¹ have a lot of variations, the identified strain rate material model proposed by A. Gavrus [43, 42] can get a fairly good accordance with acceptable small differences.

2.2.4 Planar anisotropy defined by Hill theory

For nearly all plate materials, the rolling process would bring anisotropy to the plate. The anisotropy of DP600 steel is considered as planar anisotropy according to Hill-48 theory. The Hill's potential function is an extension of the Mises function, which can be expressed in terms of rectangular Cartesian stress components in equation 1.54 :

$$f(\sigma) = [F(\sigma_{22} - \sigma_{33})^2 + G(\sigma_{33} - \sigma_{11})^2 + H(\sigma_{11} - \sigma_{22})^2 + 2L\sigma_{23}^2 + 2M\sigma_{31}^2 + 2N\sigma_{12}^2]^{1/2}$$

where F, G, H, L, M, and N are the Hill coefficients obtained by tests of the material in different orientations. The effective stress $f(\sigma)$ is a scalar that dependent on material stress state and is a key value defining the plastic flow. Generally it is assumed to estimate this effective stress from the equivalent stress corresponding to the plastic flow curve obtained by tensile tests along the rolling direction. The specimen geometry used for tensile tests is shown in figure 2.18. The planar anisotropy is estimated using

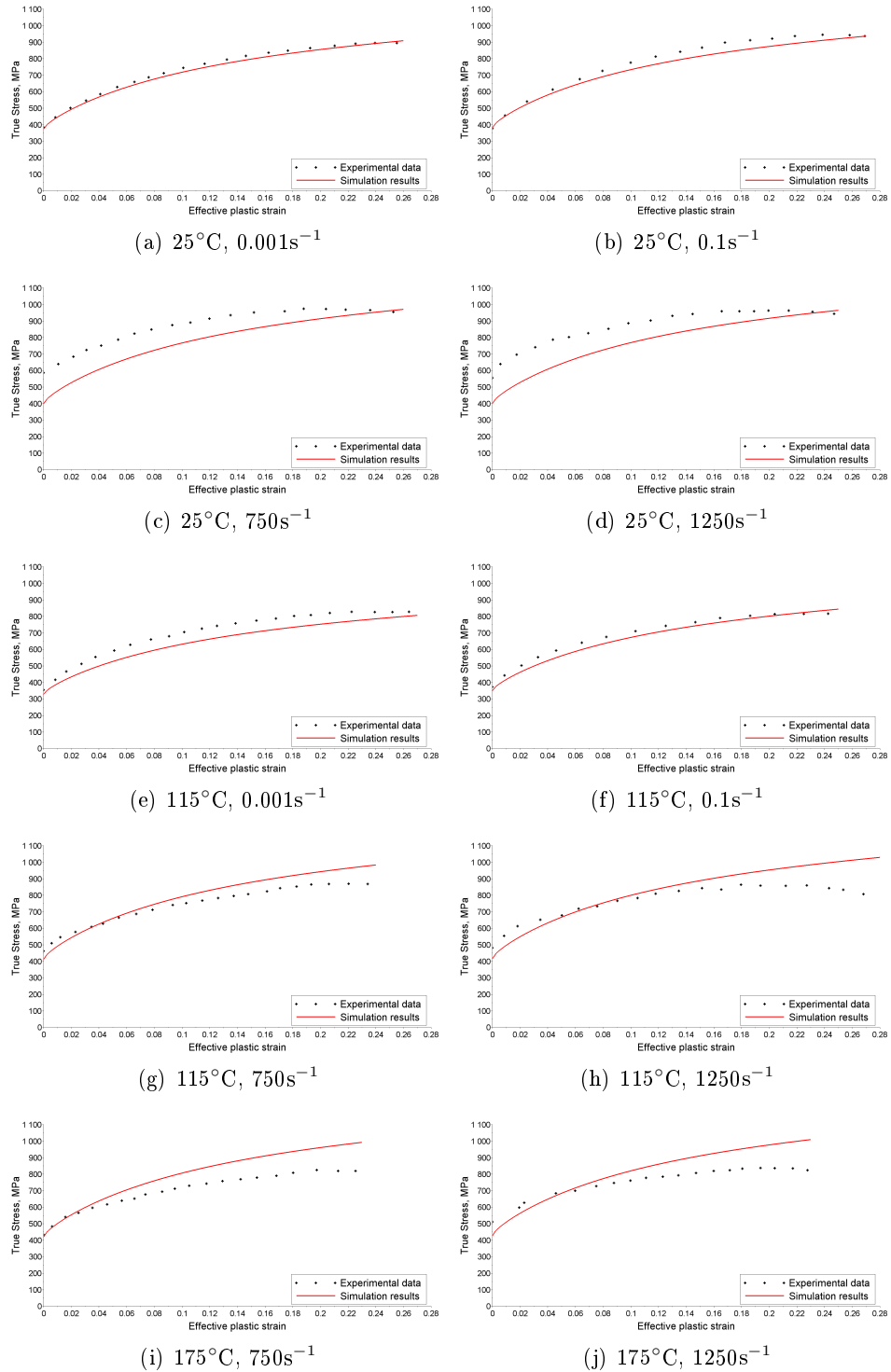


FIGURE 2.17 – The comparison between experimental data from literature [3] and simulation results of DP600 dual phase steel general constitutive model

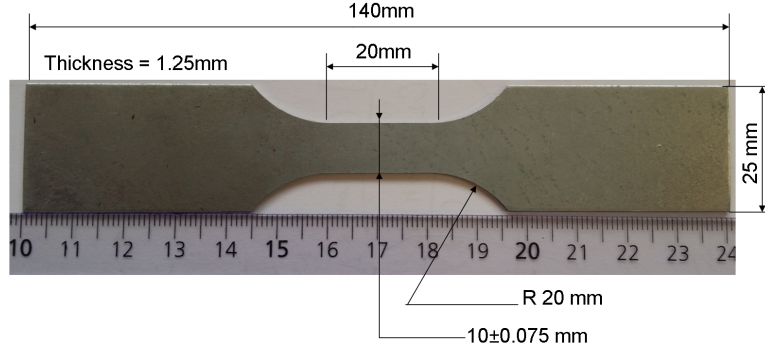


FIGURE 2.18 – Dimensions of specimen for tensile test

Hill-48 theory and the parameters are estimated according to the computation method presented in the work of Ohashi ([53]).

At the beginning, the length and width of test area are noted as l_0 and w_0 , respectively. The tensile test are conducted with a strain rate of $10^{-2} s^{-1}$. When the total strain $\varepsilon_{total} = 0.15$, specimen are unloaded and the length l_1 and width w_1 are measured. Along the three specimen directions, the corresponding measurements are presented in Table 2.4.

TABLE 2.4 – Measurement of dimension change of tensile test

	$\theta = 0^\circ$	$\theta = 45^\circ$	$\theta = 90^\circ$
Initial length l_0 /mm	19.70	19.62	19.58
Unload length l_1 /mm	21.18	21.30	21.04
Initial width w_0 /mm	10.06	10.06	10.06
Unload width w_1 /mm	9.70	9.74	9.72

The Lankford coefficient r (also known as width/thickness strain ratio) can be computed by

$$r = \frac{\ln(w_1/w_0)}{\ln(w_1 \cdot l_1/w_0 \cdot l_0)} \quad (2.42)$$

Specimens with different angles $\theta = 0^\circ$, $\theta = 45^\circ$ and $\theta = 90^\circ$ are analyzed by tensile tests. The corresponding anisotropic coefficients are noted as r_0 , r_{45} and r_{90} respectively.

Based on the r -values, the Hill parameters can be estimated using following formula :

$$F = \frac{r_0}{(1 + r_0)r_{90}} \quad (2.43)$$

$$G = \frac{1}{1 + r_0} \quad (2.44)$$

$$H = \frac{r_0}{1 + r_0} \quad (2.45)$$

$$N = \frac{(1 + 2r_{45})(r_0 + r_{90})}{2(1 + r_0)r_{90}} \quad (2.46)$$

For planar anisotropy, if set $R_{11} = 1$, the other anisotropic yield stress ratios R_{22} , R_{33} and R_{12} are defined using the following relationships

$$R_{22} = \sqrt{\frac{r_{90}(r_0 + 1)}{r_0(r_{90} + 1)}} \quad (2.47)$$

$$R_{33} = \sqrt{\frac{r_{90}(r_0 + 1)}{r_0 + r_{90}}} \quad (2.48)$$

$$R_{12} = \sqrt{\frac{3(r_0 + 1)r_{90}}{(2r_{45} + 1)(r_0 + r_{90})}} \quad (2.49)$$

Based on the test results presented in table 2.4 and using the above equations, Lankford coefficients and Hill's coefficients of DP600 steel are presented in table 2.5.

TABLE 2.5 – The Lankford coefficients and Hill's parameters of DP600 steel

r_0	r_{45}	r_{90}	R_{11}	R_{22}	R_{33}	R_{12}
1.0123	0.6487	0.9160	1	0.9748	0.9777	1.1172
F	G	H	N			
0.5492	0.4969	0.5031	1.2017			

Two yield surfaces predicted by Hill48 model and Von Mises criterion of the dual phase steel DP600 sheet are shown in figure 2.19.

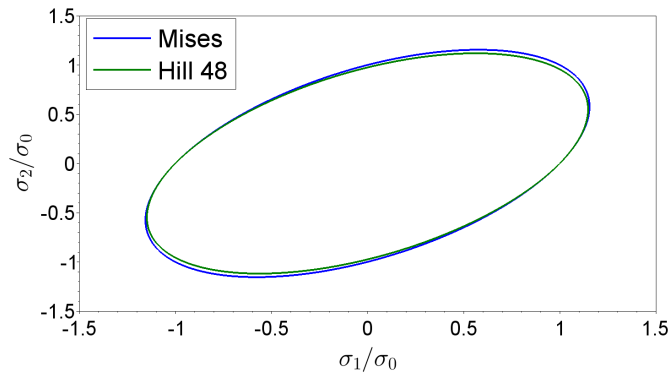


FIGURE 2.19 – Yield surface predicted by Hill48 anisotropic model and Von Mises criterion

2.3 Neutron diffraction observation

To validate the obtained numerical results, specimen experiments have been realized using neutrons diffraction technique. A gauge volume of $1 \times 1 \times 5 \text{ mm}^3$ was defined with the 5 mm aperture along the axis of the laser weld to improve intensity while has been possible (i.e. for transverse and longitudinal measurements only). For axial measurements, a sampling volume of $1 \times 1 \times 1 \text{ mm}^3$ was used. The crystallographic texture of the base material was determined by neutron diffraction technique on the dedicated 4-circles diffractometer 6T1 at LLB ([60]). From the $\{110\}$, $\{200\}$ and $\{211\}$ pole figures, using a $5^\circ \times 5^\circ$ grid, the Orientation Distribution Function (ODF) was calculated using LaboTex software ([61]). The texture exhibits slight $\{hkl\}\langle 110 \rangle$ reinforcements, typical of a cold rolled ferritic steel, but the calculated texture index is rather low (1.6). An elastic self-consistent calculation was performed considering the experimental texture to deduce the $\{110\}$ dependent values for Young's modulus (E_{110}) and Poisson's ratio (ν_{110}) : as a result, it appears that the elastic anisotropy should remain very low, with E_{110} ranging between 220 and 226 GPa, and ν_{110} between 0.31 and 0.35, depending on the considered direction. In a first approach, triaxial residual stresses were thus calculated from the measured strains applying the Hooke's law (equation 2.50) in the isotropic elasticity approximation :

$$\sigma_i = \frac{E_{110}}{1 + \nu_{110}} \left[\varepsilon_i + \frac{\nu_{110}}{1 - 2\nu_{110}} \sum_j \varepsilon_j \right] \quad (2.50)$$

where $i, j =$ axial, transverse and normal, and with the following values for Young's modulus $E_{110} = 220 \text{ GPa}$ and Poisson's ratio $\nu_{110} = 0.33$.

Since the characterized zones close to (Heat Affected Zone, HAZ) and within the weld (Fusion Zone, FZ) may have their microstructures more or less strongly affected by the welding process, chemical composition is likely to be heterogeneous depending on the distance from the center of the weld. One would thus commit an error if considering the base material as the reference material for unstrained lattice spacing. So, due to the low thickness of the studied plates, a zero normal stress state was assumed (i.e. a plane stress state), and theoretical reference lattice spacing and diffraction angles $2\theta_0$ could thus be calculated for each measurement point, applying the following formula (2.51), ([62]) :

$$2\theta_0 = 2 \cdot \sin^{-1} \left(\frac{(1 + \nu) \cdot \sin\theta_{normal} \cdot \sin\theta_{axial} \cdot \sin\theta_{transverse}}{(1 - \nu) \cdot \sin\theta_{axial} \cdot \sin\theta_{transverse} + \nu \cdot \sin\theta_{normal} \cdot (\sin\theta_{axial} + \sin\theta_{transverse})} \right) \quad (2.51)$$

Considering the difficulty to obtain a reliable unstressed reference sample, the reference (unstressed) $d_{0,\{110\}}$ lattice spacing required for strain calculations was determined assuming a zero normal stress at 5 mm in the base metal from the center of the weld.

Two plates of dual phase DP600 with geometry described in chapter 4.6 are assembled by laser lap welding with laser 4kW, welding speed 3m/min and laser focusing

point 2mm below up surface. The material is has a material rolling orientation that have 30° with transversal path. The results obtained by neutron diffraction are presented in figure 2.20.

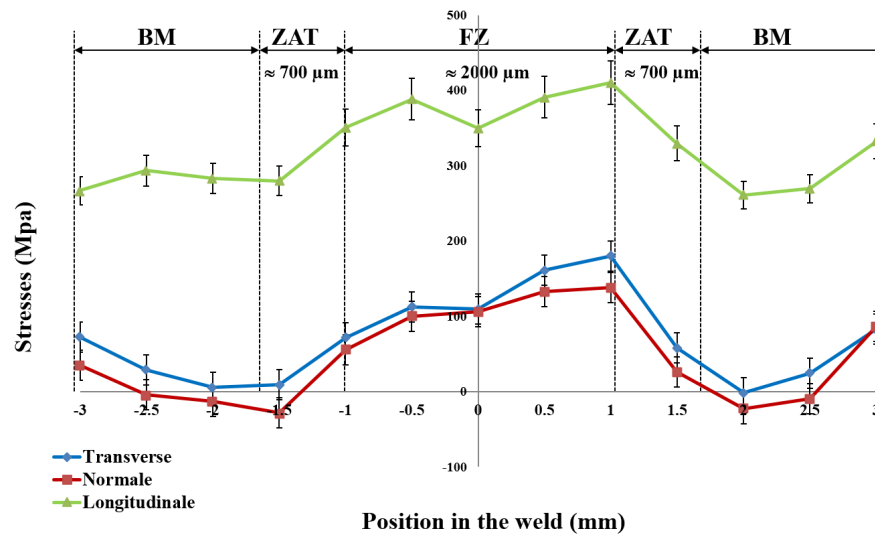


FIGURE 2.20 – The computed results of residual stresses based on neutron diffraction method

In the above figure, the green curve stands for residual stress along longitudinal direction (welding direction), the blue one for transversal direction (transverse to welding direction). The results obtained by neutron diffraction will be compared with the numerical simulation results in the chapter 5.

Chapitre 3

Cellular Automaton Model

In the laser welding of metallic plates, the solidification process offer the laser fusion which plays an important role on microstructure morphology and residual stresses estimation. This chapter present a Cellular Automaton (CA) model used to simulate growth of dendrite grains, especially concerning martensite phase obtained from fusion solidification process of dual phase DP600 steel regarded at initial time the base metal.

3.1 Development of Cellular Automaton model

The concept of Cellular Automaton (CA) was first discovered by Stanislaw Ulam and John Von Neumann, who were both researchers at the Los Alamos National Laboratory in New Mexico in the 1945 [63]. Ulam was studying the growth of crystals and Von Neumann was imagining a world of self-replicating robots which can build copies of themselves. The collision of the two thoughts gives the birth of the CA. At 1970s, a two-dimensional cellular automaton called Conway's Game of Life is created [64]. The game greatly simplify Von Neumann's idea and attracted a lot of interest. In 2002, Wolfram published a book [65], *A New Kind of Science*, which discusses the CA method in detail.

In brief, Cellular Automaton (CA) is a system made up of many "cell" objects. The cell has a state or many states and some neighborhoods. In the rule defined by programmers, the CA can iterate on itself. On the whole, the cells can provide an determined resulted according to the defined rules. Because the variation of cells is so complicated, the CA has the ability to provide us a method to simulate microstructure evolution in a reasonable way.

As a physical and flexible enough model to incorporate the complexity of simulated phenomena, CA method has been successfully used in the simulation of solidification microstructure evolution. Though CA method have many advantages in microstructure simulation, a major problem hold back the development of CA method. The problem is that the crystallographic axes orientations of dendrite grains are influenced by the CA network [66]. In 2008, a limited angles method [67] was proposed which gives the

cellular automaton a new life for microstructure solidification simulation. In this work, CA method is applied in laser welding microstructure simulation with limited angles method.

3.2 Cell

Cell is for Cellular Automaton Method as an Element such as for Finite Element Analysis. It is the basic part for doing the computation. For a problem going to be analysed, the zone of the problem has to be divided into many small parts. In Cellular Automaton, the small part is the cell. For 3D analysis, the cell may be cube, regular tetrahedron, rectangular solid or hexagonal pillar. For 2D analysis the cell may be square (such can be seen in figure 3.1), rectangle, regular triangle or regular hexagon. No matter what shape is the cell, the shape of cell has one thing in common : the shape of the cell are locally the same. In this way, the rule can be equally applied to all cells.

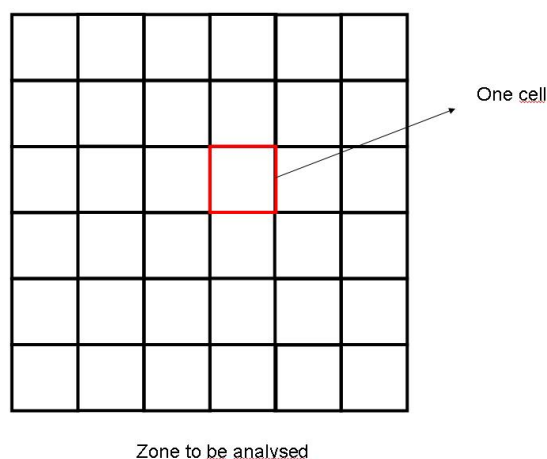


FIGURE 3.1 – A cell in analysis zone

3.3 States

In cellular Automaton, every cell have some states. The state make all the cell belong to different groups. According to the state, different rules can be applied to a cell and different colors can be assigned to a cell. A cell can have numerical computation of many states. For CA evolution, the state of cell determines which kind of rule is used for a cell. For display results, the state of cell determines which color is used on a screen. In the microstructure simulation proposed by this thesis work, some states are very important for the numerical computation as described below :

3.3.1 Bulk, mould and base metal

The state of cell may be bulk for the melting weld, mould wall for the weld or base metal. The two state, bulk or mould, differ the rules of nucleation probability to a cell. The state of bulk or mould or base metal are determined by the temperature history of the weld. As is generally known, the heterogeneous nucleation is much faster than an homogeneous nucleation. The energy needed to form a nucleus at a surface is less than that in the bulk, so the nucleation probability at the mould wall of weld is much bigger than the nucleation probability in the bulk. As is seen in the figure 3.2, the bulk of the weld is red (liquid part), the mould wall is green (semi-solid part), and the base metal (solid part) that is not melt yet is grey. The green part has the most probability to form a nuclei.

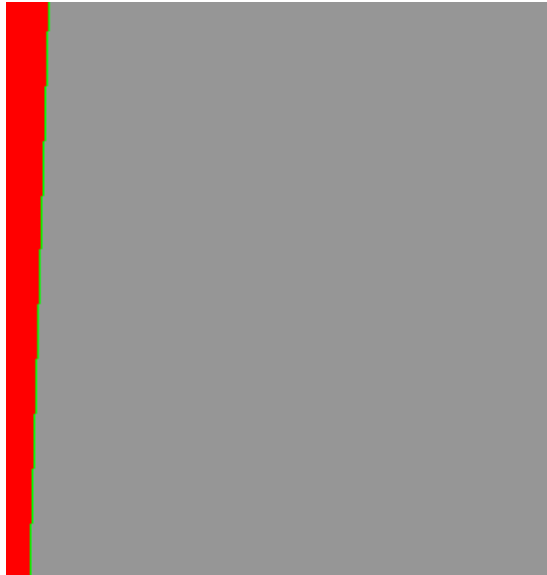


FIGURE 3.2 – The bulk and the mould wall of the weld

3.3.2 Liquid, growing or solid

The state of cell may be solid, growing (at the interface) or liquid. As is seen in figure 3.3. The color blue means the cell is solidified, the color green means the cell in transition state from liquid to solid and the white part means the cell in melting liquid. In a circle of the program simulation solidification, different computations are used on cells of different state. For example, the nucleation is only used on liquid cells, while the green and blue part are free of nucleation consideration. In solidification simulation, the white part turns to green, and green part turns to blue if condition is suitable, which means that liquid cell changes to semisolid cell (growing cell or cell at the interface) and semisolid cell changes to solid cell.

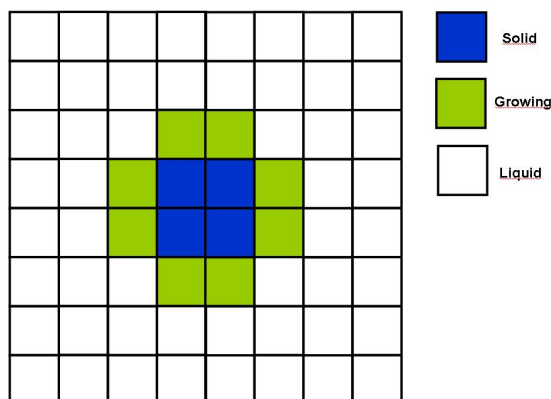


FIGURE 3.3 – States of a growing grain

3.3.3 Direction Index

A state number of growth direction is needed in the dendrite grain growth simulation. In Cellular Automaton, the message is passed by neighborhood cells and cannot jump the neighborhood cell to the other cell. This way of passing message induce a problem that the preferential growth direction is affected by the mesh type. The simulation can not keep the preferential growth direction [66]. A method proposed by Zhan [68] use several cells to remember the growth direction. In this work, the method proposed by Zhan is used to solve problem of the preferential direction of growth.

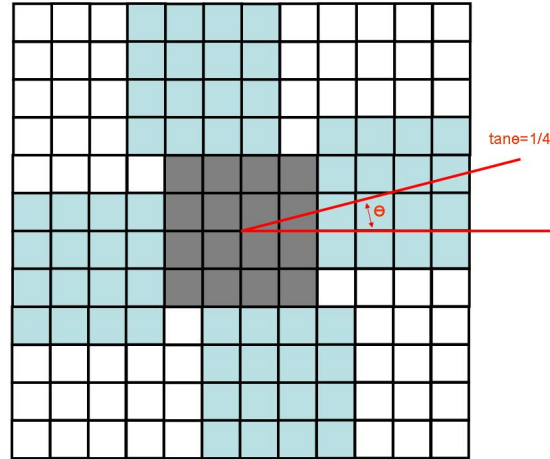
As is seen in figure 3.4, a schematic of preferential direction of growth is presented. The center cell with grey color is a big cell made up of 16 small cells. The small cell is the basic element of CA model and the big cell is just used to solve with the problem of preferential direction of growth. After the big center cell solidify, four big neighbor cells are set to growing state and the center point of the neighbor big cell is just on preferential direction of growth. The growth direction angle θ is the angle between the preferential direction of growth and x-direction. In theory, the growth direction angle θ can be any value when $\arctan(n/m)$ take any n and m value. But if the value of n and m is too big, the big cell will become to large which is not good for CA simulation.

In this work, 12 different θ values are used to present 48 preferential direction of growth. The big cell is still small comparing with the whole simulation zone. All solid cell have a state number of direction index, from 1 to 12, indicating the growth direction. The direction index number is shown in table 3.1

TABLE 3.1 – $\tan \theta$ and direction index

Direction Index	1	2	3	4	5	6	7	8	9	10	11	12
$\tan \theta$	1	3/4	2/3	1/2	1/3	1/4	0	-1/4	-1/3	-1/2	-2/3	-3/4

With respect to table 3.1, different preferential directions are presented in figure 3.5.

FIGURE 3.4 – The growth direction angle θ

When a small cell nucleates (the cell change its state from liquid to growing), the cell gets a random direction index number marking the preferential direction of growth of the grain. With the direction index randomly selected, the nucleation cell change its own state to growing, together with other small cells, they form a big nucleation cell. All the small cell that is in the zone of the big nucleation cell will change their state from liquid to growing. When the big nucleation cell solidify(change state from growing to solid), all the small cells in the big nucleation cell changes their state from liquid to solid. Meanwhile, according to the direction index, four big cell will nucleation around the solidified big cell. In this way, the dendrite grain grows along a specific direction. For 48 directions with 12 direction index numbers, please see the figure 3.5 below.

3.4 Parameters

Every cell of a CA model contains some parameters regarded as the message of every cell. Focusing on one parameter of one cell, the parameter will be changed step by step according to some rules defined by the programmer. In solidification simulation, these rules should reflects the reality and be reasonable to ensure that the computation is meaningful.

In the microstructure simulation, the temperature, the solute concentration, the solid fraction, the growing velocity and all the other parameters change according to some rules during the solidification process. For numerical computation, all the parameters are put into a cell and are considered. In figure 3.6, a small cell contains the parameters of : local cell temperature, concentration of the solution of liquid, concentration of the solution of solid, solid fraction, interface growth velocity and so on.

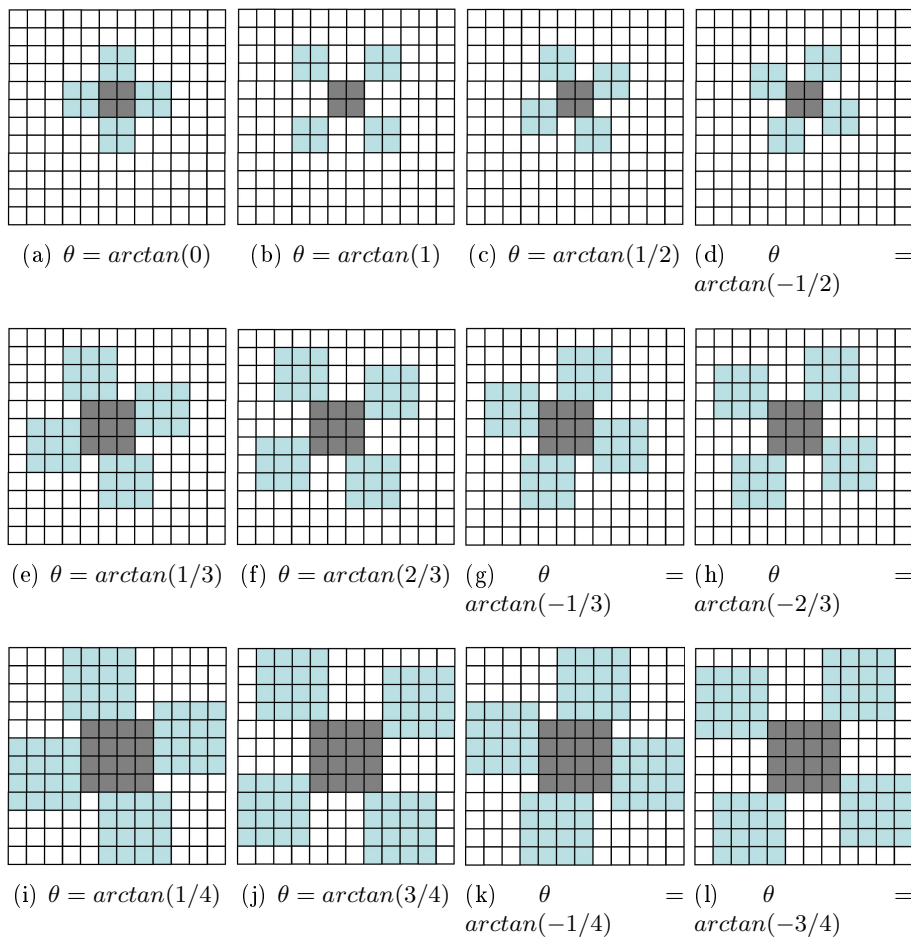


FIGURE 3.5 – The direction of the grain

- Temperature
- Solute Concentration in liquid
- Solute Concentration in solid
- Solid fraction
- Solute Concentration in total
- Interface curvature
- Interface growth velocity
-
-
-

FIGURE 3.6 – Parameters in a cell

3.4.1 Parameters of the 2D CA model

The parameters are approximated according to literatures [69, 70]. In the developed 2D CA model for microstructure simulation during a laser welding solidification process, the parameters are presented in table 3.2.

TABLE 3.2 – Parameters of CA model

Symbol	Meaning	Magnitude
k	Partition coefficient	0.3
d_l	Liquid diffusion coefficient	$3.0 \times 10^{-9} \text{m}^2 \text{s}^{-1}$
d_s	Solid diffusion coefficient	$3.0 \times 10^{-12} \text{m}^2 \text{s}^{-1}$
a	Cell size	$1.0 \times 10^{-6} \text{m}$
T_L^{EQ}	liquidus temperature	1530 °C
Γ	Gibbs Thomson Coefficient	$1.9 \times 10^{-7} \text{Km}$
m_L	Liquidus slope	-80 °C/%wt
$\Delta T_{e,\sigma}$	edge undercooling deviation	20°C
$\Delta T_{b,\sigma}$	bulk undercooling deviation	50°C
$\Delta T_{e,max}$	edge mean undercooling	20°C
$\Delta T_{b,max}$	bulk mean undercooling	50°C

3.5 Operation of update parameters

Figure 3.7 shows the general iteration rules for CA. For a cell, it has many parameters, noted as $Para(x, y, z, \dots)$. To explain the calculation rule, just take one parameter “x” as example. At step “n”, the parameter “x” of the center cell is “ $Para_x^n = x_5^n$ ”. At step “n+1”, according to rules of calculation, the state changes to “ $Para_x^{n+1} = x_5^{n+1}$ ”.

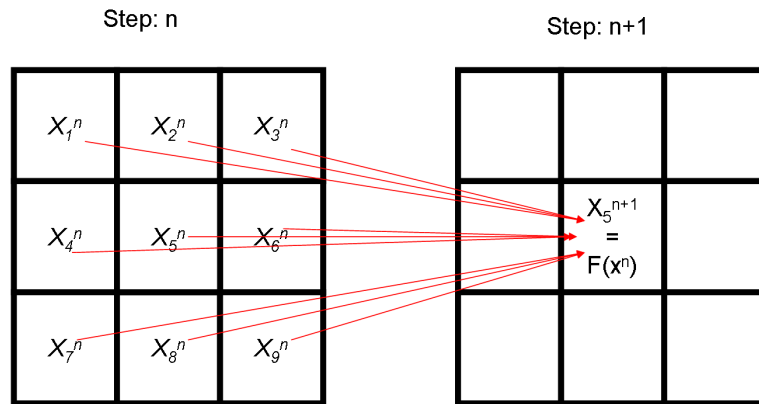


FIGURE 3.7 – basic iteration rule for each cell

The rule can be generally described as :

$$Para_x^{n+1} = x_5^{n+1} = f(x_1^n, x_2^n, x_3^n, x_4^n, x_5^n, x_6^n, x_7^n, x_8^n, x_9^n) \quad (3.1)$$

To update parameters, all cells in the simulation zone is scanned. For every one single cell, according to the state, some rules is applied to the single cell. The parameters of the single cell(here also named as the center cell) is changed, using the parameters from a previous step of the center cell and the neighbor cell. The operation of update parameters happens step by step until that some condition is reached.

3.6 Neighbourhood

In square CA model, two kinds of neighborhood is usually used. One is Von Neumann neighborhood and the other one is Moore neighborhood (see figure 3.8). Von Neumann neighborhood takes four cells as neighbor cells while Moore neighborhood takes eight.

As has been described in figure 3.7, the function rule $f(x)$ is the rules defined by the programmer. If the parameters from x_1^n to x_9^n are all used to compute the x_5^{n+1} , then Moore neighborhood is used. If only x_5^n and $x_2^n, x_4^n, x_6^n, x_8^n$ are used, then Cellular Automaton uses Von Neumann neighborhood is used.

The parameters of center cell are computed using the parameters from the previous step of the center cell and its neighbor cells. Since Von Neumann neighborhood takes less cell than Moore neighborhood for calculation, Von Neumann neighborhood usually has more efficiency but less accuracy than Moore neighborhood.

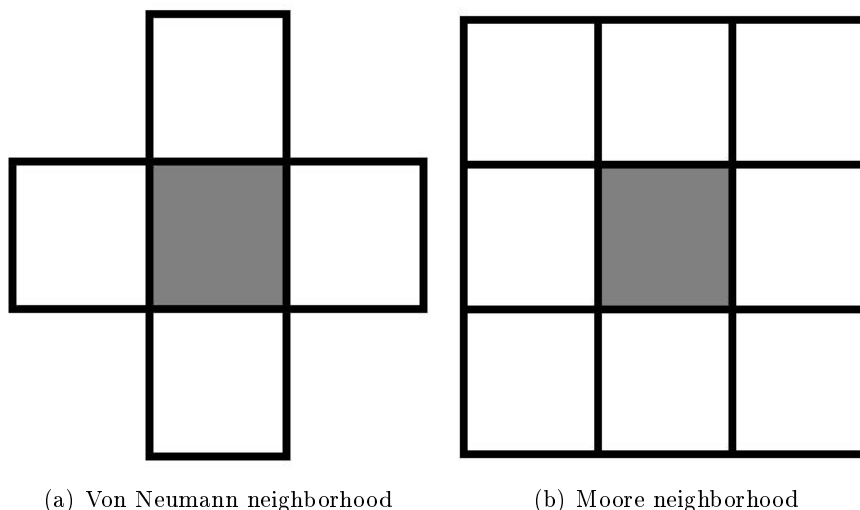


FIGURE 3.8 – Two types of neighborhood of Cellular Automaton

3.7 Rules of CA model

As is presented in figure 3.7, the function rule is now $F(x)$ as a mathematical function. For different parameter or state of different state cell, the function rule can be different. The most simple rule $F(x)$ is $x^{n+1} = F(x) = x^n$, which means the parameter keeps the same.

Two examples about function rule are introduced, one rule is to change the state, another is to define the growth action of dendrite grain.

3.7.1 Melting rule

As is seen in figure 3.9, the melt rule can be described as :

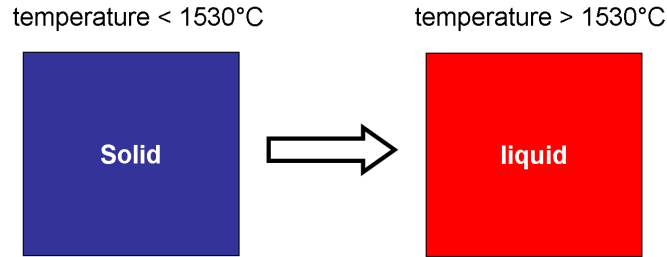


FIGURE 3.9 – Rule for state change

$$S_m^{n+1} = F(\text{cellt}) = \begin{cases} 0 & , \text{cellt} > 1530^\circ\text{C} \\ 9 & , \text{cellt} < 1530^\circ\text{C} \end{cases} \quad (3.2)$$

Where S_m^{n+1} is the state of melt of the $n+1$ step, “cellt” is the temperature of the center cell. The liquidus temperature of DP600 is 1530°C . The state number 0 means the cell is melt and 9 means the cell is in solid state.

3.7.2 Grain growth rule

Based on function rule of the CA model, state parameters of the cells will be changed. In time sequence, all the parameters of cells will be changed according to its neighborhood cell states and its own state one step by another step.

As is seen in figure 3.9, four figures describe the grain growth rule. In the figure, the white cell stands for liquid cell, green for growing, and blue for solid. The color change is through change the state number of the cell.

First in figure 3.10(a), nucleation is made at center point. The center big cell began to grow. Second in figure 3.10(b), the center big cell became solid. All small cells around the center big cell turn to growing state. Third in figure 3.10(c), four big neighbor cell turn their states to growing. The position of the big neighbor cell is determined according

to the direction index number. Four in figure 3.10(d), when four big neighbor cells turn to solid, all small cells around the solid big cell turn to growing state. Based on the way that four figures describe, a dendrite grain can grow along a particular direction.

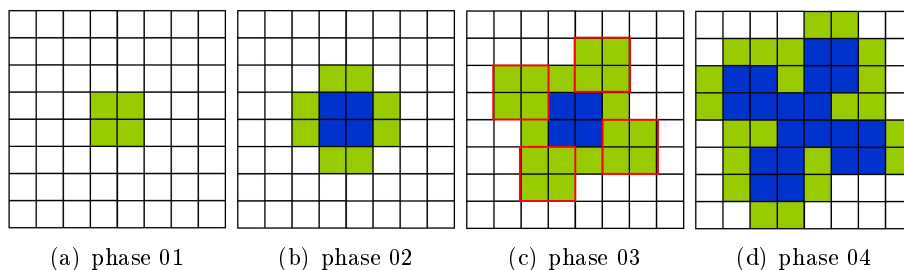


FIGURE 3.10 – Rule of grain growth

3.8 Mathematical description of the solidification model

The flowchart in the figure 3.11 describes the program procedure of numerical simulation concerning the solidification of weld. The temperature database is got from 3D Abaqus Simulation. T_{melt} stands for melting temperature. The concentration of all cells are the same at the beginning.

In the flowchart, a certain step of calculation is performed.

Step 1 : Read temperature. Load temperature data from ABAQUS, compute local temperature for every cell in the Microstructure Evolution Model.

Step 2 : Determine the cell state. If the cell temperature is above liquidus temperature, then the cell state is liquid. Some cells' state maybe growing because of nucleation or growing calculation. The solid state of cell can be achieved by solidification, which means that fs (fraction solid is equal to 1).

Step 3 : Compute time increase. If temperature of all the cell is above the liquidus temperature, no solidification behavior need to be computed. Calculate time increment to let temperature drop down.

Step 4 : nucleation. Based on the undercooling degree, the nucleation probability is computed and applied to every suitable cell.

Step 5 : Growth. For those cells whose state is growing. The fs (solid fraction) is computed, using the velocity value of previous step. If fs (solid fraction) is equal to 1, then the growing cell will change to solid cell.

Step 6 : Curvature and anisotropy. Based on the fs value around the growing cell, the curvature is computed. The curvature is used, same as anisotropy, for calculation interface concentration of growing cells.

Step 7 : Concentration at the interface. Calculate liquid and solid concentration at the interface.

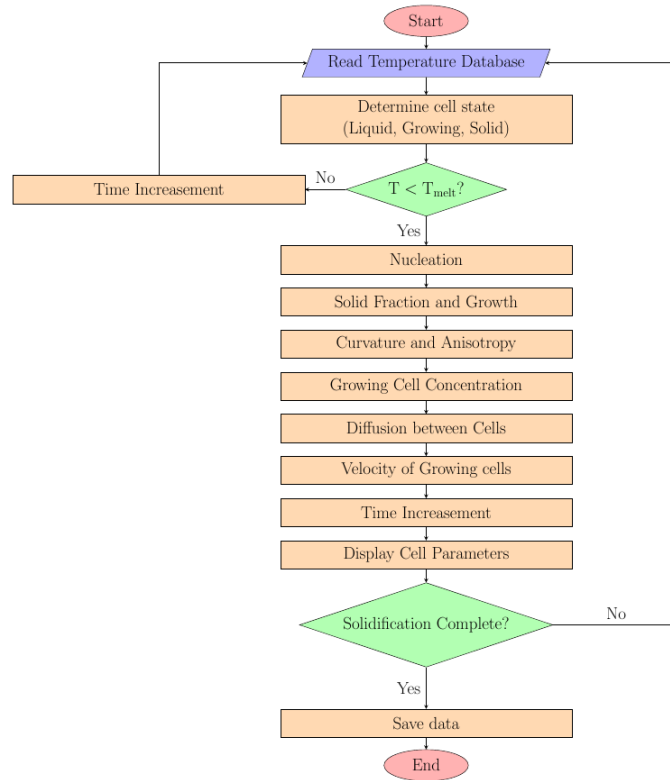


FIGURE 3.11 – flowchart of the microstructure evolution model

Step 8 : Concentration diffusion. Calculate the diffusion of concentration for all cells.

Step 9 : Interface growing velocity. Based on the concentration and solid fraction, the growing velocity of interface(or growing) cell is computed.

Step 10 : Time increment Based on the growth velocity, chose an suitable time increment for further calculation.

Step 11 : Display the cell state on the screen. Liquid, growing, solid state, index, temperature, concentration, solid fraction and other parameters can be selected to be displayed on screen.

After some loop times, all the cell will turn to solid and the program stops.

3.9 Microstructure simulation of weld solidification

3.9.1 Read temperature database

During welding, different part of the weld goes through different heating and cooling process. The weld temperature distribution field is simulated by a Finite Element Analysis (FEA) using a conical heat source.

According to Gaussian distribution[71] for a conical heat source, the heat model can be described in figure 3.12 :

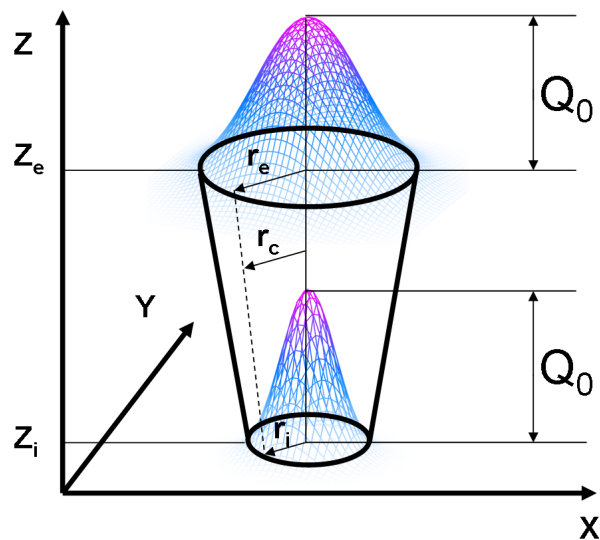


FIGURE 3.12 – Conical heat source with Gaussian distribution
The model can be described by the following mathematical function :

$$Q(r, z) = \frac{9\eta P e^3}{\pi(e^3 - 1)} \cdot \frac{e^{-\frac{3r^2}{r_e^2}}}{(z_e - z_i)(r_e^2 + r_e r_i + r_i^2)} \quad (3.3)$$

and

$$r_c = r_i + \frac{(r_e - r_i)(z - z_i)}{z_e - z_i} \quad (3.4)$$

The parameters of heat source used to simulation the welding temperature are shown in table 3.3 :

TABLE 3.3 – Parameters of Heat Source Model		
Symbol	Meaning	Value
r_e	radius of top	0.65 mm
r_i	radius of bottom	0.50 mm
r_c	radius at the height of z	Eqn.(3.4) mm
z_e	z position of top	1.25 mm
z_i	z position of bottom	-1.26 mm
P	power of laser	4.0 kW
η	efficiency	42.00 %
v	welding speed	0.05 m/s

During the 2D CA simulation, the temperature of every cell of every step is computed from the results of ABAQUS. The ABAQUS temperature simulation result is cut to many small parts and one of the small part is used by CA model to reduce the computing times. The whole weld zone and its heat affected zone is too large to compute. To get rid of the long time run in computer, a small zone selected for Cellular Automaton is depicted in figure 3.13. The ABCD zone is meshed by 300×313 cells, and each cell is displayed by a pixel.

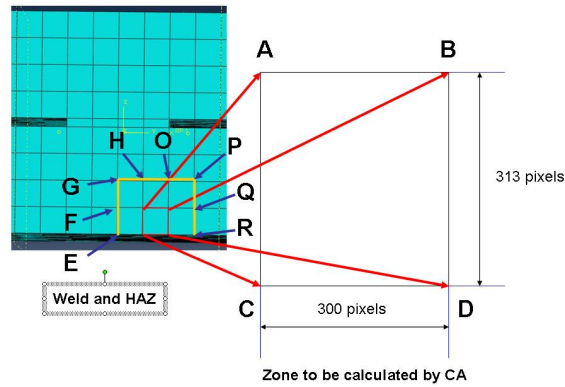


FIGURE 3.13 – Selected zone for calculating

3.9.2 Temperature

After the FEA simulation using ABAQUS software, the computed history of temperature during welding are input into CA model. The position of four nodes A, B, C, D and the bigger square nodes E, F, G, H, O, P, Q, R are shown in figure 3.14. All the temperature data used by CA model is computed based on the original data of the 12 points. There are two kinds of calculation method for cell temperature : one is distance interpolation and the other is linear interpolation. The two methods are presented in detail in the following part.

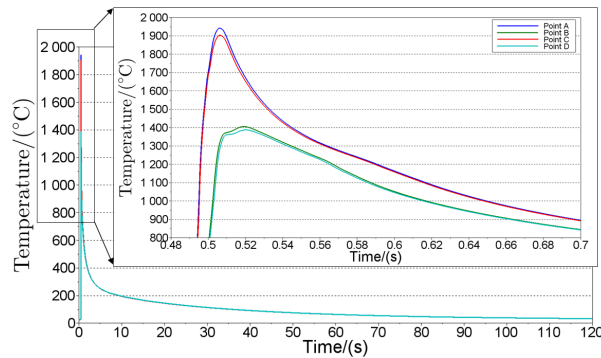


FIGURE 3.14 – The history temperature of node A

3.9.3 Distance weighting factor for cell temperature computation

In a distance weighting factor method, the distance from center cell to the four node A, B, C, D even the bigger square nodes E, F, G, H, O, P, Q, R, is viewed as the weighting factor. The data are read by CA program and interpolated by the below formula [72] :

$$T_p = \frac{\sum_{i=1}^N l_i^{-1} T_i}{\sum_{i=1}^N l_i^{-1}} \quad (3.5)$$

where T_p is the temperature of small center cell of CA model. l_i is the distance of CA cell to node of the ABAQUS element. T_i is the temperature of the node of the ABAQUS element. N is the number of used node for simulation. If the four node A, B, C, D are used, then $N = 4$; if node A, B, C, D and node E, F, G, H, O, P, Q, R are used, then $N = 12$.

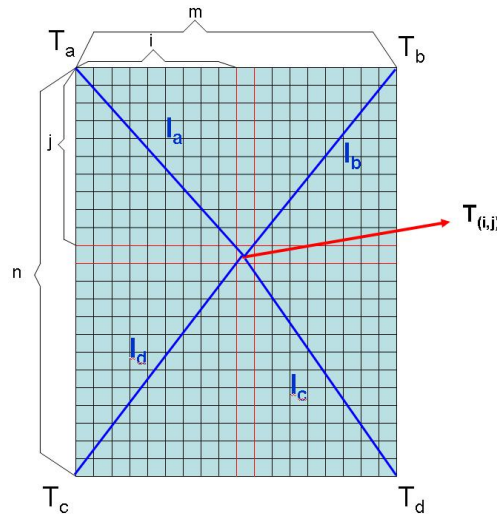


FIGURE 3.15 – The schematic of distance weighting factor

According to Tiziani [73], the melting temperature of DP600 steel is 1530°C. Thus, based on the equation 3.5, temperatures and fusion line is drawn in figure 3.17. The 4 nodes interpolation of ABCD and 12 nodes interpolation of ABCDEFGHOPQR method are tested. They have a common problem which shows an unreal temperature distribution at the beginning and ending of the simulation, as can be seen in figure 3.17 (a) and (c). So a revised method is used for temperature estimation.

3.9.4 Linear Interpolation for cell temperature estimation

In laser welding, the temperature gradient is very important, so there is a huge difference of temperature history between the outer square nodes E,F,G,H,O,P,Q,R and nodes A,B,C,D. If used in calculation the cell temperature, the outer square nodes will have a very strong influence. Thus, the revised method only use A,B,C,D four node data to compute the district of ABCD.

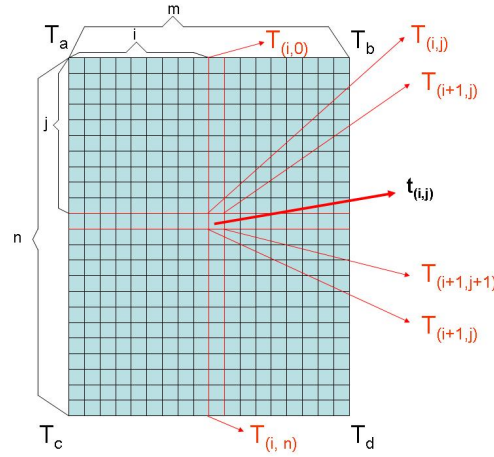


FIGURE 3.16 – The schematic of linear interpolation

First, the temperatures of the edge, $T_{(i,0)}$ and $T_{(i,n)}$ are computed.

$$T_{(i,0)} = \frac{i}{m}(T_b - T_a) + T_a = \frac{i}{m}T_b + \frac{m-i}{m}T_a \quad (3.6)$$

$$T_{(i,n)} = \frac{i}{m}(T_d - T_c) + T_c = \frac{i}{m}T_d + \frac{m-i}{m}T_c \quad (3.7)$$

Then the node temperature is interpolated from $T_{(i,0)}$ and $T_{(i,n)}$,

$$\begin{aligned} T_{(i,j)} &= \frac{j}{n}(T_{(i,n)} - T_{(i,0)}) + T_{(i,0)} \\ &= \frac{1}{m \cdot n}[(m-i)(n-j)T_a + i \cdot (n-j) \cdot T_b \\ &\quad + (m-i) \cdot j \cdot T_c + i \cdot j \cdot T_d] \end{aligned} \quad (3.8)$$

With the above method, $T_{(i,j)}$, $T_{(i+1,j)}$, $T_{(i,j+1)}$ and $T_{(i+1,j+1)}$ can be estimated. Then the cell temperature $t_{(i,j)}$ is achieved by the function written by :

$$t_{(i,j)} = \frac{1}{4}(T_{(i,j)} + T_{(i+1,j)} + T_{(i,j+1)} + T_{(i+1,j+1)}) \quad (3.9)$$

In figure 3.17, the region with temperature above the melting point is red while the region unmelted is black. Subfigure (a) presents the simulation position of weld.

In subfigure (b), areas around A point and C point are melt but the area between A point and C point doesn't melt. This doesn't agree with the experiment observation. Subfigure (c) is the revised result for temperature distribution, compared with subfigure (b), the subfigure (c) shows a more reasonable result.

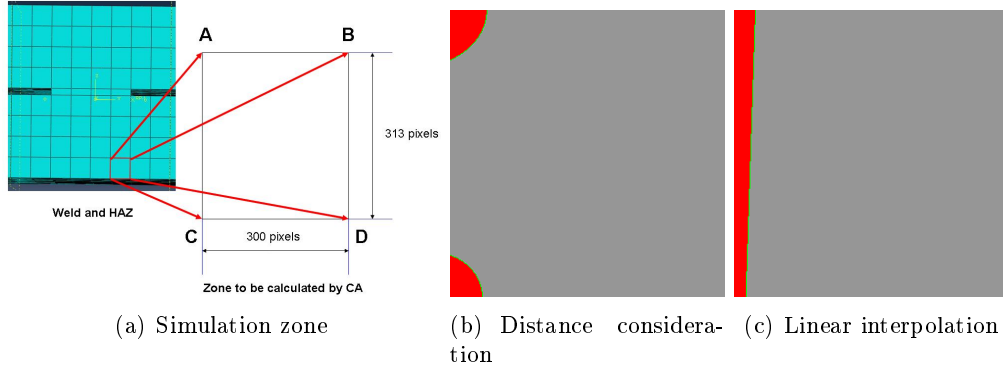


FIGURE 3.17 – Temperature distribution

3.10 Nucleation

3.10.1 The number of the nucleation

According to the nucleation model described by Thevoz et al. [4], the nucleation density of the microstructure solidification is shown in figure 3.18 :

Because concentrations at the mould are different from that in the bulk, the curvature undercooling at the mould computed from the concentration will differ from the curvature in the bulk. As the undercooling influence, the nucleation density at the mould will not be same as that in the bulk. Thus, there are two kinds of computation methods [66]. One is for the mould wall, the other is for the bulk of alloy liquid.

For the mould wall (“s” stands for surface),

$$\delta n_s = n_s[\Delta T + \delta(\Delta T)] - n_s \Delta T = \int_{\Delta T}^{\Delta T + \delta(\Delta T)} \frac{n_{s,max}}{\sqrt{2\pi\Delta T_\sigma}} e^{-\frac{1}{2}\left(\frac{t - \Delta T_{s,max}}{\Delta T_\sigma}\right)^2} dt \quad (3.10)$$

For the bulk of the alloy liquid (“v” stands for volume),

$$\delta n_v = n_v[\Delta T + \delta(\Delta T)] - n_v \Delta T = \int_{\Delta T}^{\Delta T + \delta(\Delta T)} \frac{n_{v,max}}{\sqrt{2\pi\Delta T_\sigma}} e^{-\frac{1}{2}\left(\frac{t - \Delta T_{v,max}}{\Delta T_\sigma}\right)^2} dt \quad (3.11)$$

In the above formula, ΔT is the whole undercooling of the bulk or the mould wall, it means $\Delta T = T_{liq} - T_p$ for mould cells or bulk cells, T_{liq} is the liquidus temperature in the

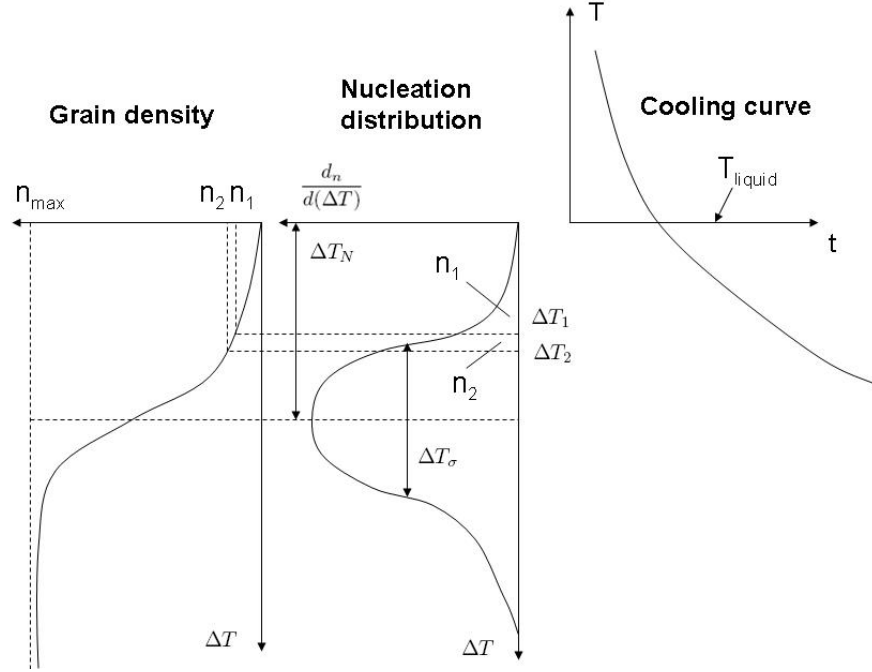


FIGURE 3.18 – The schematic of calculation of nucleation density [4]

phase diagram, n_s is the nucleation density of the mould wall and n_v is the nucleation density of the bulk of the alloy liquid. $n_{s,max}$ and $n_{v,max}$ are the maximum nucleation density for surface and volume, respectively, ΔT_σ is the standard deviation of the degree of undercooling. $\Delta T_{v,max}$ and $\Delta T_{s,max}$ is the maximum degree of undercooling of nucleation for surface and volume, respectively.

If the liquid cell number decreased by grain growing is considered, the equation can be modified as :

$$\delta n_s = n_s[\Delta T + \delta(\Delta T)] - n_s \Delta T = \int_{\Delta T}^{\Delta T + \delta(\Delta T)} \frac{n_{s,max}}{\sqrt{2\pi}\Delta T_\sigma} (1 - f_{vs}) e^{-\frac{1}{2}\left(\frac{t - \Delta T_{s,max}}{\Delta T_\sigma}\right)^2} dt \quad (3.12)$$

$$\delta n_v = n_v[\Delta T + \delta(\Delta T)] - n_v \Delta T = \int_{\Delta T}^{\Delta T + \delta(\Delta T)} \frac{n_{v,max}}{\sqrt{2\pi}\Delta T_\sigma} (1 - f_{vs}) e^{-\frac{1}{2}\left(\frac{t - \Delta T_{v,max}}{\Delta T_\sigma}\right)^2} dt \quad (3.13)$$

In this equation, f_{vs} is the volume fraction of solid already formed. The increase of grains density, δn_v or δn_s multiplied by the bulk cell number N_v or the mould wall number N_s follows the number of grains nucleated at step n.

3.10.2 The position of the nucleation

The nucleation position is chosen among all of the remaining liquid cells at random. The nucleation probabilities for “liquid” cells located in the bulk of the liquid and at the surface of the mold (dp_e and dp_c) to nucleate during each time step are given by

$$dp_e = \frac{\delta N_e}{N_s} \quad (3.14)$$

and

$$dp_c = \frac{\delta N_c}{N_v} \quad (3.15)$$

where δN_e and δN_c are the number of cells at the edge of welding pool (at the mould surface) and in the center of welding pool (in the bulk) at one step. N_v and N_s are the number of cells in the bulk and at the mold surface, respectively. During the time step calculation both the mold-surface cells and bulk cells are scanned and a random number, *rand*, is generated for each of them ($0 \leq \text{rand} \leq 1$). The nucleation of a “liquid” cell will occur only if $\text{rand} \leq dp_e$ or $\text{rand} \leq dp_c$.

3.11 Solid fraction

The solid fraction of growing cells can be determined by [69]

$$\delta f_s = \frac{\delta t}{a} \left(V_x + V_y - V_x V_y \frac{\delta t}{a} \right) \quad (3.16)$$

Here, a is the mesh size, V_x is the maximum growth velocity of growing cell, δt is the increment of time.

3.11.1 Interface Curvature

The solid/liquid interface curvature can affect the computation of solute concentration in the growing cell. An accurate approach for calculating interface curvature is reported by Xin et al. [74] :

$$K = \frac{2 \frac{\partial f_s}{\partial x} \frac{\partial f_s}{\partial y} \frac{\partial^2 f_s}{\partial x \partial y} - \left(\frac{\partial f_s}{\partial y} \right)^2 \frac{\partial^2 f_s}{\partial x^2} - \left(\frac{\partial f_s}{\partial x} \right)^2 \frac{\partial^2 f_s}{\partial y^2}}{\left[\left(\frac{\partial f_s}{\partial x} \right)^2 + \left(\frac{\partial f_s}{\partial y} \right)^2 \right]^{3/2}} \quad (3.17)$$

A finite different method is used to solve the partial derivatives of the solid fraction in the equation (3.17). For every node, for example ua , the value of the node is :

$$ua = \frac{1}{4} [f_s(i-1, j-3) + f_s(i, j-3) + f_s(i-1, j-2) + f_s(i, j-2)] \quad (3.18)$$

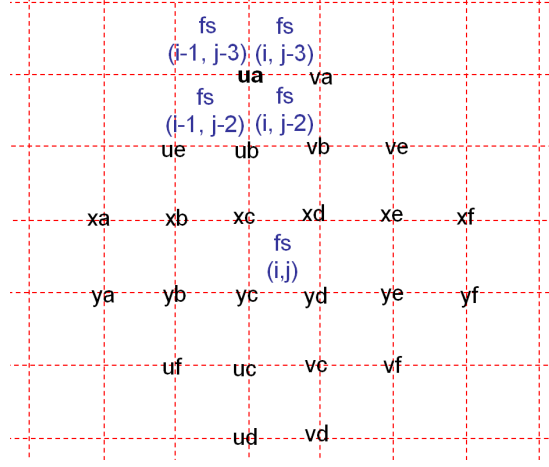


FIGURE 3.19 – The sketch of parameters used in solid fraction computation

For the node (i, j) , Δx is the length of the cell, so the partial derivatives are computed as below :

$$\frac{\partial f_s}{\partial x} = \frac{[(xd + xe + yd + ye)/4 - (xb + xc + yb + yc)/4]}{2\Delta x} \quad (3.19)$$

$$\frac{\partial f_s}{\partial y} = \frac{[(ub + vb + xc + xd)/4 - (yc + yd + uc + vc)/4]}{2\Delta x} \quad (3.20)$$

$$\frac{\partial^2 f_s}{\partial y^2} = \frac{[(xe + xf + ye + yf + xa + xb + ya + yb) - 2(xc + xd + yc + yd)]}{16(\Delta x)^2} \quad (3.21)$$

$$\frac{\partial^2 f_s}{\partial x^2} = \frac{[(ua + ub + va + vb + uc + ud + vc + vd) - 2(xc + xd + yc + yd)]}{16(\Delta x)^2} \quad (3.22)$$

$$\frac{\partial^2 f_s}{\partial y \partial x} = \frac{[(yd + ye + vc + vf + ub + ue + xb + xc) - (yb + yc + uc + uf + vb + ve + xd + xe)]}{16(\Delta x)^2} \quad (3.23)$$

Combined with the equation (3.19), (3.20), (3.21), (3.22), and (3.23), the curvature of equation 3.17 can be then computed.

A more simple solid/liquid interface curvature for a cell is given by [69] :

$$K = \frac{1}{a} \left(1 - 2 \frac{f_s + \sum_{k=1}^N f_s(k)}{N + 1} \right) \quad (3.24)$$

In the equation (3.24), a is the mesh length of CA model, f_s is solid fraction and N stands for the number of neighbor cells. The result of the curvature calculation range from $-1/a$ to 0 for concave interface and 0 to $1/a$ for convex interface.

3.12 Interface Concentration

To compute solute concentrations in the growing cells, the interface temperature (T^*) is first given by :

$$T^* = T_L^{EQ} + (C_L^* - C_0)m_L - \Gamma\bar{k}f(\varphi, \theta) \quad (3.25)$$

Here T_L^{EQ} is the equilibrium liquidus temperature of the alloy, C_L^* is the interface solute concentration and C_0 is the initial concentration in the material. In the simulation, the carbon element equivalent concentration are used to simulate DP600 dual phase steel. m_L is the liquidus slope of the phase diagram, \bar{k} is the mean curvature of the S/L interface, Γ is the Gibbs-Thomson coefficient and $f(\varphi, \theta)$ is a coefficient used to account for growth anisotropy where θ is the growth angle (i.e. the angle between the normal and the x-axis) and φ is the preferential crystallographic orientation angle. In equation 2.20, the third term on the right-hand side is the constitutional undercooling and the second term on the right-hand side is the curvature undercooling (that reduces the total undercooling at the dendrite tip, that is, has a stabilizing effect on the S/L interface).

X.H.Zhan point out that [68] the interface temperature is also affected by the kinetic undercooling $\frac{v}{\mu_k}$ as an interface dynamic undercooling (ΔT_{kin}). Here v is the growth velocity, and μ_k is the coefficient of dynamic of crystal growth.

So, C_L^* can be computed by :

$$C_L^* = C_0 + \frac{T^* - T_L^{EQ} + \Gamma\bar{k} + \frac{v}{\mu_k}}{m_L} \quad (3.26)$$

In figure 2.7.1, "S" stands for solid and "L" stands for liquid. The solute concentration gradient G_C can be determined by :

$$G_C = \frac{C_L^* - C_L}{(1 - f_S)\Delta x/2} \quad (3.27)$$

Here Δx is the mesh size in the x direction. Then, the solute concentration in liquid can be expressed as :

$$C_L = C_L^* - \frac{1 - f_S}{2}\Delta x G_C \quad (3.28)$$

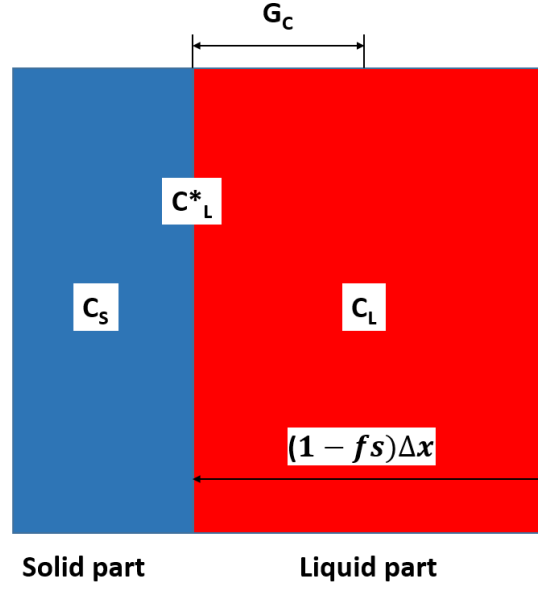


FIGURE 3.20 – Model of concentration in single cell

3.13 Surface tension anisotropy

The anisotropy of surface tension [69] is determined from :

$$f(\varphi, \theta) = 1 + \delta \cos(4(\varphi - \theta)) \quad (3.29)$$

Here, $\delta = 0.04$, θ is the angle between growth direction, +x direction and the φ angle is defined by :

$$\varphi = \arccos\left(\frac{V_x}{[V_x^2 + V_y^2]^{1/2}}\right) \quad (3.30)$$

3.14 Diffusion Equation

3.14.1 Equation widely accepted

After solute concentrations in the growing cells are first computed, solute diffusions in a time step between different cells are estimated.

In the process of growing cells solidification, the solute released by growing cells can break the equilibrium and the solute concentration in solid and liquid cells should be determined.

At the S/L interface, it can be written :

$$C_S^* = kC_L^* \quad (3.31)$$

where C_S^* is the solute concentration in the solid at the S/L interface and k is the partition coefficient.

According to Fick's second law, the partitioning of solute in liquid is given by

$$\frac{\partial C_L}{\partial t} = \frac{\partial}{\partial x} \left(D_L \frac{\partial C_L}{\partial y} \right) + \frac{\partial}{\partial y} \left(D_L \frac{\partial C_L}{\partial x} \right) \quad (3.32)$$

Where C_L is the solute concentration in liquid and D_L is the solute diffusion coefficient in liquid.

The partitioning of solute in solid is given by :

$$\frac{\partial C_S}{\partial t} = \frac{\partial}{\partial x} \left(D_S \frac{\partial C_S}{\partial y} \right) + \frac{\partial}{\partial y} \left(D_S \frac{\partial C_S}{\partial x} \right) \quad (3.33)$$

Where C_S is the solute concentration in solid and D_S is the solute diffusion coefficient in solid.

The partitioning of solute in growing cells is considered as follows. In the simulation, the neighbours of a solid cell can be solid or growing. The neighbours of a liquid cell can be liquid or growing whereas the neighbours of a growing cell can be solid, liquid and even growing.

Equations (2.25) and (2.26) are used if the computing center is a solid or liquid cell. The neighbours of a solid or liquid cell may be growing. The growing cell is in semisolid state and the solute concentrations in the solid and liquid parts are C_S^g and C_L^g respectively. When the growing cell takes part in computation as the neighbour of a solid cell, the solid concentration C_S^g is used. When the growing cell takes part in computation as the neighbour of a liquid cell, the liquid concentration C_L^g is used.

When the computing center is a growing cell, regardless of the state (i.e. solid, liquid or growing) of the neighbour of the growing cell, the solute concentration of the growing cell can be expressed as an equivalent concentration C_E , which is defined as :

$$C_E = C_L(1 - f_S) + C_S f_S = C_L[1 - (1 - k)f_S] \quad (3.34)$$

where f_S is the solid fraction. In the extreme condition, C_E is equal to C_S when f_S is 1, and C_E equals C_L when f_S is zero.

Therefore, the diffusion equations can be expressed by :

$$\frac{\partial C_E}{\partial t} = \nabla(D_E \nabla C_E) \quad (3.35)$$

where C_E is the equivalent concentration, which is defined by equation (2.27) and D_E is the equivalent diffusion coefficient estimated by :

$$D_E = (1 - f_S)D_L + f_S k D_S g f_S \quad (3.36)$$

3.14.2 Revised Equation

In Left cell, top part is solid and base part is liquid. In the right cell, the back part is viewed as solid and the front part is viewed as liquid.

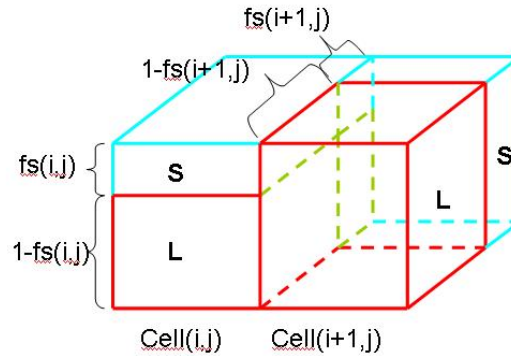


FIGURE 3.21 – Schematic diagram of cells contact

According to Fick’s second law, in x-direction, it can be written :

$$\frac{\partial C(x, t)}{\partial t} = -\frac{\partial J}{\partial x} \tag{3.37}$$

Figure 3.22 shows the interface between cell(i,j) and cell(i+1,j). Considering the contact region can be grouped to four area. The whole contact surface area is A. The green region A1 and A4 means liquid contact with solid. The blue region A2 means solid contact with solid. The red region A3 means liquid contact with liquid.

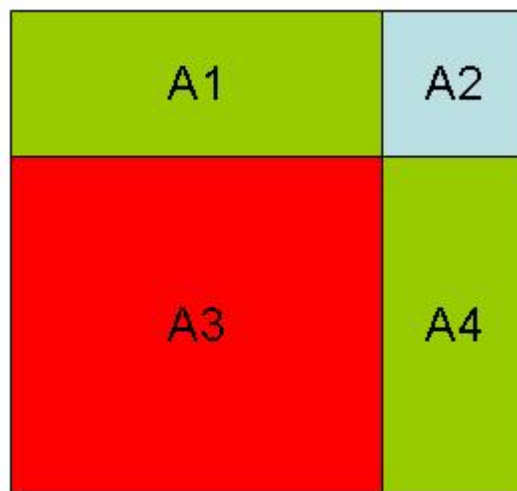


FIGURE 3.22 – Schematic diagram of cells contact

The surface area can be described by the following equations :

$$A1 = fs(i, j) * [1 - fs(i + 1, j)] * A \quad (3.38)$$

$$A2 = fs(i, j) * fs(i + 1, j) * A \quad (3.39)$$

$$A3 = [1 - fs(i, j)] * [1 - fs(i + 1, j)] * A \quad (3.40)$$

$$A4 = fs(i + 1, j) * [1 - fs(i, j)] * A \quad (3.41)$$

So every part is considered.

$$\begin{aligned} \frac{\partial C(x, t)}{\partial t} = & -\frac{\partial J}{\partial x} \times fs(i, j) \times fs(i + 1, j) \\ & -\frac{\partial J}{\partial x} \times [1 - fs(i, j)] \times fs(i + 1, j) \\ & -\frac{\partial J}{\partial x} \times fs(i, j) \times [1 - fs(i + 1, j)] \\ & -\frac{\partial J}{\partial x} \times [1 - fs(i, j)] \times [1 - fs(i + 1, j)] \end{aligned} \quad (3.42)$$

$$\begin{aligned} \frac{\partial C(x, t)}{\partial t} = & d_l \times \frac{\partial^2 C}{\partial x^2} \times fs(i, j) \times fs(i + 1, j) \\ & + \sqrt{d_l \times d_s} \times \frac{\partial^2 C}{\partial x^2} \times [1 - fs(i, j)] \times fs(i + 1, j) \\ & + \sqrt{d_l \times d_s} \frac{\partial^2 C}{\partial x^2} \times fs(i, j) \times [1 - fs(i + 1, j)] \\ & + dl \frac{\partial^2 C}{\partial x^2} \times [1 - fs(i, j)] \times [1 - fs(i + 1, j)] \end{aligned} \quad (3.43)$$

$$\begin{aligned} \frac{\partial C(x, t)}{\partial t} = & d_l \times \frac{C_s(i + 1, j) - C_s(i, j)}{cella^2} \times fs(i, j) \times fs(i + 1, j) \\ & + \sqrt{d_l \times d_s} \times \frac{C_s(i + 1, j) - C_l(i, j)}{cella^2} \times [1 - fs(i, j)] \times fs(i + 1, j) \\ & + \sqrt{d_l \times d_s} \frac{C_l(i + 1, j) - C_s(i, j)}{cella^2} \times fs(i, j) \times [1 - fs(i + 1, j)] \\ & + dl \frac{C_l(i + 1, j) - C_l(i, j)}{cella^2} \times [1 - fs(i, j)] \times [1 - fs(i + 1, j)] \end{aligned} \quad (3.44)$$

3.15 Growth velocity of the interface

3.15.1 Fick's laws of diffusion

Fick's laws of diffusion is first developed by Adolf Fick in 1855. The Fick's laws describe diffusion behavior. Fick's first law provide a relationship between diffusive flux and the concentration gradient under steady state. Fick's second law describes the concentration field evolution with time.

Fick's first law assumes that diffusive flux goes from a area of high concentration to a area of low concentration and the diffusive rate of flux is proportional to the concentration gradient :

$$J = -D \nabla \phi \quad (3.45)$$

In the equation, J stands for diffusive flux. Diffusive flux means the amount substance goes through an unit area at an unit time. For the microstructure simulation in this work, the unit of diffusive flux J can be $\frac{wt\%}{m^2 \cdot s}$

D is the diffusion coefficient with a unit of $\frac{m^2}{s}$

ϕ means the amount of substance per unit volume, in this work, unit is $\frac{wt\%}{m^3}$

∇ is gradient operator which can also be written as $\frac{\partial}{\partial x_i}$

Fick's second law describes the concentration change with time in a field. The equation is given as :

$$\frac{\partial \phi}{\partial t} = D \frac{\partial^2 \phi}{\partial x_i^2} \quad (3.46)$$

In the equation, t stands for time and x_i means any dimension such as x, y, z, ... For microstructure simulation in CA method, Fick's second law tells that the change of solute with time in center cell is equal to the addition of flux in and out of the cell during the time.

3.16 Conservation equation

In the figure 3.23, the growing cell and its neighborhood cells in x direction are presented. The red part of cell is liquid and the blue part is solid. In the figure, fs(i,j) stands for the solid fraction of cell(i,j). The length of the cell edge are Δx , Δy , and Δz , respectively. The growing velocity of interface in the cell(i,j) is V_x .

In a time step, the solid volume of cell(i,j) increases $V_x \delta(t) \Delta y \Delta z$, so the solute in the cell(i,j) will decrease of $V_x \delta(t) \Delta y \Delta z (C_L^{(i,j)} - C_S^{(i,j)})$. Consideration with Fick's law, the conservation of solute is given by [75] :

$$V_x \delta(t) \Delta y \Delta z (C_L^{(i,j)} - C_S^{(i,j)}) = D_L \Delta y \Delta z \frac{\partial C_L}{\partial x} - D_S \Delta y \Delta z \frac{\partial C_S}{\partial x} \quad (3.47)$$

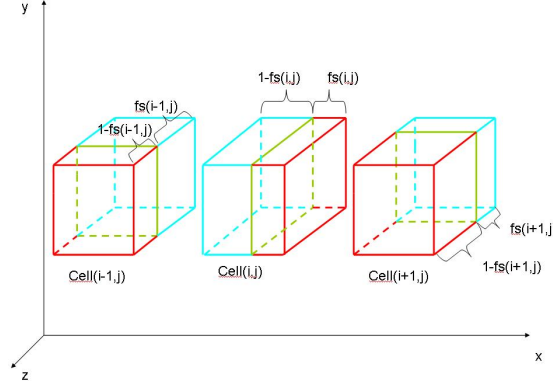


FIGURE 3.23 – Growth velocity of the interface in a cell

Assuming $C_S(i, j) = kC_L(i, j)$ at the interface, the function can be changed to :

$$V_x \delta(t) C^L(i, j) (1 - k) = D_L \frac{\partial C_L}{\partial x} - D_S \frac{\partial C_S}{\partial x} \quad (3.48)$$

If the solid fraction in the neighborhood cell is considered, the conservation equations is revised as [69] :

$$\begin{aligned} V_x(i, j) = & \frac{D_L}{a(1-k)} \left[\left(1 - \frac{C_L(i-1, j)}{C_L^*(i, j)}\right) f_L(i-1, j) + \left(1 - \frac{C_L(i+1, j)}{C_L^*(i, j)}\right) f_L(i+1, j) \right] \\ & + \frac{kD_S}{a(1-k)} \left[\left(1 - \frac{C_S(i-1, j)}{kC_L^*(i, j)}\right) f_S(i-1, j) + \left(1 - \frac{C_S(i+1, j)}{kC_L^*(i, j)}\right) f_S(i+1, j) \right] \end{aligned} \quad (3.49)$$

In y-direction, similar equation for growth velocity can be obtained :

$$\begin{aligned} V_y(i, j) = & \frac{D_L}{a(1-k)} \left[\left(1 - \frac{C_L(i, j-1)}{C_L^*(i, j)}\right) f_L(i, j-1) + \left(1 - \frac{C_L(i, j+1)}{C_L^*(i, j)}\right) f_L(i, j+1) \right] \\ & + \frac{kD_S}{a(1-k)} \left[\left(1 - \frac{C_S(i, j-1)}{kC_L^*(i, j)}\right) f_S(i, j-1) + \left(1 - \frac{C_S(i, j+1)}{kC_L^*(i, j)}\right) f_S(i, j+1) \right] \end{aligned} \quad (3.50)$$

3.17 Time increment

The increment time is computed as [69] :

$$\delta t = \frac{1}{5} \left(\frac{a}{V_{max}}, \frac{a^2}{D_L}, \frac{a^2}{D_S} \right) \quad (3.51)$$

Here, a is the mesh size, V_{max} is the maximum growth velocity of growing cell. D_L is the diffusion coefficient of liquid and D_S is the diffusion coefficient of solid.

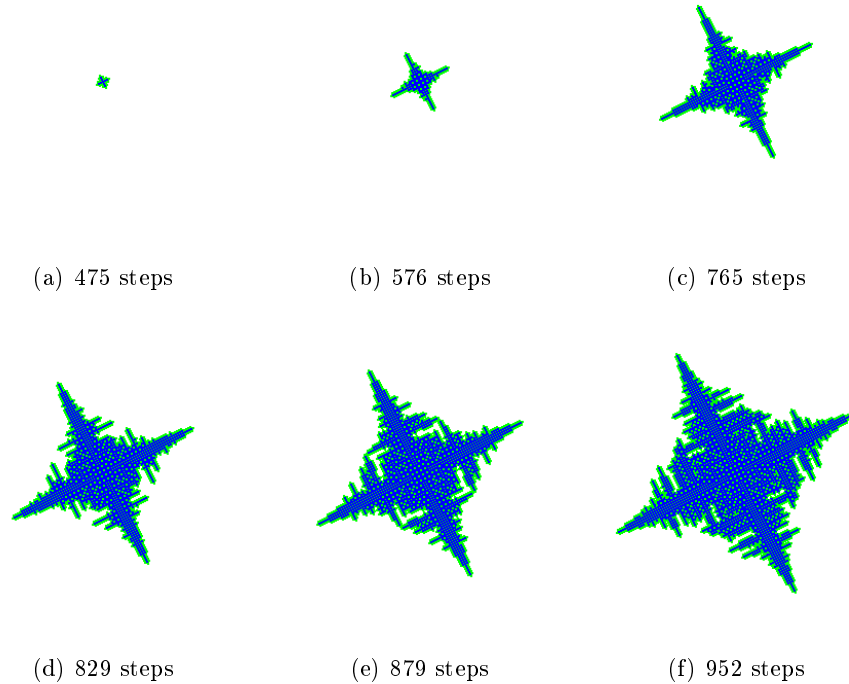
3.18 Simulation results

3.18.1 Equiaxed dendrite grain growth

With the microstructure solidification simulation of CA model, equiaxed dendrite grain growth is simulated from a temperature history of node A. In the view of space, temperatures of all cells in the simulation zone are the same. In the view of time, temperature changes every step according to the temperature of node A. The simulation zone are all at liquid state and the nucleation is made in the center zone of the simulation zone. The cell in center of the simulation zone is growing.

As is shown in figure 3.24, a equiaxed dendrite grain growth is presented. From a small start(There are already 12 big blue cells and even more green big cells in figure 3.24 (a)), the dendrite grain grows gradually to a big equiaxed dendrite grain which take up the whole simulation zone.

The figure 3.24 proves that CA can simulate equiaxed dendrite grain growth. Another point should be noticed that equiaxed grain grows along a particular direction. In figure 3.25, the direction has a angle $\theta = \arctan 1/2$ with x-direction.



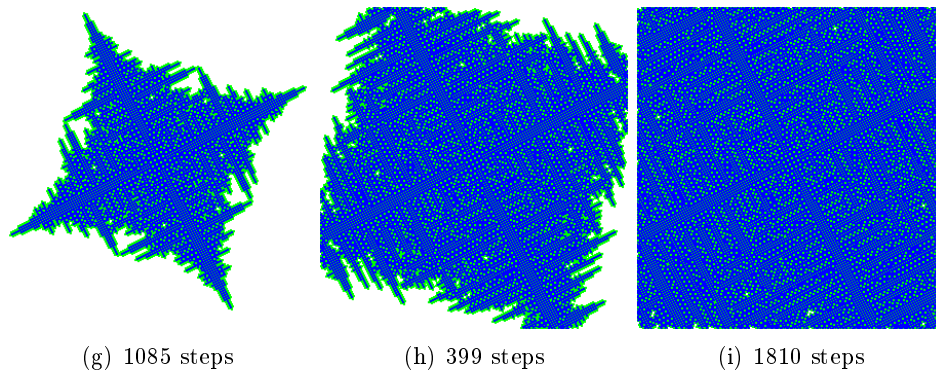
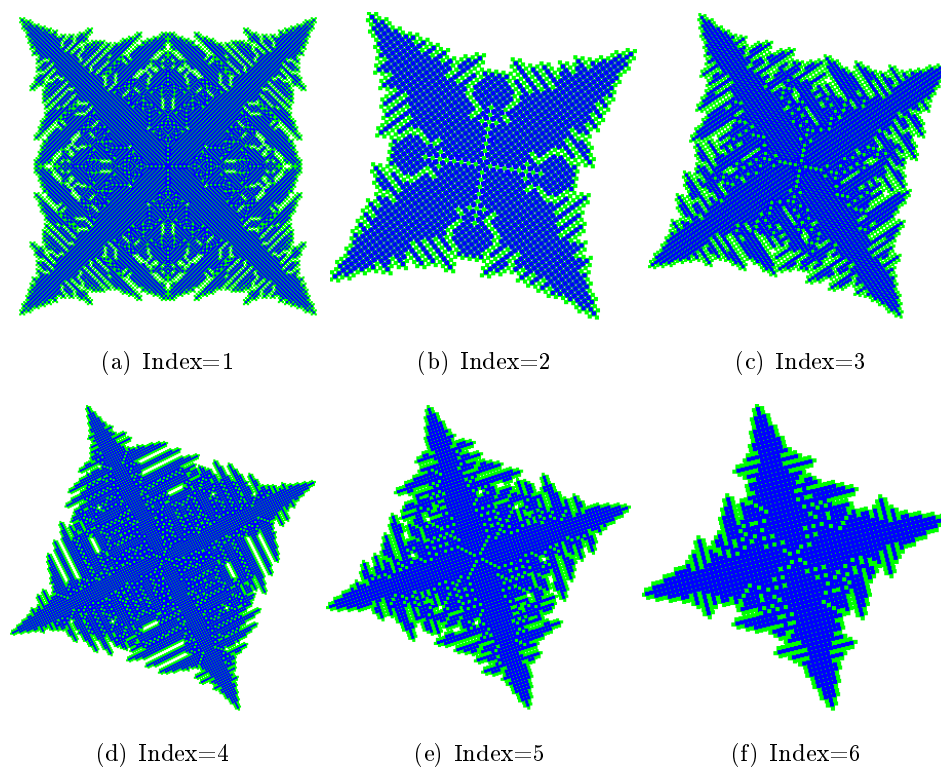


FIGURE 3.24 – The growth of equiaxed dendrite grain

3.18.2 Equiaxed dendrite grain of 48 directions

In figure 3.25, the equiaxed dendrite grain with 12 direction index of 48 directions are presented.



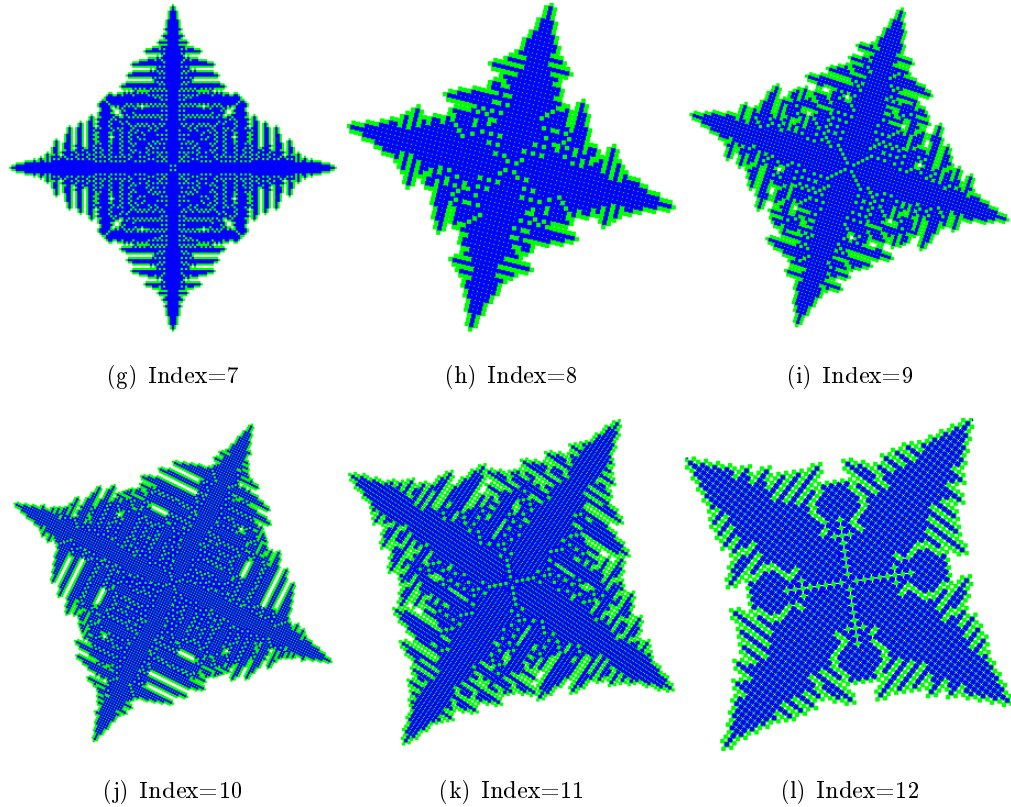


FIGURE 3.25 – The equiaxed dendrite grain of different directions

3.18.3 Column dendrite grain growth

In column dendrite grain growth simulation, the same above temperature environment is used. With the microstructure solidification simulation of CA model, column dendrite grain growth is simulated in a temperature history of node A. In the view of space, temperatures of all cells in the simulation zone are the same. In the view of time, temperature changes every step according to the temperature of node A. The simulation zone are all at liquid state and the nucleation is made at the edge of the simulation zone. There are 11 nucleations at the edge of the simulation zone. 11 big growing cells are set at the edge of simulation zone.

As it is seen in figure 3.26, the column dendrite grain growth is presented. 11 nuclei grow up from small dendrite grain to column dendrite grain. The 11 dendrites tips grows at the same speed towards the same direction.

The figure 3.26 proves that CA can simulate column dendrite grain growth. With the model, the CA can simulate the column dendrite grain growth until the grains take up the whole simulation zone. Under uniform temperature circumstance, the growth velocity of all the column dendrite grains are all the same until the end.

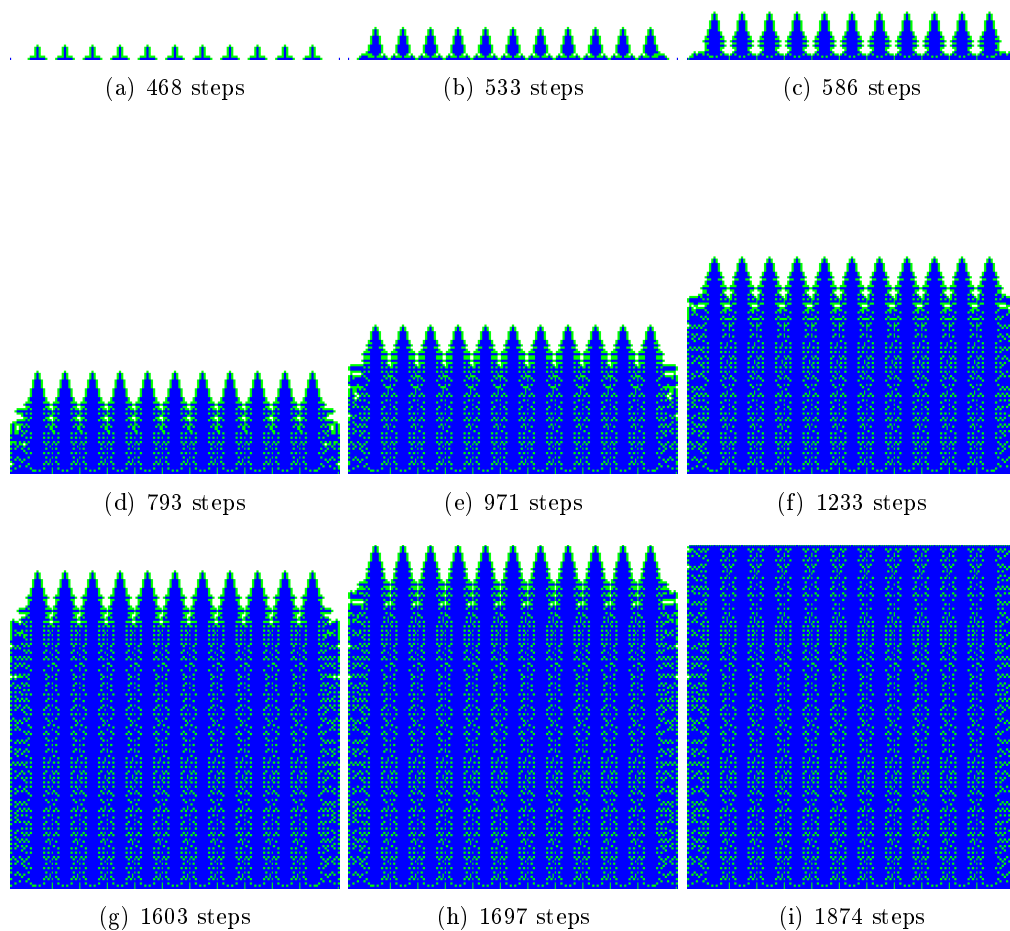


FIGURE 3.26 – The growth of column dendrite grains

3.18.4 Two equiaxed dendrite grain growth

Figure 3.27 shows two nuclei growth. At the beginning, two nuclei are set in the liquid. The nuclei grow gradually to take up the whole screen. The evolution of temperature distribution is the same as figure 3.24 : all the cell temperature in one step is the same, the value of the temperature is equal to the temperature of node A. The temperature of node A is computed from ABAQUS. Because the temperature is the same in all direction, the equiaxed dendrite grain grows in rotational symmetry along four direction.

When two edges of dendrite grains meet, their parameters can influence each other and may affect the simulation result. A state select procedure is made to avoid bad influences on the edge solidification simulation.

Figure 3.27 proves that two dendrites grains grow well with each other, they grow normally when the two grains meet each other. The calculation rule at the edge of the dendrite grain is used in the microstructure solidification model. The CA cells changed their state and parameters normally according to the calculation rule.

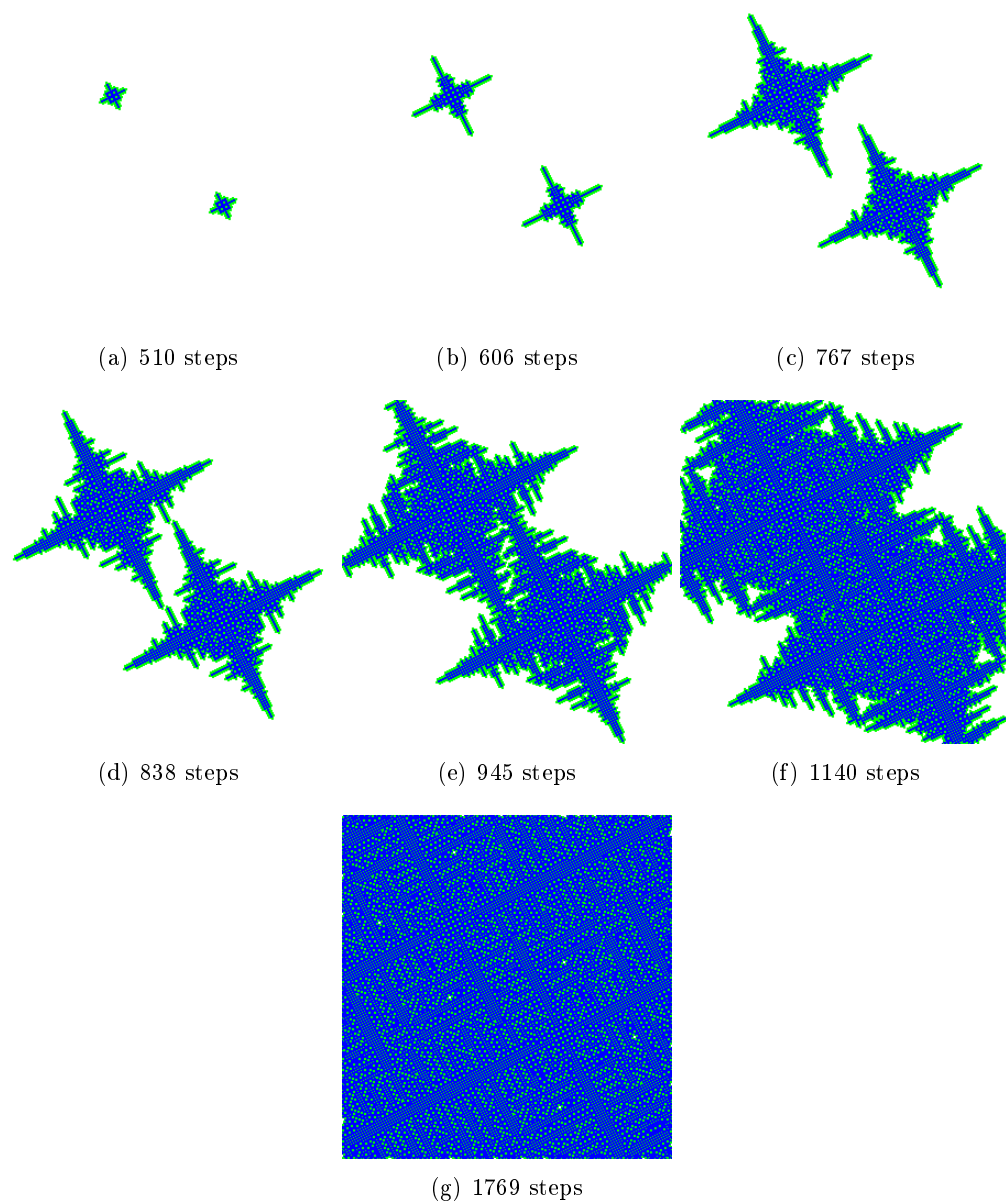


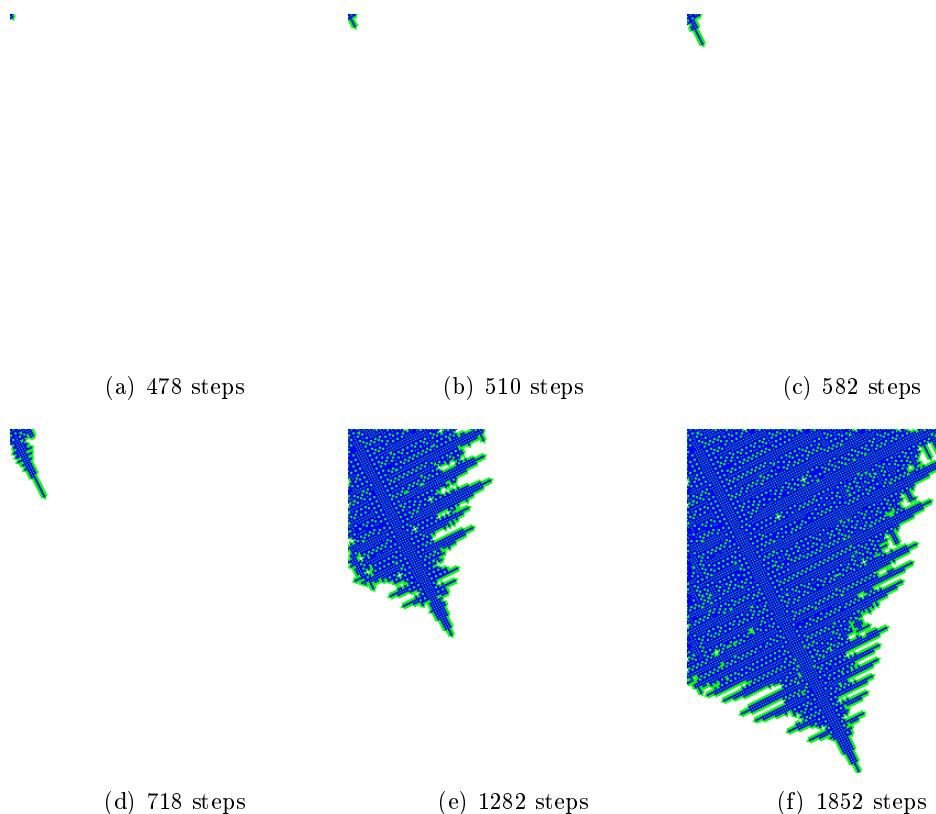
FIGURE 3.27 – The growth of two dendrite grains

3.18.5 Corner Nucleation Growth

In figure 3.28, a nucleation is made at the corner of the simulation zone. The evolution of temperature distribution is as the same as figure 3.24 : all the cell temperature in one step is the same, the value of the temperature is equal to the temperature of node A. With gradually drop of temperature values, the nucleation gradually grows to the whole simulation zone.

When a nucleation is made at the corner, some of its neighbour cells is out of the simulation zone. Some adjustment is taken into account so that the parameters can be supposed in the cell out of the simulation zone.

Figure 3.28 shows that the nuclea at the corner grows well to the whole simulation zone, it grows normally at the edge of the simulation zone. The calculation rule at the edge of the simulation zone is used in the microstructure solidification model. The CA cells changed their state and parameters normally according to the calculation rule.



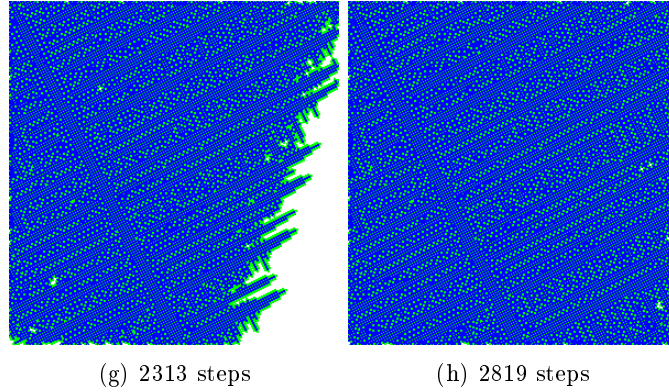
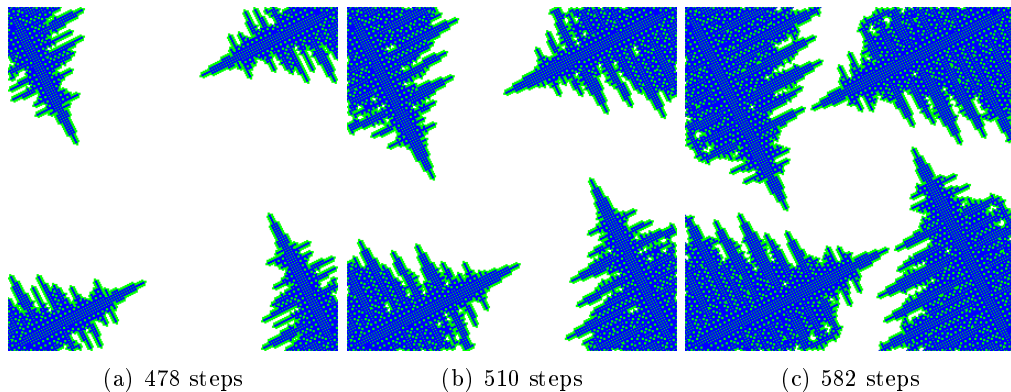


FIGURE 3.28 – The equiaxed dendrite grain growth

3.18.6 The final solidification of the liquid

As is seen in figure 3.29, four nuclei are made at four corners. They grow simultaneously towards the center simulation zone. The evolution of temperature distribution is as the same as figure 3.24 : all the cell temperature in one step is the same, the value of the temperature is equal to the temperature of node A. With gradually drop of temperature values, four nuclei gradually grows to the whole simulation zone.

The liquid in the middle solidify at last. The solidify procedure slows down obviously when the dendrite grows, some elements are released to liquid, make the solute concentration in liquid different form the concentration in solid. Finally, because of the solute concentration increases, the equivalent temperature of the material changes, making the solidification difficult.



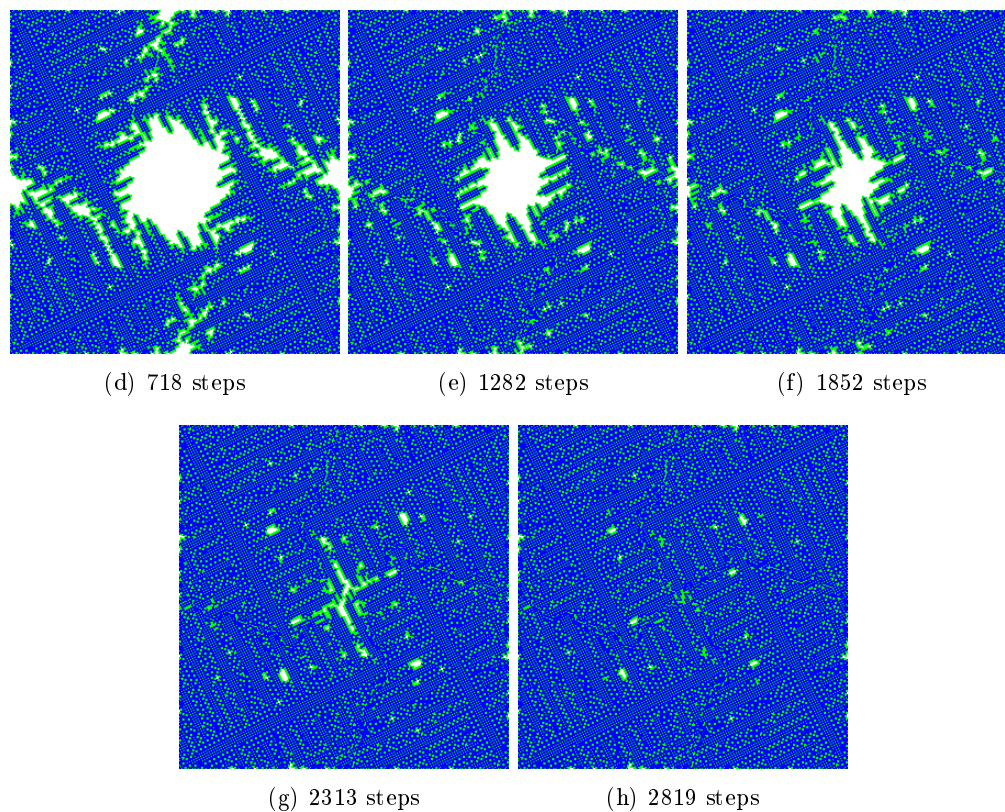


FIGURE 3.29 – Nucleation at the corner

3.18.7 Dendrite grain growth of two directions

In figure 3.30, two dendrite grain with different growth direction is presented. The evolution of temperature distribution is as the same as figure 3.24 : all the cell temperature in one step is the same, the value of the temperature is equal to the temperature of node A. With gradually drop of temperature values, two dendrite grains grows big and meet with each other. Finally, they take up the whole simulation zone.

Two dendrite grains with different growth directions are shown in different color. The blue color is for grain with growth direction of $\theta = \arctan(1/2)$ while the yellow color is for grain with growth direction of $\theta = \arctan(-1/2)$. At the bottom part of the simulation zone, the blue grain takes more space, which means the solidified grain grows bigger. Because when the two dendrite meets, the competition growth happens, the key point is taken by the blue grain, so the growth of yellow grain is affected by the blue one. The result is the grain who takes the key point in the competition grows bigger.

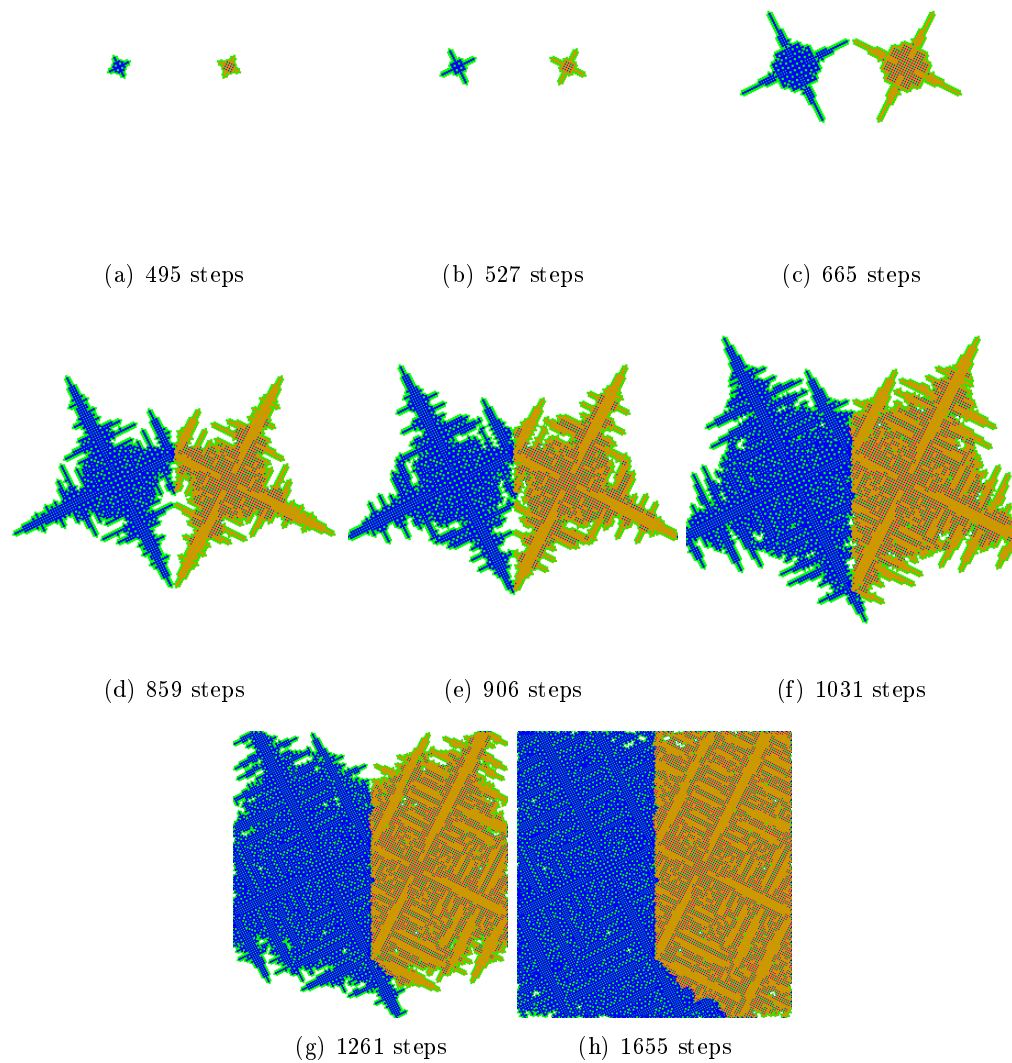


FIGURE 3.30 – Equiaxed grain competition growth of two directions

3.18.8 Equiaxed dendrite grain 12 different directions

The evolution of temperature distribution is as the same as figure 3.24 : all the cell temperature in one step is the same, the value of the temperature is equal to the temperature of node A.

In figure 3.31, equiaxed dendrite grains with 12 different growth direction number is presented. In the figure, 12 grains at different points grow to big at the same velocity

and finally they take up the whole simulation zone.

The grains grow smoothly with the other grains with different growth direction. The growth velocity are the same, just the direction is different. In final result, some grains are bigger just because there are more space at the edge.

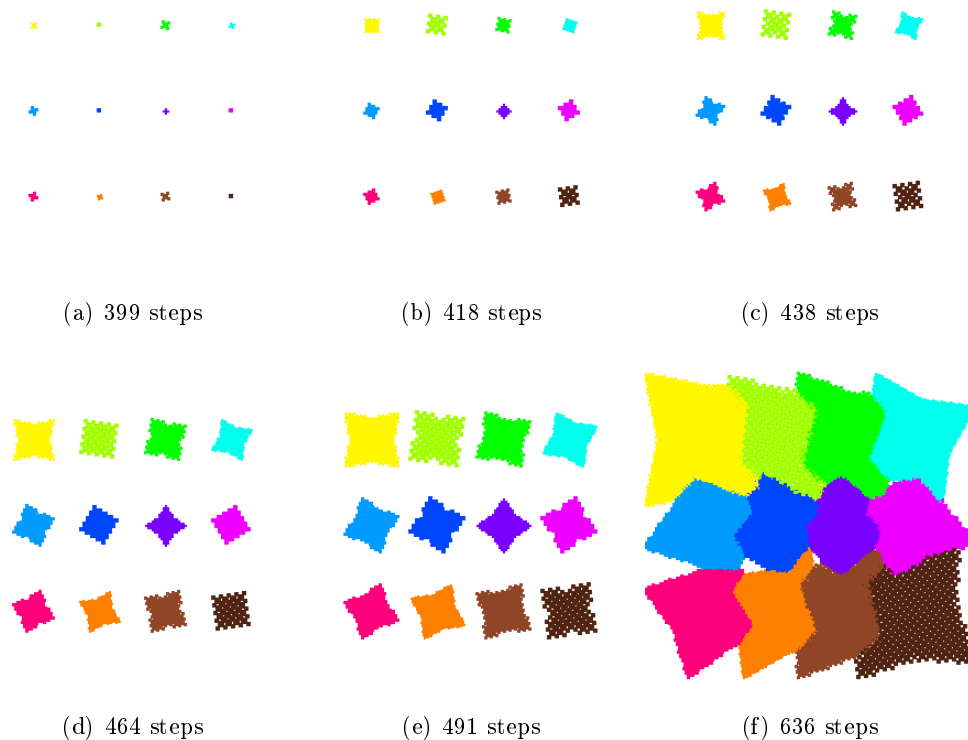


FIGURE 3.31 – Grains with different growth direction growth at the same speed

3.18.9 Microstructure simulation of weld

Unlike the isotropic temperature distributions used in the former part, those of weld part are also estimated. The linear interpolation is used for every cell to compute their own cell temperature. The result shows the corresponding weld microstructure.

As is seen in figure 3.32, a high resolution ratio is applied to the Weld Microstructure Simulation Model. Nine pixels are used for one small cell in CA.

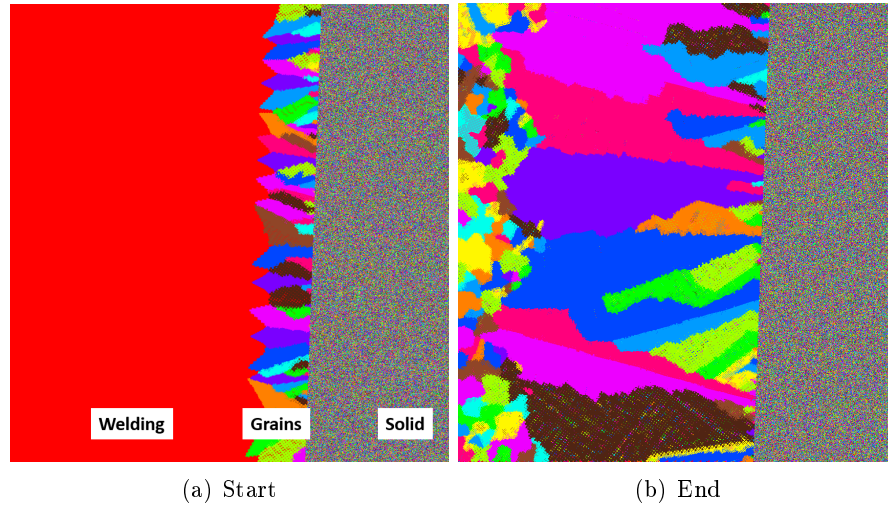


FIGURE 3.32 – Weld Microstructure Simulation of fine mesh

In figure 3.32(a), the beginning of dendrite grain growth is presented. The left part of figure with red color stands for melting alloy, the middle part with different colors represents grains with different growth direction. The right part of figure with random distributed colors is the never melt alloy. In figure, the nucleations are made randomly at the mould wall of weld and the nucleations grow to little grains.

In figure 3.32(b), the competition of dendrite grain growth is presented. As we all know, the grains with the direction near the preferential growth direction grow faster than those grains whose direction are far from the preferential growth direction. As is shown in result figure, growth of some grains are depressed by grains with faster growth directions.

In figure 3.32(b), the equiaxed dendrite grain and column dendrite grain are presented. For simulation of weld, proper parameters should be measured by experiment. In this simulation, the probability of nucleation of bulk of weld is increased manually so that the equiaxed dendrite grain is obtained in the same simulation zone. In left part of figure, equiaxed dendrite grains solidified. In the middle, there are column dendrite grains. In the right, the unmelt HAZ and base metal is shown.

In figure 3.33, simulation results with coarse mesh(compared with figure 3.32) is applied to the Weld Microstructure. The temperature used here are from the simulation of the weld. The linear interpolation is used for every cell to compute their own cell temperature. With coarse mesh, similar result is obtained with coarse grains.

At the bottom part of the figure 3.33, three grains with the same growth direction grow towards the centre of weld pool. In the end, three column dendrite grains form into one big purple part in figure 3.33(c).

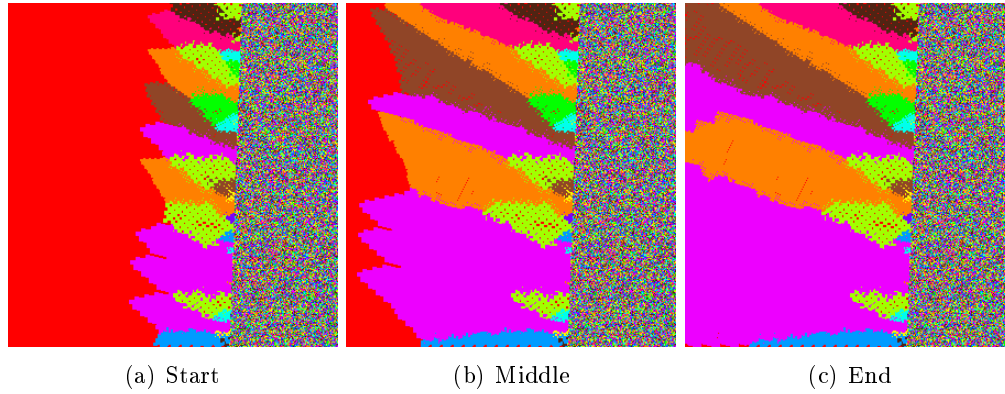
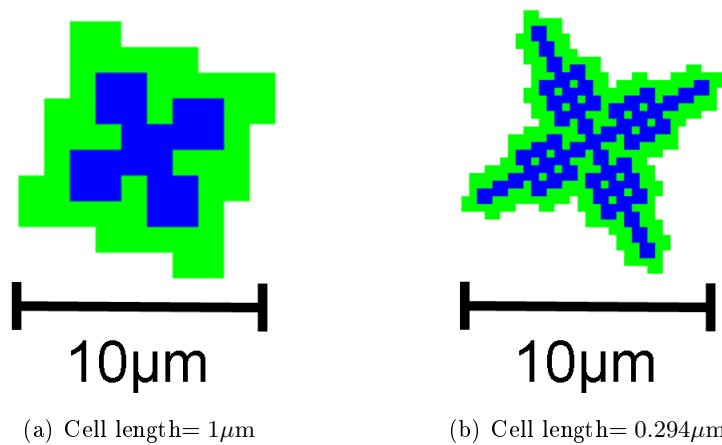


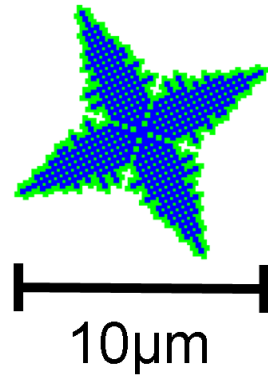
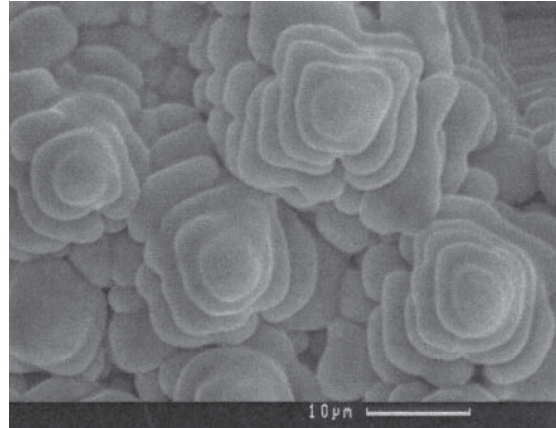
FIGURE 3.33 – Weld Microstructure Simulation with coarse mesh

3.19 Cellular Automaton Simulation validation

3.19.1 Equiaxed dendrite

Simulation results of 2D dendrite with different cell length are compared with the SEM observation of microstructure of DP600 weld in figure 3.34(d) [76].



(c) Cell length $h = 0.067\mu\text{m}$ 

(d) DP600 microstructure [76]

FIGURE 3.34 – Dendrite morphology of 2D simulation and experimental SEM observation

In microscopic comparison, the equiaxed dendrite morphologies between simulation result and experimental observation are similar. As the cell length of 2D CA model decrease, the resolution of simulation increase and more detailed morphologic information can be achieved.

3.19.2 Microstructure of laser welding

3.19.2.1 Weld cross section

A laser beam with power of 4KW and welding speed of 3m/min is applied to dual phase steel DP600. The microstructure of laser weld cross section is observed and the corresponding simulation result is presented in figure 3.35 :

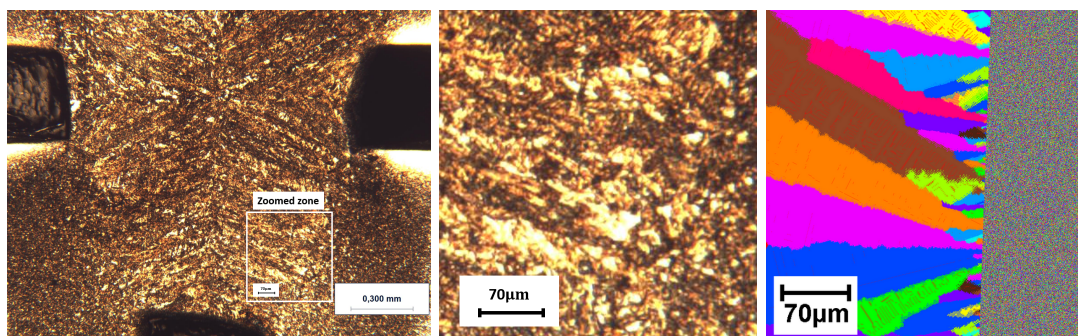


FIGURE 3.35 – Microstructure of FZ and HAZ of DP600 weld cross section

3.19.2.2 Weld upper surface

The microstructure of laser weld cross section is observed and the corresponding simulation result is presented in figure 3.36 :

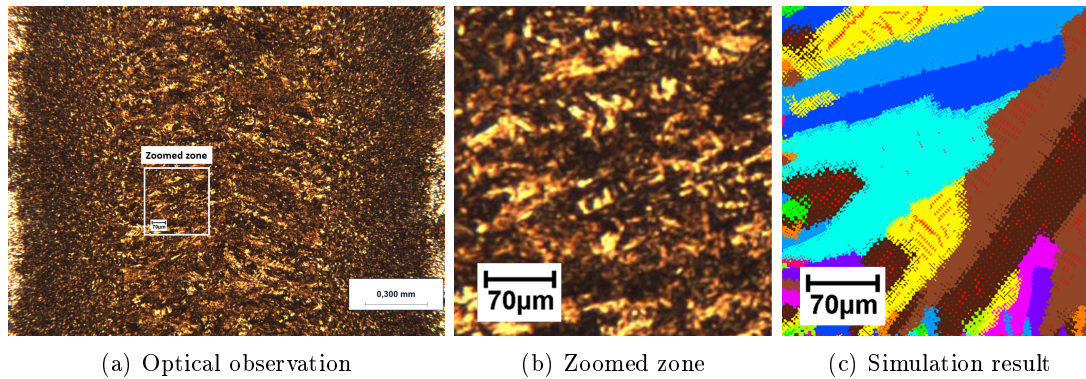


FIGURE 3.36 – Microstructure of FZ and HAZ of DP600 weld upper surface

Using the temperature interpolation technique, a part of weld zone is simulated and compared with the optical observation. In a cross-section of weld simulation, dendrite with random orientations grow from the edge to center of the weld have good accordance with experimental results. At the beginning dendrites has random growth orientation at the edge, finally orientations of grains influenced by welding temperature distribution and dendrites interaction are similar to experimental observation.

Chapitre 4

Finite Element Model and FEM-CA coupling for numerical simulation of residual stresses

4.1 Model Information

The residual stress analysis uses an incremental sequentially coupled thermal-mechanical analysis. The used incremental simulation model consists in two parts :

1. Thermal analysis part
 - Heat source, heat transfer, radiation and convection are considered to analyze the thermal data of the model
 - The computed thermal data is stored in a data file which is prepared for the mechanical analysis.
2. Mechanical analysis part
 - A predefined field introduced by reading the thermal data of thermal analysis model is used as thermal load for mechanical analysis .
 - With the consideration of material properties, such as elastic modulus and plasticity, the expansion behavior of the material due to temperature increase, the elastic and plastic response of the material, and the relaxation of the material at the cooling step are considered to estimate the residual stresses.

The introduction of ABAQUS models will be parted into following sections :

1. Basic material properties. The described properties are used in all the numerical simulation work.
2. Two Models with different geometries and mesh types. This part introduces the geometry parameters and mesh information used for laser welding simulation model.

3. Important terms of material constitutive model. Several terms are introduced in detail. The information of hardening, temperature sensitivity, strain rate sensitivity, elastic and plastic anisotropy via different welding numerical models are introduced in detail.

4.2 Basic material properties

4.2.1 Unit system used in ABAQUS/FEM

To introduce the material properties, one important thing should be noticed that there are no explicit unit system in ABAQUS/FEM. User can select there their favorite unit system. Usually the IS unit system based on N, m, and s is selected. But for laser welding process, the author's unit system are based on N, mm, ms. All the other important units can be derived from the basic unit system of N, mm, ms.

TABLE 4.1 – Unit definition

	IS unit	User defined unit
Mass	$\frac{\text{N} \cdot \text{s}^2}{\text{m}} = \text{kg}$	$\frac{\text{N} \cdot (\text{ms})^2}{\text{mm}} = \text{g}$
Energy	$\text{N} \cdot \text{m} = \text{J}$	$\text{N} \cdot \text{mm} = \text{mJ}$
Pressure	$\text{N}/\text{m}^2 = \text{Pa}$	$\text{N}/\text{mm}^2 = \text{MPa}$
Power	$\text{J}/\text{s} = \text{W}$	$\text{mJ}/\text{ms} = \text{W}$
Density	kg/m^3	g/mm^3

4.2.2 Conductivity

The conductivity of material is a temperature dependent parameter, the data of conductivity is show in Table 4.2 :

TABLE 4.2 – Conductivity of model [77]

Conductivity (W/(m · °C))	Temperature (°C)
34.6	0
34.8	25
35	200
35	254
21.4	1100
25.5	1200
60	1300
70	1400
70	3000

4.2.3 Density

The material density of dual phase steel is a temperature dependent parameter, the data of density is show in Table 4.3 :

TABLE 4.3 – Density of model [77]

Mass density (Kg/m ³)	Temperature (°C)
7594	0
7300	1000
7210	1200
7200	1500

4.2.4 Specific Heat

The specific heat of dual phase material is defined to change with temperature. The parameters of specific heat are show in Table 4.4 :

TABLE 4.4 – Specific heat of model [77]

Specific heat (J/(Kg.° C))	Temperature (°C)
520	0
550	200
600	400
748	600
690	800
520	1100
610	1200
620	1500

4.2.5 Elastic property

In all welding processes, temperature can change from environment temperature to several thousand degrees The Young's modulus and Poisson's ratio is affected by this change. The temperature dependent Young's modulus and Poisson's ratio are show in Table 4.5 :

TABLE 4.5 – Elastic property of model [77]

Young's modulus (Pa)	Poisson's ratio	Temperature (°C)
2.1×10^{11}	0.28	0
1.9×10^{11}	0.295	300
1.2×10^{11}	0.31	600
3×10^{10}	0.33	800

4.2.6 Plastic property

A simple linear material constitutive model of DP600 steel is used based on the work of F Ozturk [78] and Ju Chen [57]. The plastic property of DP600 steel is plotted in figure 4.1. This material constitutive model is only used for mesh type, mesh density and boundary condition analyses. Analyses of material constitutive model of hardening, temperature and strain rate sensitivity use nonlinear material constitutive model identified in chapter 2 and describe in the following part.

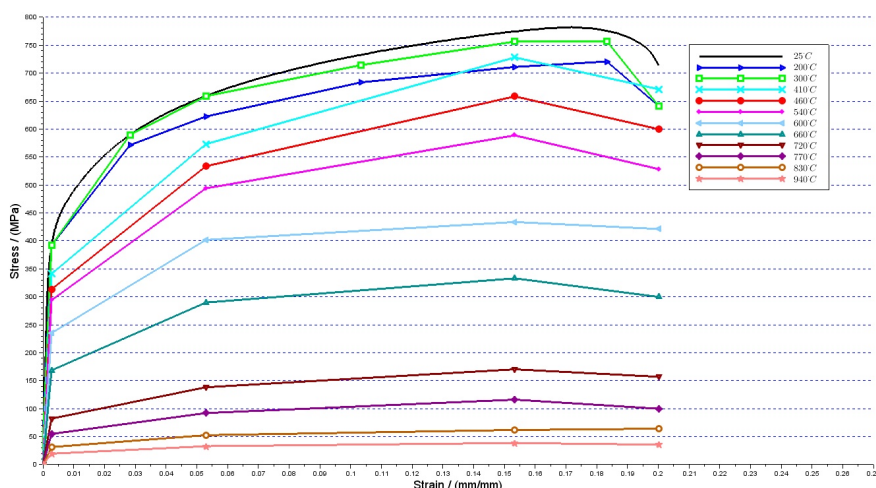


FIGURE 4.1 – Linear material constitutive model of DP600 steel

4.2.7 Expansion

As shown in table 4.6, the expansion coefficient is also set as a temperature dependent parameter :

4.2.8 Heat source model

The shape of heat source model, Gauss heat distribution and corresponding heat source parameters are presented in figure 4.2 and in table 4.7.

TABLE 4.6 – Expansion coefficient [77]

Expansion coefficient	Temperature (°C)
1.2×10^{-05}	0
1.6×10^{-05}	400
1.6×10^{-05}	800
2.2×10^{-05}	1000
2.5×10^{-05}	1200

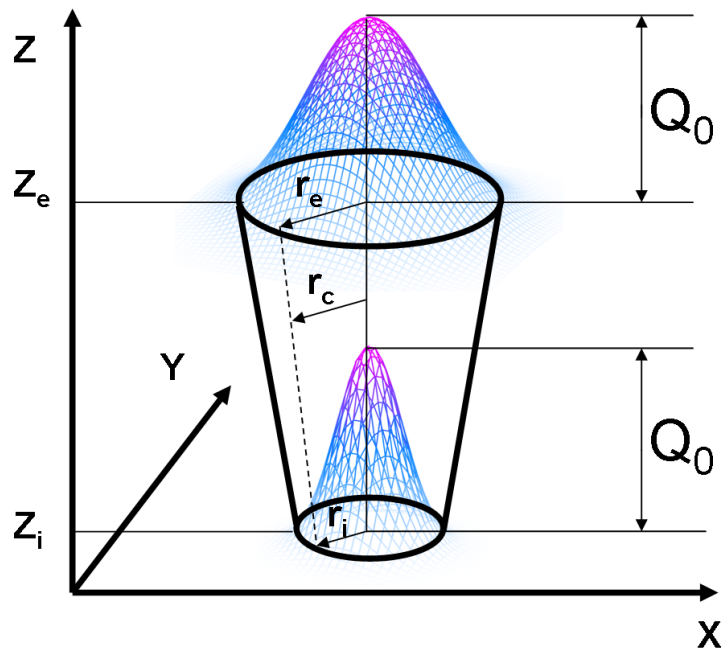


FIGURE 4.2 – The shape of heat source and Gauss heat distribution

TABLE 4.7 – Parameters of heat source

Symbol	Meaning	Magnitude
r_e	radius superior	6.5×10^{-4} m
r_i	radius inferior	5×10^{-4} m
r_c	variational radius	$r_i \leq r_c \leq r_e$
z_e	top surface position in Z axis	0 m
z_i	bottom surface position in Z axis	-2×10^{-3} m
P	laser power	4 Kw
η	efficiency	42 %
V	welding speed	3 m/min

4.3 Model geometry

4.3.1 A geometry

The dimension of thermal analysis model as well as mechanical analysis model are presented in Figure 4.3. The plate has 1.25mm thickness and there is a 0.1mm gap to improve the weld area.

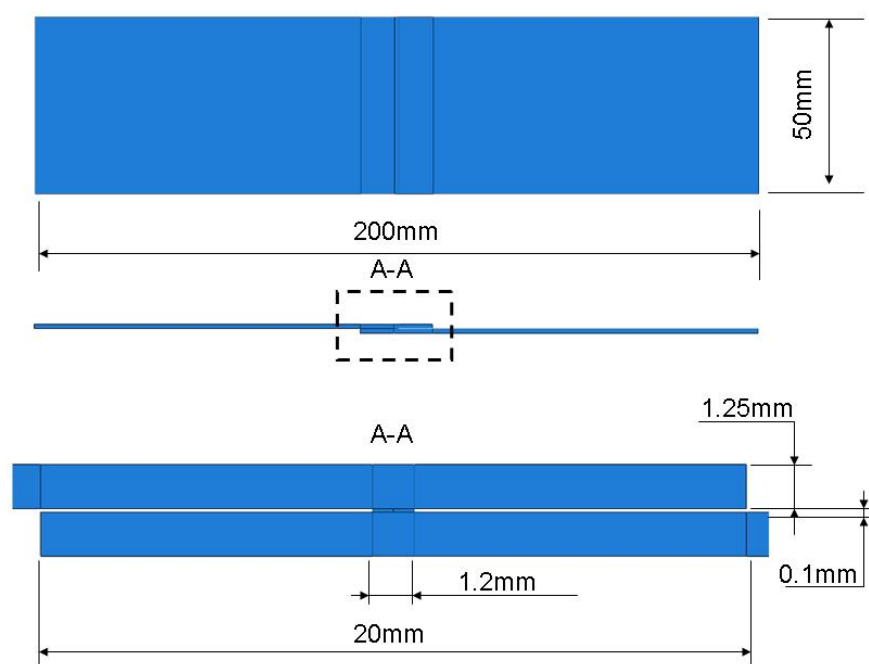


FIGURE 4.3 – The A geometry of welding simulation model

4.3.2 B geometry and mesh method

B geometry are used to study the material constitutive model influences on residual stresses induced by laser welding process. This model are smaller and thus can save more computation time.

The length, width and thickness of plate and the relevant position are presented in figure 4.4.

The model contains 22080 elements and 28350 nodes. The element type of the model is C3D8R. At center weld, the smallest element is $0.3 \times 0.317 \times 0.5$ mm. At the end of the plate, the biggest element is $3.815 \times 0.317 \times 0.5$ mm.

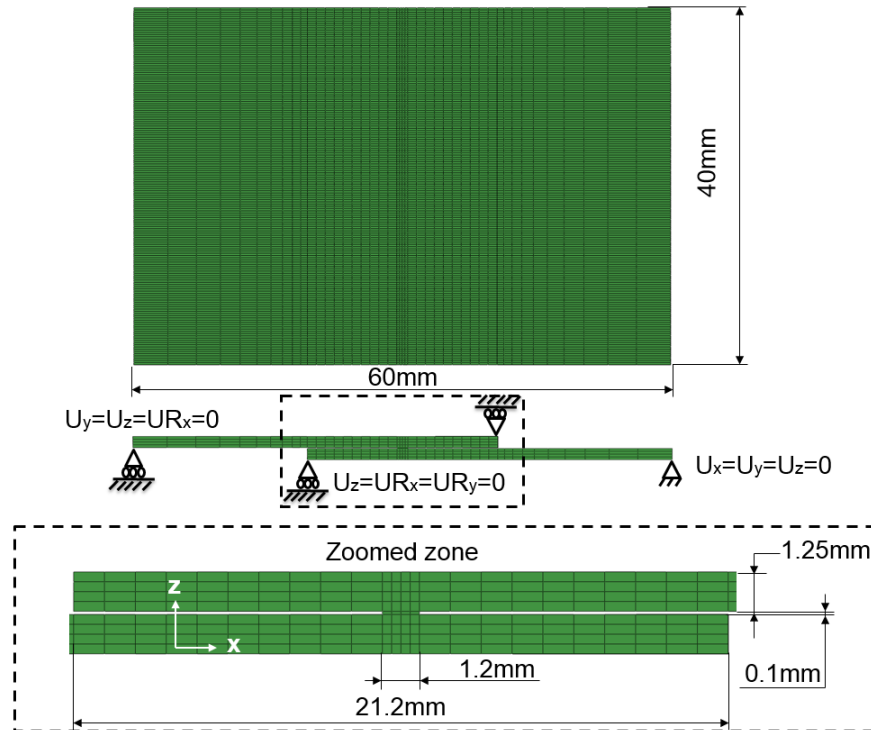


FIGURE 4.4 – The B geometry of welding simulation model

4.4 Boundary conditions

4.4.1 Thermal boundary conditions

The heat convection and the radiation are simulated through surface film condition proposed by ABAQUS FEM thermal simulation model. The film coefficient amplitude and sink amplitude are both instantaneous. The sink temperature is $25\text{ }^{\circ}\text{C}$. The film coefficient (heat transfer coefficient or film effectiveness) is $73.5\text{ W}/(\text{m}^2 \cdot \text{K})$ for convection and $0.25\text{ W}/(\text{m}^2 \cdot \text{K})$ for radiation. The film coefficient is applied to the areas shown in figure 4.5.

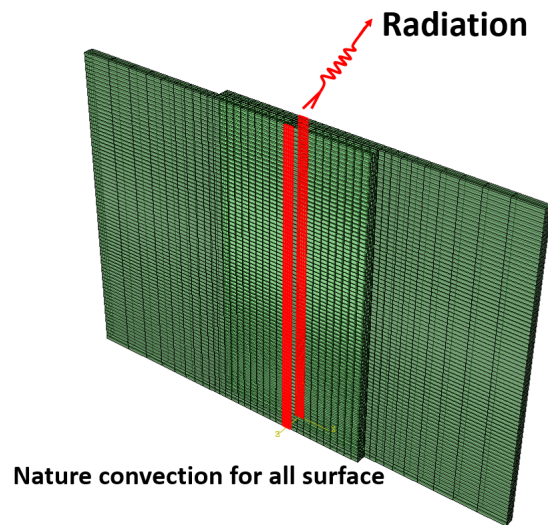


FIGURE 4.5 – Boundary conditions of thermal analysis model using B geometry

4.4.2 Mechanical boundary conditions

In mechanical analysis model, the boundary conditions are defined according to the laser welding process of real experiment. In figure 4.6, the boundary conditions are presented. The right end of the plate is fixed while the left surface can move freely in x direction. Around the weld, the plates are clamped to not move in z direction.

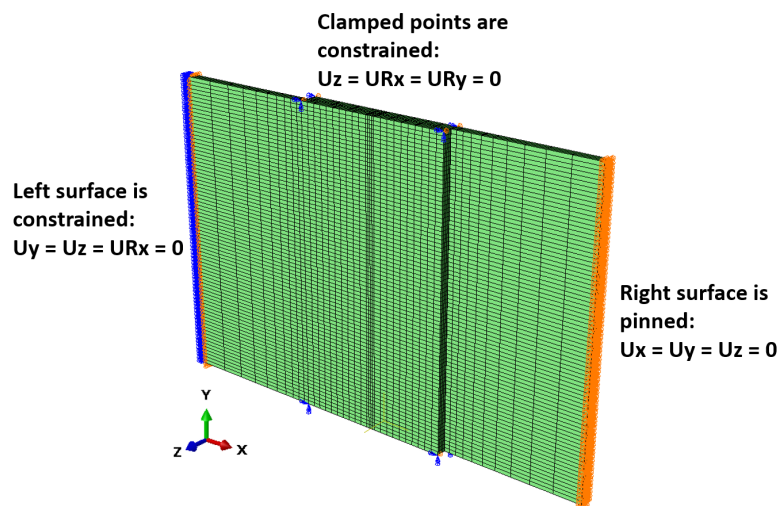


FIGURE 4.6 – Boundary conditions of mechanical analysis model using B geometry

4.5 Analysis steps

Concerning the time history, for both thermal analysis and mechanical analysis model, the laser welding numerical FEM model are divided into three steps : the initial condition, the welding process and the cooling process. The duration time of welding process is dependent on the length of weld and the speed of laser beam. The duration time of cooling process is 100s.

TABLE 4.8 – Analysis job content assigned for each step in thermal analysis model

Name	Initial condition	Welding process	Cooling process
Convection		Created	Propagated
Radiation		Created	Inactivated
Heatsource		Created	Inactivated
Room temperature	Created	computed	computed

The heat diffusion to environment through convection and the environment room temperature are simulated through the whole welding process and cooling process, while radiation and heat source (laser beam input energy) are only simulated at welding process.

4.6 FEM Models with different hardening terms

In this work, FEM welding process is simulated through ABAQUS commercial software. In ABAQUS, the plasticity constitutive model can be defined through UHARD subroutine. Three key terms need to be defined : the hardening term, the strain sensitivity term and temperature sensitivity term.

In figure 4.7, starting from the general constitutive model proposed by A. Gavras [43, 42, 44, 45], the hardening term and one kind of hardening term shape are presented. This general constitutive model is for materials undergoing important thermo-mechanical gradients dynamic softening phenomenon, phase transformation described by ψ dynamic softening fraction or dual phase mixture described by principle phase fraction w . The hardening term describing plastic deformation properties of a material at fixed temperature and strain rate. Based on previous experimental tests, the hardening term of dual phase steel DP600 are generated with Ludwik hardening term σ_{hm} , Voce hardening term σ_{hf} and a synthesis hardening term using mixture Avrami formulation of martensite and ferrite phase (where w is martensite fraction).

The influence of material hardening term definition on final results of residual stresses of laser welding process is studied through 5 FEM welding simulation models with different hardening terms. The 5 hardening terms are obtained in chapter 2 and the figure 2.7, figure 2.8, figure 2.9 and figure 2.10 are re-presented here to further discuss of FEM simulation purposes.

$$\sigma(\varepsilon_e^p, \dot{\varepsilon}, T) = [\sigma_{hm}(\varepsilon_e^p) \cdot w + \sigma_{hf}(\varepsilon_e^p) \cdot (1 - w)] \cdot G(\dot{\varepsilon}) \cdot F(T)$$

Hardening $H(\varepsilon_e^p)$

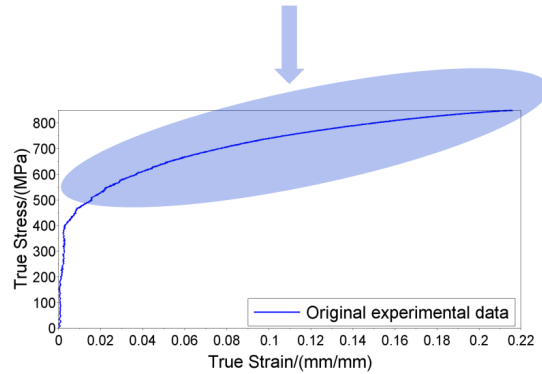
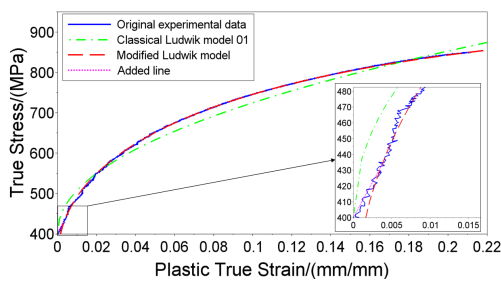
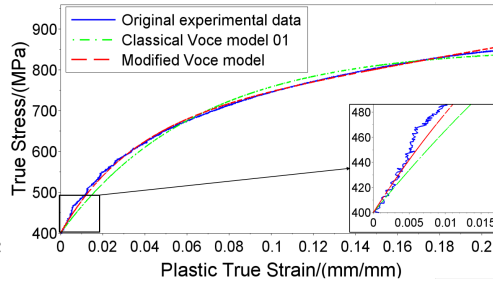


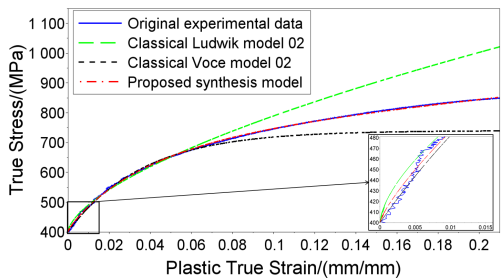
FIGURE 4.7 – Hardening term of material constitutive model



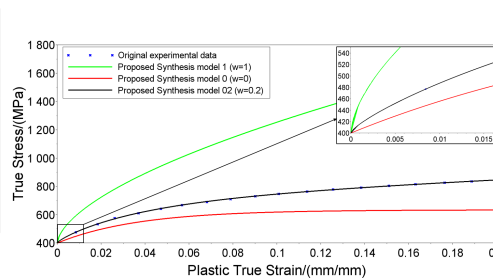
(a) Modified Ludwik model



(b) Modified Voce model



(c) Classical Ludwik model 02, classical Voce model 02 and proposed synthesis model



(d) Proposed synthesis model 0, model 02 and model 1 (w=0, w=0.2 and w=1)

FIGURE 4.8 – Hardening models used in FEM laser welding simulation models

In figure 4.8, the modified Ludwik model, the modified Voce model and the proposed synthesis model 02 all have good accordance with the original experimental data. The modified Ludwik model, the modified Voce model are not in classical form. The proposed synthesis model 02 is the synthesis of classical Ludwik model and classical Voce model. With different mathematical form, the three results in similar stress-strain curves describing the plasticity of dual phase steel DP600. In figure 4.8 (c) and (d), the classical Ludwik model 02 and the classical Voce model 02 have good accordance with the original experimental data only in plastic strain range of $[0, 0.05]$ while the proposed synthesis model 02 has good accordance in range of $[0, 0.2]$ and can be used for a lot of welding or other dynamic forming processes.

Five hardening models described in chapter 2.2.1.4 are simulated through commercial software ABAQUS/FEM. The numerical models are based on basic material properties identified in chapter 4.2, B geometry and mesh presented in chapter 4.3.2, boundary conditions detailed in chapter 4.4 and analysis steps described in chapter 4.5. The parameters of the five hardening models are reminded in table 4.9.

TABLE 4.9 – Rheological coefficients corresponding to different DP600 hardening models

	σ_y	n_1	n_2	n_3	n_4	w	Equation	Nonlinear regression on ε_p range
Classical Ludwik model 01	400	980	0.48	-	-	-	(2.11)	$[0, 0.2]$
Classical Ludwik model 02	400	1660	0.63	-	-	-	(2.19)	$[0, 0.05]$
Modified Ludwik model	400	1690	0.5	-1240	-65	-	(2.13)	$[0, 0.2]$
Classical Voce model 01	400	555	15.5	-	-	-	(2.14)	$[0, 0.2]$
Classical Voce model 02	400	340	27.5	-	-	-	(2.20)	$[0, 0.05]$
Modified Voce model	400	270	30	900	-	-	(2.16)	$[0, 0.2]$
Proposed synthesis model (w=0.4)	400	1660	0.63	340	27.5	0.40	(2.17 et 2.18)	$[0, 0.2]$
Proposed synthesis model 02 (w=0.2)	400	3411.3	0.60	234.4	27.1	0.20	(2.17 et 2.21)	$[0, 0.2]$
Proposed synthesis model 1 (w=1)	400	3411.3	0.60	234.4	27.1	1	(2.17)	-

For the results of hardening models, one should keep in mind that the results will be revised after the temperature sensitivity is discussed. For the present, the condition $F(298K)=1$ and $F(1803K)=0.05$ are used with a Johnson-Cook temperature sensitivity model. It can be noted also here that a constant martensite fraction is used. The strain rate sensitivity term $G(\dot{\varepsilon}) = 1$ is used in order to focus the behavior analysis on hardening influence. In future work, the martensite fraction w during the solidification should be considered dependent on the temperature in the range of fusion temperature T_f and ambient temperature T_0 using a variation $w(T)$ obtained from solid fraction computation of CA model. According to $G(\dot{\varepsilon}) = 1$, the proposed synthesis model 02 is written in the form : $H(\varepsilon_c^p) = w \cdot (400 + 3411.28\varepsilon_p^{0.6014}) + (1 - w) \cdot \{400 + 234.40 \cdot [1 - \exp(-27.1092\varepsilon_p)]\}$ where identification has made for w=0.2.

By comparing the modified Ludwik model, the modified Voce model and the proposed synthesis model 02, the influence of constitutive equation form on FEM welding simulation results of residual stresses is evaluated. By comparing the classical Ludwik model 02, the classical Voce model 02 and the proposed synthesis model 02, the influence of hardening term in the plastic strain range of laser welding on residual stresses of FEM are studied. Results and discussion will be presented in chapter 5.

4.7 FEM Models with different temperature sensitivity terms

In figure 4.9, starting from the general constitutive model proposed by A. Gavras [43, 42, 44, 45], the temperature sensitivity term and its influence on the plastic deformation properties of a material are presented. The temperature sensitivity term $F(T)$ can influence the magnitude of elasto-plastic flow behavior. The stress-strain curve will be influenced by temperature. Normally, the higher the temperature is, the lower the temperature sensitivity will be.

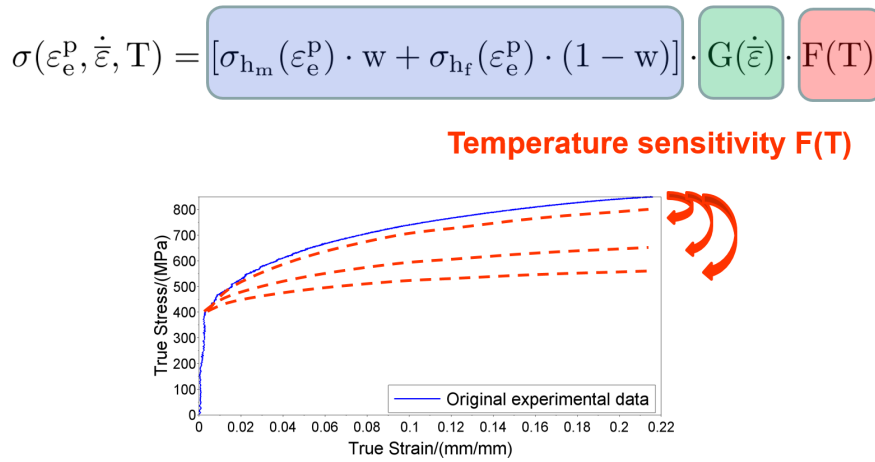


FIGURE 4.9 – Temperature sensitivity term of material constitutive model

Based on temperature sensitivity of a high strength steel in the work of Chen [57], the temperature sensitivity term of dual phase steel DP600 are obtained with Johnson-Cook model, Chen model, a proposed model and a polynomial temperature sensitivity term. Figure 2.11 are re-presented here to present the difference of Johnson-Cook, Chen, proposed and polynomial temperature sensitivity models.

Johnson-Cook temperature sensitivity term use only one parameter to describe the temperature sensitivity of material. It has a good accordance with experimental data from room temperature to about 700K, but not good for temperature bigger than 700K. Chen temperature sensitivity term use two parameters to describe the temperature sensitivity of material while the proposed temperature sensitivity term use three. Chen and proposed temperature sensitivity terms are similar in figure 4.10. Polynomial temperature sensitivity term can precisely describe the experimental data but it has to be identified for every materials and do not have a physical sense.

The 4 temperature sensitivity terms which are used in FEM welding simulation are listed below :

- Johnson-Cook temperature sensitivity term :

$$F(T) = 1 - T^{*1.5} \quad (4.1)$$

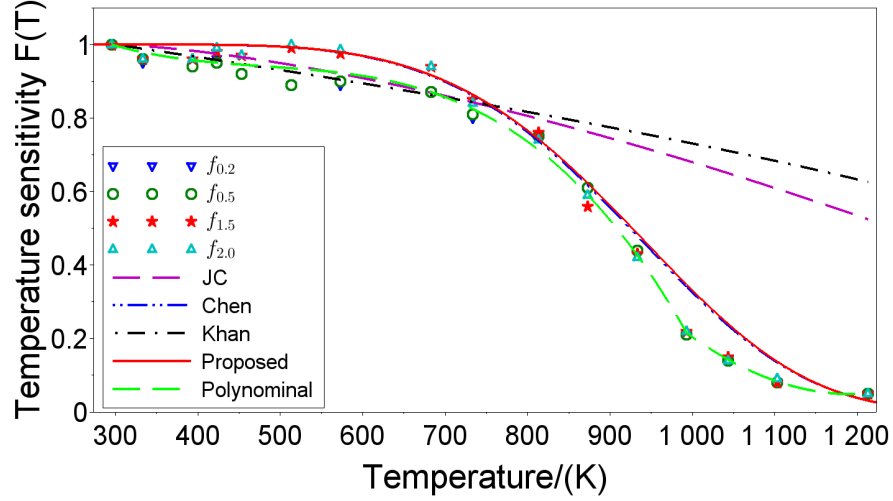


FIGURE 4.10 – The 4 temperature sensitivity terms used in FEM laser welding simulation models

- Chen temperature sensitivity term :

$$F(T) = \exp(4.254 \cdot T^{*-28.418}) \quad (4.2)$$

- Proposed temperature sensitivity term :

$$F(T) = (1 - 0.699 \cdot T^{*4.027})^{38.629} \quad (4.3)$$

- Polynomial temperature sensitivity term :

$$295.15K < T < 993.15K :$$

$$F(T) = 1.55 - 3.50 \times 10^{-3} \cdot T + 7.00 \times 10^{-6} \cdot T^2 - 4.82 \times 10^{-9} \cdot T^3 \quad (4.4)$$

$$993.15K < T < 1213.15K :$$

$$F(T) = 5.18 - 7.83 \times 10^{-3} \cdot T + 2.30 \times 10^{-6} \cdot T^2 + 5.35 \times 10^{-10} \cdot T^3 \quad (4.5)$$

Johnson-Cook temperature sensitivity term is similar with polynomial temperature sensitivity term at low temperature but have obvious difference at high temperature. Chen and proposed temperature sensitivity model both have difference at low and high temperature with polynomial temperature sensitivity model. The influences of temperature sensitivity difference on FEM welding simulation results of residual stresses are investigated. Results and discussions will be presented in chapter 5.

4.8 FEM Models with different strain rate sensitivity terms

In figure 4.11, starting from the general constitutive model proposed by A. Gavras [43, 42, 44, 45], the strain rate sensitivity term and its influence on the plastic deformation properties of a material are presented. The strain rate sensitivity term $G(\dot{\epsilon})$ can

influence the magnitude of elasto-plastic flow behavior. Normally, the higher the strain rate is, the higher the strain rate sensitivity will be.

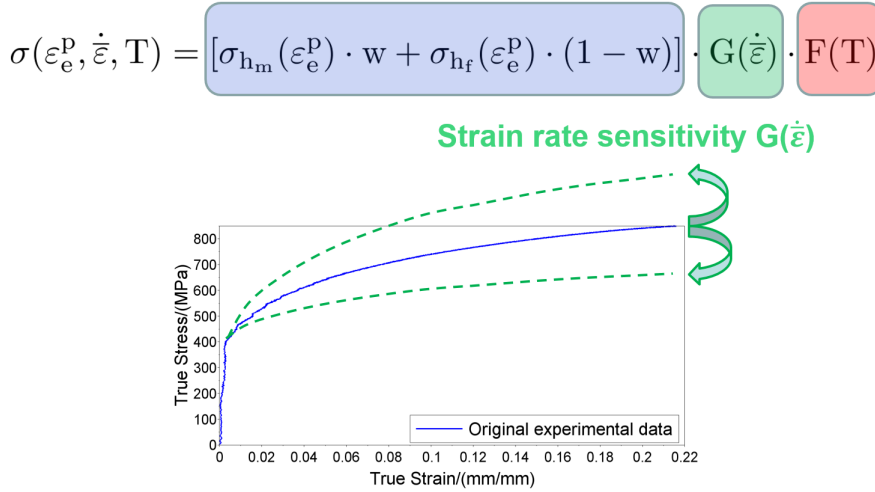


FIGURE 4.11 – Temperature sensitivity term of material constitutive model

Based on experimental and literature data [3], the strain rate sensitivity term of dual phase steel DP600 are obtained in section 2.2.3.4. In figure 4.12, strain rate sensitivity values under different temperatures are plotted.

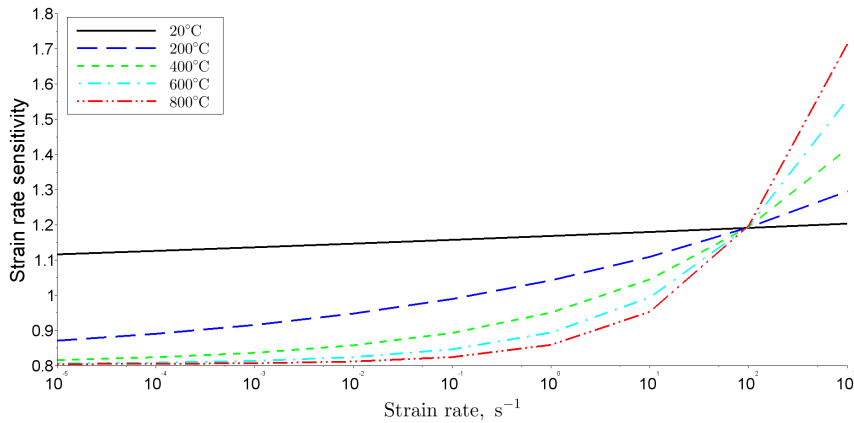


FIGURE 4.12 – The strain rate sensitivity term under different temperatures

In figure 4.12, it is shown that the strain rate sensitivity value is around 1 at ambient temperature. The strain rate sensitivity value will change according to strain rate and temperature. The strain rate sensitivity used for FEM welding simulation is written in in section 2.2.3.4 and rewritten here derived from proposed Arcsinus hyperbolic strain rate law proposed by A. Gavrus [43, 42, 44, 45] :

$$G(\dot{\bar{\epsilon}}) = 0.8042232 \times \left[1 + Ash \left(\frac{1}{2} (\dot{\bar{\epsilon}}/96.077)^{0.0005410 \times T - 0.1443611} \right) \right] \quad (4.6)$$

The reference strain rate $\dot{\bar{\epsilon}} = 96.077$ represents the transition between static and dynamic loads. By comparing this strain rate sensitivity term with $G(\dot{\bar{\epsilon}}) = 1$, the influence of strain rate sensitivity term on FEM welding simulation model results of residual stresses are analyzed. Results and discussions will be presented in chapter 5.

4.9 FEM Models with different material anisotropy properties

The anisotropy of dual phase steel DP600 plate is generated by rolling manufacturing process. The definition of dual phase steel DP600 plate is strongly related with the rolling direction. To investigate the anisotropy of DP600 plate influence on FEM laser welding numerical model results concerning residual stresses, the plate are cut into small pieces which have particular angles with rolling direction and then welded in experiments. Figure 4.13 illustrates the cutting method.

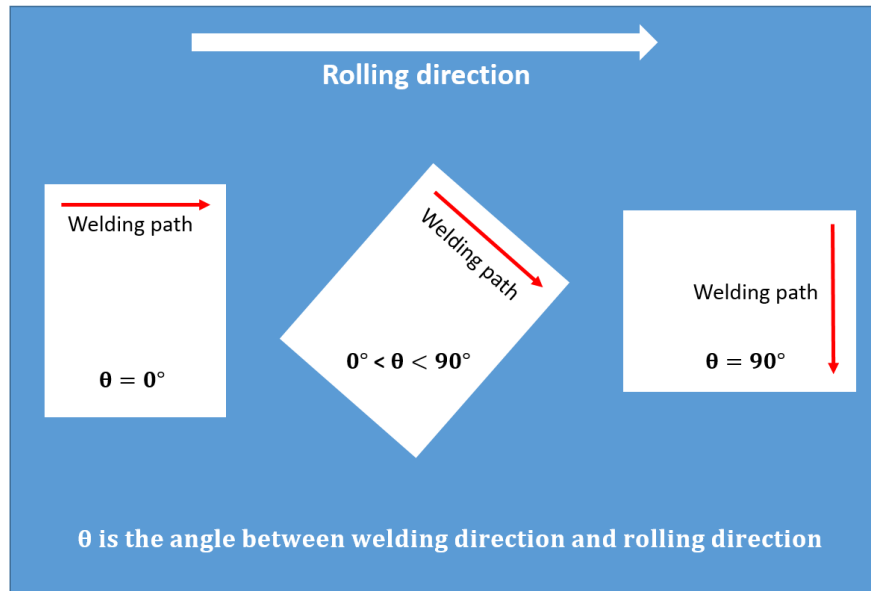


FIGURE 4.13 – The specimens cut with different angles on dual phase steel DP600 plate

In figure 4.14, FEM laser welding models with 5 rolling directions ($\theta = 0^\circ, 30^\circ, 45^\circ, 60^\circ$ and 90°) are simulated to evaluate the anisotropy influence on simulation results of residual stresses.

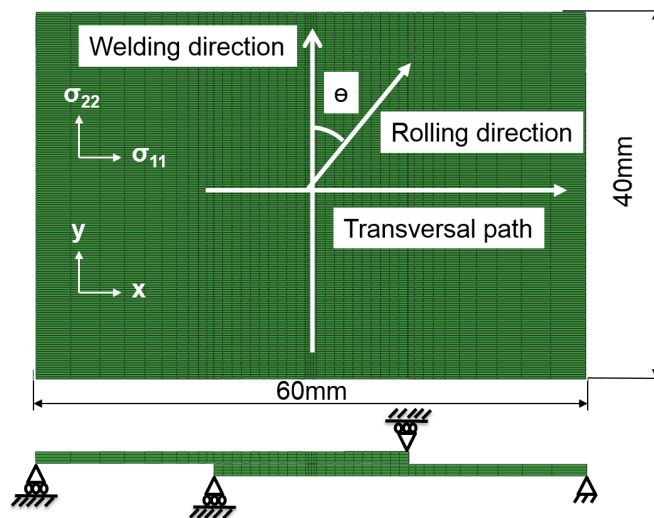


FIGURE 4.14 – Rolling direction defined in numerical laser welding model

Here two anisotropic effects are analyzed : the orthotropic elastic one and the Hill plastic plate anisotropy according to chapter 2.2.4.

4.10 Cellular Automaton - Finite Element coupling

4.10.1 Base metal elasticity

In the computation of residual stresses, the elasticity property of DP600 steel has an important influence on the simulation results, so the temperature influences are considered and the Young's modulus and Poisson's ratio of DP600 steel are presented in Table 4.10.

TABLE 4.10 – Young's Modulus and Poisson's ratio of DP600 [77]

Temperature (°C)	0	300	600	800
Young's Modulus (GPa)	210	190	120	30
Poisson's ratio	0.280	0.295	0.310	0.330

4.10.2 Weld material elasticity

The cellular automaton is applied in the welding fusion zone to simulate the micro-structure of solidification process. In figure 4.15, the position of CA simulation zone is presented. The temperature of the four corner points is computed by ABAQUS/FEM model and then interpolated into CA simulation model.

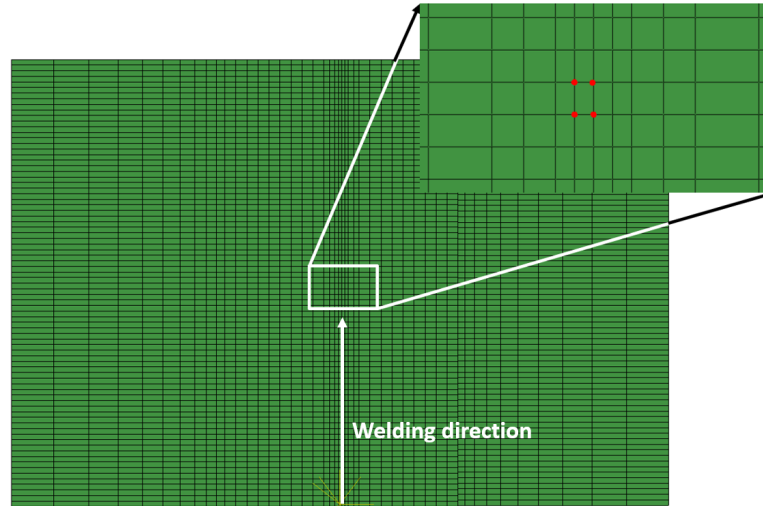


FIGURE 4.15 – The CA simulation position in ABAQUS/FEM model

The results of ABAQUS thermal simulation model is presented in figure 4.16. The weld zone experienced a sudden increase and decrease of temperature. The liquid status of melting pool only last less than 1 second.

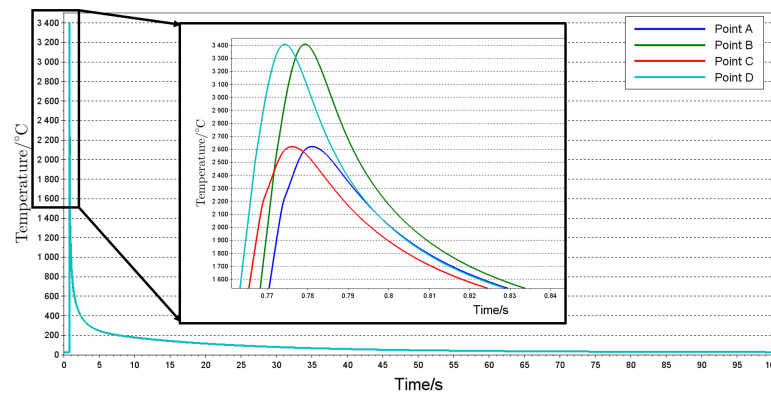


FIGURE 4.16 – Temperature history data of 4 points

In figure 4.17, the flowchart of CA-FE coupling model for residual stress simulation is shown. The crystalline orientation and orientation fraction is computed based on CA model, the results combines with the martensite elastic constants is used to calculate the weld elastic constants that are used in ABAQUS/FEM simulation for residual stresses.

Because of the high cooling rate of laser welding, the face centered cubic austenite in DP600 weld turns to body centered tetragonal martensite in solidification process. This phase transformation phenomenon are observed in many works [21, 79]. Due to the

$$[\alpha_{ij}]^{-1} = \begin{bmatrix} \cos^2\theta & \sin^2\theta & 0 & 0 & 0 & 2\sin\theta\cos\theta \\ \sin^2\theta & \cos^2\theta & 0 & 0 & 0 & -2\sin\theta\cos\theta \\ 0 & 0 & 1 & 0 & 0 & 0 \\ 0 & 0 & 0 & \cos\theta & -\sin\theta & 0 \\ 0 & 0 & 0 & \sin\theta & \cos\theta & 0 \\ -\sin\theta\cos\theta & \sin\theta\cos\theta & 0 & 0 & 0 & \cos^2\theta - \sin^2\theta \end{bmatrix} \quad (4.11)$$

and $[\beta_{ij}]$ is :

$$[\beta_{ij}] = \begin{bmatrix} \cos^2\theta & \sin^2\theta & 0 & 0 & 0 & -\sin\theta\cos\theta \\ \sin^2\theta & \cos^2\theta & 0 & 0 & 0 & \sin\theta\cos\theta \\ 0 & 0 & 1 & 0 & 0 & 0 \\ 0 & 0 & 0 & \cos\theta & \sin\theta & 0 \\ 0 & 0 & 0 & -\sin\theta & \cos\theta & 0 \\ 2\sin\theta\cos\theta & -2\sin\theta\cos\theta & 0 & 0 & 0 & \cos^2\theta - \sin^2\theta \end{bmatrix} \quad (4.12)$$

In equation 4.11 and equation 4.12, θ is martensite rotation angle in plane and the direction cosines between x, y, z axials of A coordinate x_A, y_A, z_A and x, y, z axials of B coordinate x_B, y_B, z_B are :

TABLE 4.11 – Direction cosines values in plane rotation with angle θ

	x_A	y_A	z_A
x_B	$\cos\theta$	$-\sin\theta$	0
y_B	$\sin\theta$	$\cos\theta$	0
z_B	0	0	1

The temperature influence on elastic constants are considered proportionally the same as those of DP600 Young's modulus and Poisson's modulus in table 4.10. Linear interpolation is applied to decrease elastic constants proportionally as the temperature increases for 300°C, 600°C and 800°C.

$$\frac{W_T}{W_0} = \frac{B_T}{B_0} \quad (4.13)$$

Where W_T stands for the weld material Young's Modulus and Poisson's ratio values of $E_1, E_2, E_3, \nu_{12}, \nu_{13}, \nu_{23}, G_{12}, G_{13}$ and G_{23} in table 6.2 at temperature T (T can be 0°C, 300°C, 600°C and 800°C) and B_T stands for the corresponding base material Young's Modulus and Poisson's ratio values in table 4.10. The computed values are shown in table 6.2 and the units of $E_1, E_2, E_3, G_{12}, G_{13}$ and G_{23} are of GPa.

TABLE 4.12 – Elastic constants of weld material

$T/^\circ C$	E_1	E_2	E_3	ν_{12}	ν_{13}	ν_{23}	G_{12}	G_{13}	G_{23}
0	203.40	203.07	202.72	0.2943	0.2902	0.2942	79.06	78.72	78.85
300	184.03	183.73	183.42	0.3101	0.3057	0.3100	71.53	71.22	71.34
600	116.23	116.04	115.84	0.3258	0.3213	0.3258	45.18	44.98	45.06
800	29.06	29.01	28.96	0.3469	0.3420	0.3468	11.29	11.25	11.26

Based on above analyze, the elasticity of weld is redefined according to martensite properties and cellular automaton orientation results. If the same material orientations are used, the elastic constants considering CA orientations can be give in table 6.3 :

TABLE 4.13 – Elastic constants of weld material with CA orientations

$T/^\circ C$	E_1	E_2	E_3	ν_{12}	ν_{13}	ν_{23}	G_{12}	G_{13}	G_{23}
0	203.78	203.70	202.72	0.2924	0.2924	0.2935	78.93	78.85	78.55
300	184.37	183.30	183.42	0.3080	0.3081	0.3092	71.42	71.34	71.07
600	116.45	116.40	115.84	0.3237	0.3237	0.3249	45.10	45.05	44.88
800	29.11	29.10	28.96	0.3446	0.3446	0.3459	11.28	11.26	11.22

The influence of weld elasticity on FEM welding simulation model results of residual stresses are analyzed. Results and discussions will be presented in chapter 5.

It can be noted that regarding all the nine elastic modulus the differences are relatively small in this case (max 0.5%). The model permits to take into account the orthotropic elasticity and microstructure morphology obtained from the CA simulation in the case of alloys with more anisotropic elasticity sensitivity.

Chapitre 5

Numerical simulation results, experimental analysis and discussions

5.1 Mesh type

As is shown in Figure 5.1 and Figure 5.2, the lap joint is meshed. The fusion zone are meshed with the maximum mesh density due to big temperature gradient. Except for the fusion zone(HAZ zone and base metal zone), transition mesh are used to diminish the computation time. The rectangular model use a rectangular type of mesh transition (Figure 5.1) while wedge model use a wedge type of mesh transition (Figure 5.2).

The weld of the rectangular model and the wedge model both are of 50mm length in longitudinal direction and meshed to 40 equal parts with 1.25mm for each part. The two models both have one transition layer. The efficiency of the two type transition layers are investigated.

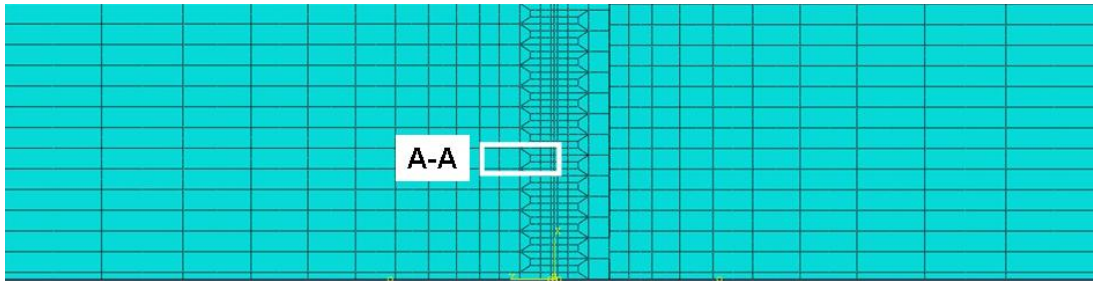
It should be noted that before discussion of material constitutive model, a simple linear material constitutive model of DP600 steel is used for mesh type analysis. The material plasticity property are based on the work of F Ozturk [78] and Ju Chen [57].

5.1.1 Rectangular type of mesh transition

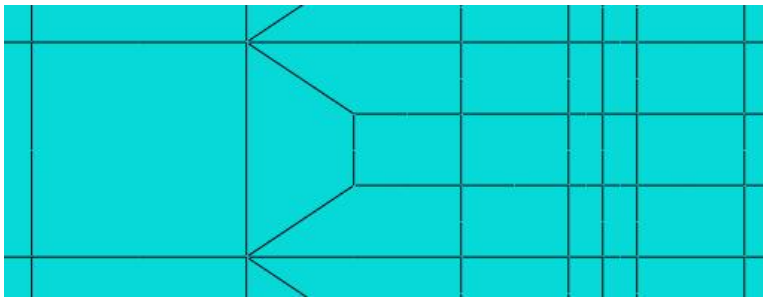
In Figure 5.1, the rectangular type of mesh transition is presented.

5.1.2 Wedge type of mesh transition

In Figure 5.2, the wedge type of mesh transition is presented.

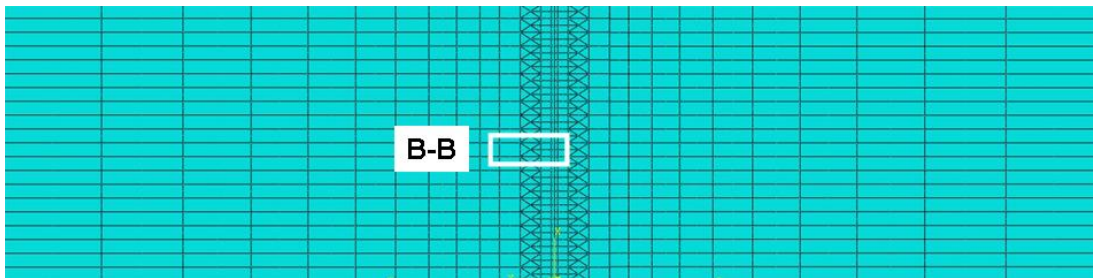


(a) Whole model



(b) A-A

FIGURE 5.1 – Rectangular type of mesh transition



(a) Whole model



(b) B-B

FIGURE 5.2 – Wedge type of mesh transition

5.1.3 Computation time

In total, there are 8 models created to analysis computation effect of transition mesh. The names of models and their computation time are listed in Table 5.1. All the simulations are done with the same condition in clusters.

TABLE 5.1 – Computation time of models

Model name	Wedge	Rect	8 nodes	20 nodes	Temp	Stress	Time (s)
Stress02-square3to1-C3D20R	-	✓	-	✓	-	✓	5134
Stress02-square3to1-C3D8R	-	✓	✓	-	-	✓	1235
Stress02-wedge2to1-C3D20R	✓	-	-	✓	-	✓	6226
Stress02-wedge2to1-C3D8R	✓	-	✓	-	-	✓	1173
Temperature02-square3to1-DC3D20	-	✓	-	✓	✓	-	1567
Temperature02-square3to1-DC3D8	-	✓	✓	-	✓	-	1632
Temperature02-wedge2to1-DC3D20	✓	-	-	✓	✓	-	1914
Temperature02-wedge2to1-DC3D8	✓	-	✓	-	✓	-	1805

In the table, “Wedge” means the wedge type of transition mesh and “Rect” for rectangular type. For all the rectangular elements, “8 nodes” means an element has 8 nodes for computation and the same is true for “20 nodes”. For temperature computation, the element type of “8 nodes” is DC3D8 and that of “20 nodes” is DC3D20. For stress computation, the element type of “8 nodes” is C3D8R and that of “20 nodes” is C3D20R. “Temp” means model for temperature computation and “Stress” means model for stress computation. “✓” means the model is of this type and “–” not.

5.1.3.1 Comparison between rectangular type and wedge type

Based on simulation results, computation times are drawn in Figure 5.3. The rectangular of transition mesh consumes less time than wedge type in all the models for temperature simulation. As for stress simulation, the model of rectangular type takes 82.6 % time of wedge type to solve the simulation with C3D20R, while rectangular type takes nearly the same time (105% time) of wedge type with C3D8R.

The computation time of 8 nodes element type model are much less than that of 20 nodes element type model for stress computation, while the computation time are nearly the same for temperature computation. For stress model, the element with 8 nodes and 20 nodes are C3D8R and C3D20R, respectively. For temperature model, the the element with 8 nodes and 20 nodes are DC3D8 and DC3D20, respectively.

The computation time of temperature model are less than that of stress model with 20 nodes element type, while the computation time of temperature model are more than that of stress model with 8 nodes element type.

In general, the rectangular type of transition mesh can reduce more computation time than wedge type of transition mesh when the same mesh of weld and the same number of transition mesh layers are used. As is presented in Figure 5.1(b) and Figure 5.2(b), rectangular type can reduce 3 elements to 1 element while the wedge type only

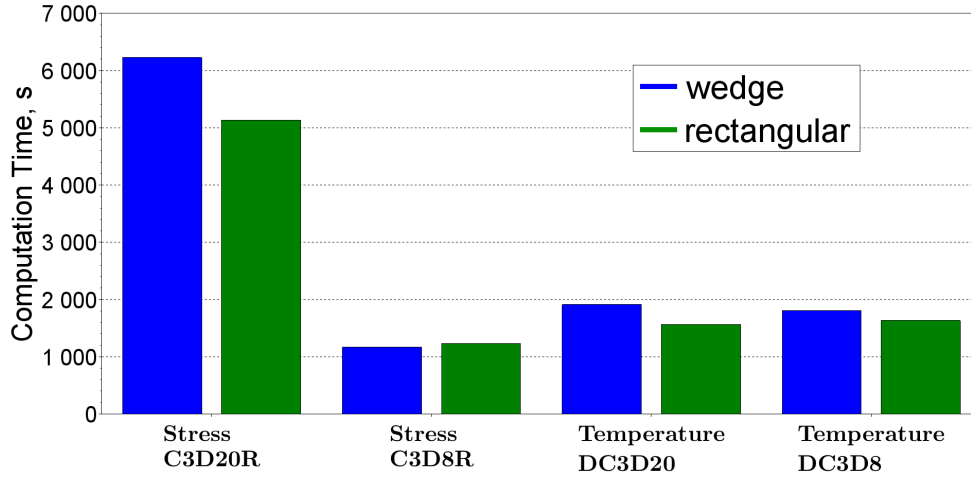


FIGURE 5.3 – Comparison of computation time between wedge type and rectangular type

reduce 2 elements to 1 element.

A further compare for element type of stress model is investigated. The transition layer is rectangular type and the element type is C3D20, C3D20R, C3D8 and C3D8R, seperately. The computation is done on a computer with 4 CPU of Intel Core i7-4700HQ.

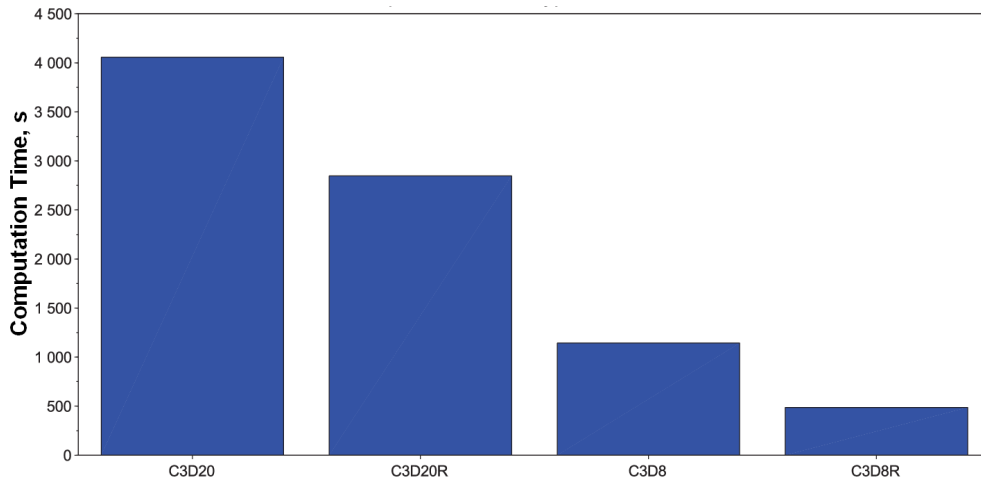


FIGURE 5.4 – Comparison of computation time of different element type model

As can be seen in Figure 5.4, among all element type models, the model with C3D8R consumes the least time.

Based on above analyses, two conclusion are listed below :

- The rectangular type of transition mesh can reduce more computation time than wedge type of transition mesh when the same mesh of weld and the same number

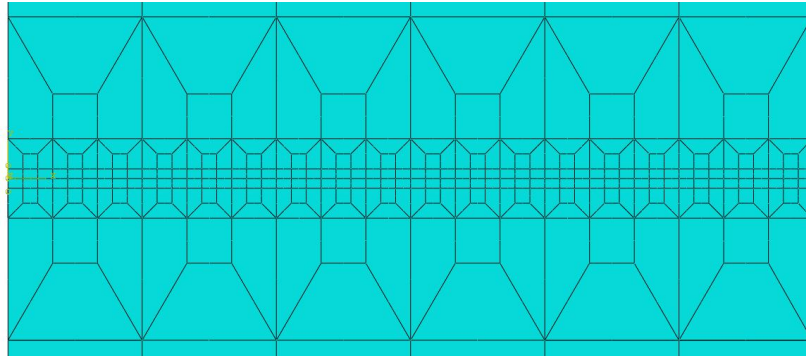
of transition mesh layers are used.

- The model of element type C3D8R, compared with C3D8, C3D20R and C3D20, consume the least computation time.

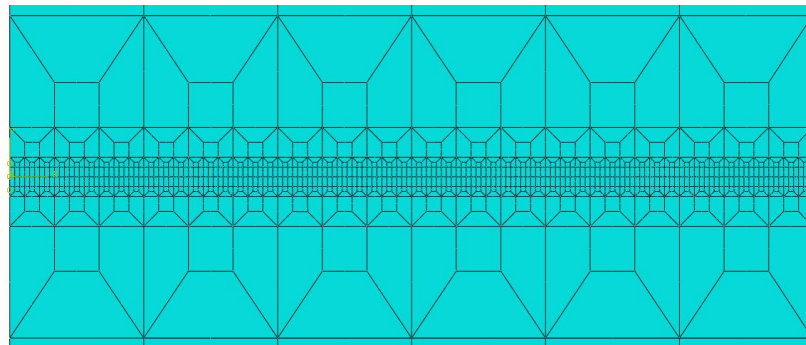
5.2 Mesh density

5.2.1 Mesh of longitudinal direction

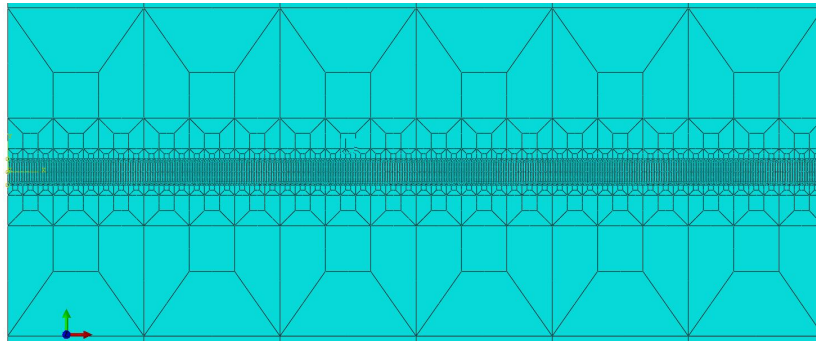
Weld are meshed in longitudinal direction with 54, 162, and 486 intervals. The 3 models with 2 transition mesh layers are shown in Figure 5.5 (a), 3 layers in Figure 5.5 (b), and 4 layers in Figure 5.5 (c). The three models are labeled 2layers, 3layers, and 4layers, respectively.



(a) 2layers



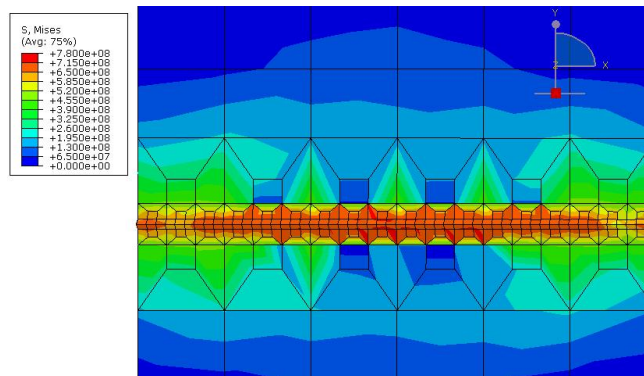
(b) 3layers



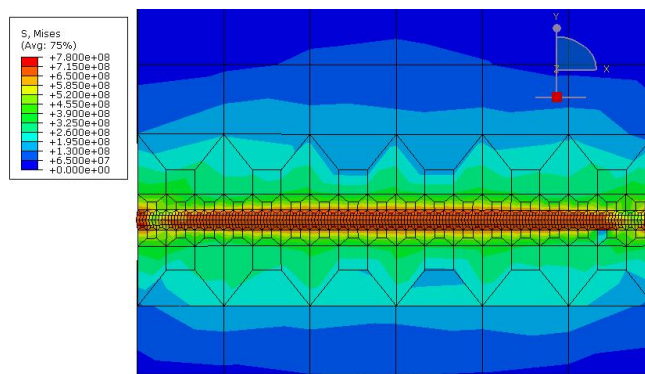
(c) 4layers

FIGURE 5.5 – Mesh of longitudinal direction

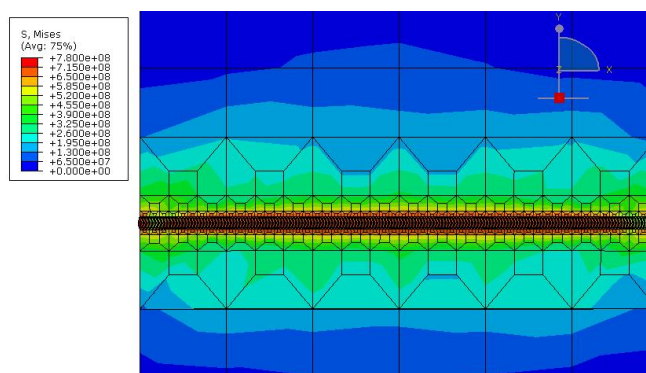
The residual stress distributions of models are presented in Figure 5.6. The equivalent stress at weld zone is the highest and the equivalent stress decreases outward the weld-transverse in-plate direction. With the intervals increase, the residual stress in the zone adjacent to middle weld increase.



(a) 2layers



(b) 3layers



(c) 4layers

FIGURE 5.6 – Residual stress distribution

In Table 5.2, the computation times and results of models are presented. Further analysis is in Figure 5.7, Figure 5.8 and Figure 5.9.

TABLE 5.2 – Computation time and result of models

Model Name	Time (s)	Fluctuation Temperature (°C)	Maximal Residual Stress (Pa)
Temperature-2layers	1316	3027~4281	-
Temperature-3layers	2047	3670~3799	-
Temperature-4layers	5392	3681~3697	-
Stress-2layers	615	-	7.217×10^8
Stress-3layers	1872	-	7.796×10^8
Stress-4layers	9844	-	7.758×10^8

In Figure 5.7, for both temperature model and stress model, the computation time, increase rapidly as the number of layers increase.

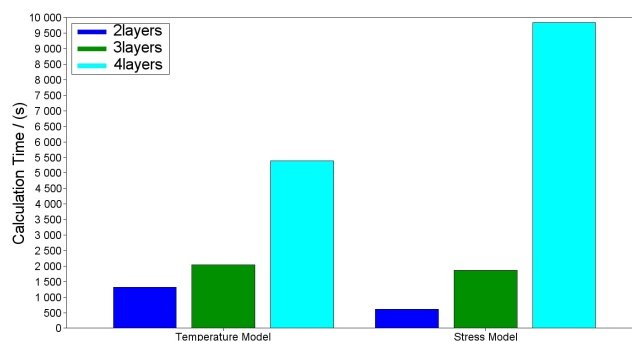


FIGURE 5.7 – Computation time of temperature and stress models

From the results of temperature models 2layers, 3layers, and 4layers, the fluctuation of the temperature of molten pool are drawn in figure 5.8. The temperature model 2layers has 54 intervals, 3layers 162 intervals, and 4layers 486 intervals. With the number of layers increase, meaning the mesh size decrease, the fluctuation of temperature decrease.

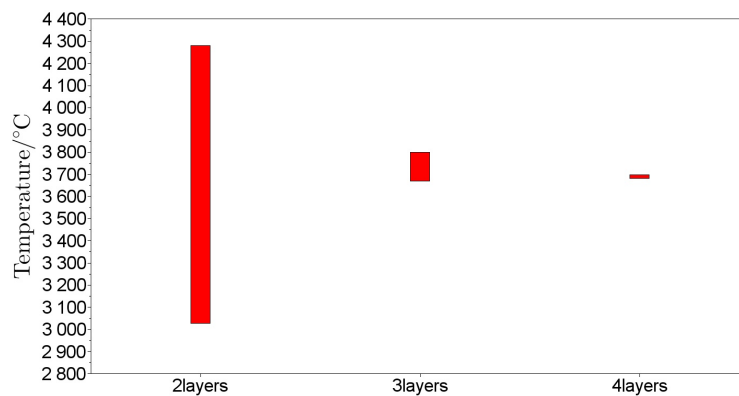


FIGURE 5.8 – Numerical results of temperature range of melting pool heated by laser

The maximal residual stress calculated from the stress models are presented in Figure 5.9. The maximal residual stress of the “stress-2layers” model has a big difference with results of “stress-3layers” and “stress-4layers” model. The non correct result may result from the fluctuation of the weld pool temperature. The maximal residual stress of “stress-3layers” model only have a 5% difference with the “stress-4layers” model while the time consumption of the “stress-3layers” model is only 19% of the “stress-4layers” model.

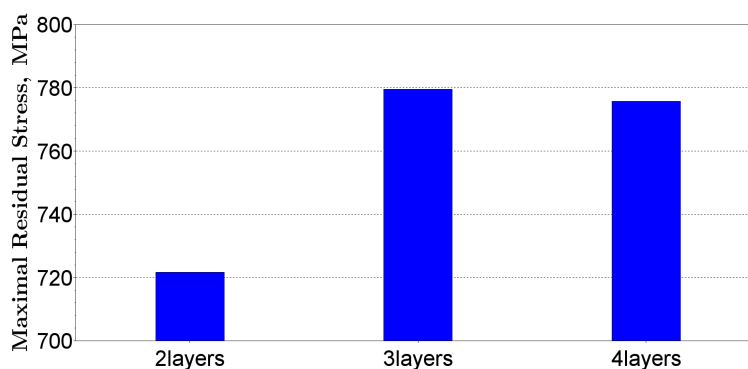
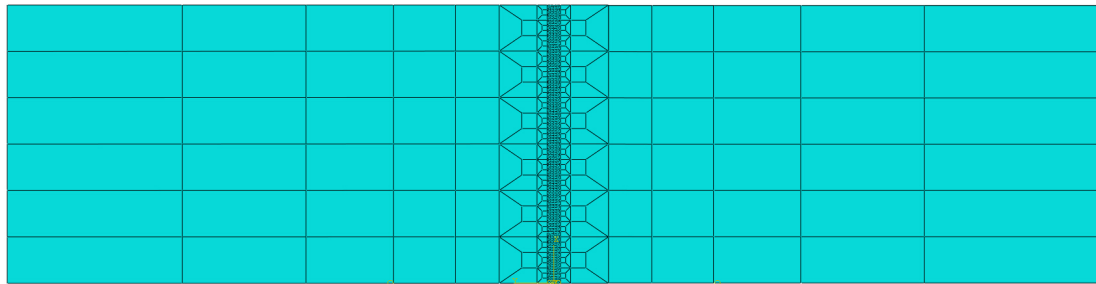


FIGURE 5.9 – The maximal residual stress of models with different layers

5.2.2 Mesh of thickness direction

5.2.2.1 Thickness section of weld

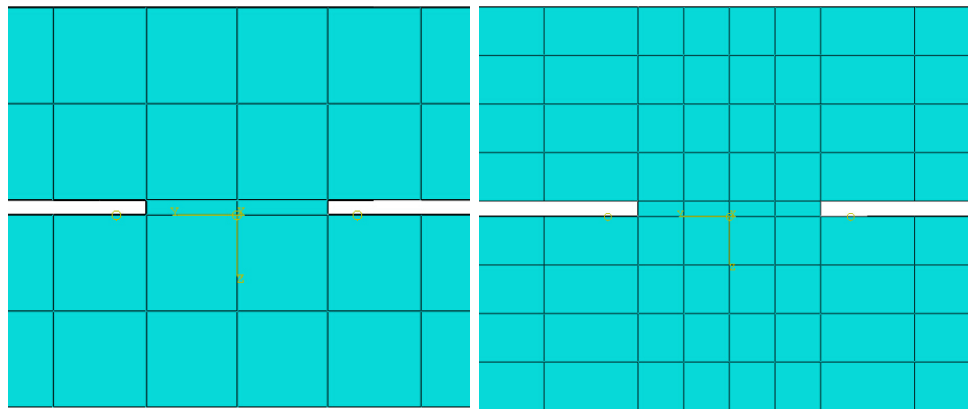
In the Figure 5.10 (a) and Figure 5.10 (b), the mesh of the plane of plate and the cross section is presented. The difference of cross section of weld of Model-2x2 and Model-4x4 are shown in Figure 5.10 (c) and Figure 5.10 (d), respectively.



(a) Plane mesh with 3 layers



(b) Transversal section



(c) Transversal section of weld of Model-2x2

(d) Transversal section of weld of Model-4x4

FIGURE 5.10 – Mesh transverse to weld

5.2.2.2 CPU time

The comparison of computation time is in Figure 5.11. With the same mesh, the stress model needs more time than the temperature model. In both temperature and stress model, the computation time of Model-4x4 is bigger than the computation time of Model-2x2.

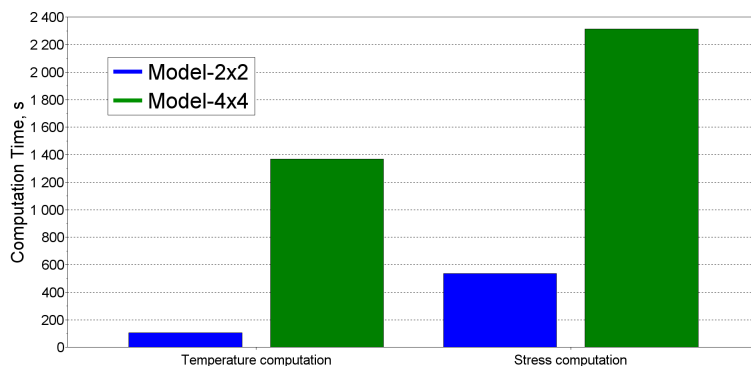
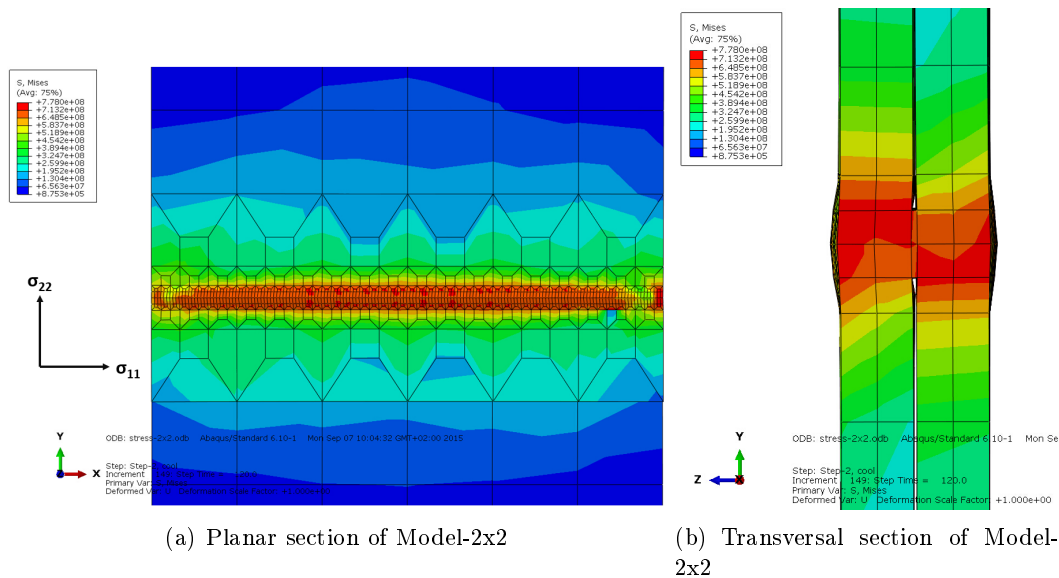


FIGURE 5.11 – The comparison of computation time between Model-2x2 and Model-4x4

5.2.2.3 Residual stress distribution

The residual stress distribution is presented in Figure 5.12. No big difference is found from the Figure 5.12.



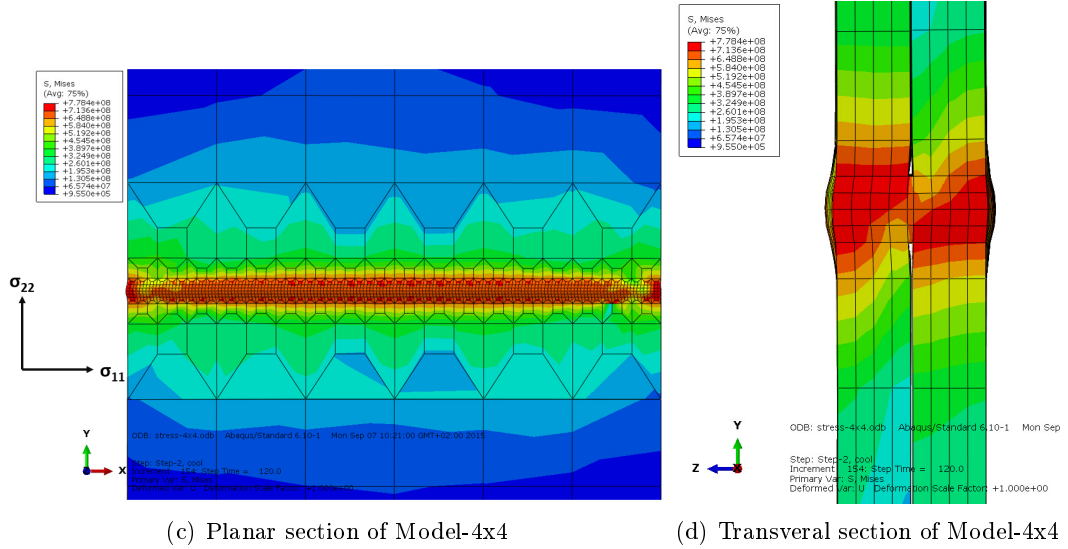


FIGURE 5.12 – Residual stress distribution

5.3 Boundary condition

5.3.1 Constrain position

The influence of boundary on residual stress distribution is evaluated in this section. As is seen in Figure 5.13, the inward lines, middle lines, and outward lines are constrained, respectively. The z direction move is restrained for the lines. The models constrained at outward lines, middle lines, and inward lines are labeled “boundary01”, “boundary02”, and “boundary03”.

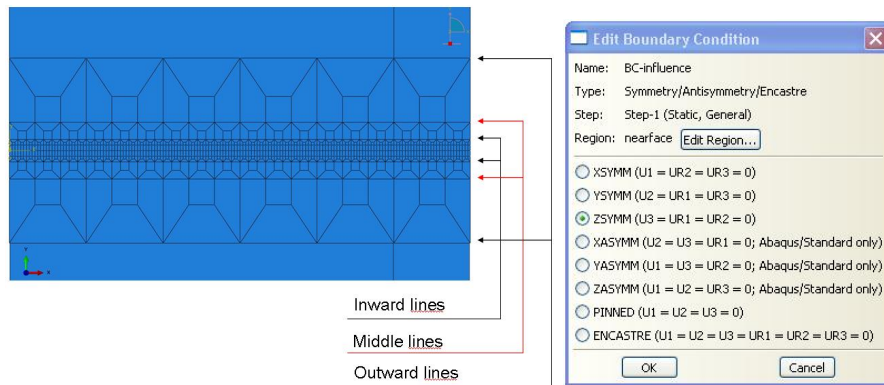


FIGURE 5.13 – Three lines fixed in thickness direction

5.3.2 Simulation results

In the figure below, "L01-Mises" means the equivalent stress along weld longitudinal path of model "boundary01". "L" means longitudinal path and "T" means transversal path. "01" means model "boundary01", "02" means model "boundary02", and "03" means model "boundary03". "Mises" means the equivalent stress, " σ_{11} " means the residual stress along weld longitudinal direction σ_{11} and " σ_{22} " means the residual stress along weld-transversal direction σ_{22} .

5.3.2.1 Equivalent residual stress

In Figure 5.14, equivalent stress along weld longitudinal path are presented. The model "boundary03" with the inward lines constrained has the most stable and the highest equivalent stress along weld longitudinal path. The equivalent stress of model "boundary02" with the middle lines constrained and model "boundary01" with the outward lines constrained decrease at the zone of two ends of the weld.

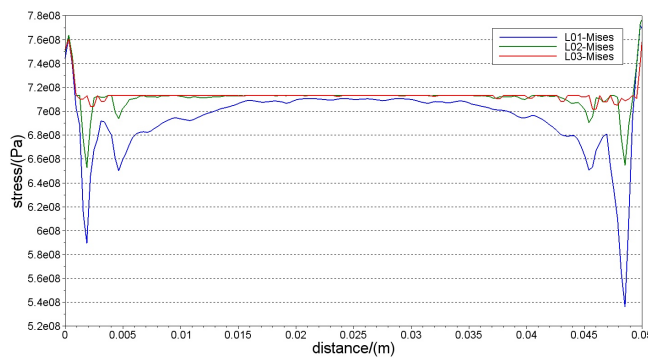


FIGURE 5.14 – Equivalent stress along weld longitudinal path

In Figure 5.15, mises stress along transversal path are presented. The mises stress along transversal path of Model "boundary01", "boundary02", and "boundary03" are nearly the same.

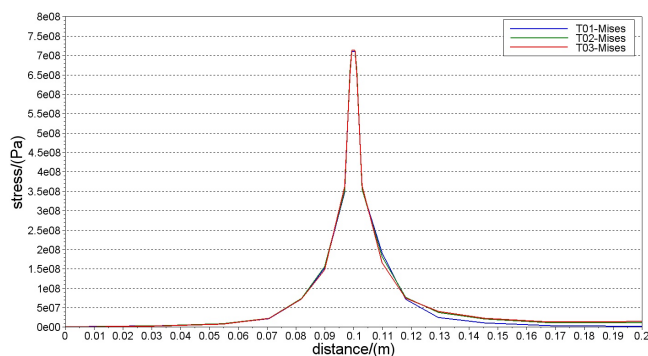


FIGURE 5.15 – equivalent stress along transversal path

5.3.2.2 Weld longitudinal direction residual stress

In Figure 5.16, σ_{11} along weld longitudinal path are presented. With the constrain moves from outer lines to inner lines, the longitudinal residual stress σ_{11} along weld longitudinal path decreases.

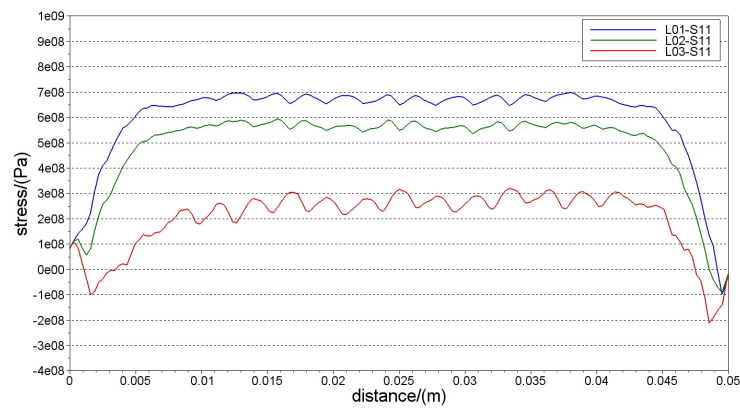


FIGURE 5.16 – σ_{11} along weld longitudinal path

In Figure 5.17, σ_{11} along transversal path are presented. With the constrain moves from outer lines to inner lines, the longitudinal residual stress σ_{11} decreases at the weld zone and tends to be the same at the HAZ and base metal. σ_{11} is tensile residual at weld zone, and compress residual adjacent to the weld zone, and gradually decrease to zero at the zone further than 40mm from the weld.

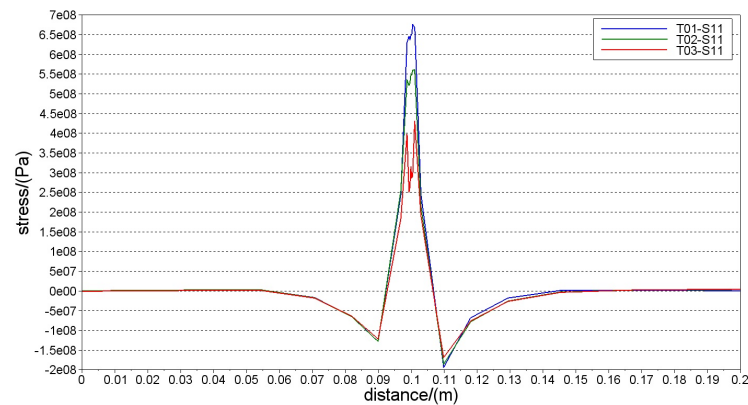


FIGURE 5.17 – σ_{11} along transversal path

5.3.2.3 Weld transversal direction residual stress

In Figure 5.18, σ_{22} along weld longitudinal path are presented. With the constrain moves from outer lines to inner lines, the compress longitudinal residual stress σ_{22} along weld longitudinal path increases.

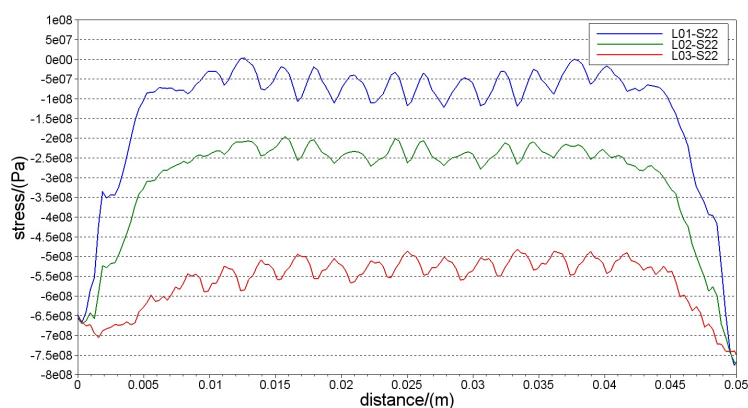


FIGURE 5.18 – σ_{22} along weld longitudinal path

In Figure 5.19, σ_{22} along transversal path are presented. The transversal residual stress σ_{22} along transversal path of Model “boundary01”, “boundary02”, and “boundary03” are nearly the same.

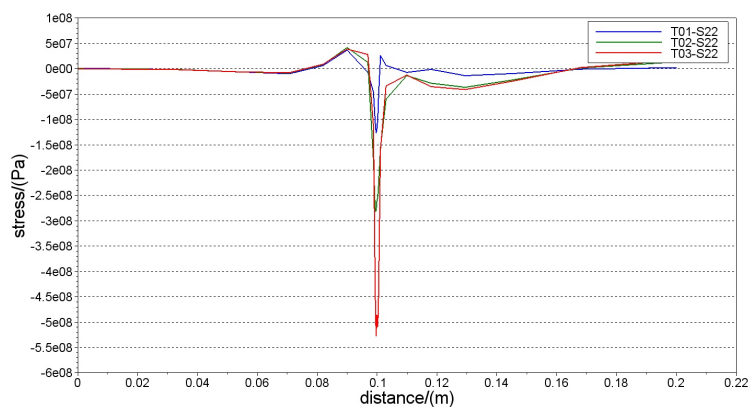


FIGURE 5.19 – σ_{22} along transversal path

5.4 Hardening analysis of DP600

5.4.1 Simulation results of equivalent residual stresses

The distribution of equivalent residual stresses are presented in figure 5.20. The results are in MPa. The color range in the left of 6 figures are set to be the same. Comparison shows that the usage of the first five different hardening terms in FEM numerical models result in similar equivalent residual stress distributions. Higher equivalent residual stresses are found in the model using Classical Ludwik model (assuming the plate using martensite hardening behavior).

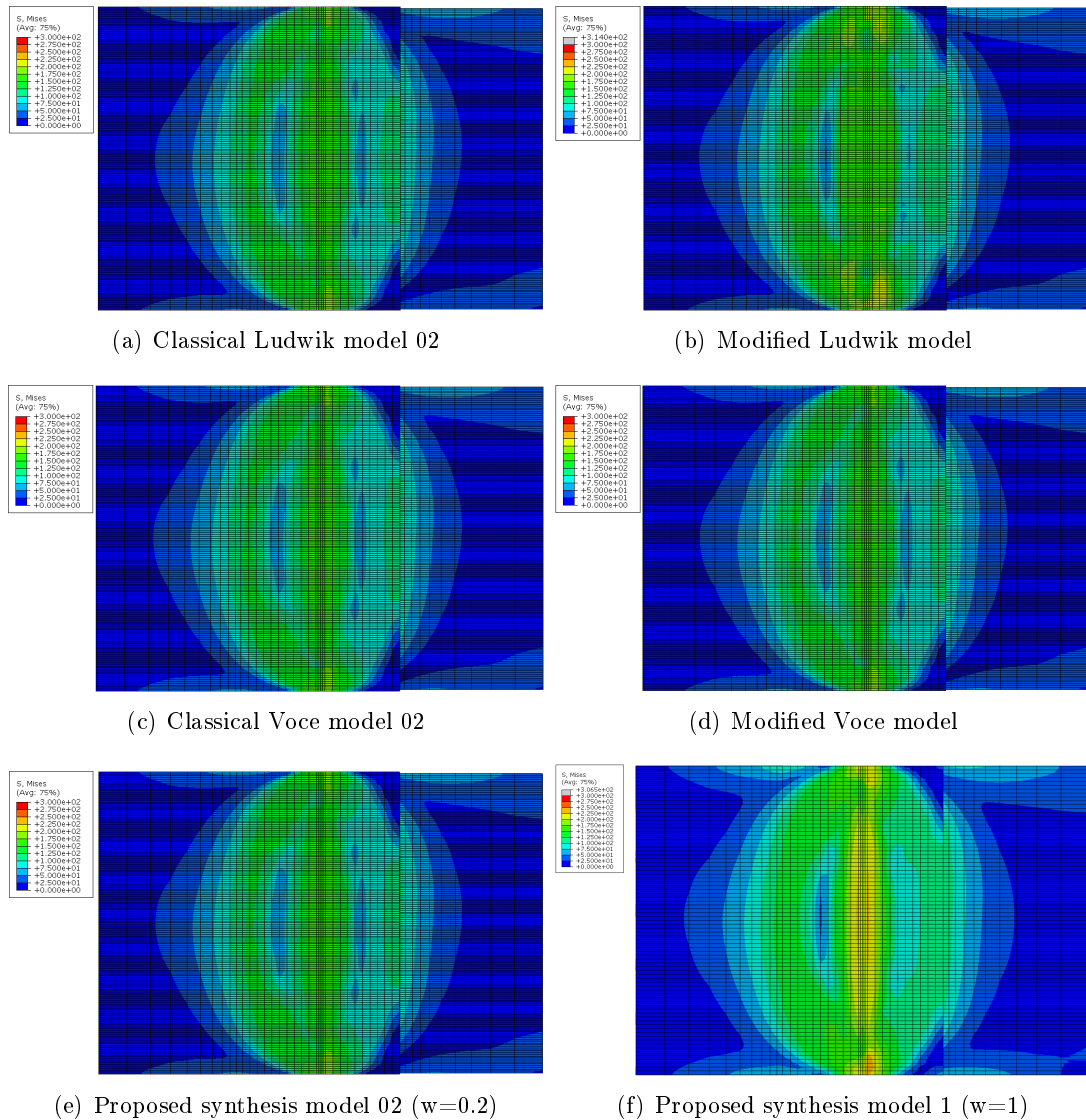


FIGURE 5.20 – The distribution of equivalent residual stresses of welding simulation with different hardening models

Along welding longitudinal path and transversal path, the magnitudes of equivalent residual stresses are shown in figure 5.21.

For the first five models, equivalent residual stresses of welding simulation model along welding longitudinal path are nearly the same for most part. But at the beginning and ending part of welding longitudinal path, the equivalent residual stresses of model using a modified Ludwik model present a difference with the other 4 models. This is because a small line introduced in the model (see figure 2.7). The difference proves that a small change in material constitutive model can result a big difference in residual stresses. Except the modified Ludwik model, the other 4 hardening models have nearly the same simulation results of equivalent residual stresses. This indicates that different material constitutive models can have nearly the same influences on equivalent residual stresses simulation.

The last model "Proposed synthesis model 1 (w=1)", equivalent residual stresses are found higher than the other models. Comparing with DP600 steel hardening behavior, the martensite hardening behavior will increase equivalent residual stresses of numerical welding model.

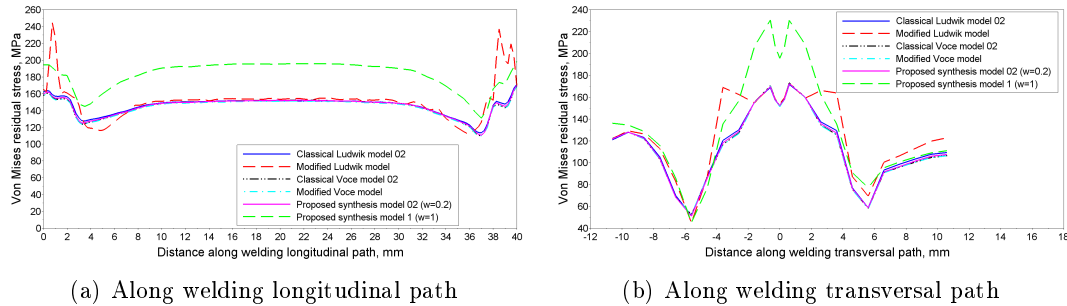


FIGURE 5.21 – The magnitude of equivalent residual stresses of welding simulation with different hardening models

Other simulation results of residual stresses of σ_{11} , σ_{22} and strains of ϵ_{11}^e , ϵ_{22}^e , ϵ_{11}^p , ϵ_{22}^p and equivalent plastic strain $\bar{\epsilon}^p$ are presented to further demonstrate :

- A small difference of material hardening constitutive model can result in a big difference on simulation results.
- Different material constitutive models can have nearly the same influences on residual stress and strain simulations for this laser welding process (the plastic strain $\epsilon < 0.05$).
- The numerical simulation results of model with martensite hardening behavior (Proposed synthesis model 1 (w=1)) are different from those results of models with DP600 hardening behavior. The hardening term influences the residual stresses and strains of numerical welding model.

5.4.2 Simulation results of σ_{11} residual stresses

The distribution of σ_{11} residual stresses are presented in figure 5.22. The distribution are similar except figure 5.22 (b) has some differences of red regions.

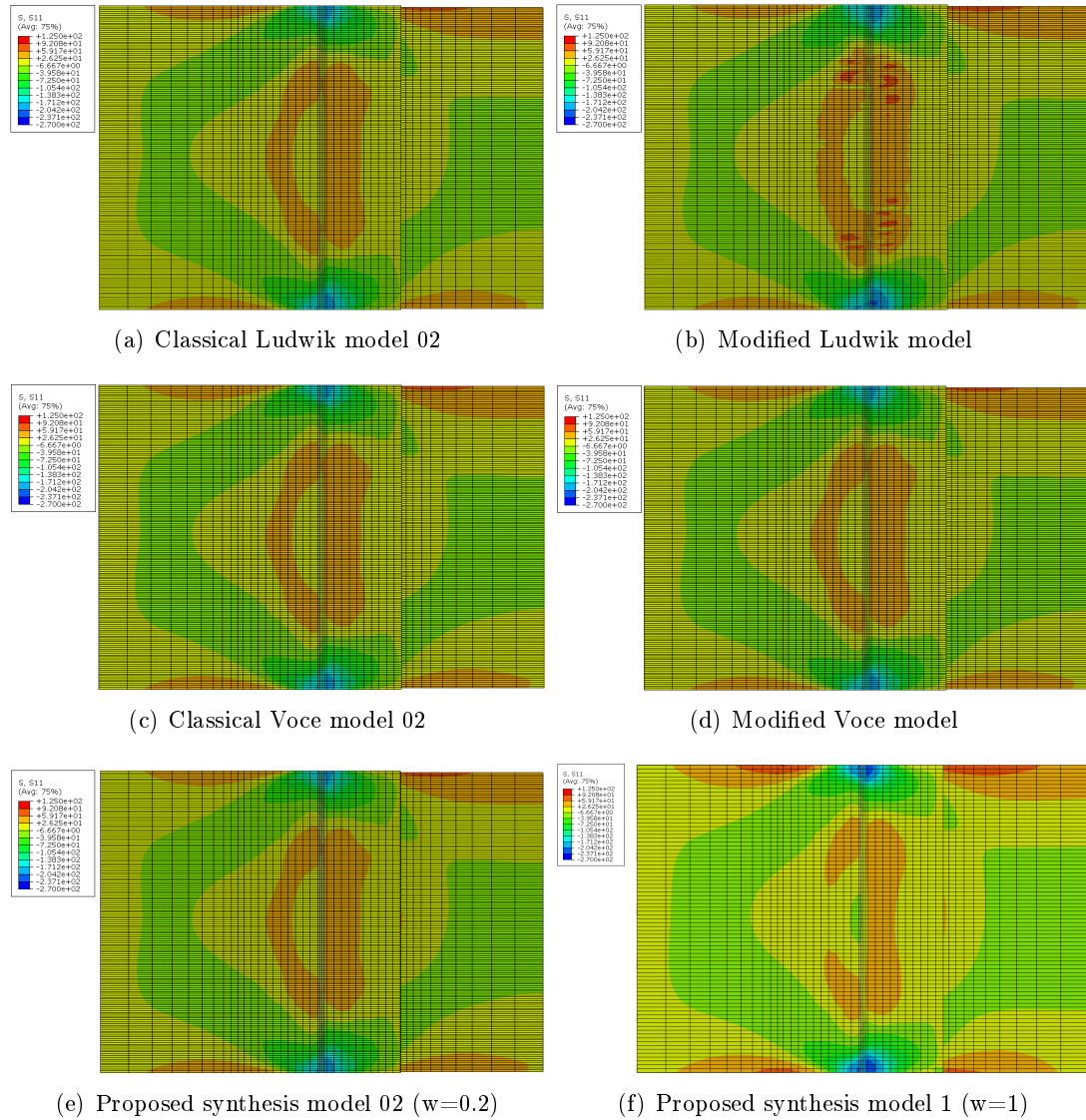


FIGURE 5.22 – The distribution of σ_{11} residual stresses of welding simulation with different hardening models

Along welding longitudinal path and transversal path, the magnitude of σ_{11} are shown in figure 5.23. The equivalent residual stresses of model using a modified Ludwik model also present a difference with the other 4 models.

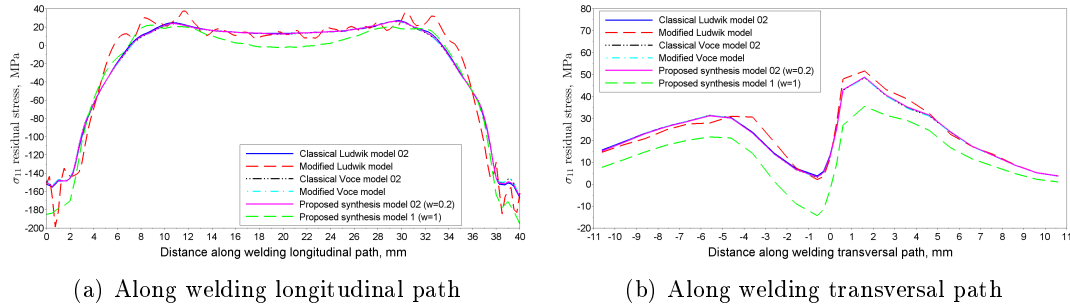
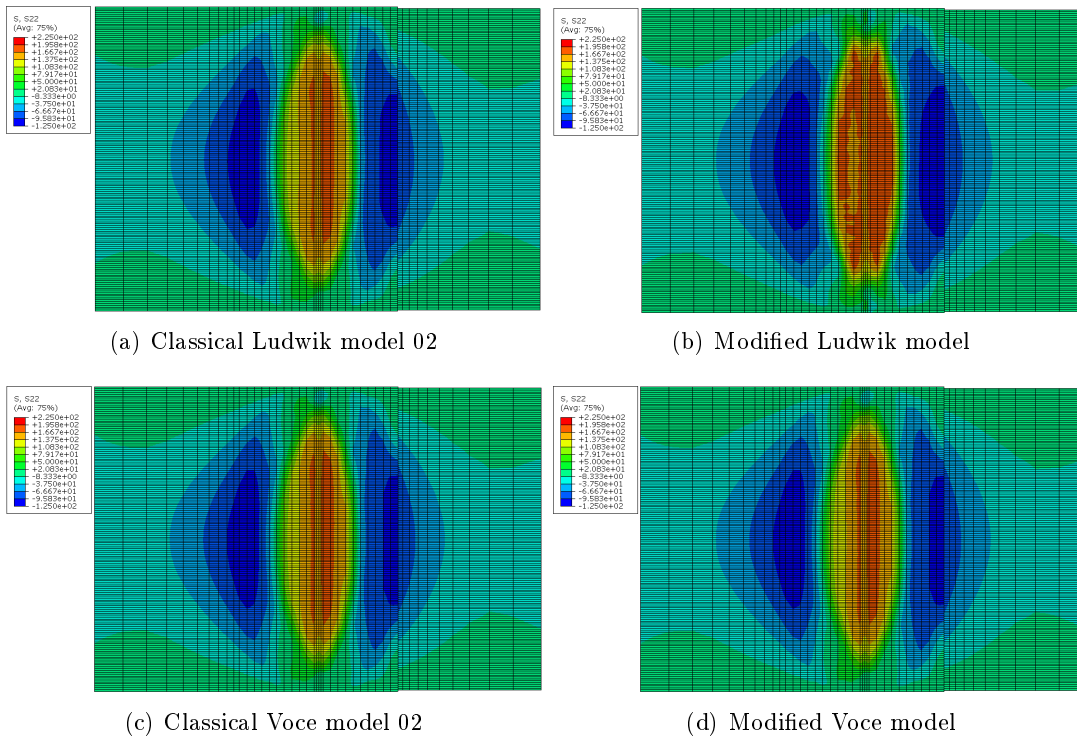


FIGURE 5.23 – The magnitude of σ_{11} residual stresses of welding simulation with different hardening models

5.4.3 Simulation results of σ_{22} residual stresses

The distribution of σ_{22} residual stresses are presented in figure 5.24.



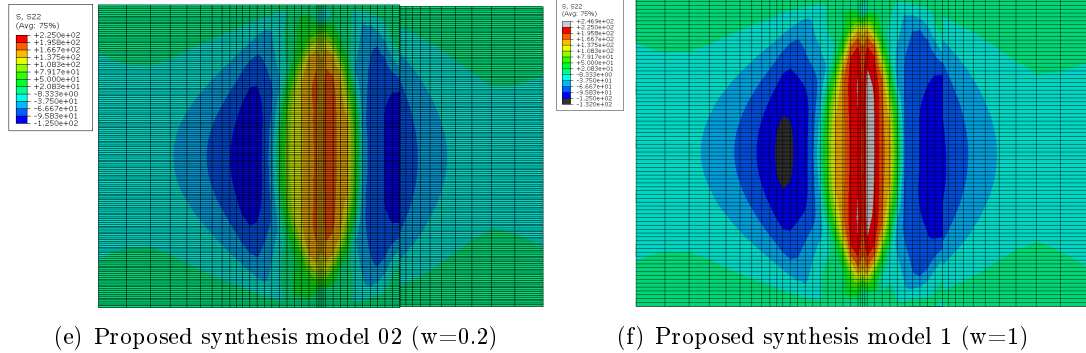


FIGURE 5.24 – The distribution of σ_{22} residual stresses of welding simulation with different hardening models

Along welding longitudinal path and transversal path, the magnitude of σ_{22} are shown in figure 5.25.

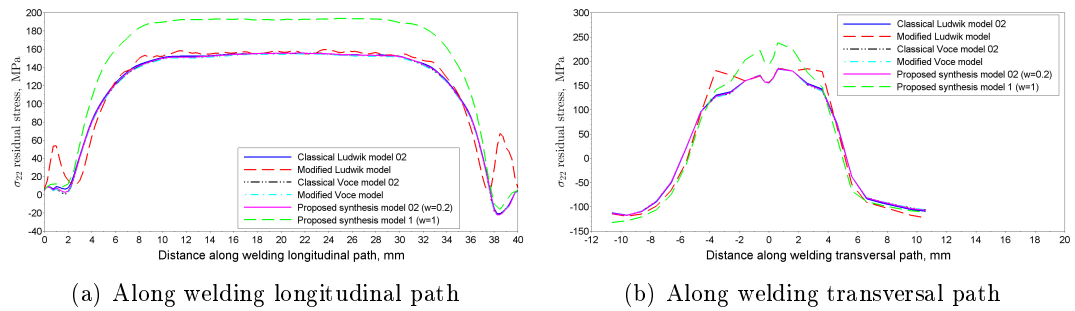
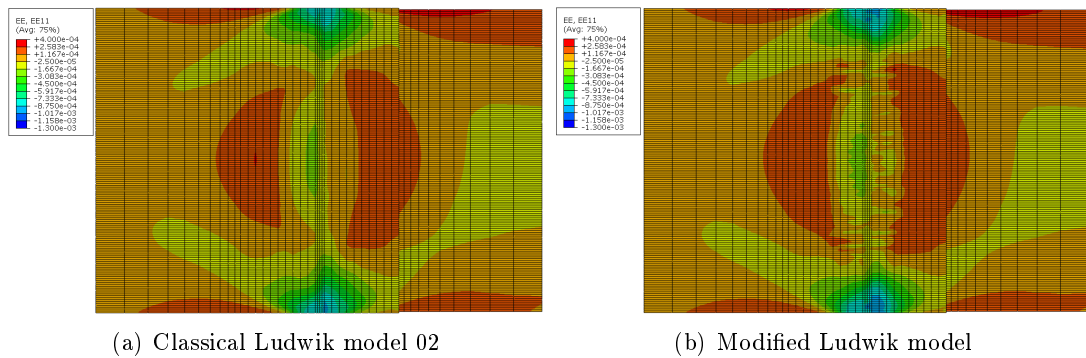


FIGURE 5.25 – The magnitude of σ_{22} residual stresses of welding simulation with different hardening models

5.4.4 Simulation results of ϵ_{11}^e residual elastic strains

The distribution of ϵ_{11}^e residual elastic strains are presented in figure 5.26.



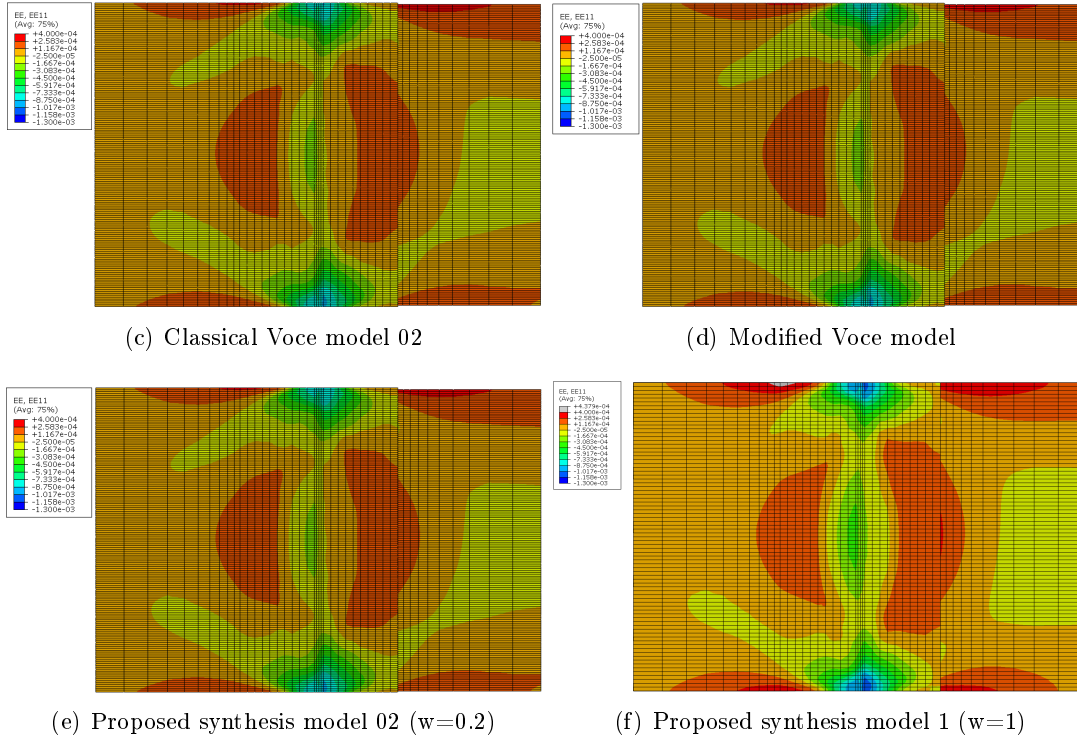


FIGURE 5.26 – The distribution of ϵ_{11}^e residual strains of welding simulation with different hardening models

Along welding longitudinal path and transversal path, the magnitude of ϵ_{11}^e are shown in figure 5.27.

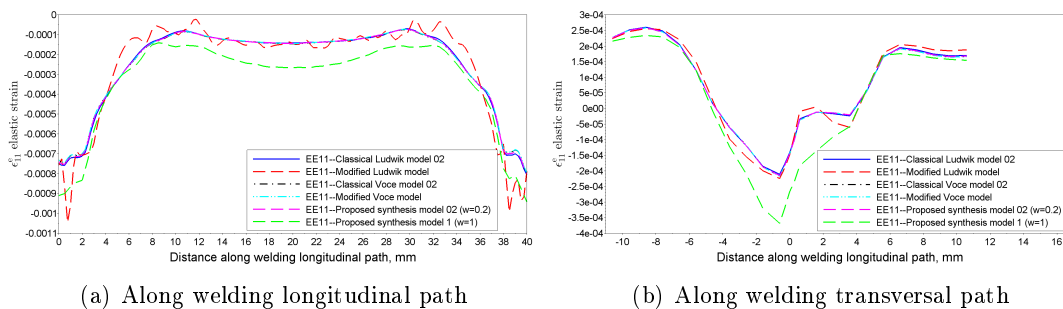


FIGURE 5.27 – The magnitude of ϵ_{11}^e residual strains of welding simulation with different hardening models

5.4.5 Simulation results of ϵ_{22}^e residual elastic strains

The distribution of ϵ_{22}^e residual elastic strains are presented in figure 5.28.

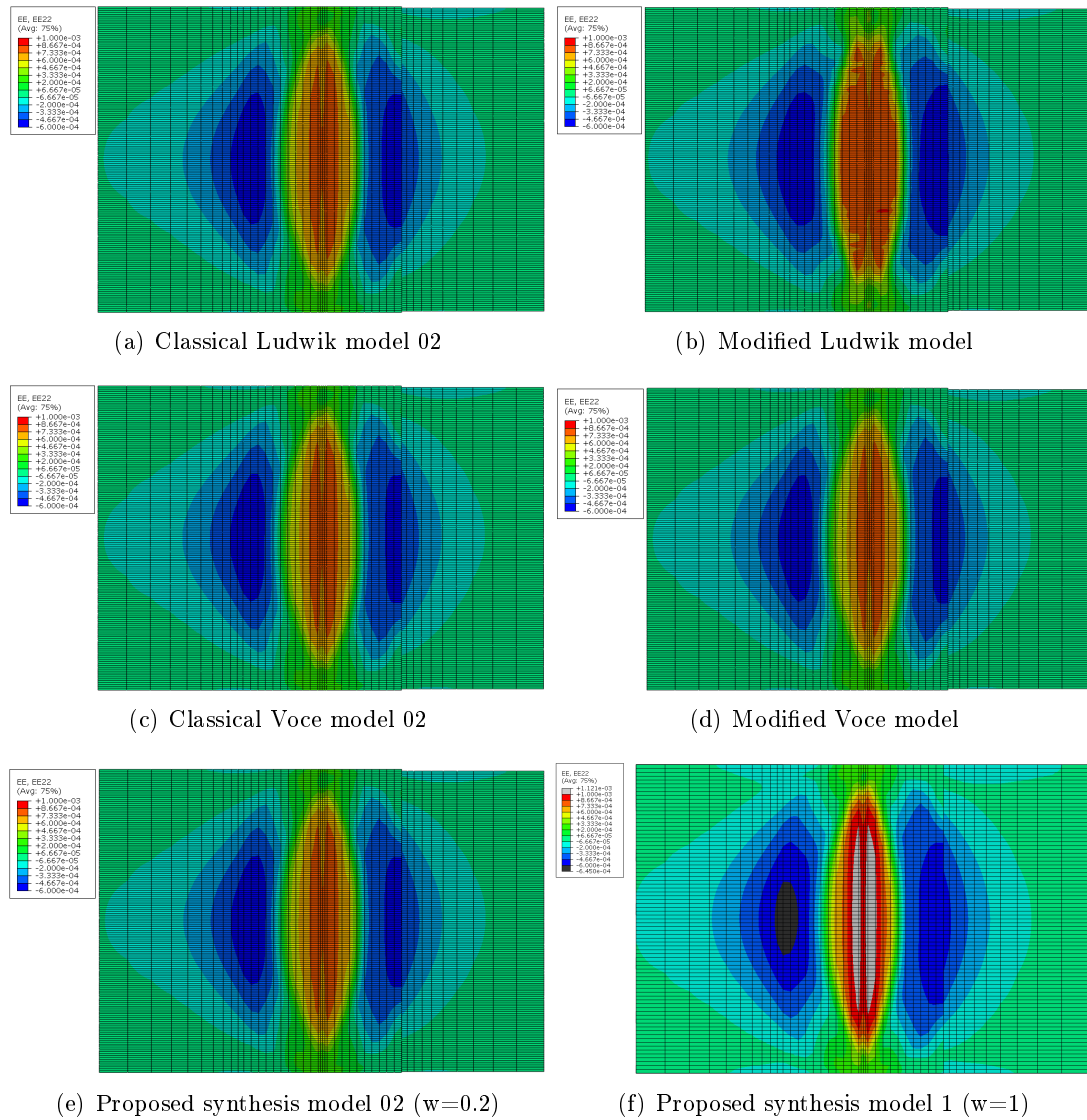


FIGURE 5.28 – The distribution of ϵ_{22}^e residual strains of welding simulation with different hardening models

Along welding longitudinal path and transversal path, the magnitude of ϵ_{22}^e are shown in figure 5.29.

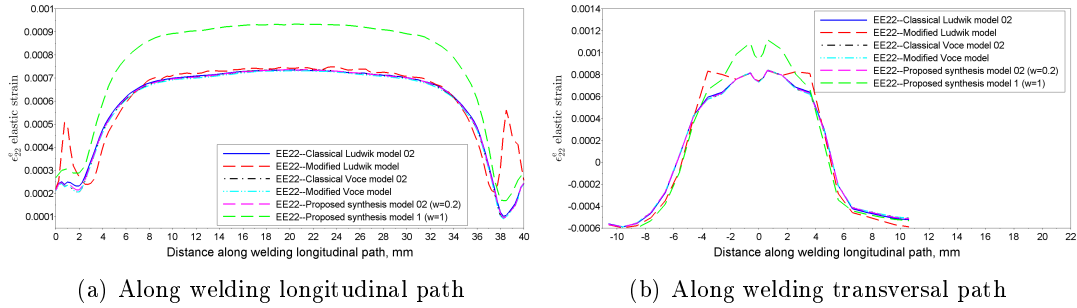
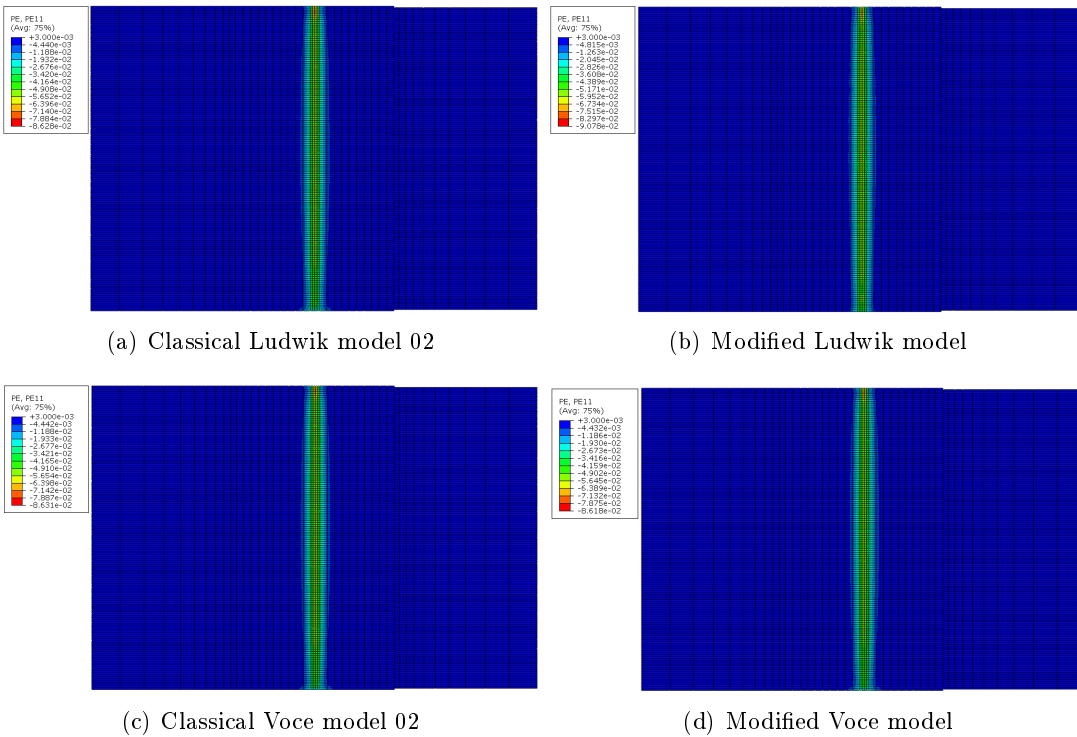


FIGURE 5.29 – The magnitude of ϵ_{22}^e residual strains of welding simulation with different hardening models

5.4.6 Simulation results of ϵ_{11}^p residual plastic strains

The distribution of ϵ_{11}^p residual plastic strains are presented in figure 5.30.



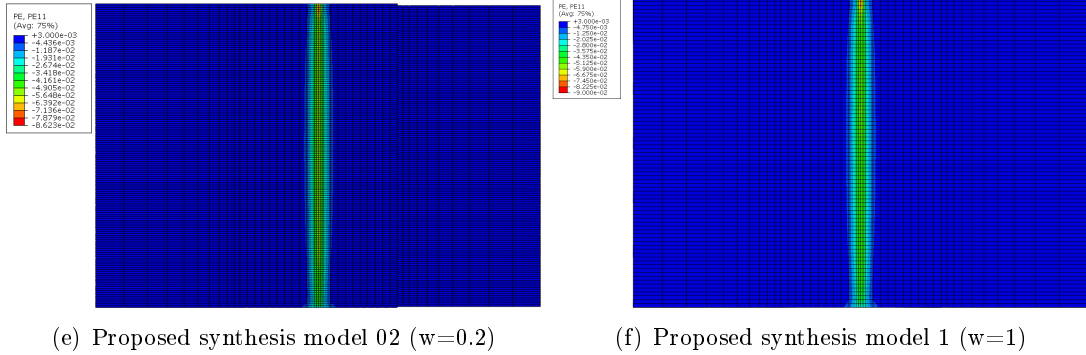


FIGURE 5.30 – The distribution of ϵ_{11}^p residual strains of welding simulation with different hardening models

Along welding longitudinal path and transversal path, the magnitude of ϵ_{11}^p are shown in figure 5.31.

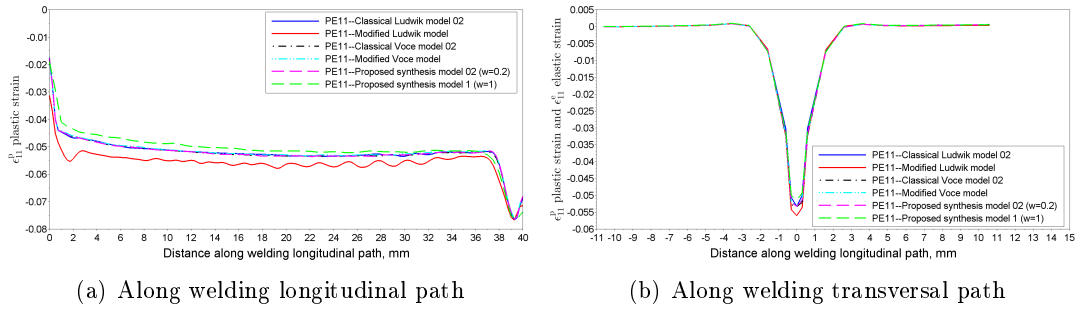
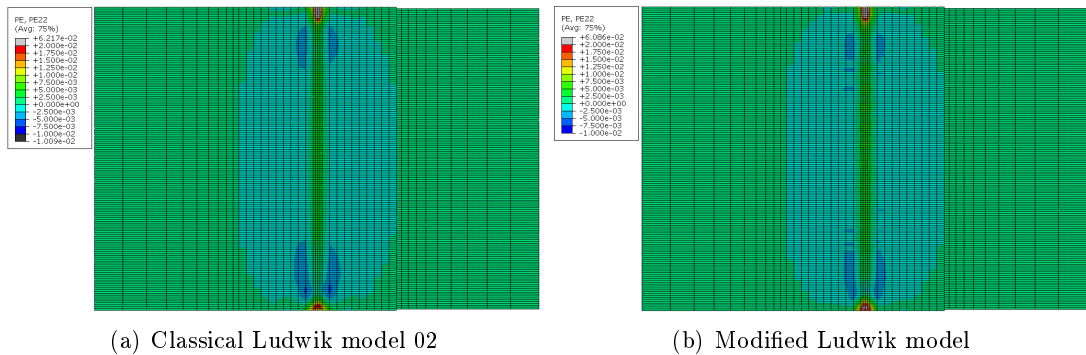


FIGURE 5.31 – The magnitude of ϵ_{11}^p residual strains of welding simulation with different hardening models

5.4.7 Simulation results of ϵ_{22}^p residual plastic strains

The distribution of ϵ_{22}^p residual plastic strains are presented in figure 5.32.



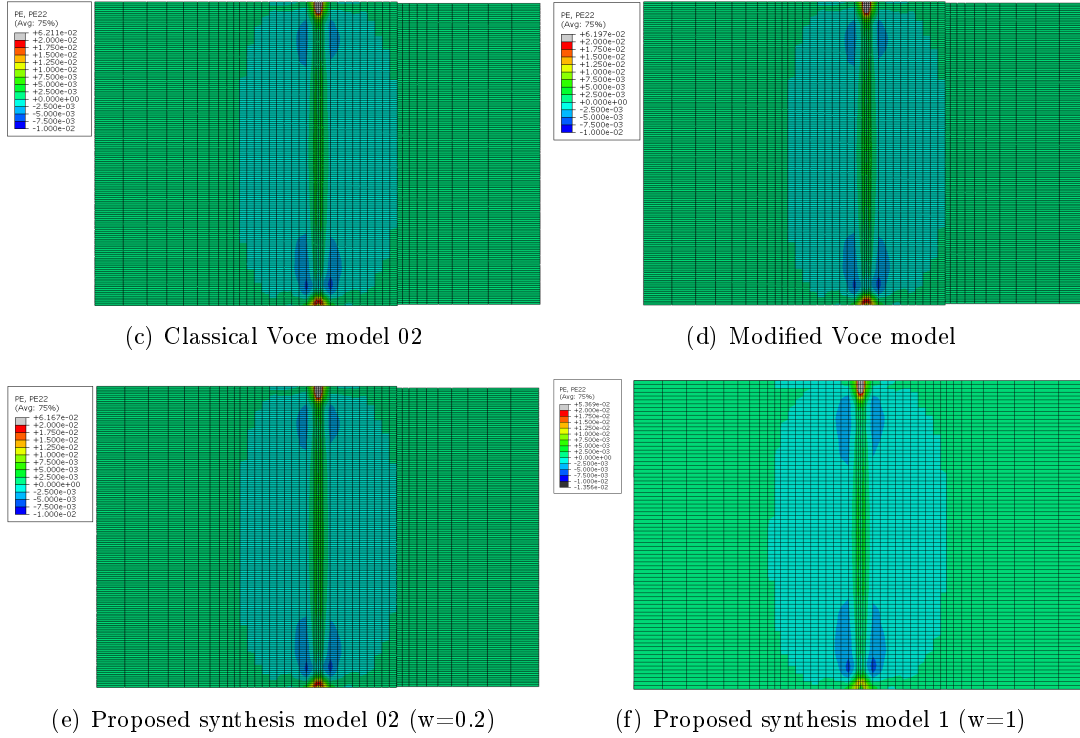


FIGURE 5.32 – The distribution of ϵ_{22}^p residual strains of welding simulation with different hardening models

Along welding longitudinal path and transversal path, the magnitude of ϵ_{22}^p are shown in figure 5.33.

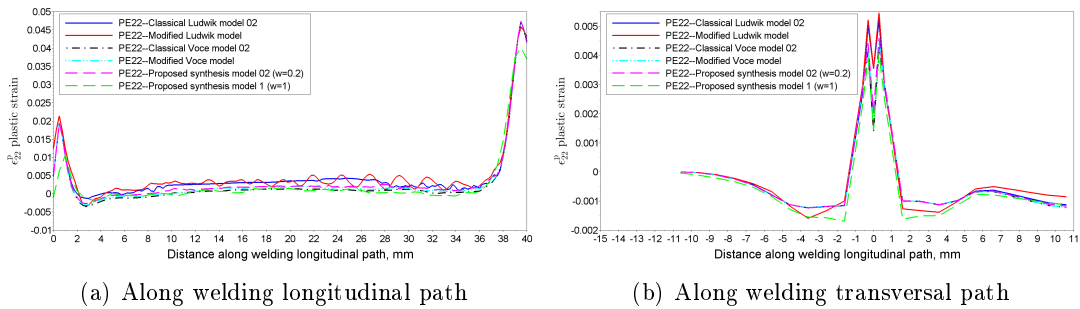


FIGURE 5.33 – The magnitude of ϵ_{22}^p residual strains of welding simulation with different hardening models

5.4.8 Simulation results of $\bar{\epsilon}^p$ residual equivalent plastic strains

The distribution of $\bar{\epsilon}^p$ residual equivalent plastic strains are presented in figure 5.34.

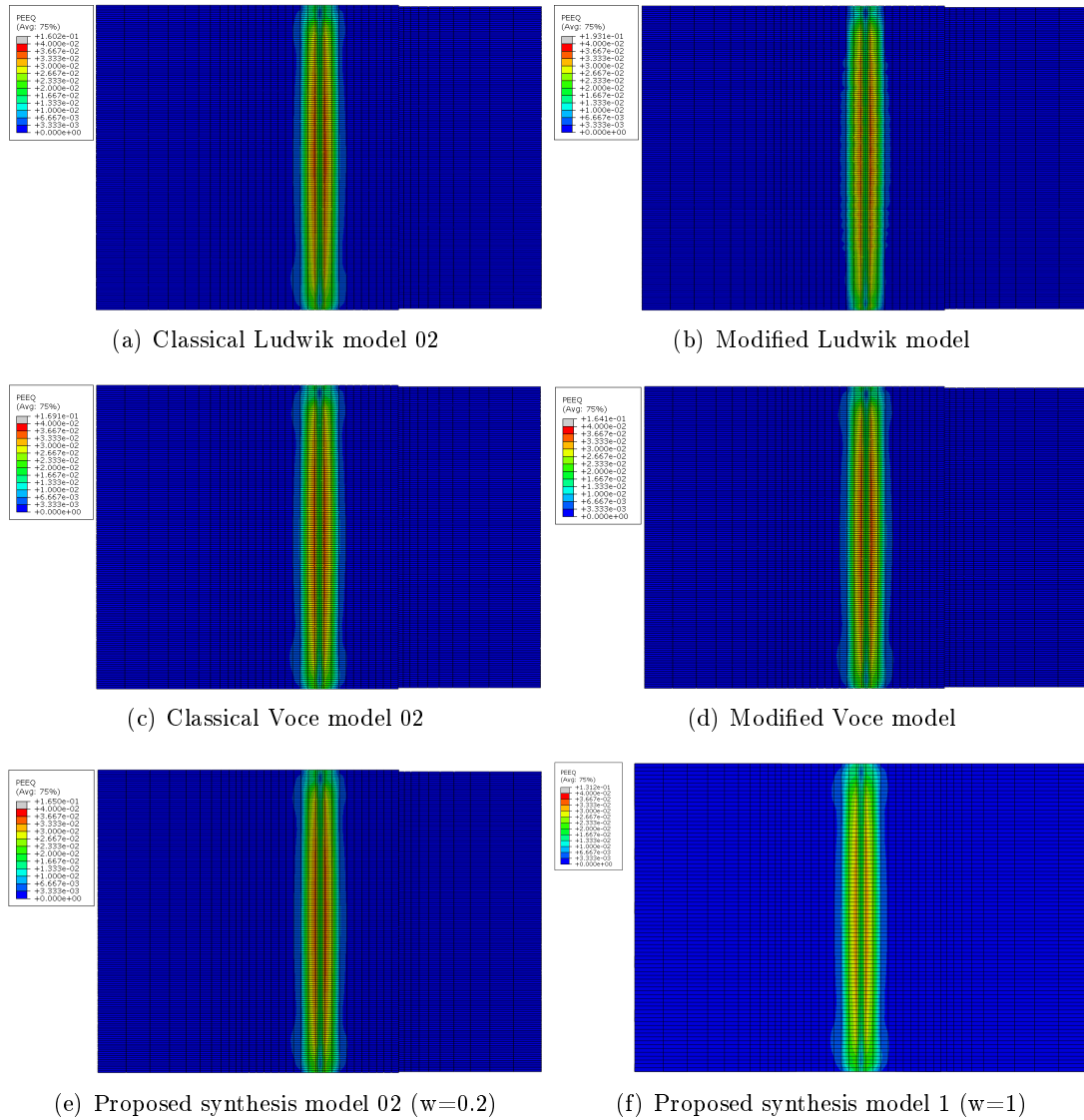


FIGURE 5.34 – The distribution of $\bar{\epsilon}^p$ residual strains of welding simulation with different hardening models

Along welding longitudinal path and transversal path, the magnitude of $\bar{\epsilon}^P$ are shown in figure 5.35.

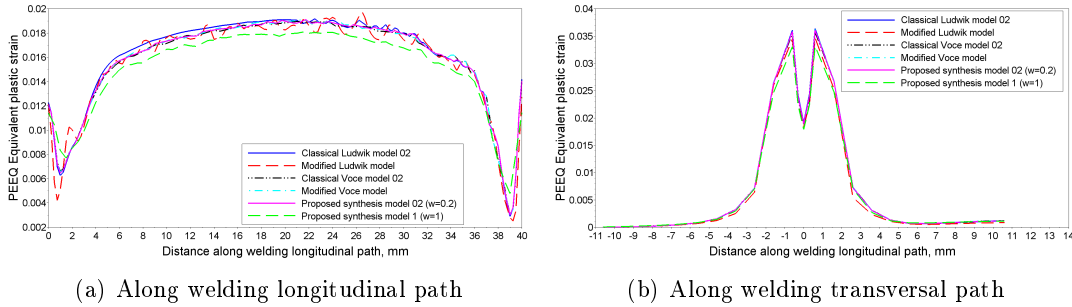


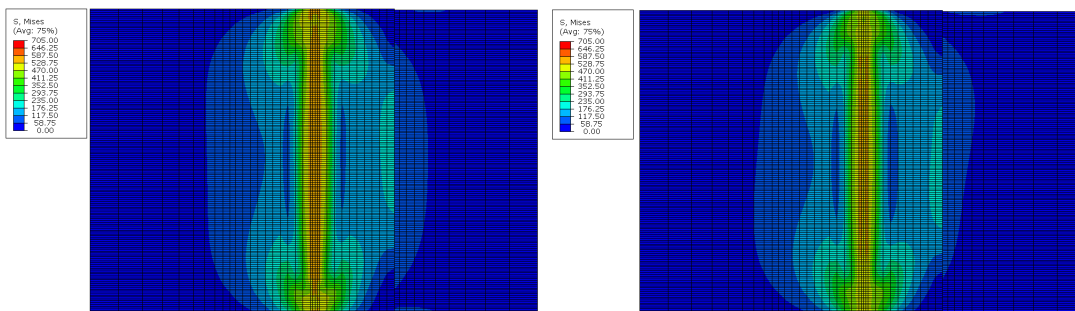
FIGURE 5.35 – The magnitude of $\bar{\epsilon}^P$ residual strains of welding simulation with different hardening models

In all the above figures, simulation results of the modified Ludwik model are found different with those results of the other 4 models. Except the modified Ludwik model, the other 4 hardening models have nearly the same simulation results of residual stresses and strains for this laser welding process (the plastic strain $\epsilon < 0.05$).

5.5 Temperature sensitivity analysis of DP600

5.5.1 Simulation results of equivalent residual stresses

The distribution of equivalent residual stresses are presented in figure 5.36. The results are in MPa. The color range in the left of 4 figures are set to be the same. Comparison shows that equivalent residual stresses of 4 temperature sensitivity models are similar. In the center weld, results of Johnson-Cook temperature sensitivity model are a little higher than the other three temperature sensitivity models because the classical Johnson-Cook temperature sensitivity model do not describe precisely experimental data at high temperature.



(a) Johnson-Cook temperature sensitivity model

(b) Chen temperature sensitivity model

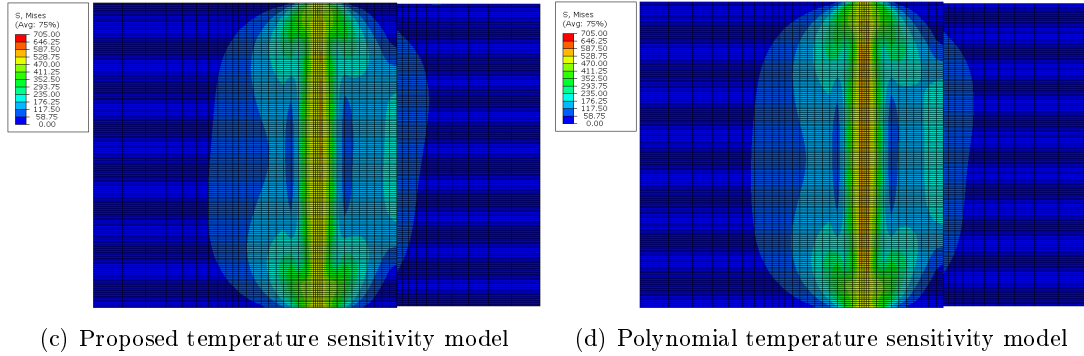


FIGURE 5.36 – The distribution of equivalent residual stresses of welding simulation with 4 different temperature sensitivity terms

Along welding longitudinal path and transversal path, equivalent stresses are shown in figure 5.37. The obtained simulation results are similar for Chen, proposed and polynomial temperature sensitivity model. Along welding longitudinal path, the equivalent residual stresses of Johnson-Cook temperature sensitivity model is about 50MPa higher than stresses of the other three model.

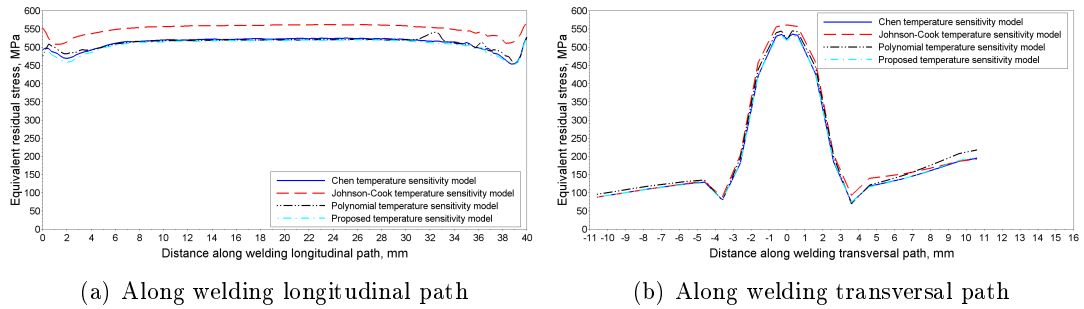


FIGURE 5.37 – The magnitude of equivalent residual stresses of welding simulation models with 4 different temperature sensitivity terms

Comparing with corresponding results of equivalent residual stresses in hardening analysis of DP600 (section 5.4), equivalent residual stresses are increased a lot which proves that material constitutive model of temperature sensitivity have a important influence on numerical simulation results of equivalent residual stresses.

Other simulation results of residual stresses of σ_{11} , σ_{22} and strains of ϵ_{11}^e , ϵ_{22}^e , ϵ_{11}^p , ϵ_{22}^p and equivalent plastic strain $\bar{\epsilon}^p$ are presented to further compare the influence of temperature sensitivity on residual stresses and strains.

5.5.2 Simulation results of σ_{11} residual stresses

The distribution of σ_{11} residual stresses are presented in figure 5.38. The unit of σ_{11} is in MPa. The color range in the left of 4 figures are set to be the same. Comparison shows that σ_{11} residual stress distributions of 4 temperature sensitivity models are similar. At the beginning and ending of weld (blue and green part), compress σ_{11} residual stresses are obtained. At the center part neighbor to weld (orange part), tensile σ_{11} residual stresses are obtained.

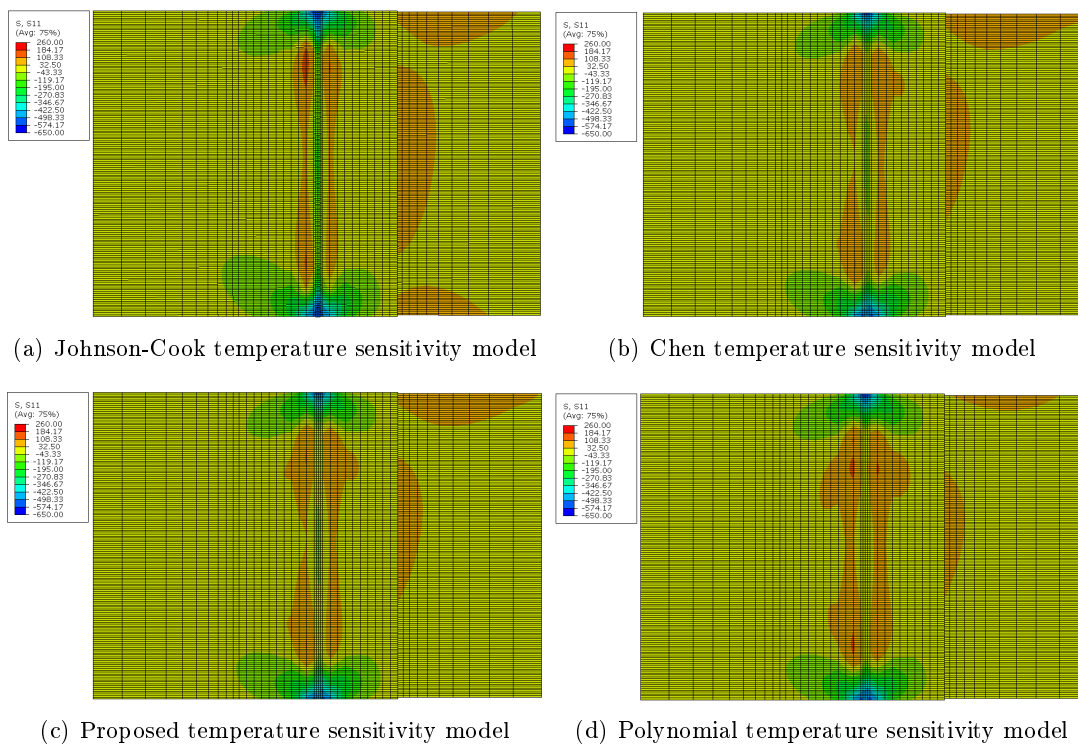


FIGURE 5.38 – The distribution of σ_{11} residual stresses of welding simulation with 4 different temperature sensitivity terms

A closer look on welding longitudinal path and transversal path for σ_{11} residual stresses are shown in figure 5.39. For Chen and proposed temperature sensitivity model, the obtained numerical simulation results of σ_{11} are similar. They both are higher than σ_{11} results of Johnson-Cook temperature sensitivity model and lower than σ_{11} results of polynomial sensitivity model.

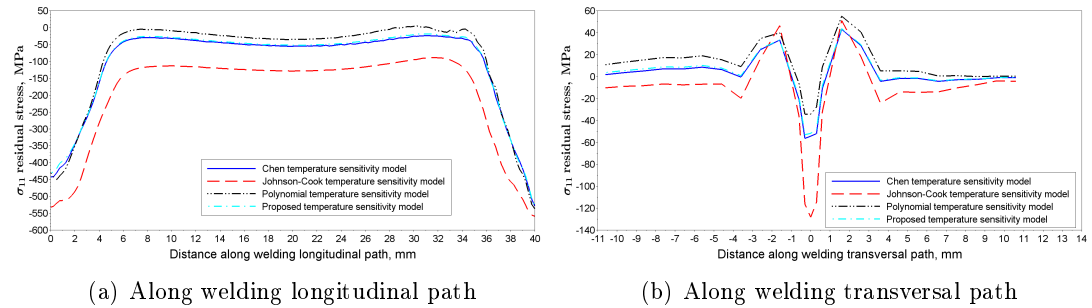


FIGURE 5.39 – The magnitude of σ_{11} residual stresses of welding simulation models with 4 different temperature sensitivity terms

5.5.3 Simulation results of σ_{22} residual stresses

The distribution of σ_{22} residual stresses are presented in figure 5.40. The unit of σ_{22} is in MPa. The color range in the left of 4 figures are set to be the same. Comparison shows that σ_{22} residual stress distributions of 4 temperature sensitivity models are similar. At weld region and the region around weld (orange and green part), tensile σ_{22} residual stresses are obtained. At the outer part far from weld (blue part), compress σ_{22} residual stresses are obtained.

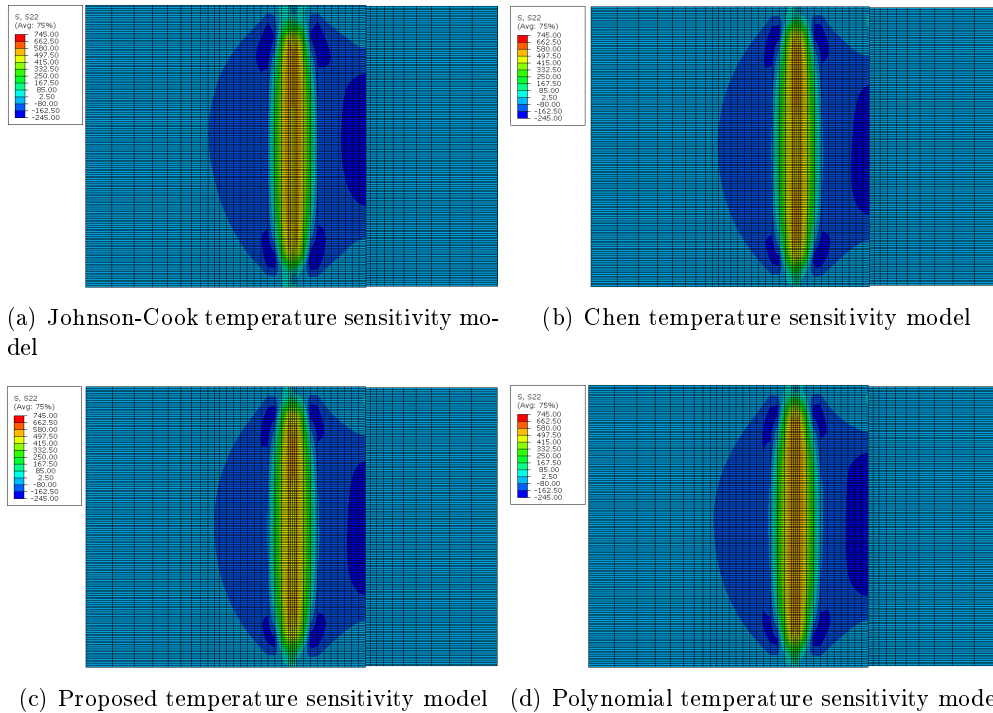


FIGURE 5.40 – The distribution of σ_{22} residual stresses of welding simulation with 4 different temperature sensitivity terms

A closer look on welding longitudinal path and transversal path for σ_{22} residual stresses are shown in figure 5.41. For Chen, proposed and polynomial temperature sensitivity model, the obtained numerical simulation results of σ_{22} are similar. At the beginning and ending part along welding longitudinal path in figure 5.41 (a), the σ_{22} results of Johnson-Cook temperature sensitivity model are a little lower than σ_{22} results of the other three temperature sensitivity models.

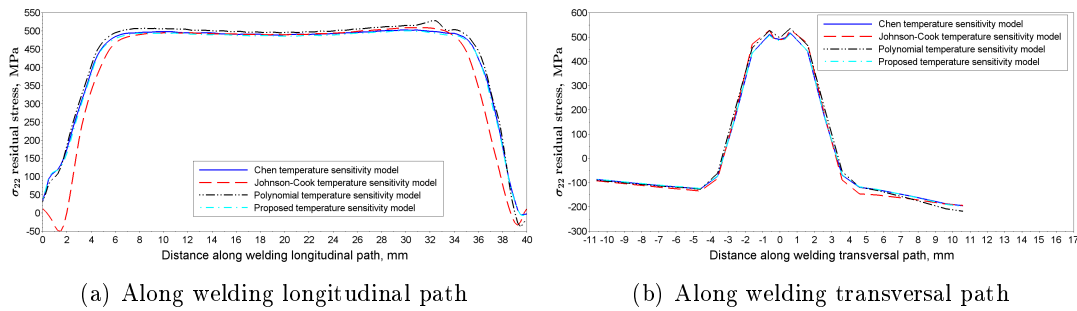
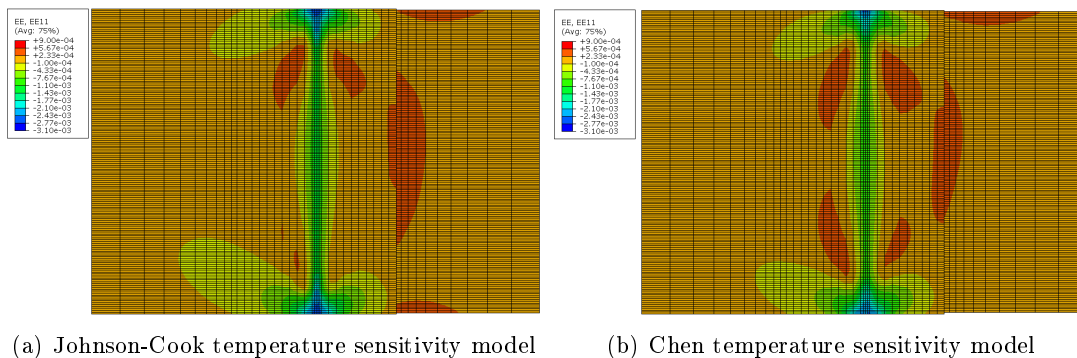


FIGURE 5.41 – The magnitude of σ_{22} residual stresses of welding simulation models with 4 different temperature sensitivity terms

5.5.4 Simulation results of ϵ_{11}^e residual elastic strains

The distribution of ϵ_{11}^e elastic strains are presented in figure 5.42. The color range in the left of 4 figures are set to be the same. Comparison shows that ϵ_{11}^e elastic strain distributions of 4 temperature sensitivity models are similar. At weld region and the region around weld (blue, green and yellow part), compressible ϵ_{11}^e elastic strains are obtained. At the center plate neighbor to weld (red and orange part), tensile ϵ_{11}^e elastic strains are obtained.



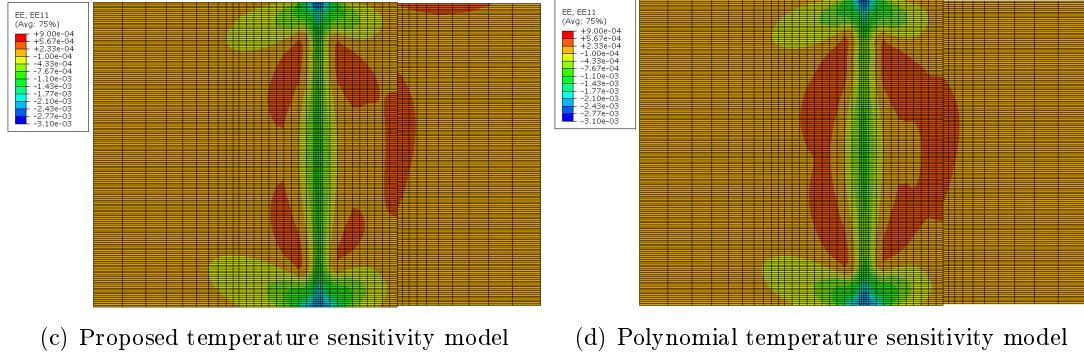


FIGURE 5.42 – The distribution of ϵ_{11}^e elastic strains of welding simulation with 4 different temperature sensitivity terms

A closer look on welding longitudinal path and transversal path for ϵ_{11}^e elastic strains are shown in figure 5.43. For Chen and proposed temperature sensitivity model, the obtained numerical simulation results of ϵ_{11}^e elastic strains are similar. They both are higher than ϵ_{11}^e results of Johnson-Cook temperature sensitivity model and lower than ϵ_{11}^e results of polynomial sensitivity model.

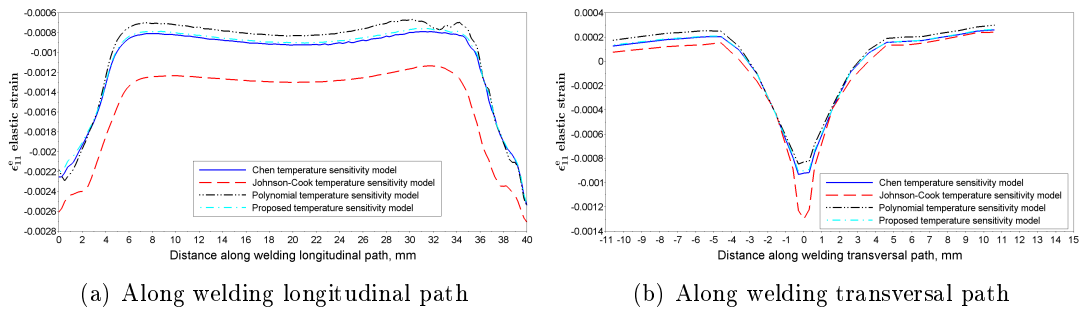


FIGURE 5.43 – The magnitude of ϵ_{11}^e elastic strains of welding simulation models with 4 different temperature sensitivity terms

5.5.5 Simulation results of ϵ_{22}^e residual elastic strains

The distribution of ϵ_{22}^e elastic strains are presented in figure 5.44. The color range in the left of 4 figures are set to be the same. Comparison shows that ϵ_{22}^e elastic strain distributions of 4 temperature sensitivity models are similar. At weld region and the region around weld (red, orange and green part), tensile ϵ_{22}^e elastic strains are obtained. At the outer part far from weld (blue and cyan part), compressible ϵ_{22}^e elastic strains are obtained.

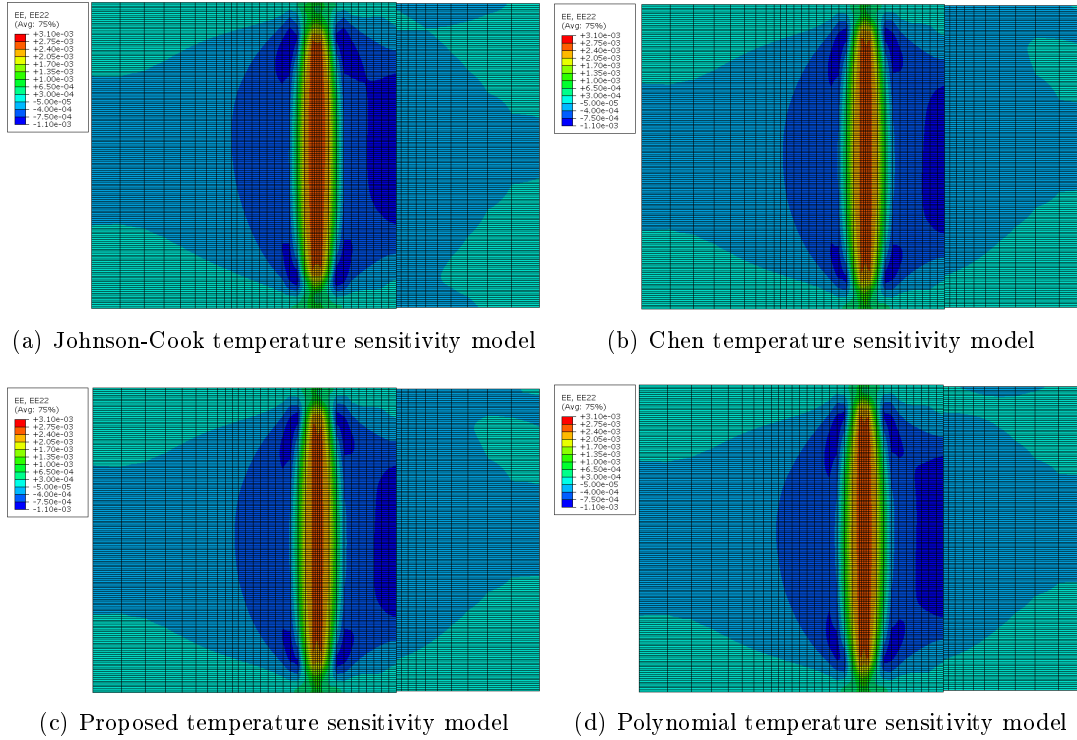


FIGURE 5.44 – The distribution of ϵ_{22}^e elastic strains of welding simulation with 4 different temperature sensitivity terms

A closer look on welding longitudinal path and transversal path for ϵ_{22}^e elastic strains are shown in figure 5.45. For Chen, proposed and polynomial temperature sensitivity model, the obtained numerical simulation results of ϵ_{22}^e elastic strains are similar. In figure 5.45 (a), ϵ_{22}^e results of Johnson-Cook temperature sensitivity model are lower at the beginning and ending part and higher in the center part than ϵ_{22}^e results of the other three sensitivity models.

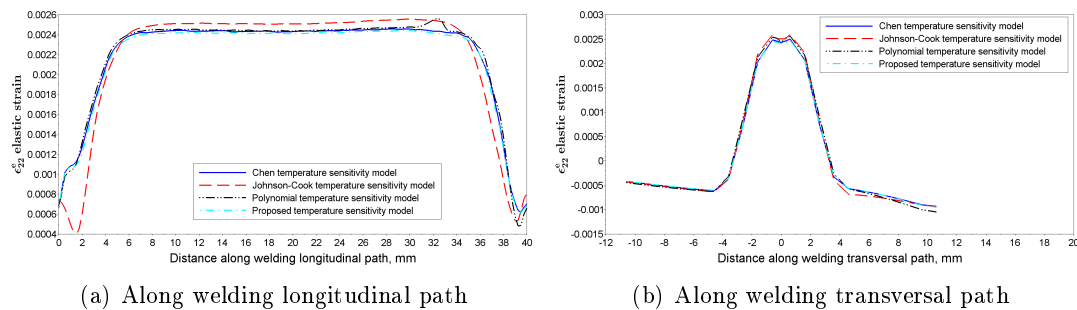


FIGURE 5.45 – The magnitude of ϵ_{22}^e elastic strains of welding simulation models with 4 different temperature sensitivity terms

5.5.6 Simulation results of ϵ_{11}^p residual plastic strains

The distribution of ϵ_{11}^p plastic strains are presented in figure 5.46. The color range in the left of 4 figures are set to be the same. Comparison shows that ϵ_{11}^p plastic strain distributions of 4 temperature sensitivity models are different. A wider green region of ϵ_{11}^p plastic strain distributions of Johnson-Cook temperature sensitivity model are found than the other three models, a red region which stands for more lower value of ϵ_{11}^p plastic strain is obtained by Chen temperature sensitivity model .

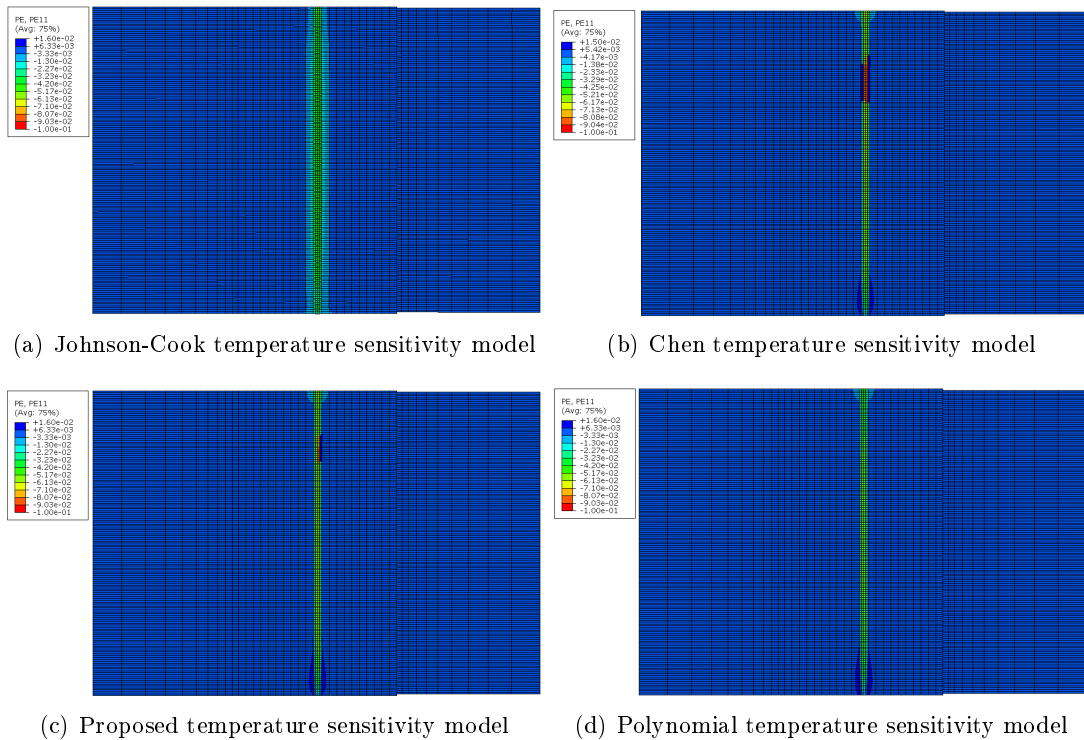


FIGURE 5.46 – The distribution of ϵ_{11}^p plastic strains of welding simulation with 4 different temperature sensitivity terms

A closer look on welding longitudinal path and transversal path for ϵ_{11}^p plastic strains are shown in figure 5.47. At the weld region and the region around the weld, compressible ϵ_{11}^p plastic strains are obtained. For Johnson-Cook temperature sensitivity model along welding longitudinal and transversal path, the obtained numerical simulation results of ϵ_{11}^p plastic strains have a big difference with ϵ_{11}^p of polynomial, proposed and Chen temperature sensitivity models. Along welding longitudinal path, ϵ_{11}^p plastic strains of polynomial temperature sensitivity model are also different with ϵ_{11}^p of proposed and Chen temperature sensitivity models. ϵ_{11}^p of proposed and Chen temperature sensitivity models are similar and only a little difference is present at the ending part of weld.

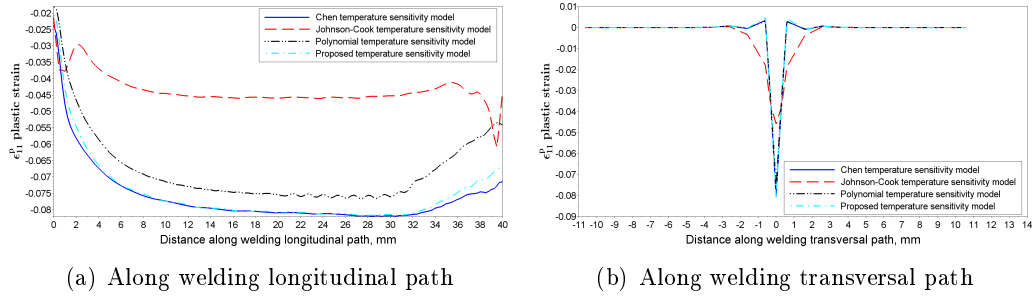


FIGURE 5.47 – The magnitude of ϵ_{11}^p plastic strains of welding simulation models with 4 different temperature sensitivity terms

5.5.7 Simulation results of ϵ_{22}^p residual plastic strains

The distribution of ϵ_{22}^p plastic strains are presented in figure 5.48. The color range in the left of 4 figures are set to be the same. Comparison shows that ϵ_{22}^p plastic strain distributions of 4 temperature sensitivity models are similar. For all the plate, ϵ_{22}^p plastic strain distributions are found $\epsilon_{22}^p = 0$ based on figure 5.49(b) (green region), a lower value of ϵ_{22}^p plastic strain is obtained at weld (blue part).

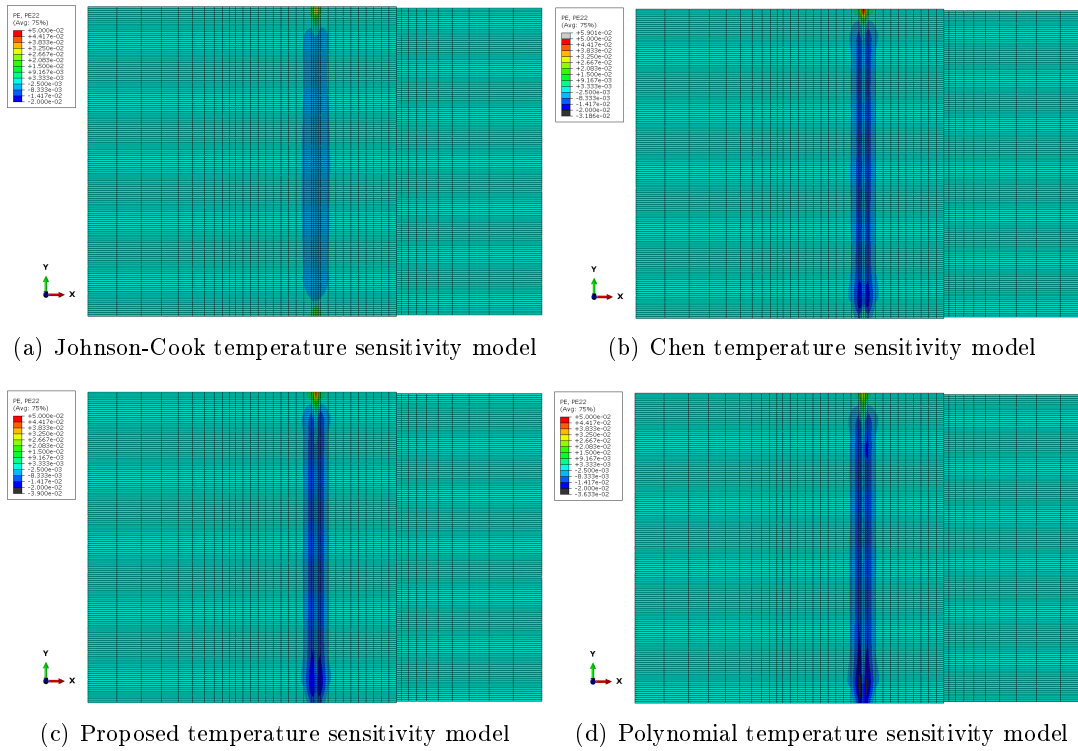


FIGURE 5.48 – The distribution of ϵ_{22}^p plastic strains of welding simulation with 4 different temperature sensitivity terms

A closer look on welding longitudinal path and transversal path for ϵ_{22}^p plastic strains are shown in figure 5.49. Along welding longitudinal path in figure 5.49 (a), ϵ_{22}^p plastic strains of four temperature sensitivity models are around 0 at the center part and have some differences at the beginning and ending part. Along welding transversal path in figure 5.49 (b), ϵ_{22}^p plastic strains of proposed temperature sensitivity model are more closed to polynomial model and have some difference with Chen and Johnson-Cook temperature sensitivity model.

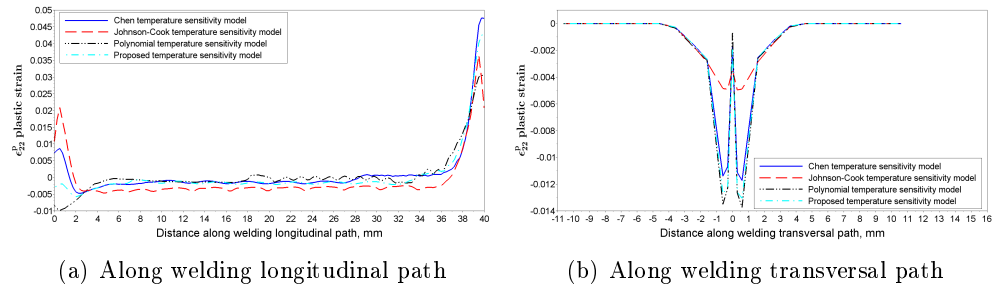
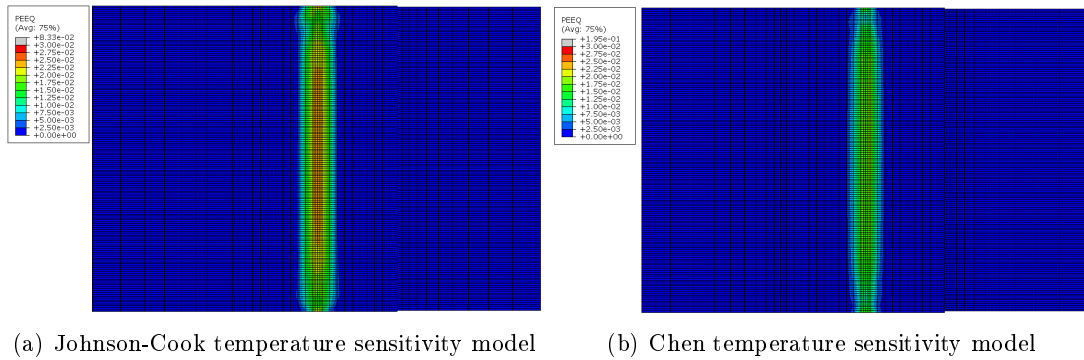


FIGURE 5.49 – The magnitude of ϵ_{22}^p plastic strains of welding simulation models with 4 different temperature sensitivity terms

5.5.8 Simulation results of $\bar{\epsilon}^p$ equivalent residual strains

The distribution of $\bar{\epsilon}^p$ effective plastic strains are presented in figure 5.50. The color range in the left of 4 figures are set to be the same. Comparison shows that $\bar{\epsilon}^p$ effective plastic strain distributions of 4 temperature sensitivity models are different. A wider green region of $\bar{\epsilon}^p$ effective plastic strain distributions of Johnson-Cook temperature sensitivity model are found than the other three models, and red region which stands for higher value of $\bar{\epsilon}^p$ effective plastic strain is found at center weld. The red region is also found in $\bar{\epsilon}^p$ distribution of polynomial temperature sensitivity model. $\bar{\epsilon}^p$ distribution of Chen and proposed temperature sensitivity models are similar.



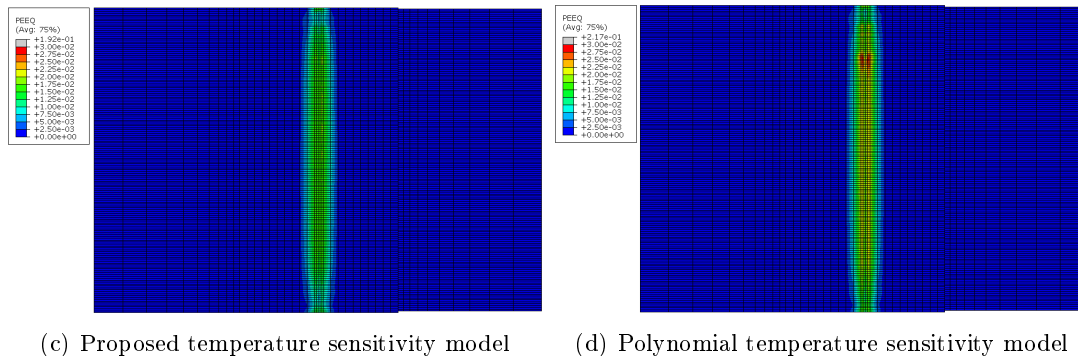


FIGURE 5.50 – The distribution of $\bar{\epsilon}^P$ effective plastic strains of welding simulation with 4 different temperature sensitivity terms

A closer look on welding longitudinal path and transversal path for $\bar{\epsilon}^P$ effective plastic strains are shown in figure 5.51. A big difference of $\bar{\epsilon}^P$ of Johnson-Cook temperature sensitivity model is found compared with $\bar{\epsilon}^P$ of the other three models. $\bar{\epsilon}^P$ of polynomial model is similar along longitudinal path but a little different along transversal path with $\bar{\epsilon}^P$ of proposed and Chen temperature sensitivity model. $\bar{\epsilon}^P$ of proposed and Chen temperature sensitivity models are similar.

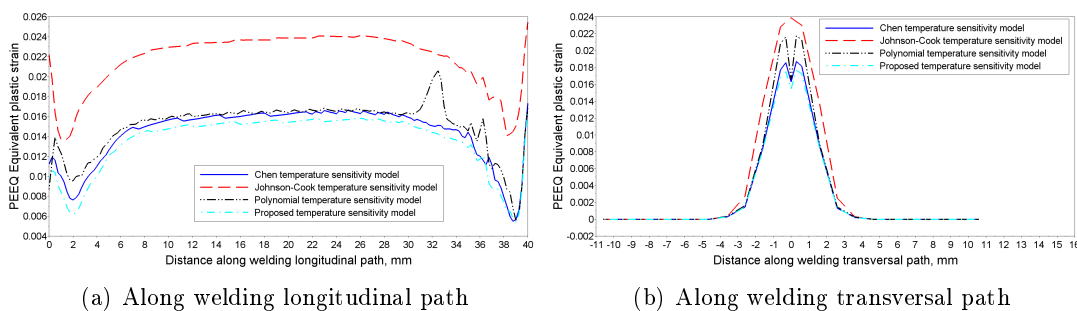


FIGURE 5.51 – The magnitude of $\bar{\epsilon}^P$ effective plastic strains of welding simulation models with 4 different temperature sensitivity terms

In all above figures, simulation results analyzing temperature sensitivity are found different with those results analyzing hardening in section 5.4. These comparison proves that temperature sensitivity has an important influence on simulation results of residual stresses and strains in laser welding process.

5.6 Strain rate sensitivity analysis of DP600

5.6.1 Simulation results of equivalent residual stresses

The distribution of equivalent residual stresses are presented in figure 5.52. The unit of results is in MPa. The color range in the left of 2 figures are set to be the same. Comparison shows that equivalent residual stresses of models with and without strain rate influence are similar.

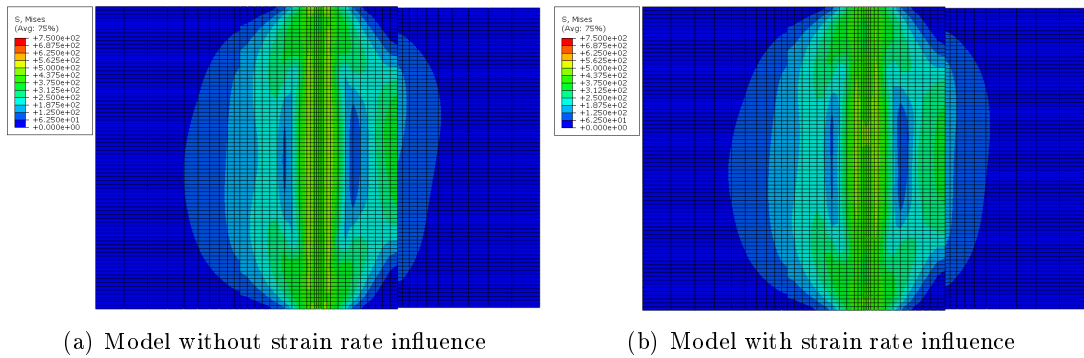


FIGURE 5.52 – The distribution of equivalent residual stresses of welding simulation models with and without strain rate influence

Along welding longitudinal path and transversal path, equivalent stresses are shown in figure 5.53. The obtained simulation results are around 400 MPa. Along welding longitudinal path, equivalent residual stresses of model with strain rate influence have a peak value in center while equivalent stresses of model without strain rate influence are stable. Along welding transversal path, two curves of equivalent residual stresses have some difference around 20 MPa.

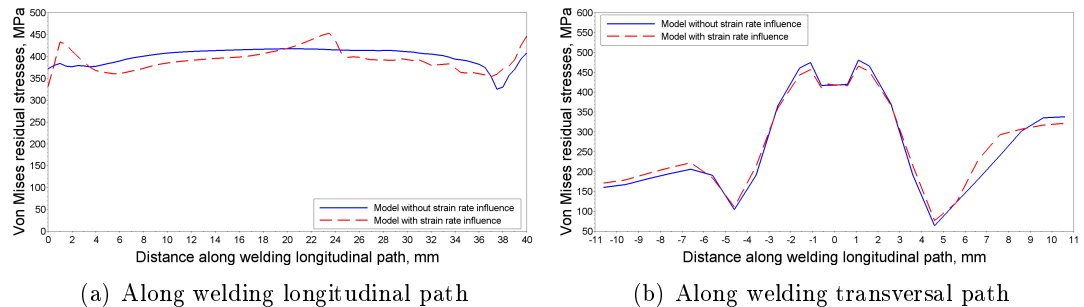


FIGURE 5.53 – The magnitude of equivalent residual stresses of welding simulation models with and without strain rate influence

5.6.2 Simulation results of σ_{11} residual stresses

The distribution of σ_{11} residual stresses are presented in figure 5.54. The unit of σ_{11} is in MPa. The color range in the left of 2 figures are set to be the same. Comparison shows that σ_{11} residual stress distributions of models with and without strain rate influence are similar. At the beginning and ending of weld (blue and green part), compress σ_{11} residual stresses are obtained. At the center part neighbor to weld (orange part), tensile σ_{11} residual stresses are obtained.

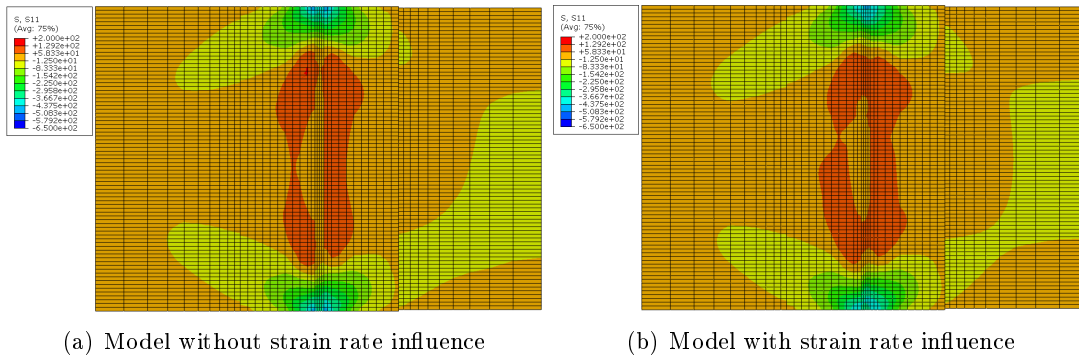


FIGURE 5.54 – The distribution of σ_{11} residual stresses of welding simulation models with and without strain rate influence

A closer look on welding longitudinal path and transversal path for σ_{11} residual stresses are shown in figure 5.55. For model with strain rate influence, the obtained numerical simulation results of σ_{11} are higher than those without strain rate influence.

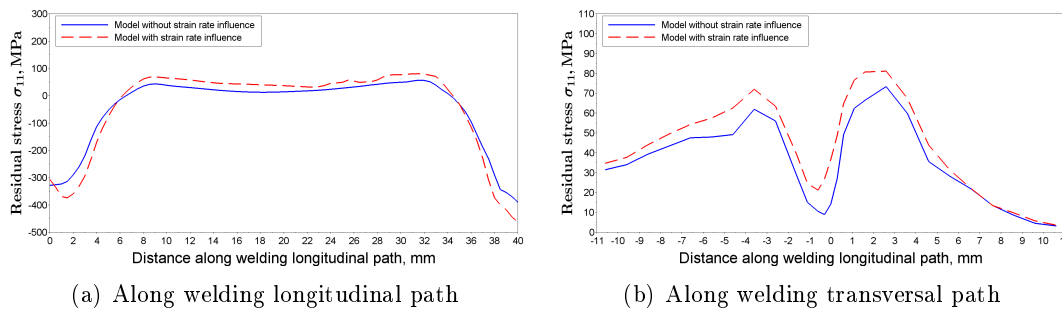


FIGURE 5.55 – The magnitude of σ_{11} residual stresses of welding simulation models with and without strain rate influence

5.6.3 Simulation results of σ_{22} residual stresses

The distribution of σ_{22} residual stresses are presented in figure 5.56. The unit of σ_{22} is in MPa. The color range in the left of 2 figures are set to be the same. Comparison shows that σ_{22} residual stress distributions of models with and without strain rate influence are similar. At weld region and the region around weld (orange and green part), tensile σ_{22} residual stresses are obtained. At the outer part far from weld (blue part), compress σ_{22} residual stresses are obtained.

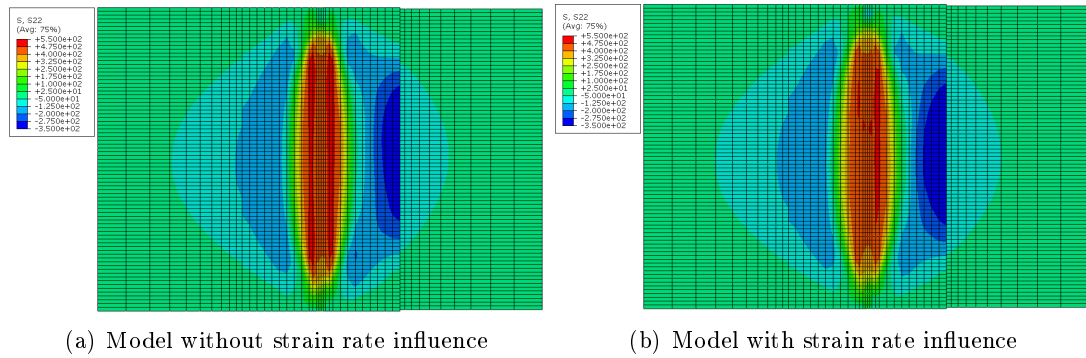


FIGURE 5.56 – The distribution of σ_{22} residual stresses of welding simulation models with and without strain rate influence

A closer look on welding longitudinal path and transversal path for σ_{22} residual stresses are shown in figure 5.57. Along longitudinal path, the obtained numerical simulation σ_{22} of model with strain rate influence have a peak at center while those without strain rate influence are stable.

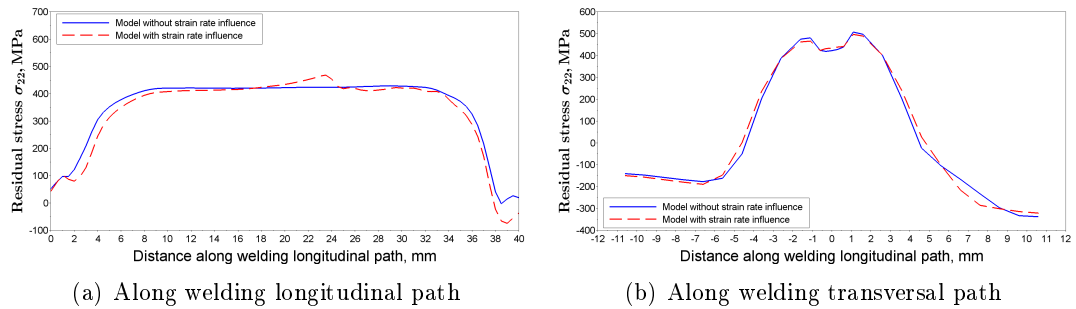


FIGURE 5.57 – The magnitude of σ_{22} residual stresses of welding simulation models with and without strain rate influence

5.6.4 Simulation results of ϵ_{11}^e residual elastic strains

The distribution of ϵ_{11}^e elastic strains are presented in figure 5.58. The color range in the left of 2 figures are set to be the same. Comparison shows that ϵ_{11}^e elastic strain distributions of 2 models with and without strain rate influence are similar. At weld region and the region around weld (blue, green and yellow part), compressible ϵ_{11}^e elastic strains are obtained. At the center plate neighbor to weld (red and orange part), tensile ϵ_{11}^e elastic strains are obtained.

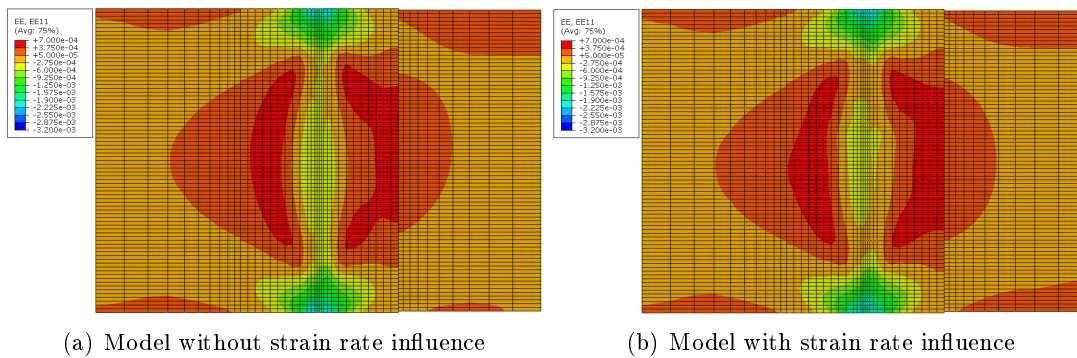


FIGURE 5.58 – The distribution of ϵ_{11}^e elastic strains of welding simulation models with and without strain rate influence

A closer look on welding longitudinal path and transversal path for ϵ_{11}^e elastic strains are shown in figure 5.59. Along welding longitudinal path, the ϵ_{11}^e elastic strains of model with strain rate influence are higher at center but lower at beginning and ending of path than those of model without strain rate influence. Along welding transversal path, the ϵ_{11}^e elastic strains of model with strain rate influence are higher than those of model without strain rate influence.

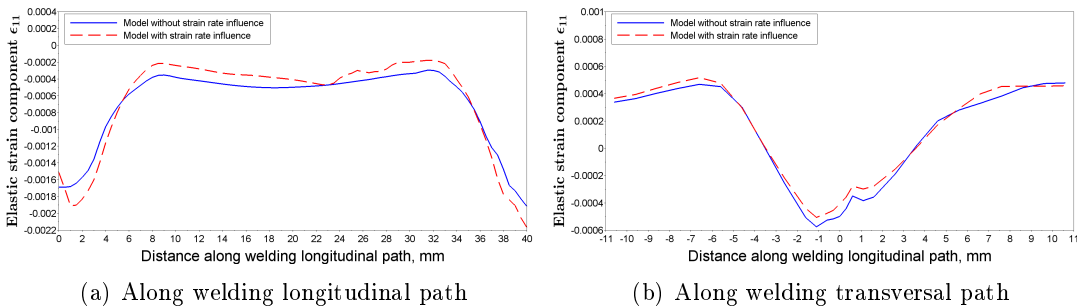


FIGURE 5.59 – The magnitude of ϵ_{11}^e elastic strains of welding simulation models with and without strain rate influence

5.6.5 Simulation results of ϵ_{22}^e residual elastic strains

The distribution of ϵ_{22}^e elastic strains are presented in figure 5.60. The color range in the left of two figures are set to be the same. Comparison shows that ϵ_{22}^e elastic strain distributions of welding simulation models with and without strain rate influence. At weld region and the region around weld (red, orange and green part), tensile ϵ_{22}^e elastic strains are obtained. At the outer part far from weld (blue and cyan part), compressible ϵ_{22}^e elastic strains are obtained.

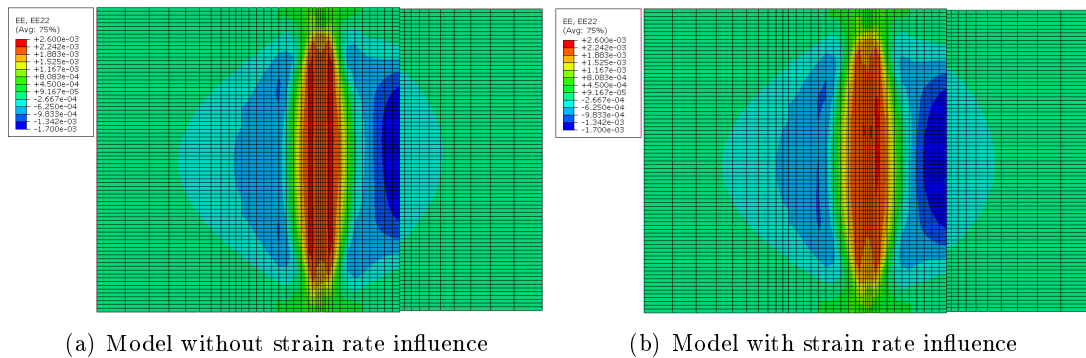


FIGURE 5.60 – The distribution of ϵ_{22}^e elastic strains of welding simulation models with and without strain rate influence

A closer look on welding longitudinal path and transversal path for ϵ_{22}^e elastic strains are shown in figure 5.61. Along welding longitudinal path, the ϵ_{22}^e elastic strains of model with strain rate influence are higher at center but lower at other part than those of model without strain rate influence. Along welding transversal path, the ϵ_{11}^e elastic strains of models with and without strain rate influence are similar.

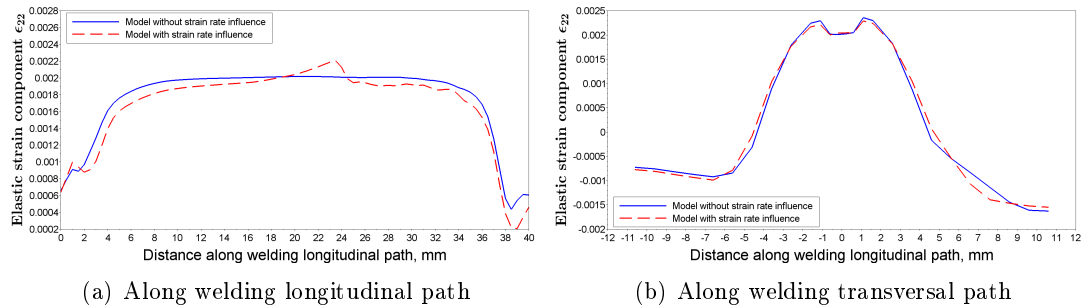


FIGURE 5.61 – The magnitude of ϵ_{22}^e elastic strains of welding simulation models with and without strain rate influence

5.6.6 Simulation results of ϵ_{11}^p residual plastic strains

The distribution of ϵ_{11}^p plastic strains are presented in figure 5.62. The color range in the left of 2 figures are set to be the same. Comparison shows that ϵ_{11}^p plastic strain distributions of models with and without strain rate influence are different. An additional orange region of ϵ_{11}^p plastic strain distributions of model with strain rate influence are found.

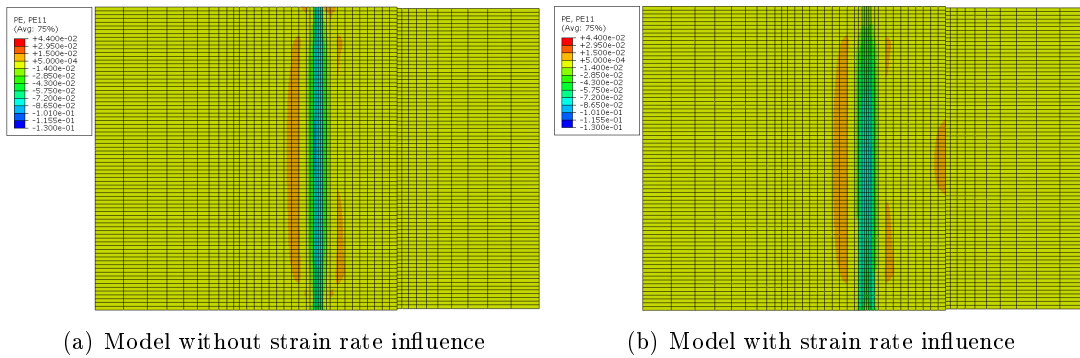


FIGURE 5.62 – The distribution of ϵ_{11}^p plastic strains of welding simulation models with and without strain rate influence

A closer look on welding longitudinal path and transversal path for ϵ_{11}^p plastic strains are shown in figure 5.63. The magnitude of ϵ_{11}^p plastic strains with and without strain rate influence have a difference around 0.02 for welding longitudinal path. The magnitude are similar along welding transversal path except a difference about 0.01 at weld part.

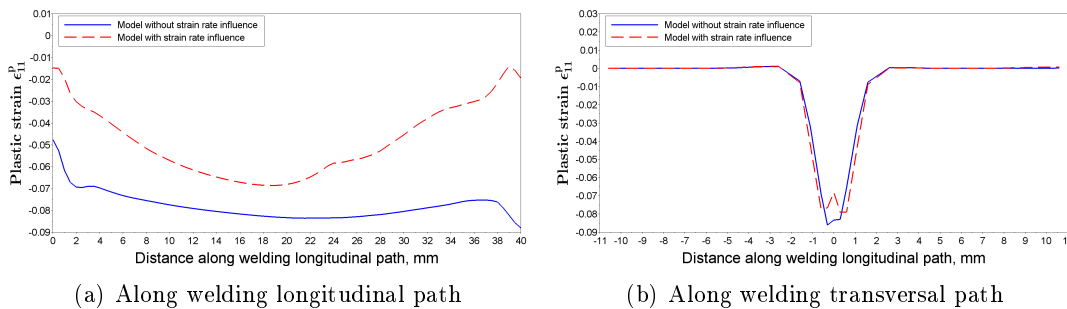


FIGURE 5.63 – The magnitude of ϵ_{11}^p plastic strains of welding simulation models with and without strain rate influence

5.6.7 Simulation results of ϵ_{22}^p residual plastic strains

The distribution of ϵ_{22}^p plastic strains are presented in figure 5.64. The color range in the left of 2 figures are set to be the same. Comparison shows that ϵ_{22}^p plastic strain distributions of welding simulation models with and without strain rate influence are different. The model with strain rate influence has a larger green region at weld (green part).

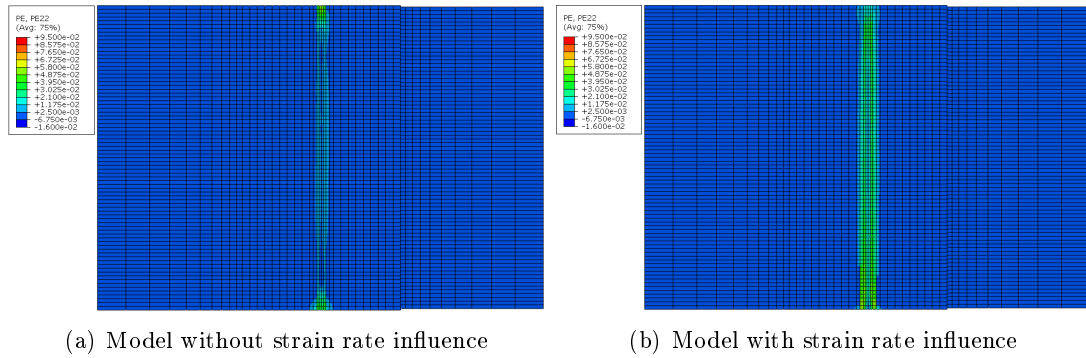


FIGURE 5.64 – The distribution of ϵ_{22}^p plastic strains of welding simulation models with and without strain rate influence

A closer look on welding longitudinal path and transversal path for ϵ_{22}^p plastic strains are shown in figure 5.65. Along welding longitudinal path in figure 5.65 (a), ϵ_{22}^p plastic strains of model with strain rate influence are higher at center part while lower at beginning and ending part of weld. Along welding transversal path in figure 5.65 (b), ϵ_{22}^p plastic strains of model with strain rate influence are higher at weld region than those of model without strain rate influence.

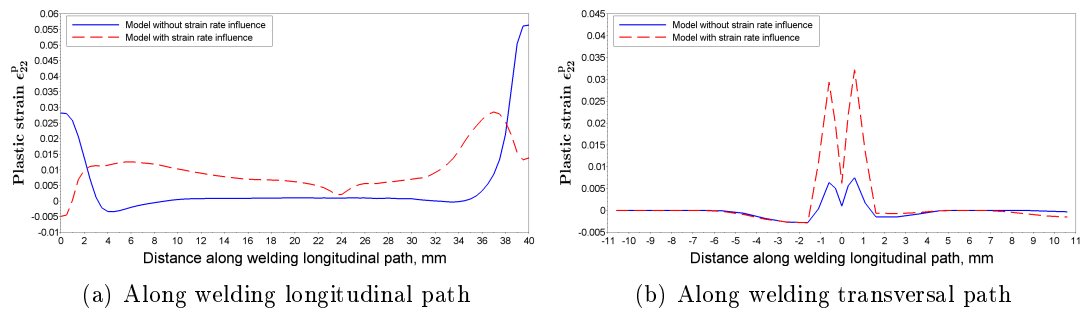


FIGURE 5.65 – The magnitude of ϵ_{22}^p plastic strains of welding simulation models with and without strain rate influence

5.6.8 Simulation results of $\bar{\epsilon}^p$ equivalent plastic strains

The distribution of $\bar{\epsilon}^p$ effective plastic strains are presented in figure 5.66. The color range in the left of 2 figures are set to be the same. Comparison shows that $\bar{\epsilon}^p$ effective plastic strain distributions are different. For model with strain rate influence, a red region which stands for higher value of $\bar{\epsilon}^p$ effective plastic strain is found at center weld.

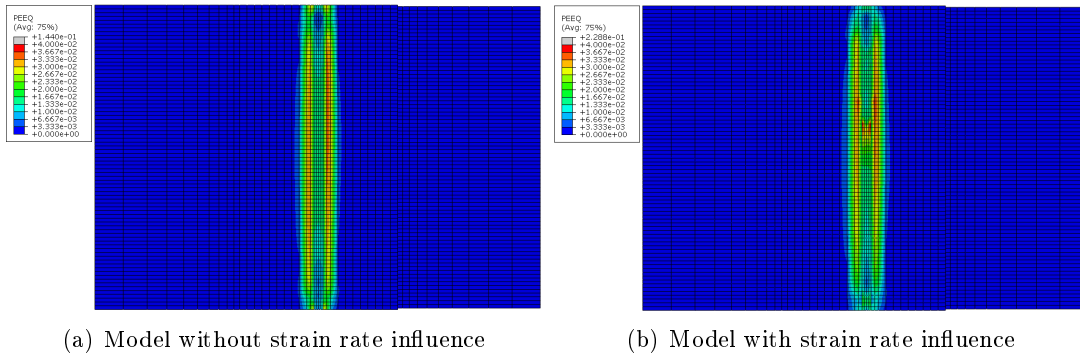


FIGURE 5.66 – The distribution of $\bar{\epsilon}^p$ effective plastic strains of welding simulation models with and without strain rate influence

A closer look on welding longitudinal path and transversal path for $\bar{\epsilon}^p$ effective plastic strains are shown in figure 5.67. Along both welding longitudinal and transversal path, $\bar{\epsilon}^p$ of model with strain rate influence are higher at center part of weld.

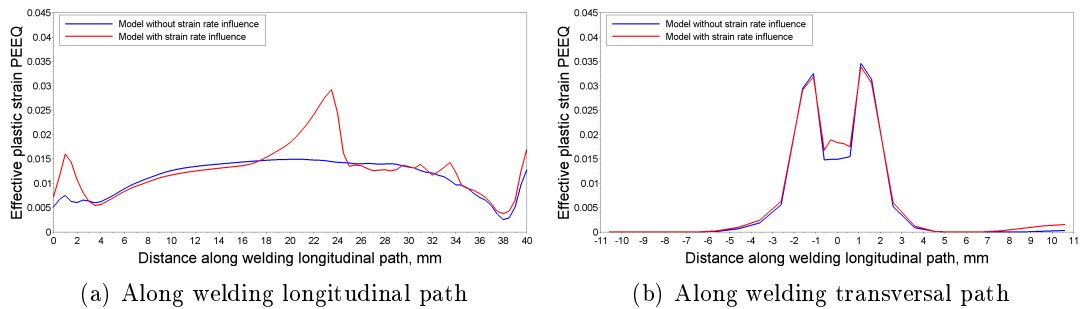


FIGURE 5.67 – The magnitude of $\bar{\epsilon}^p$ effective plastic strains of welding simulation models with and without strain rate influence

In all above figures, residual stress and strain results of the model considering strain rate sensitivity are different with those no considering strain rate sensitivity. The most noticeable influence is that the considering strain rate sensitivity will get a peak value of equivalent stress in the center weld instead of a stable value not considering strain rate sensitivity.

5.7 Plastic planar anisotropy analysis using Hill coefficients

5.7.1 Simulation results of equivalent residual stresses

The distribution of equivalent residual stresses are presented in figure 5.68. The unit of results is in MPa. The color range in the left of figures are set to be the same. Comparison shows that equivalent residual stresses of models with material anisotropy of $\theta = 0^\circ, 30^\circ, 45^\circ, 60^\circ, 90^\circ$ and isotropic material are similar.

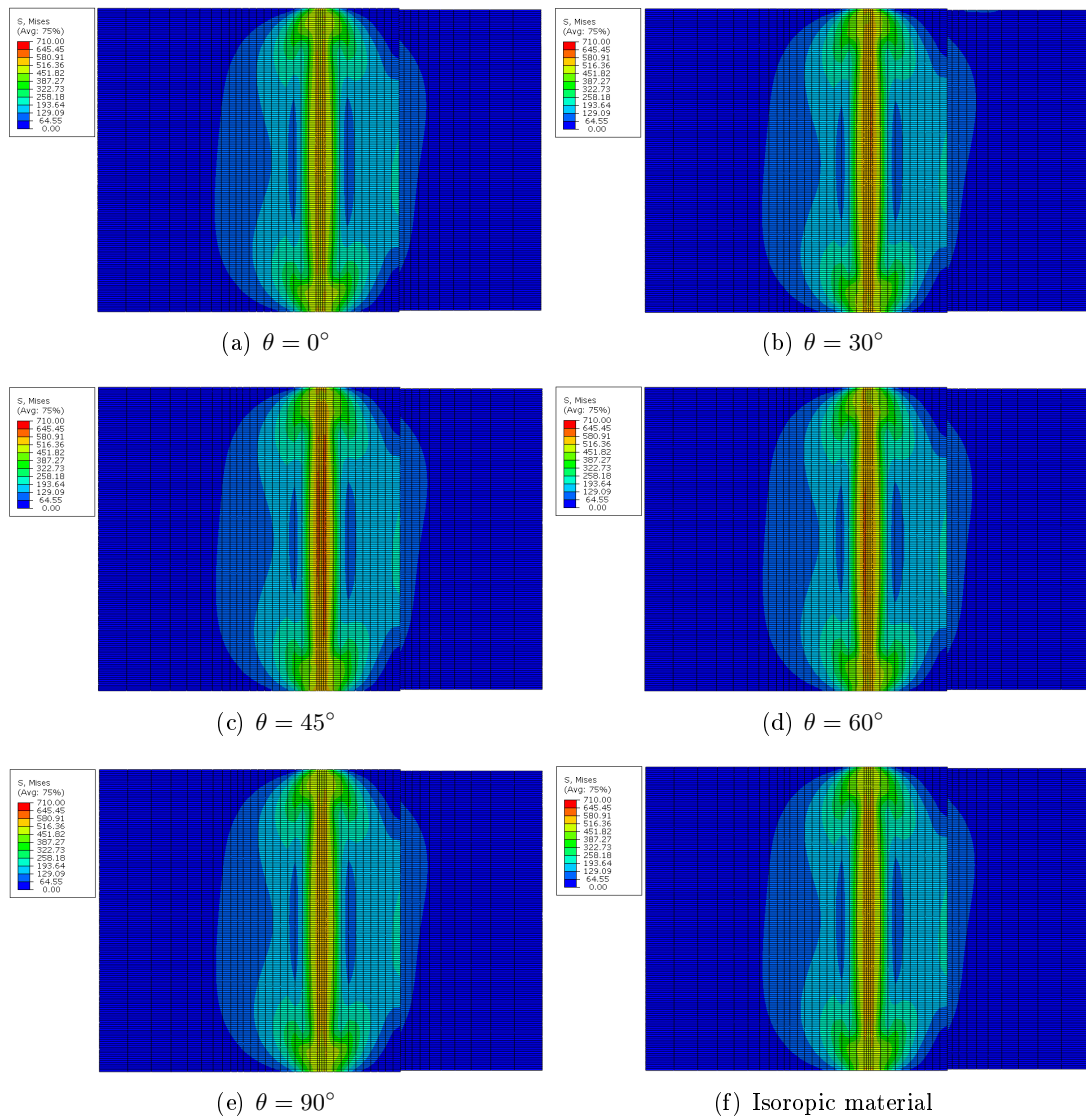


FIGURE 5.68 – The distribution of equivalent residual stresses of welding simulation models with material anisotropy of $\theta = 0^\circ, 30^\circ, 45^\circ, 60^\circ, 90^\circ$ and isotropic material

Along welding longitudinal path and transversal path, equivalent residual stresses are shown in figure 5.69. The obtained simulation results are around 500 MPa. Along welding longitudinal and transversal path, equivalent residual stresses are influenced by anisotropy about 70 MPa at weld fusion zone and heat affected zone.

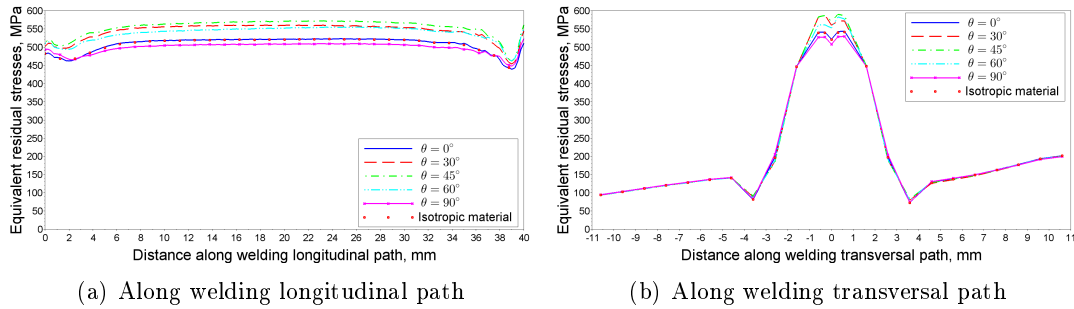
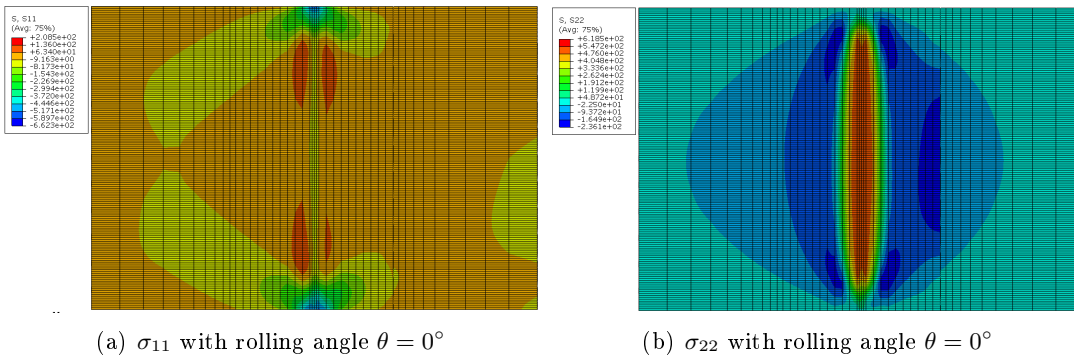


FIGURE 5.69 – The magnitude of equivalent residual stresses of welding simulation models with material anisotropy of $\theta = 0^\circ, 30^\circ, 45^\circ, 60^\circ, 90^\circ$ and isotropic material

5.7.2 Simulation results of σ_{11} and σ_{22} residual stresses

The contour of residual stresses of two material rolling orientations $\theta = 0^\circ$ and $\theta = 90^\circ$ are presented in figure 5.70. With the material rolling orientation setting from longitudinal to transversal direction, the simulated distributions of residual stresses σ_{11} and σ_{22} turn over. The distributions of σ_{11} and σ_{22} with material rolling orientation $\theta = 0^\circ$ correspond to the distribution of σ_{22} and σ_{11} with material rolling orientation $\theta = 90^\circ$, respectively.



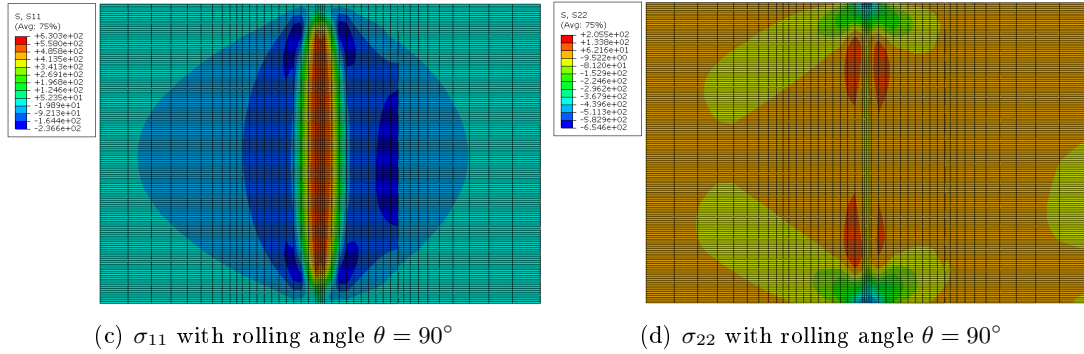


FIGURE 5.70 – Contour of residual stresses with different material rolling orientations

Residual stresses σ_{11} and σ_{22} along transversal path are simulated. Different material rolling orientations with $\theta = 0^\circ, 45^\circ$ and 90° are applied in models. The simulation results are presented in figure 5.71. The material rolling orientation influence the magnitude of longitudinal and transversal residual stresses.

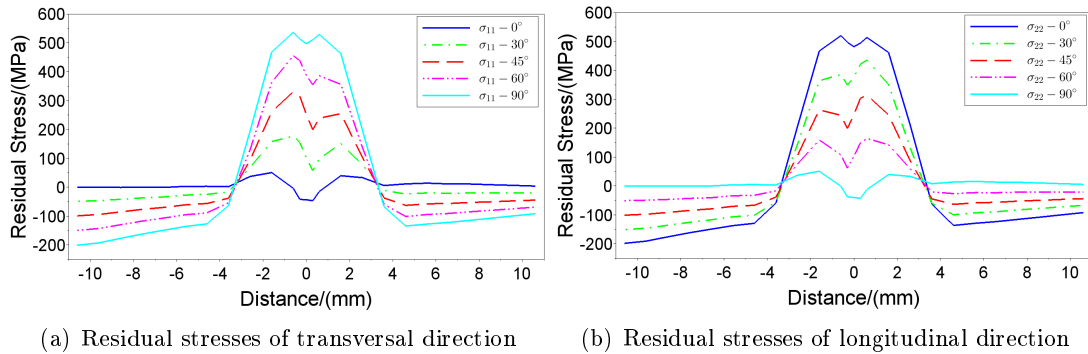


FIGURE 5.71 – Numerical welding residual stresses obtained from different rolling orientations

5.7.3 Simulation results of $\bar{\epsilon}^p$ residual equivalent plastic strains

The distribution of $\bar{\epsilon}^p$ residual equivalent strains are presented in figure 5.72. The color range in the left of figures are set to be the same. Comparison shows that $\bar{\epsilon}^p$ residual equivalent strains of models with material anisotropy of $\theta = 0^\circ, 30^\circ, 45^\circ, 60^\circ, 90^\circ$ and isotropic material are similar.

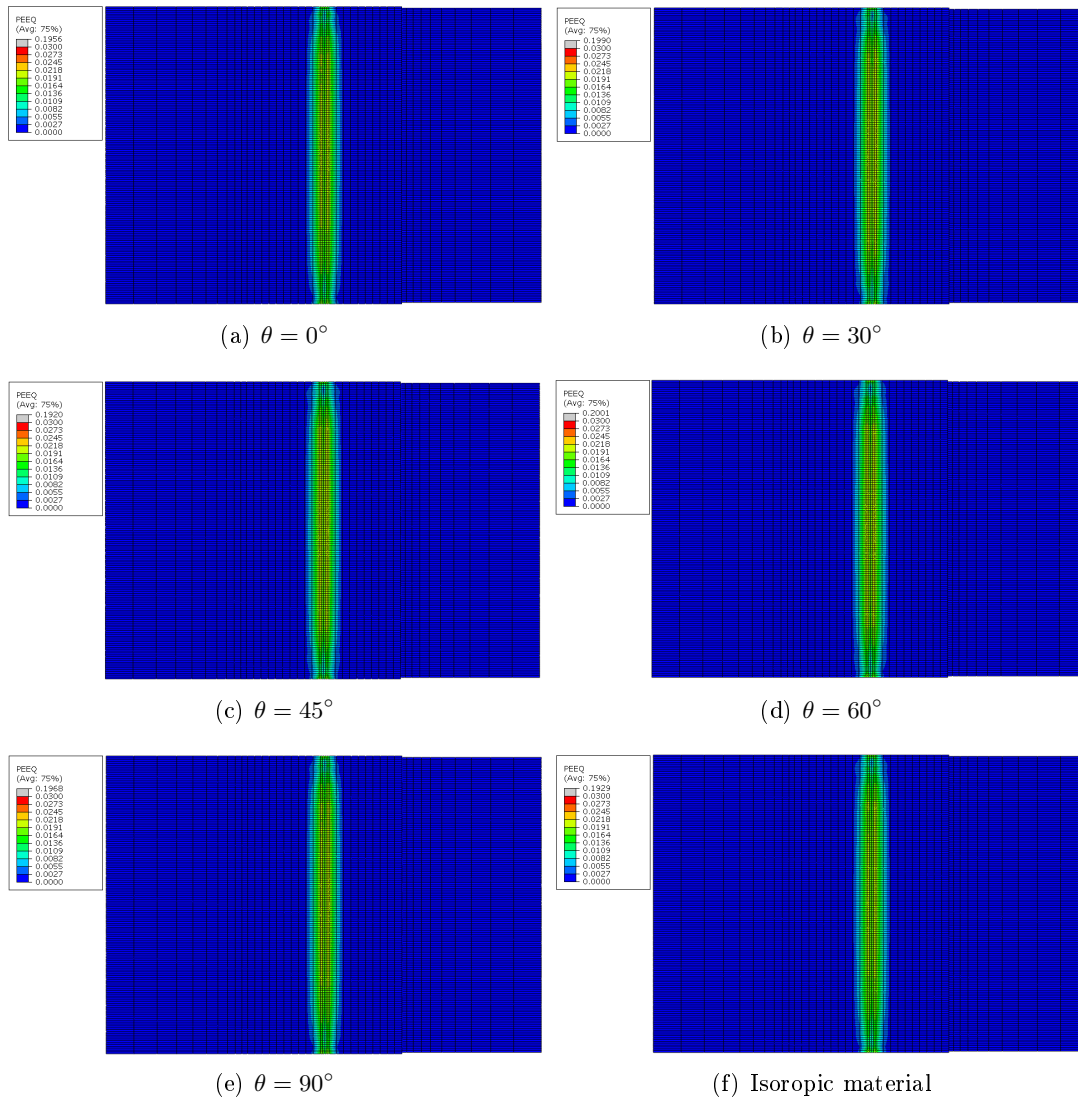


FIGURE 5.72 – The distribution of equivalent residual stresses of welding simulation models with material anisotropy of $\theta = 0^\circ, 30^\circ, 45^\circ, 60^\circ, 90^\circ$ and isotropic material

Along welding longitudinal path and transversal path, $\overline{\epsilon^P}$ residual equivalent strains are shown in figure 5.73. The obtained simulation results are around 0.016 at center weld. Along welding longitudinal and transversal path, $\overline{\epsilon^P}$ residual equivalent strains are influenced by anisotropy about 0.001 at weld fusion zone and heat affected zone.

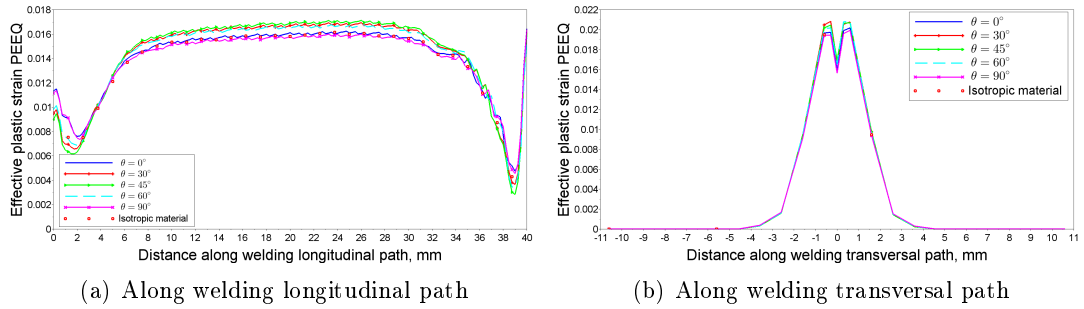


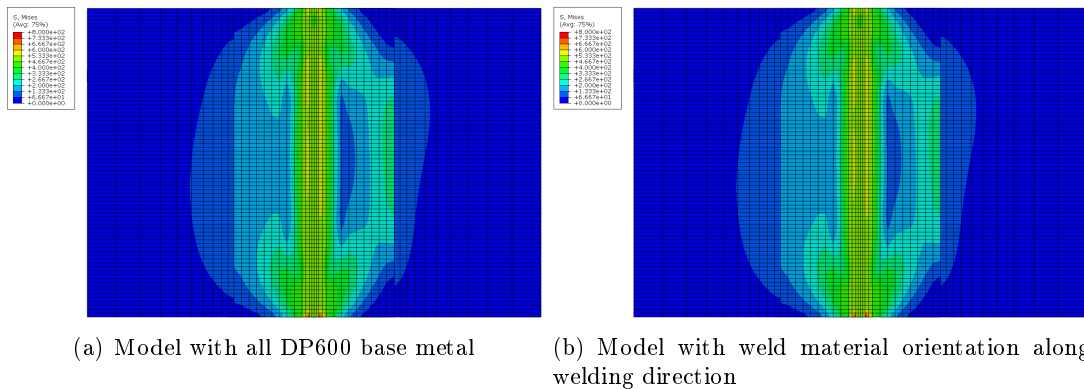
FIGURE 5.73 – The magnitude of equivalent residual stresses of welding simulation models with material anisotropy of $\theta = 0^\circ, 30^\circ, 45^\circ, 60^\circ, 90^\circ$ and isotropic material

5.8 Elastic orthotropic anisotropy analysis using cellular automaton

5.8.1 Simulation results of equivalent residual stresses

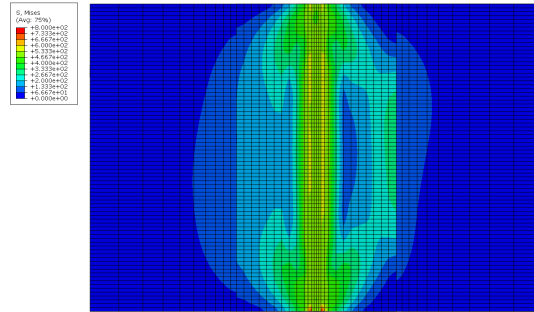
The distribution of equivalent residual stresses are presented in figure 5.74. The unit of results is in MPa. The color range in the left of figures are set to be the same. Comparison shows that equivalent residual stresses of models with all DP600 base metal and with weld material orientations along welding direction and obtained by CA model are similar.

A closer look along welding longitudinal path and transversal path, equivalent residual stresses are shown in figure 5.75. The obtained simulation results are around 500 MPa. Along welding longitudinal and transversal path, equivalent residual stresses are different by considering the orthotropic elasticity. The zoomed figures show that results of simulation considering CA model orientations are a little higher than those results of base metal and those results of weld material without material orientations (not considering the orthotropic elasticity).



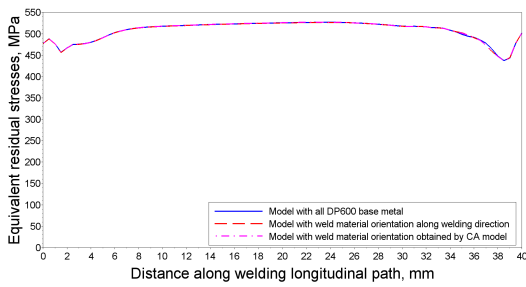
(a) Model with all DP600 base metal

(b) Model with weld material orientation along welding direction

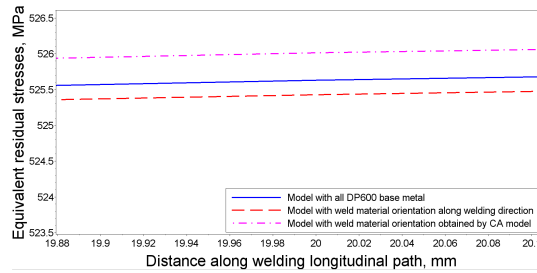


(c) Model with weld material orientation obtained by CA model

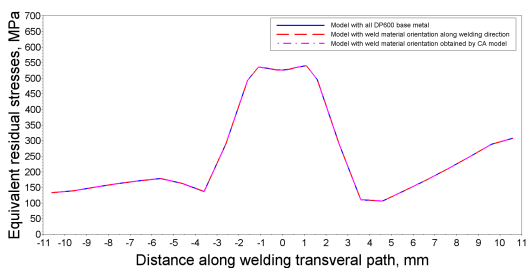
FIGURE 5.74 – The distribution of equivalent residual stresses of welding simulation models with all DP600 base metal and with weld material orientations along welding direction and obtained by CA model



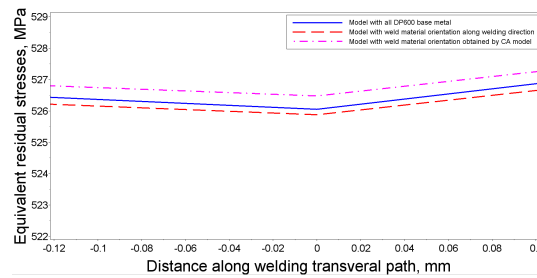
(a) Along welding longitudinal path



(b) Zoomed center part in figure (a)



(c) Along welding transversal path



(d) Zoomed center part in figure (c)

FIGURE 5.75 – The magnitude of equivalent residual stresses of welding simulation models with all DP600 base metal and with weld material orientations along welding direction and obtained by CA model

5.8.2 Simulation results of $\bar{\epsilon}^p$ residual equivalent plastic strains

The distribution of $\bar{\epsilon}^p$ residual equivalent strains are presented in figure 5.76. The color range in the left of figures are set to be the same. Comparison shows that $\bar{\epsilon}^p$ residual

equivalent strains distributions of models with all DP600 base metal and with weld material orientations along welding direction and obtained by CA model are similar.

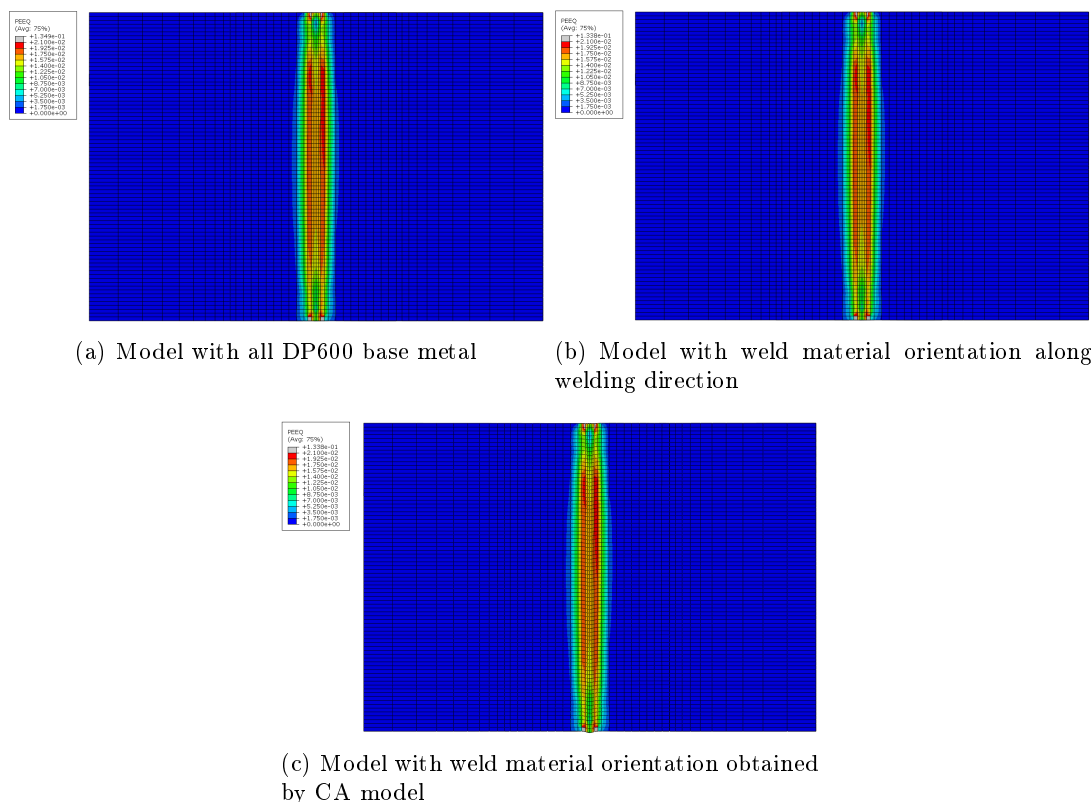


FIGURE 5.76 – The distribution of equivalent residual stresses of welding simulation models with all DP600 base metal and with weld material orientations along welding direction and obtained by CA model

A closer look along welding longitudinal path and transversal path, $\overline{\epsilon^p}$ residual equivalent strains are shown in figure 5.77. The obtained simulation results are around 0.016 at center weld. Along welding longitudinal and transversal path, $\overline{\epsilon^p}$ residual equivalent strains are different. The zoomed figures show that results of simulation considering CA model orientations are a little higher than those results of base metal and those results of weld material without material orientations (not considering the orthotropic elasticity) .

5.9 Model validation by experimental analysis

In the previous analysis, the material constitutive model of strain rate sensitivity and the orthotropic elastic anisotropy are found to have influences but not very big influences on residual stress and strains of numerical laser welding model. So only the combination

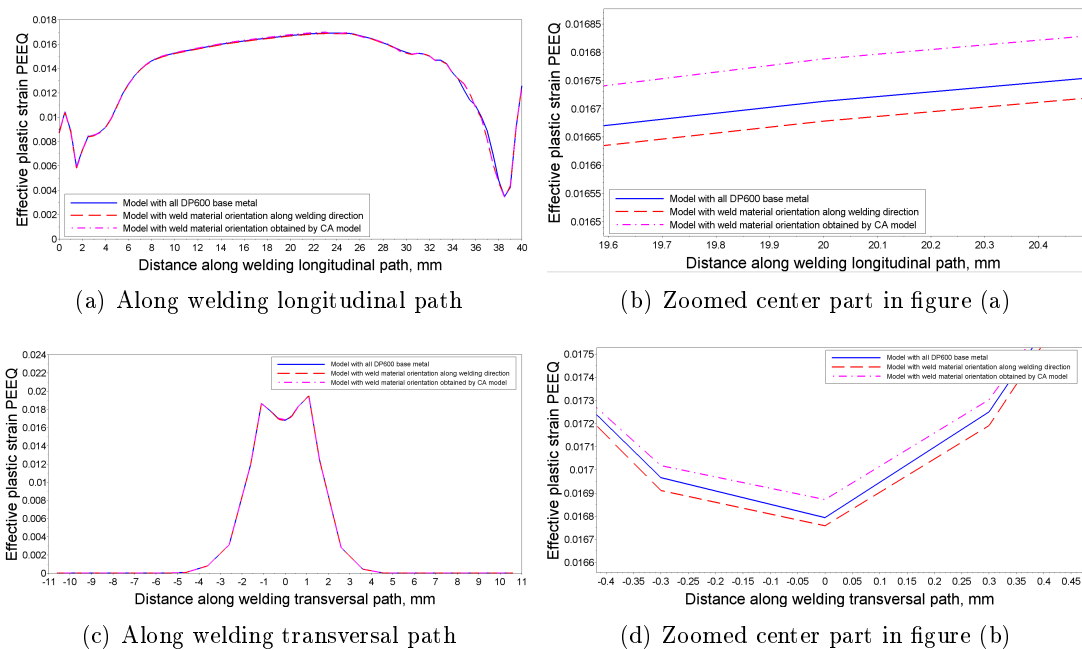


FIGURE 5.77 – The magnitude of equivalent residual stresses of welding simulation models with all DP600 base metal and with weld material orientations along welding direction and obtained by CA model

of hardening, temperature sensitivity and plastic anisotropy material constitutive model are used in numerical laser welding simulation. The FEM model information can be found in chapter 4.6 with proposed synthesis model, proposed temperature sensitivity and material anisotropy defined by Hill theory. The material is assigned a material rolling orientation that have 30° with transversal path.

In figure 5.78, along the transversal path of weld, experimental and numerical results of residual stresses variations with the different material orientations are shown. The residual stresses of σ_{11} and σ_{22} are measured by Neutron Diffraction method along transversal path. The simulation results show a good accordance with experiment measurements.

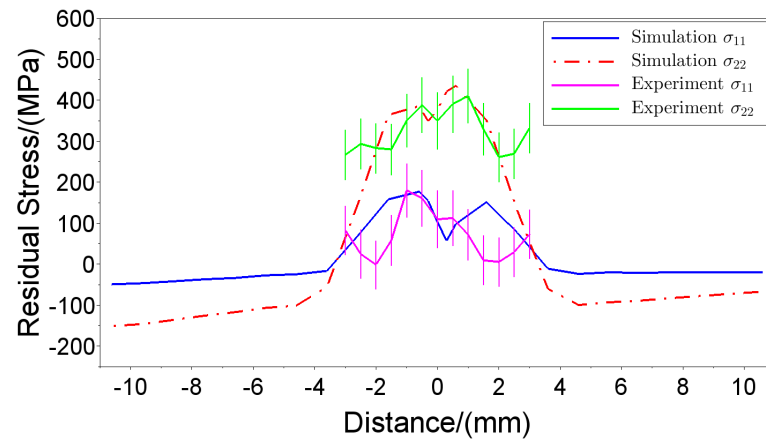


FIGURE 5.78 – Comparison between the experimental and the numerical residual stresses

General Conclusions

This thesis studies residual stresses produced in Nd :YAG laser beam overlap welding of dual phase DP600 steel plates. The DP600 steel constitutive model is considered as an important factor in general dynamic forming process and the laser welding numerical analysis. Thus a lot of experimental tensile tests are conducted to precisely identify thermo-elasto-plastic behavior of DP600 dual phase steel considering hardening term, strain rate sensitivity, temperature sensitivity, planar plastic anisotropy and orthotropic elastic anisotropy. A 2D Cellular Automaton model is introduced to simulate laser welding solidification process so that the microstructure information are considered for defining orthotropic elastic anisotropy and computing residual stresses. FEA numerical simulations are applied based on the identified material constitutive models and corresponding results are analyzed. Computation of residual stresses through neutron diffraction are conducted to validate the numerical model and good accordance are found.

In introduction chapter, laser welding process, DP600 dual phase steel, residual stresses and continuum mechanics are introduced. Laser welding process is widely used in assembly work of automobile industry. DP600 dual phase steel is a high strength steel to reduce automobile weight. Important residual stresses are produced during laser welding of analyzed dual phase steel. Finite Element Model based on an incremental sequential coupled elasto-thermo-plastic analysis of commercial code Abaqus together with specific constitutive equations introduced via UMAT subroutine is used to simulate residual stresses. General information of Nd :YAG laser weld such as its development, mesoscopic mechanism and laser welding parameters are presented. The characteristics of dual phase DP600 steel such as application area, elastic, thermal, mechanical and chemical properties during a laser welding are described. The orders, research meaning and the production mechanism of residual stress in welding are also taken into account. Mathematical description of yield criteria, elasticity and plasticity are reviewed as a base for this research work.

In chapter 2, material thermo-mechanical constitutive model of DP600 are analyzed based on a lot of experimental tensile tests. The constitutive model consists of hardening term, strain rate sensitivity, temperature sensitivity and anisotropy are identified for DP600 material.

The DP600 hardening term according to Ludwik law, Voce law, a proposed synthesis model and polynomial equations are studied. It is found that the plastic flow behavior of

DP600 dual phase steel can not be described only using classical Ludwik law or Voce law. A physically based synthesis hardening model considering a mixture of ferrite softening effect (using classical Voce law) and martensite hardening effect (using classical Ludwik law) is proposed and proved to describe perfectly the plastic flow behavior of DP600 dual phase steel for large plastic strain range in order to cover numerical applications for different welding conditions and other dynamic forming processes.

The DP600 steel temperature sensitivity of Johnson-Cook, Khan, Chen and a proposed temperature sensitivity model are investigated. Both Johnson-Cook and Khan temperature sensitivity model are found to be limited to describe DP600 dual phase steel at large temperature range, while Chen temperature sensitivity model and a proposed temperature sensitivity model can represent DP600 steel temperature sensitivity model at large temperature rang with a few parameters. A polynomial temperature sensitivity term is not suitable for other steel materials. It is identified only based on DP600 steel experimental data to yield precise results in subsequent residual stresses welding finite element analysis.

The strain rate sensitivity model proposed by A. Gavrus is physically based on dislocations glide kinetics. It is shown from the flow stress curves that the identified material plasticity model of dual-phase DP600 steel predicts well the hardening and strain rate sensitivity at room temperature and with some acceptable difference at high temperatures.

Based on tensile tests results of literature and corresponding experimental analysis at ambient temperature, DP600 steel material constitutive model are obtained and written finally as :

$$\sigma(\varepsilon_p, T, \dot{\varepsilon}) = \left\{ w \times (2772.93 \times \varepsilon_p^{0.5765} + 331.74) + (1 - w) \times [289.34 \times (1 - e^{-11.5505 \times \varepsilon_p}) + 331.74] \right\} \times (1 - 0.49 \times T^{*4.21})^{103.17} \times 0.8042232 \times \left[1 + Ash \left(\frac{1}{2} (\dot{\varepsilon}/96.077)^{0.0005410 \times T - 0.1443611} \right) \right]$$

where w was chosen equal to 0.2 for analyzed DP600 base metal.

Planar anisotropy defined by Hill theory are used for DP600 dual phase steel. Lankford coefficients and Hill's coefficients are given by :

TABLE 5.3 – The Lankford coefficients and Hill's parameters of DP600 steel

r_0	r_{45}	r_{90}	R_{11}	R_{22}	R_{33}	R_{12}
1.0123	0.6487	0.9160	1	0.9748	0.9777	1.1172
F	G	H	N			
0.5492	0.4969	0.5031	1.2017			

In chapter 3, 2D Cellular Automaton (CA) model has been developed for the simulation of solidification microstructure evolution during a laser welding process. The

temperature field of CA are imported from a finite element analysis model. The analysis function of nucleation, solid fraction, interface concentration, surface tension anisotropy, diffusion, interface growth velocity and conservation equations are presented in detail. Starting from initial conditions with different parameters, different results are obtained :

1. In section 3.18.1, CA model results of figure 3.24 prove that unlike traditional ones, the CA model programmed by the author keeps well the growing direction using limited angles method. The CA model are also able to simulate equiaxed dendrite grain growth.
2. In section 3.18.2, CA model results of figure 3.25 show that the CA model can simulate the equiaxed dendrite grain growth with 48 growth directions.
3. In section 3.18.3, CA model results of figure 3.26 claim that CA can simulate column dendrite grain growth.
4. In section 3.18.4, CA model results of figure 3.27 make evidence that two dendrite grain grows well with each other, they grow normally when the two grains dendrite meet each other.
5. In section 3.18.5 and section 3.18.6, CA model results of figure 3.28 and 3.29 mean that the nuclei at the corner grows well to the whole simulation zone, it grow normally at the edge of the simulation zone.
6. In section 3.18.7, CA model results of figure 3.30 indicate that CA model can simulate two equiaxed dendrite grain competition growth.
7. In section 3.18.8, CA model results of figure 3.31 show that grains grow smoothly with the other grains with different growth direction.
8. In section 3.18.9 welding temperature environment and random nucleation conditions are applied, CA model results of figure 3.31 present that CA model can simulate the welding solidification microstructure.

By comparing the dendrite grains growth simulation of CA model during welding process and the corresponding experimental observation of weld microstructures, good accordances are found. The microstructure obtained from weld of laser welding DP600 steel and those simulated by CA-FE model show similar growth microstructure orientations.

In chapter 4, information of finite element model of laser welding process are presented. Geometry of specimen, heat source, boundary conditions, DP600 dual phase steel material properties such as conductivity, density, specific heat, expansion, elasticity and plasticity are introduced. Models analyzing hardening term, strain rate sensitivity, temperature sensitivity, plastic anisotropy and elastic anisotropy are described in detail and simulated. The corresponding results are presented and discussed in chapter 5.

In chapter 5, simulation results of σ_{11} , σ_{22} , equivalent residual stress and ϵ_{11}^e , ϵ_{22}^e , ϵ_{11}^p , ϵ_{22}^p and $\bar{\epsilon}^p$ of laser welding DP600 steel process are presented. The influence of hardening term, strain rate sensitivity, temperature sensitivity and anisotropy on residual stresses are analyzed.

1. Rectangular and wedge type of mesh transition are compared. Rectangular type of mesh transition is found to save more time than wedge type. Comparing with C3D8, C3D20 and C3D20R element type, C3D8R element type is found to consume less computation time.
2. The increment of mesh density in longitudinal direction increase precision of results and computation time. The increment of mesh density in thickness direction is not found obvious difference.
3. Different boundary conditions of three clamping distances are simulated. The equivalent, σ_{11} and σ_{22} residual stresses along welding longitudinal and transversal path are compared. The equivalent residual stress along welding longitudinal path is found to be more stable with a small clamping distance. The simulation results of σ_{11} and σ_{22} is smaller with a small clamping distance.
4. In the analysis of hardening constitutive model, the modified Ludwik model have different simulation results of residual stresses and strains due to a small modification (a straight line is added). Hardening models identified for DP600 steel are applied in FEM welding simulation, results of equivalent residual stresses, σ_{11} , σ_{22} , ϵ_{11}^e , ϵ_{22}^e , ϵ_{11}^p , ϵ_{22}^p and $\bar{\epsilon}^p$ are compared and similar welding residual stresses and strains are obtained. A small difference of material hardening constitutive model is found to result in a big difference on simulation results. Different DP600 steel constitutive models can have similar numerical simulation results of residual stresses and strains. Martensite hardening behavior using classical Ludwik model 03 is applied in numerical simulation model and the simulation results are different from those results of models with DP600 hardening models.
5. Four temperature sensitivity models identified for DP600 steel are applied in FEM welding simulation, results of equivalent residual stresses, σ_{11} , σ_{22} , ϵ_{11}^e , ϵ_{22}^e , ϵ_{11}^p , ϵ_{22}^p and $\bar{\epsilon}^p$ are compared. The Chen, proposed and polynomial temperature sensitivity models which describe well of DP600 temperature sensitivity behavior are found to have similar simulation results of residual stresses and strains. The classical Johnson-Cook temperature sensitivity model which have some differences with the former three models at high temperature are found to higher equivalent residual stresses and equivalent residual strains. By comparing with results in the analysis of DP600 steel hardening, temperature sensitivity is found to have important influence on numerical simulation results of residual stresses and strains.
6. Models with and without considering strain rate influence on DP600 steel plastic material constitutive model are simulated and results of equivalent residual stresses, σ_{11} , σ_{22} , ϵ_{11}^e , ϵ_{22}^e , ϵ_{11}^p , ϵ_{22}^p and $\bar{\epsilon}^p$ are compared. Model with considering strain rate influence presents a peak value of residual stress and strain while model without considering strain rate influence presents a stable curve along welding longitudinal path.
7. Models considering DP600 steel plastic anisotropy are simulated and results of equivalent residual stresses and $\bar{\epsilon}^p$ are compared and found influenced by anisotropy. When the angle between rolling and welding direction is 45° , the residual

stresses around weld is found the highest. When the angle between rolling and welding direction is 90° , the residual stresses around weld is found the lowest. The material rolling orientation influence the magnitude of longitudinal and transversal residual stresses.

8. Models considering DP600 steel orthotropic elastic anisotropy are simulated and results of equivalent residual stresses and $\bar{\epsilon}^p$ are compared. Simulation results of stresses and strains are found different. For this material and laser welding conditions, considering orthotropic elastic anisotropy with microstructure orientations is found to increase residual stresses and strains of welding FEM simulation results, though not much.

Finally, specimen experiments have been realized using neutrons diffraction technique. Experimental data is compare with numerical results, a good accordance is found between neutrons diffraction observation data and FEA model simulation results.

At the end of this research work, three interesting areas may be analyzed in the future :

1. Instead of a constant value, the martensite fraction w may be defined as a function of material position, strain, temperature and strain rate. This analysis can improve the description of DP600 material constitutive model, especially corresponding to the thermo-mechanical properties simulation during solidification process.
2. Not only dependent on temperature, the elasticity may also take into account strain rate influence. The investigation of elasticity during laser welding process can improve the residual stresses prediction.
3. Mechanical response can be introduced in a future 3D CA model to better describe the laser welding process considering thermo-microstructure-mechanical properties evolution.

Based on the proposed synthesis hardening term $H(\epsilon_p) = w \cdot (\sigma_{y_m} + n_1 \epsilon_p^{n_2}) + (1 - w) \cdot \{\sigma_{y_f} + n_3 \cdot [1 - \exp(-n_4 \epsilon_p)]\}$ by using equation 2.41 and considering the variation of martensite volume fraction w , the material constitutive model is defined with the w value setting to 1 at welding area and decrease to 0.2 at the base metal.

In the figure 5.79, the magnitude of equivalent residual stresses of welding simulation considering martensite volume fraction w change is presented and compared with results of other hardening models.

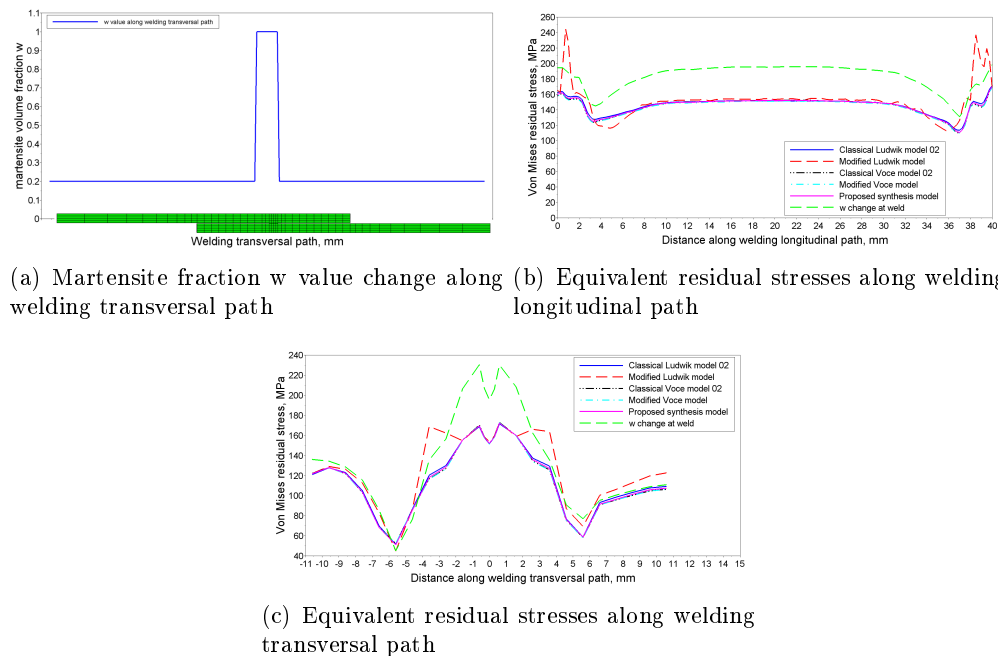


FIGURE 5.79 – The magnitude of equivalent residual stresses of welding simulation considering martensite volume fraction w change

The numerical simulation results of equivalent residual stresses of the model considering martensite fraction w change (green curves) are different with the DP600 hardening models. The results proves that using the proposed synthesis hardening term, the phase transformation influence on residual stresses can be analyzed. If martensite in the welding area increase, the final numerical results of equivalent residual stresses will also increase. But it should be noticed that the numerical results are not real because the martensite fraction w of welding area is not always 1. The martensite fraction w has variations during the laser welding process. So in the future research work, strain, temperature and strain rate should be considered to define the variation of the martensite fraction w .

Chapitre 6

Résumé détaillé - Étude numérique et expérimentale des contraintes résiduelles générées lors du soudage laser sur des plaques d'acier dual phase DP600

6.1 Introduction

Le laser Nd : YAG a d'abord été inventé par J. E. Geusic et al. dans les laboratoires de Bell dans les années 1960 [8]. Depuis lors, il est largement utilisé dans les procédés de fabrication dans l'industrie grâce à sa polyvalence et à l'utilisation de fibres optiques. Pour l'acier, le laser est devenu incontournable grâce au coefficient élevé d'absorption de chaleur pour ce type de matériau.

Pour répondre aux problèmes de crise énergétique et d'environnement, des matériaux comme les aciers de haute résistance ou haute limite d'élasticité (THR, HLE) sont utilisés dans de nombreuses industries, en particulier l'automobile, afin de réduire le poids des voitures [10]. Notre étude porte sur le soudage laser des plaques de l'acier DP 600. DP signifie que l'acier est à dual phase (martensite + ferrite) et la série 600 signifie que la résistance à la traction est supérieure à 600 MPa. C'est un acier à faible teneur en carbone avec une matrice ferritique ductile contenant une deuxième phase fragile, dont la forme se distingue principalement par des îles de martensite (3 % - 30 %) [11].

Les contraintes résiduelles sont des "contraintes internes auto équilibrantes" existant dans un corps libre sans contraintes extérieures ni contraintes sur les limites. Les contraintes résiduelles produites dans le processus de soudage au laser peuvent affecter le comportement mécanique et le comportement en corrosion des pièces soudées. L'évaluation des contraintes résiduelles est donc fondamentale pour assurer la performance d'un

produit, notamment la tenue en service (fatigue). Dans ce sens, le procédé de soudage reste encore un processus complexe : tous les effets ne sont pas encore maîtrisés.

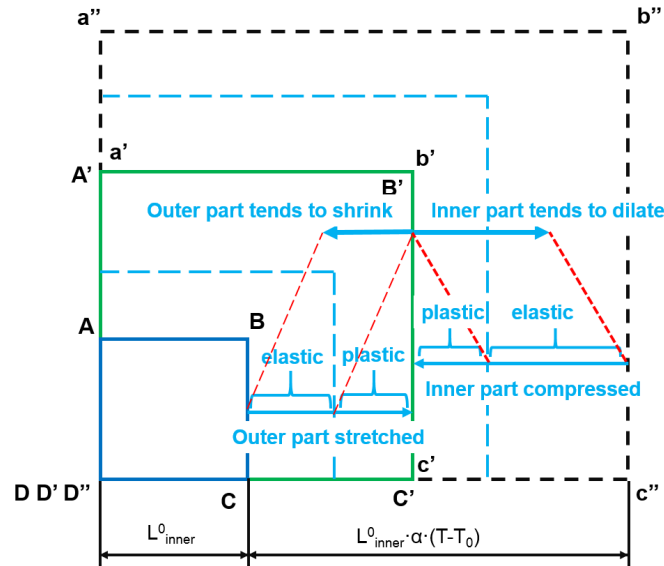


FIGURE 6.1 – Figure de l'évolution du matériau lors du processus de soudage

Pour mieux comprendre le comportement thermo-élasto-plastique de l'acier DP600, nous avons défini et identifié un modèle constitutif du matériau capable de décrire l'évolution de la contrainte équivalente pour une large plage des déformations, températures et vitesses de déformation. Le comportement plastique du DP600 dans l'analyse FEM a été déterminé par la formule ci-dessus. Pour bien prédire le comportement thermo-élasto-plastique de l'acier DP600 σ_e^{yield} , il est nécessaire d'avoir une description précise surtout par rapport aux observations expérimentales obtenues lors des essais de traction.

6.2 Chapitre 2 : Données expérimentales concernant le comportement thermo-mécanique de DP600

La valeur de la contrainte limite équivalente σ_e^{yield} a été décrite par un modèle constitutif prenant en compte le taux d'écoulement, la sensibilité à la vitesse de déformation et la sensibilité à la température. À l'aide des résultats issus des essais de traction de l'acier dual phase DP600, le comportement thermo-mécanique de DP600 a pu être identifié sur toute la plage de mesure des déformations plastiques (0 - 0.2) et surtout autour de la limite élastique du matériau en utilisant une loi définie à partir des travaux de A. GAVRUS [42, 43, 44, 45] écrité sous la forme :

$$\sigma_e^{yield} = \sigma(\varepsilon_e^p, \dot{\varepsilon}, T) = H(\varepsilon_e^p) \cdot G(\dot{\varepsilon}) \cdot F(T) \quad (6.1)$$

avec $H(\varepsilon_e^p) = w \cdot \sigma_{\text{martensite-Ludwik}} + (1 - w) \cdot \sigma_{\text{ferrite-Voce}}$ (w - fraction volumique de la martensite).

6.2.1 Écrouissage

Un essai de traction de l'échantillon de l'acier dual phase DP600 est effectué à température ambiante et à la vitesse de déformation initiale de $8.33 \times 10^{-4} \text{s}^{-1}$ le long de la direction longitudinale (0°).

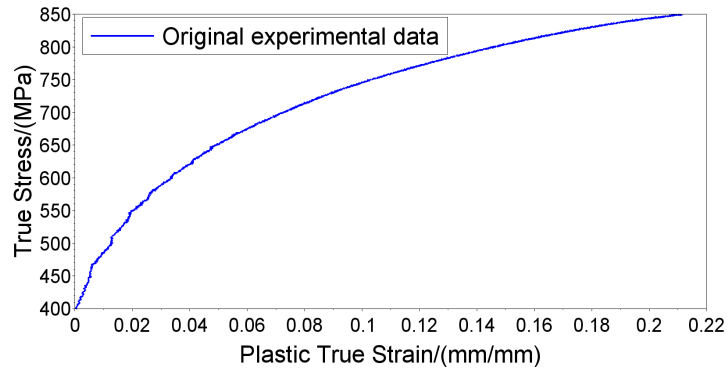


FIGURE 6.2 – La courbe plastique de l'acier dual phase DP600 à température ambiante et la vitesse de déformation initiale de $8.33 \times 10^{-4} \text{s}^{-1}$

Pour l'écrouissage du matériau, différents modèles constitutifs du matériau ont été identifiés par les équations ci-dessous présentées.

Ainsi un modèle classique de Ludwik apte à décrire l'écrouissage de la martensite avec les paramètres correspondants est défini par :

$$\sigma_e^{\text{yield}}(\varepsilon_p) = 400 + 980\varepsilon_p^{0.48} \quad (6.2)$$

Un modèle de Voce plutôt valable pour la matrice ferritique est identifié sous la forme :

$$\sigma_e^{\text{yield}}(\varepsilon_p) = 400 + 555 \cdot [1 - \exp(-15.5\varepsilon_p)] \quad (6.3)$$

Un modèle de synthèse composé du modèle de Ludwik définissant l'écrouissage de la martensite et celui de Voce définissant l'adoucissement de la ferrite a été proposé. Une formulation de type Avrami pour décrire le mélange de la phase de martensite et celle de la ferrite (via la fraction volumique de martensite $w=0.4$) est donnée par :

$$\sigma_e^{\text{yield}}(\varepsilon_p) = w \cdot (400 + 1660\varepsilon_p^{0.63}) + (1 - w) \cdot \{400 + 340 \cdot [1 - \exp(-27.5\varepsilon_p)]\} \quad (6.4)$$

Les courbes d'écrouissage correspondantes sont tracées sur la figure 6.3.

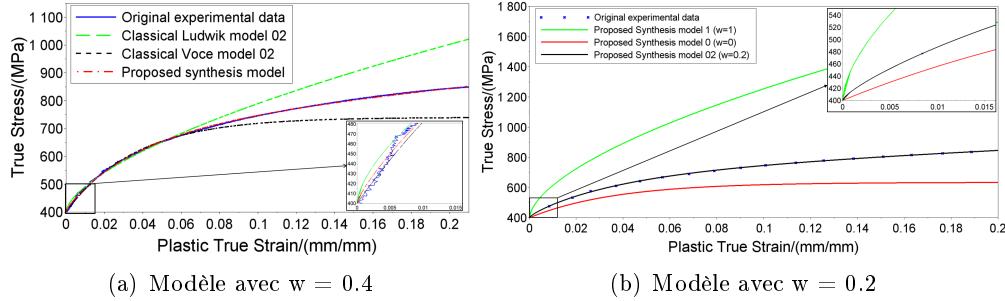


FIGURE 6.3 – Comparaison des modèles rhéologiques et des données expérimentales DP600

Par la suite, dans toutes les analyses numériques des différents modèles identifiés, nous avons utilisé un taux de martensite de $w=0.2$:

$$\sigma_e^{yield}(\varepsilon_p) = w \cdot (400 + 3411.28\varepsilon_p^{0.6014}) + (1 - w) \cdot \{400 + 234.40 \cdot [1 - \exp(-27.1092\varepsilon_p)]\}$$

6.2.2 Sensibilité à la température

Selon le travail de Aydemir et al. [58], l'influence de température sur les propriétés de DP600 est analysée de 20°C à 800°C .

Pour étudier la sensibilité à la température de l'acier DP600, nous avons utilisé différents modèles issus de la littérature : Johnson-Cook, Khan et Chen. [57].

Le modèle de sensibilité Johnson-Cook [39] a été identifié sous la forme :

$$F(T) = 1 - T^{*1.5} \quad (6.5)$$

Le modèle de sensibilité Khan [50] est écrit comme suit :

$$F(T) = \left(\frac{T_m - T}{T_m - T_r} \right)^{0.5} \quad (6.6)$$

La sensibilité à la température du modèle Chen [51] est donnée par :

$$F(T) = \exp(4.23 \cdot T^{*-51.61}) \quad (6.7)$$

Dans notre travail, un modèle a été proposé pour décrire la sensibilité à la température, identifié sous la forme suivante :

$$F(T) = (1 - 0.491 \cdot T^{*4.212})^{103.17} \quad (6.8)$$

Les courbes de sensibilité à la température correspondantes sont tracées sur la figure 6.4.

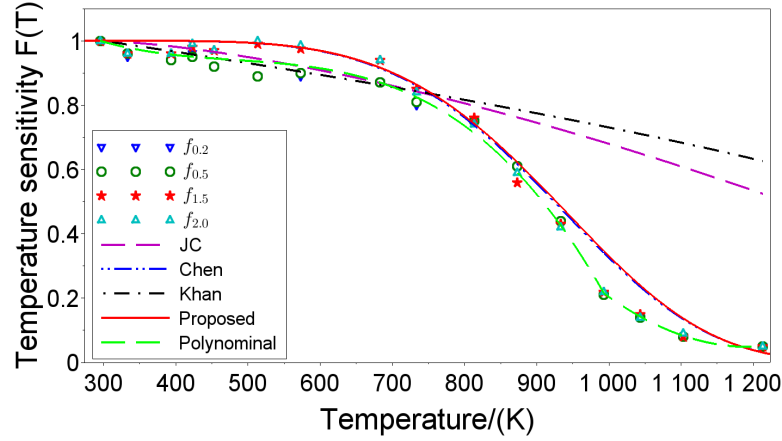


FIGURE 6.4 – Dépendance à la température des données expérimentales et des modèles de simulation

6.2.3 Sensibilité à la vitesse de déformation

La sensibilité à la vitesse de déformation à haute températures a été étudiée en partant des données de la littérature de S. Curtze et al. [3].

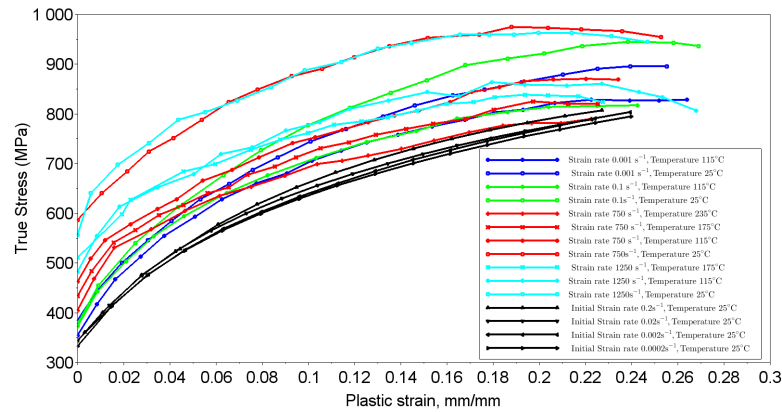


FIGURE 6.5 – Les courbes plastique de l'acier dual phase DP600 à température différentes et la vitesse de déformation différentes

Pour mettre en évidence la sensibilité à la vitesse de déformation, nous nous sommes basés sur les travaux proposés par A. Gavrus [43, 42, 44, 45] et pour l'acier dual-phase DP600 la fonction de sensibilité à la vitesse de déformation identifiée est donnée par l'équation suivante :

$$G(\dot{\epsilon}) = 0.8042232 \times \left[1 + Ash \left(\frac{1}{2} (\dot{\epsilon}/96.077)^{0.0005410 \times T - 0.1443611} \right) \right] \quad (6.9)$$

6.2.4 L'anisotropie planaire définie par la théorie de Hill

Afin de pouvoir décrire l'anisotropie plastique plane observée pour les plaques laminées de l'acier DP600, les coefficients de Lankford et les paramètres de Hill sont présentés dans le tableau 6.1.

TABLE 6.1 – Les coefficients de Lankford et les paramètres de Hill de l'acier DP600

r_0	r_{45}	r_{90}	R_{11}	R_{22}	R_{33}	R_{12}
1.0123	0.6487	0.9160	1	0.9748	0.9777	1.1172
F	G	H	N			
0.5492	0.4969	0.5031	1.2017			

Les deux surfaces de charge prédites par le modèle de Hill48 et le critère Von Mises de la plaque dual phase DP600 sont représentées sur figure 6.6.

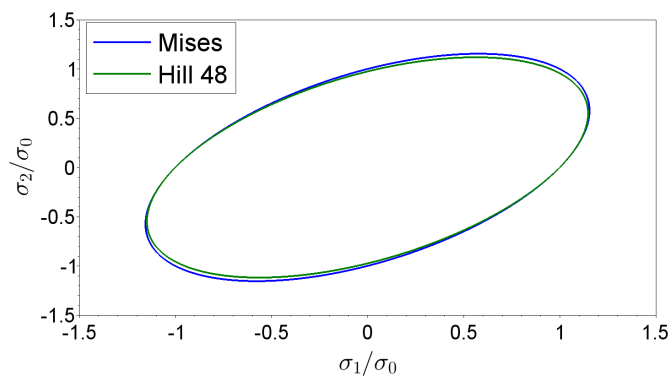


FIGURE 6.6 – Surface de fluage prédite par le modèle anisotropique Hill48 et le critère Von Mises

6.2.5 Analyse de l'anisotropie orthotrope élastique à l'aide de l'automate cellulaire

L'analyse de l'anisotropie élastique orthotrope (figure ci-dessous) a été réalisée à l'aide des résultats numériques du modèle 2D l'automate cellulaire mise en œuvre et réalisé dans ce travail de thèse.

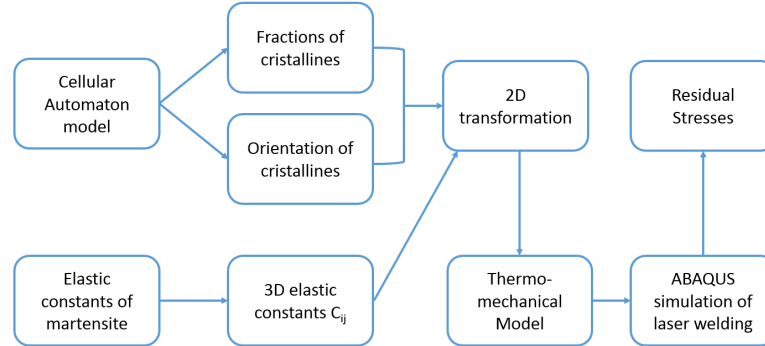


FIGURE 6.7 – The flowchart of CA-FE model used to simulate residual stresses

La zone soudée est censée être constituée principalement par de la martensite. Aussi, grâce au modèle CA, l'orientation des grains de la martensite a été simulée. De ce fait, nous avons tenu compte des nouvelles valeurs liées à la martensite avec prise en compte de l'orientation obtenue par solidification après la phase de mise en fusion : l'élasticité orthotrope en est modifiée. Les tableaux ci-dessous donnent les valeurs des constantes élastiques avec et sans prise en compte des orientations des grains de dendrite martensitique. 6.2 6.3.

TABLE 6.2 – Constantes élastiques du matériau de soudure

$T/^\circ C$	E_1	E_2	E_3	ν_{12}	ν_{13}	ν_{23}	G_{12}	G_{13}	G_{23}
0	203.40	203.07	202.72	0.2943	0.2902	0.2942	79.06	78.72	78.85
300	184.03	183.73	183.42	0.3101	0.3057	0.3100	71.53	71.22	71.34
600	116.23	116.04	115.84	0.3258	0.3213	0.3258	45.18	44.98	45.06
800	29.06	29.01	28.96	0.3469	0.3420	0.3468	11.29	11.25	11.26

TABLE 6.3 – Constantes élastiques du matériau de soudure avec des orientations CA

$T/^\circ C$	E_1	E_2	E_3	ν_{12}	ν_{13}	ν_{23}	G_{12}	G_{13}	G_{23}
0	203.78	203.70	202.72	0.2924	0.2924	0.2935	78.93	78.85	78.55
300	184.37	183.30	183.42	0.3080	0.3081	0.3092	71.42	71.34	71.07
600	116.45	116.40	115.84	0.3237	0.3237	0.3249	45.10	45.05	44.88
800	29.11	29.10	28.96	0.3446	0.3446	0.3459	11.28	11.26	11.22

6.3 Chapitre 3 : Modèle d'automate cellulaire

Pour simuler en général la croissance des grains de dendrite, un modèle 2D d'automate cellulaire (CA) a été développé en particulier en ce qui concerne la phase martensitique obtenue à partir du processus de solidification de l'acier dual phase DP600. Les résultats sont présentés dans chapitre 3.

Un modèle numérique 2D a été construit et programmé. Le champ de température du modèle CA est importé à partir d'un modèle d'analyse par éléments finis. La fonction d'analyse de la nucléation, de la fraction solide, de la concentration à l'interface solide/liquide, de l'anisotropie, de la tension superficielle, de la diffusion, de la vitesse de croissance à l'interface S/L a été étudiée. Les équations de conservation sont présentées en détail selon la séquence de la figure 6.8.

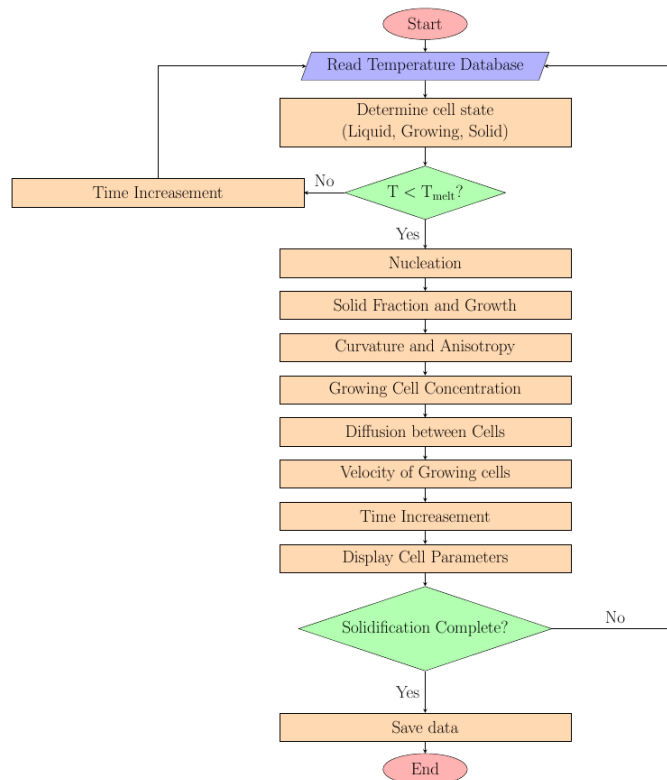


FIGURE 6.8 – Ordinoigramme du modèle d'évolution de la microstructure

Les résultats obtenus ont montré que le modèle est capable de simuler les microstructures développées lors d'un processus de solidification posteriori à une phase de mise en fusion spécifique au soudage laser. Sur la base du même modèle CA décrit ci-dessus et en utilisant différentes conditions initiales, différents résultats de microstructure ont été obtenus. Les résultats de la figure 6.9 issus de la simulation du modèle CA montrent une structure équiaxe ainsi que la croissance des grains de dendrite sous forme de colonnes.

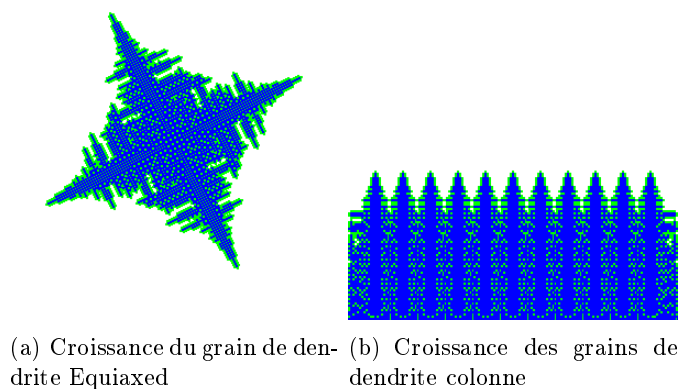


FIGURE 6.9 – Simulations numériques de la microstructure par modèle CA

Le modèle simulant les microstructures de soudage a été ainsi validé. Les comparaisons entre les résultats de simulation et les observations optiques expérimentales réalisées sur la section transversale de la soudure et la surface supérieure montrent de bonnes concordances comme le montre la figure 6.10 pour

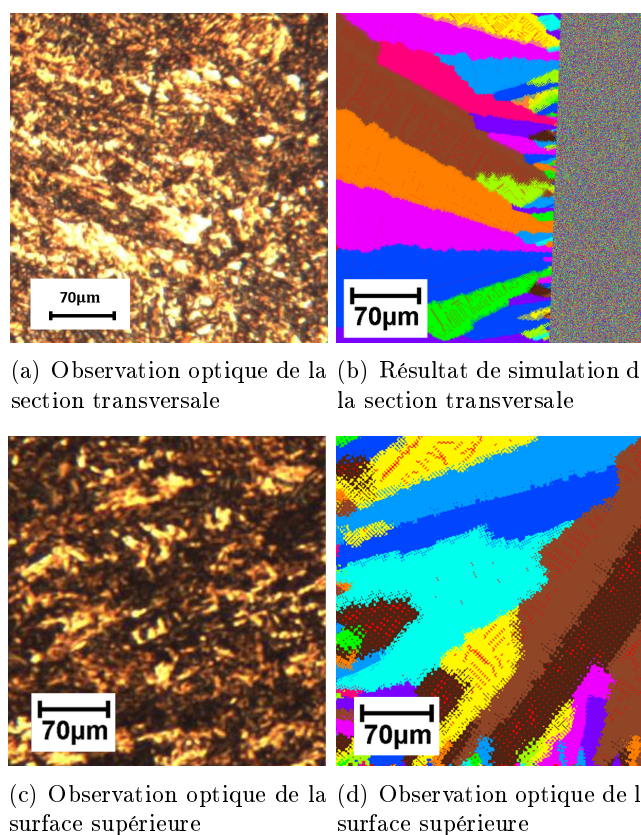


FIGURE 6.10 – Microstructure de FZ et HAZ de la section de soudure DP600 et de la surface supérieure

6.4 Chapitre 4 et 5 : ABAQUS/FEM modèles, résultats de simulation et résultats expérimentaux

6.4.1 Informations sur le modèle

Sur le plan mécanique et sur la base du comportement thermo-mécanique du matériau, le modèle FEM a été construit en deux parties :

1. Partie d'analyse thermique
 - La source de chaleur, le transfert de chaleur, le rayonnement et la convection ont été pris en compte pour analyser des données thermiques du modèle
 - Les données thermiques, calculées, ont été utilisées et implémentées pour définir le comportement mécanique.
2. Partie d'analyse mécanique
 - Pour calculer les contraintes résiduelles, nous avons tenu compte des propriétés du matériau dépendantes et indépendantes de la température comme l'expansion par exemple, le module élastique et ceux de la plasticité. A partir de cette étude, les contraintes résiduelles ont été calculées à partir de la réponse élasto-plastique du matériau et de la relaxation du matériau lors du refroidissement.

La construction du modèle a été réalisée sur le logiciel ABAQUS en plusieurs sections :

1. Propriétés du matériau de base. Ces propriétés ont été utilisées dans toutes les analyses de simulation.
2. Différents modèles ont été testés avec différentes géométries et types de maillage. Cette partie présente les paramètres de géométrie et les informations de maillage utilisées pour le modèle de simulation de soudage.
3. Par ailleurs, les paramètres importants du modèle constitutif du matériau ont été intégrés dans les modèles : l'érouissage, la sensibilité à la température, la sensibilité à la vitesse de déformation, l'anisotropie élastique et plastique. Les résultats de ces différents modèles sont présentés en détail dans le manuscrit. Les résultats nous ont permis de mettre en exergue l'influence prépondérante ou pas de ces effets.

6.4.2 Résultats de simulation des modèles de soudage numérique

6.4.2.1 Erouissage

Les effets associés à l'influence de l'érouissage sont présentés sur la figure 6.11.

Le modèle modifié de Ludwik montrent des différences dans les valeurs des contraintes résiduelles équivalentes (le modèle constitutif de l'érouissage a une petite modification :

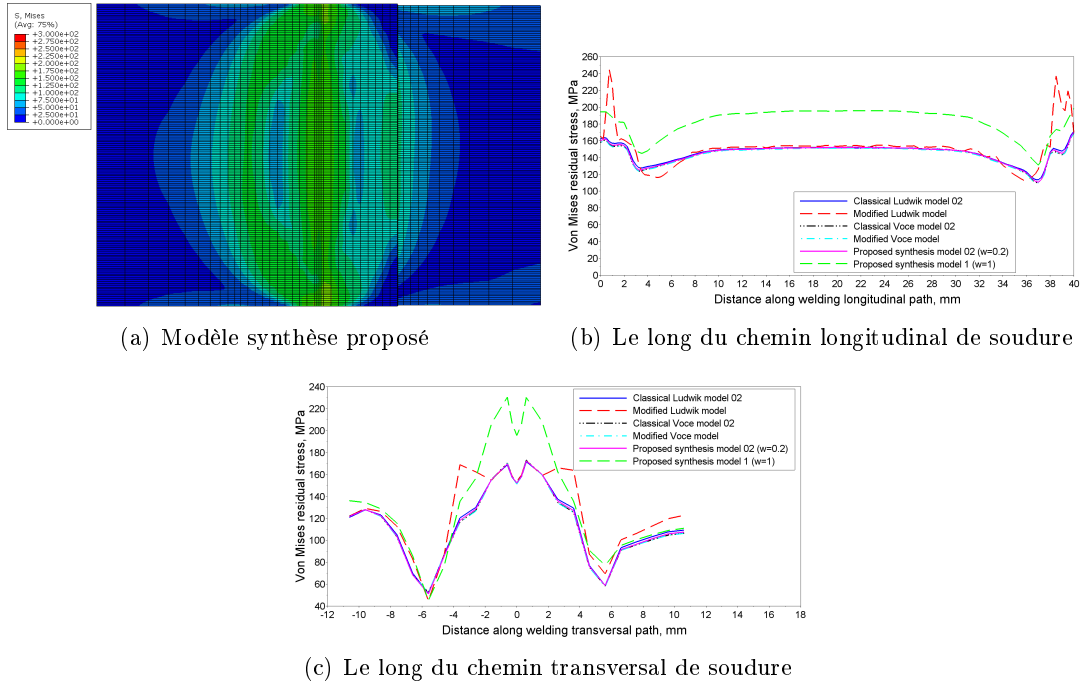
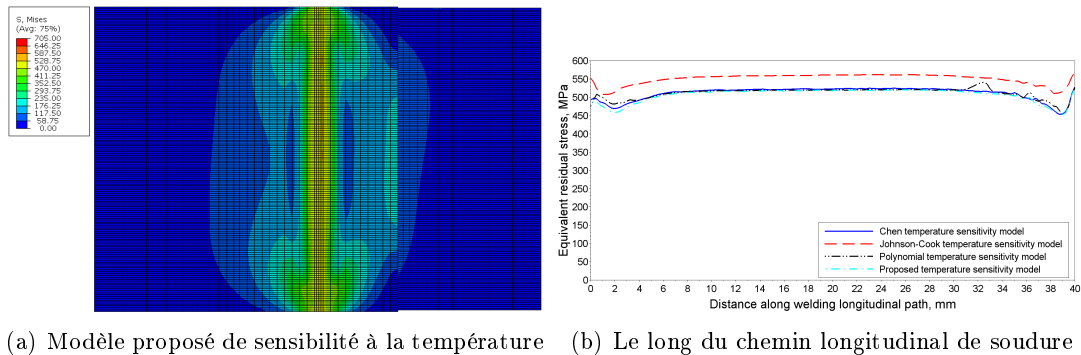


FIGURE 6.11 – La répartition des contraintes résiduelles équivalent de simulation de soudage avec 5 modèles de écrouissage différents

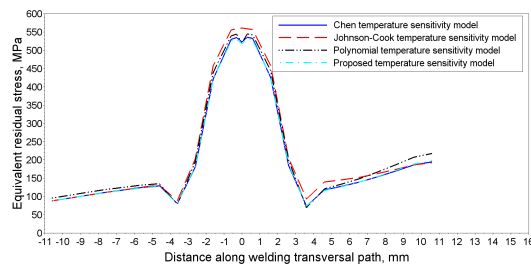
une ligne droite est ajoutée). La différence prouve qu'un petit changement dans le modèle constitutif du matériau peut entraîner une grande différence sur les contraintes résiduelles. En contrepartie, les 4 autres modèles d'écrouissage utilisés présentent presque les mêmes résultats que ceux issus de la simulation des contraintes résiduelles équivalentes. Cela indique que différents modèles constitutifs du matériau reproductible du comportement réel observé lors des essais de traction, présentent les mêmes influences sur la simulation des contraintes résiduelles équivalentes, surtout si aucun prise en compte de la variation de la fraction volumique de la martensite lors de la solidification.

6.4.2.2 Sensibilité à la température

Par la suite, nous avons étudié la sensibilité de la température. Différents modèles constitutifs sont appliqués dans la simulation éléments finis de soudage laser. Les résultats sont présentés sur figure 6.12.



(a) Modèle proposé de sensibilité à la température (b) Le long du chemin longitudinal de soudure



(c) Le long du chemin transversal de soudure

FIGURE 6.12 – La répartition des contraintes résiduelles équivalent des modèles de simulation de soudage avec 4 termes de sensibilité à la température différents

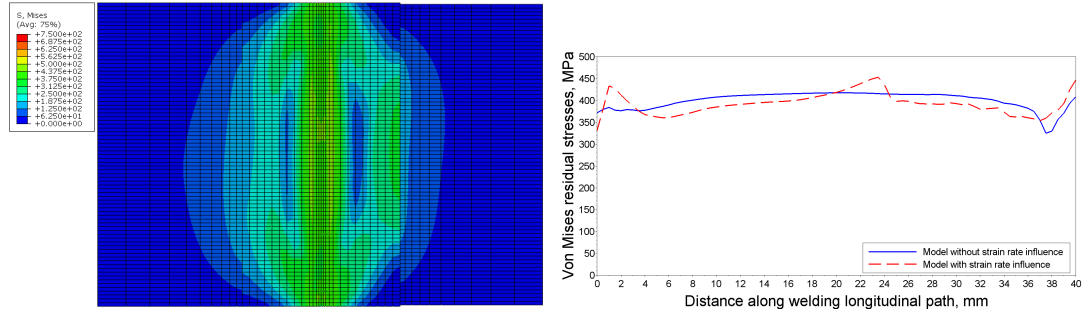
En comparaison avec les résultats correspondants à l'effet d'écoulement, on trouve une grande différence. Cela confirme que la température a une influence importante sur les contraintes résiduelles équivalentes.

Les modèles de Chen, proposé et celui polynomial décrivent bien le comportement à la sensibilité à la température DP600 et se révèlent avoir des résultats de simulation similaires. Les résultats issus du modèle classique de Johnson-Cook définissant également la sensibilité à la température montrent des différences significatives en comparaison avec les trois premiers modèles. Cette différence est surtout visible à haute température et les valeurs des contraintes résiduelles équivalentes sont plus élevées.

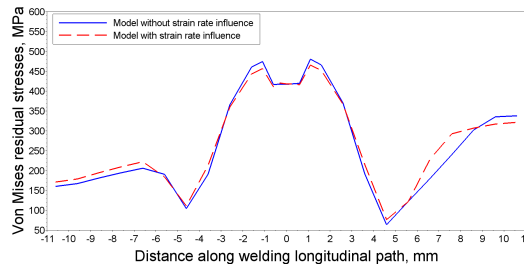
6.4.2.3 Sensibilité à la vitesse de déformation

Pour définir la sensibilité à la vitesse de déformation nous avons également utilisés plusieurs modèles constitutifs. Les résultats sont présentés sur la figure 6.13.

Les résultats ont montré une nette influence sur la valeur maximale des contraintes résiduelles lorsque nous prenons en compte l'influence de la vitesse de déformation à travers la lois utilisée. Dans le cas contraire, les résultats montrent des valeurs de contraintes résiduelles plus faibles et constantes tout au long de la zone de soudage.



(a) Modèle avec influence de la vitesse de déformation (b) Le long du chemin longitudinal de soudure

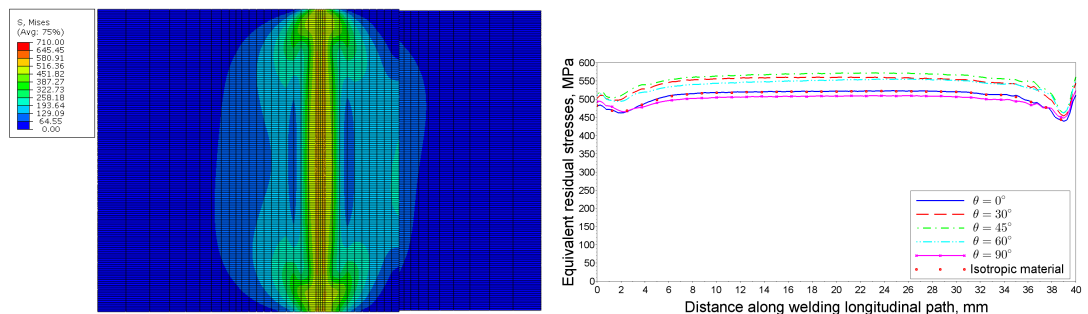


(c) Le long du chemin transversal de soudure

FIGURE 6.13 – La répartition des contraintes résiduelles équivalent des modèles de simulation de soudage avec et sans influence de la vitesse de contrainte

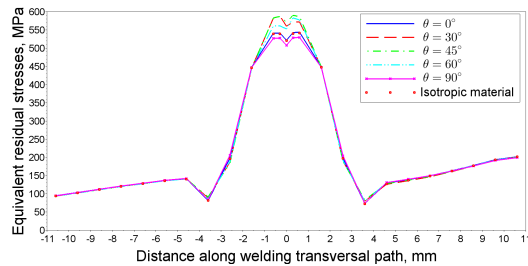
6.4.2.4 L'anisotropie plastique

Concernant l'anisotropie plastique, les modèles utilisés nous ont permis de prendre en compte les différentes orientations des plaques dont la référence est la direction du laminage. Les résultats sont présentés sur la figure 6.14.



(a) $\theta = 0^\circ$

(b) Le long du chemin longitudinal de soudure



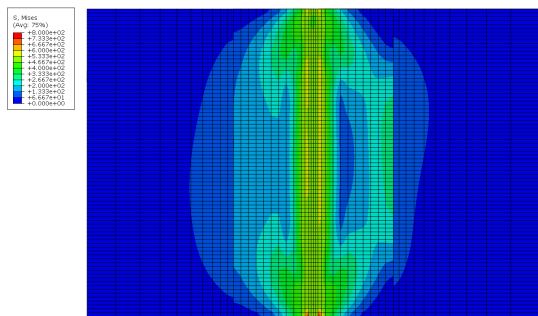
(c) Le long du chemin transversal de soudure

FIGURE 6.14 – La répartition des contraintes résiduelles équivalentes des modèles de simulation de soudage avec une anisotropie matérielle de $\theta = 0^\circ, 30^\circ, 45^\circ, 60^\circ, 90^\circ$ et matériel isotrope

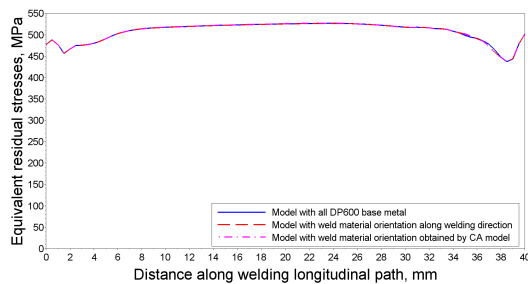
Lorsque l’angle entre la direction de laminage et de soudure est 45° , les contraintes résiduelles autour de la soudure sont les plus élevées. Lorsque l’angle est 90° , les contraintes résiduelles autour de la soudure sont les plus faibles. Ces résultats montrent l’importance de l’orientation du matériau de base par rapport à la direction de soudage. Les résultats ont montré une répartition différente des contraintes résiduelles.

6.4.2.5 L’anisotropie élastique

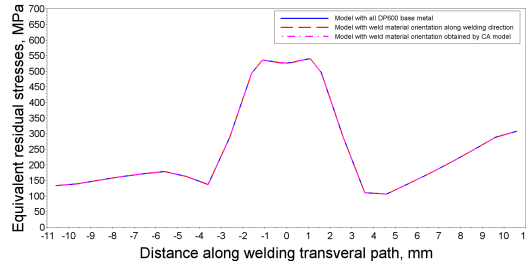
Du point de vue de l’anisotropie élastique, nous avons introduits l’orientation des grains dont les résultats sont issus du modèle CA et implémentés dans Abaqus. Les résultats sont présentés sur la figure 6.15.



(a) Modèle avec orientation du matériau de soudure obtenu par le modèle CA



(b) Le long du chemin longitudinal de soudure



(c) Le long du chemin transversal de soudure

FIGURE 6.15 – La répartition des contraintes résiduelles équivalentes des modèles de simulation de soudage avec tous les métaux de base DP600 et avec des orientations de matériau de soudure le long de la direction de soudage et obtenues par le modèle CA

Pour différentes orientations, on trouve des résultats de contraintes résiduelles similaires. Les valeurs des contraintes sont différentes et confirment que l’anisotropie élastique orthotropique prise en compte à travers la notion d’orientation de la micro-structure augmente légèrement les contraintes résiduelles. Ce résultat est cohérent car dans la zone de soudure le matériau est très peu texturé.

6.4.2.6 Validation du modèle numérique

Expérimentalement, les contraintes résiduelles de σ_{11} et σ_{22} ont été calculées à partir des déformations mesurées par la méthode de diffraction de neutrons. La comparaison des résultats expérimentaux et ceux issus de la simulation, notamment du modèle tenant compte à la fois de l’écrouissage, de la sensibilité à la température et de l’anisotropie plastique (cette trois effets couplés influencent de façon importante les résultats finaux) ont montré une bonne concordance.

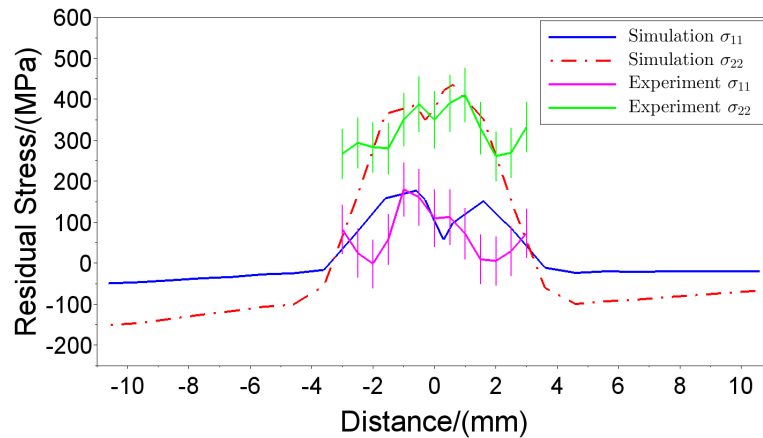


FIGURE 6.16 – Comparaison entre les contraintes résiduelles expérimentales et numériques

6.5 Conclusion

Ainsi l'ensemble de ce travail a été réalisé en plusieurs étapes, en utilisant deux modèles numériques de simulations : modèle CA et FEM. Le couplage de ces deux méthodes nous ont permis d'arriver aux conclusions suivantes :

Le modèle constitutif thermo-mécanique du matériau de DP600 a été analysé sur la base des tests de traction expérimentaux. Le modèle constitutif doit prendre en compte un terme d'écrouissage, la sensibilité à la vitesse de déformation, la sensibilité à la température et l'anisotropie plastique et orthotropique élastique de l'acier dual-phase DP600.

Une méthode de l'automate cellulaire (CA) a été programmée et mise en œuvre sous forme d'un modèle numérique 2D. Cette étape nous a permis de simuler l'évolution de la microstructure lors solidification suivant le procédé de soudage laser étudié. Le champ de température programmé dans le modèle CA est importé à partir d'un modèle d'analyse d'éléments finis. Les différents phénomènes apparaissant lors de la solidification comme la nucléation, la fraction solide, la concentration à l'interface solide/liquide, l'anisotropie de la tension de surface, la diffusion, la vitesse de croissance à l'interface solide/liquide ainsi que des équations de conservation ont été étudié et pris en compte. Les résultats du modèle CA ont été comparés aux résultats expérimentaux et nous avons pu montrer une bonne convergence des résultats.

La méthode de simulation par Eléments Finis (FEM), nous a permis de comprendre le comportement thermo-mécanique du matériau étudié. La simulation du procédé de soudage laser ainsi que les lois constitutives du matériaux ont été implémentées. D'un point de vue simulation, les effets du type d'élément, de la densité du maillage et les conditions aux limites ont été testés et consolidés. De la même façon le modèle constitutif temro-élasto-plastique du matériau prenant en compte l'écrouissage, la sensibilité à la température et la sensibilité à la vitesse de déformation sur les résultats de simulation des contraintes résiduelles ont été pris en compte et analysés. Le couplage des deux modèles CA-FE nous a permis aussi d'analyser les effets d'anisotropie élastique orthotropes du matériau soudé sur les l'évolution des contraintes résiduelles. Plusieurs conclusions importantes sont synthétisées ici :

1. L'écrouissage : les résultats ont montré une influence marquée de l'écrouissage sur les valeurs des contraintes résiduelles.
2. L'étude de la sensibilité à la température a également montré une influence importante sur les contraintes résiduelles et déformation.
3. La vitesse de la déformation présente une valeur maximale des contraintes résiduelles et de la déformation tandis que les modèles ne prenant pas en compte l'influence de la vitesse de la déformation présente des contraintes résiduelles de plus faible valeurs aux bord de la zone de soudage et une courbe plutôt stable tout au long de la zone de soudage.
4. L'étude de l'angle entre la direction de laminage et la direction de soudure a mis également en évidence l'importance de l'orientation de la tôle. Lorsque l'angle

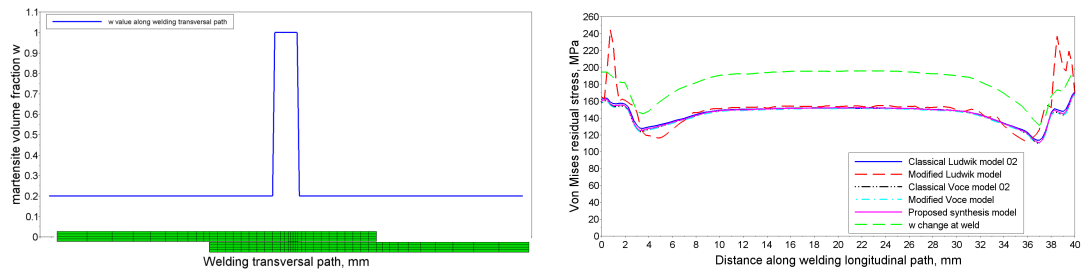
est de 45° , les contraintes résiduelles autour de la soudure sont les plus élevées. Lorsque l'angle entre le sens de roulement et de soudure est de 90° , les contraintes résiduelles autour de la soudure sont les plus faibles. L'orientation du laminage du matériau influe le niveaux des contraintes résiduelles aussi bien les contraintes résiduelles longitudinales que transversales.

5. L'anisotropie élastique orthotropique qui prend en compte l'orientation des grains dont la fraction volumique, obtenue grâce au modèle numérique 2D CA, a peu d'influence sur les contraintes résiduelles. Ce résultat était attendu car la zone soudée est très peu texturée.
6. Enfin, les résultats expérimentaux et ceux obtenus par le couplage des deux modèles CA/FEM ont montré de bonnes convergences et permet de confirmer la robustesse générale du modèle numérique de simulation du procédé de soudage laser.

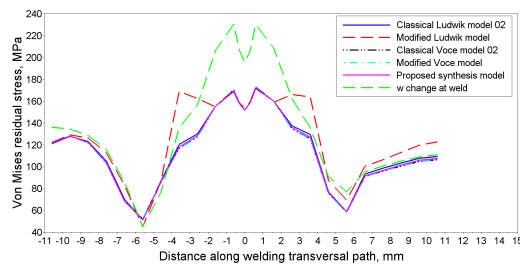
À la fin de ce travail de recherche, trois domaines intéressants peuvent être analysés à l'avenir :

- Au lieu d'une valeur constante, la fraction de martensite w peut être définie en fonction de la position du matériau, de la déformation, de la température et de la vitesse de déformation.
- L'élasticité peut prendre en compte l'influence de la température et de la vitesse de déformation.
- Une réponse mécanique peut être introduite dans un futur modèle CA 3D pour mieux décrire le processus de soudage laser en considérant l'évolution des propriétés thermo-microstructure-mécanique.

Sur la base du terme d'écrouissage de la loi de synthèse proposée $H(\varepsilon_p) = w \cdot (\sigma_{y_m} + n_1 \varepsilon_p^{n_2}) + (1 - w) \cdot \{\sigma_{y_f} + n_3 \cdot [1 - \exp(-n_4 \varepsilon_p)]\}$ partant d'un modèle constitutif général (équation 1.89 et 1.90) une variation du taux de martensite peut être prise en compte par exemple avec une valeur w de 1 à dans la zone de soudage et diminue à 0.2 au niveau du métal de base. Les contraintes résiduelles équivalentes sont présenté dans la figure 6.17.



(a) Changement de fraction de la martensite w le long du chemin transversal de soudure (b) Contraintes résiduelles équivalentes le long du chemin longitudinal de soudure



(c) Contraintes résiduelles équivalentes le long du chemin transversal de soudure

FIGURE 6.17 – Les contraintes résiduelles équivalentes de la simulation de soudage en tenant compte de la changement de fraction de martensite volumique

Les résultats prouvent que, en utilisant le terme d'écrouissage de la synthèse proposée, l'influence de la transformation de phase sur les contraintes résiduelles peut être analysée. Si la martensite dans la zone de soudure augmente, les résultats numériques finaux des contraintes résiduelles équivalentes augmenteront également.

Dans des futurs travaux de recherche il sera étudié la définition d'un taux de martensite variable en fonction des conditions de déformations, température et vitesse de déformation lors de l'étape de solidification après la mise en fusion lors d'un soudage laser.

Annexe A

List of Publications

Peer-reviewed international journals

[1] Liu S, Kouadri-Henni A, Gavrus A. Numerical simulation and experimental investigation on the residual stresses in a laser beam welded DP600 dual phase steel plate : thermo-mechanical material plasticity model, *International journal of Mechanical Sciences*, 122 (2017) 235 – 243

[2] Liu S, Kouadri-Henni A, Gavrus A. DP600 dual phase steel thermo-elasto-plastic constitutive model considering strain rate and temperature influence on FEM residual stress analysis of laser welding, *Journal of Manufacturing Processes* (reviewing).

[3]* Liu S, Kouadri-Henni A, Gavrus A. Modeling grain orientation of DP600 steel by Nd :YAG laser welding, *MATEC Web of Conferences*. EDP Sciences, 2016, 80 : 02010. NUMIFORM-2016.

Conference proceedings and scientific activities

[1] Liu S, Kouadri-Henni. Numerical simulation on the residual stress of Nd :YAG laser welding DP600, *Simulation Numérique du soudages de AFM 2016*.

[2] Liu S, Gavrus A, Kouadri-Henni A. Numerical and experimental research of residual stresses influenced by anisotropy on laser welding. *Journée Manufacturing21*, 16-18 Nov. 2016.

[3] Liu S, Kouadri-Henni. Gavrus A. Modeling Grain Orientation of LaserWelding DP600for Residual Stresses. *Journée doctorale de INSA Rennes*. 12 Jan. 2016.

[4] Liu S, Gavrus A, Kouadri-Henni A. Microstructure simulation of DP600 by laser welding. *Café scientifique de INSA Rennes*. 25 Feb. 2016.

[5] Liu S, Gavrus A, Kouadri-Henni A. Finite element method coupled with a numerical cellular automaton model used to simulate the residual stresses of dual phase DP600 steel Nd :YAG laser welding. *Congrès Français Mécanique 2017* (reviewing).

Bibliographie

- [1] ArcelorMittal. Very high strength steels : dual phase steels. Retrieved from catalogue produit édition européenne, 2008.
- [2] Alain Lodini M.E. Fitzpatrick. Analysis of Residual Stress by Diffraction using Neutron and Synchrotron Radiation. CRC Press, 2003.
- [3] S. Curtze, V.-T. Kuokkala, M. Hokka, and P. Peura. Deformation behavior of TRIP and DP steels in tension at different temperatures over a wide range of strain rates. *Materials Science and Engineering A*, 507 :124–131, 2009.
- [4] Ph Thevoz, JL Desbiolles, and M Rappaz. Modeling of equiaxed microstructure formation in casting. *Metallurgical Transactions A*, 20(2) :311–322, 1989.
- [5] Theodore H Maiman. Stimulated optical radiation in ruby. 1960.
- [6] Robert N Hall, Gunther E Fenner, JD Kingsley, TJ Soltys, and RO Carlson. Coherent light emission from GaAs junctions. *Physical Review Letters*, 9(9) :366, 1962.
- [7] Marshall I Nathan, William P Dumke, Gerald Burns, Frederick H Dill Jr, and Gordon Lasher. Stimulated emission of radiation from GaAs p-n junctions. *Applied Physics Letters*, 1(3) :62–64, 1962.
- [8] JE Geusic, HM Marcos, and LeGrand Van Uitert. Laser oscillations in nd-doped yttrium aluminum, yttrium gallium and gadolinium garnets. *Applied Physics Letters*, 4(10) :182–184, 1964.
- [9] Seiji Katayama. Handbook of laser welding technologies. Elsevier, 2013.
- [10] Geoffrey Davies. Materials for automobile bodies. Elsevier, Butterworth-Heinemann, 2012.
- [11] Marion Calcagnotto, Yoshitaka Adachi, Dirk Ponge, and Dierk Raabe. Deformation and fracture mechanisms in fine-and ultrafine-grained ferrite/martensite dual-phase steels and the effect of aging. *Acta Materialia*, 59(2) :658–670, 2011.
- [12] DL Chen, ZG Wang, XX Jiang, SH Ai, and CH Shih. The dependence of near-threshold fatigue crack growth on microstructure and environment in dual-phase steels. *Mater. Sci. Eng., A*, 108 :141–151, 1989.
- [13] Shuang Kuang, Yong-lin Kang, Hao Yu, and Ren-dong Liu. Effect of continuous annealing parameters on the mechanical properties and microstructures of a cold rolled dual phase steel. *Int J. Miner. Metall. Mater.*, 16(2) :159–164, 2009.

- [14] JR Fekete and AM Stibich. A comparison of the response of hsla and dual phase sheet in dynamic crush. *IBEC*, 01 :3101, 2001.
- [15] Olivier Bouaziz, Hatem Zurob, and Mingxin Huang. Driving force and logic of development of advanced high strength steels for automotive applications. *Steel Res. Int.*, 84(10) :937–947, 2013.
- [16] Milan TURÁĀGA, Jozef ONDRUÁĀKA, and Petr NESVADBA. Solid state welding of DP600 to austenitic CrNi steel. *METAL*, 2010.
- [17] GCC Correard, GP Miranda, and MSF Lima. Development of laser beam welding of advanced high-strength steels. *The International Journal of Advanced Manufacturing Technology*, 83(9-12) :1967–1977, 2016.
- [18] Yanli Song, Lin Hua, Dongning Chu, and Jian Lan. Characterization of the inhomogeneous constitutive properties of laser welding beams by the micro-vickers hardness test and the rule of mixture. *Materials and Design*, 37 :19–27, 2012.
- [19] M. Hazratinezhad, N. B. Mostafa Arab, A. R. Sufizadeh, and M. J. Torkamany. Mechanical and metallurgical properties of pulsed neodymium-doped yttrium aluminum garnet laser welding of dual phase steels. *Materials and Design*, 33 :83–87, 2012.
- [20] N. Farabi, D. L. Chen, and Y. Zhou. Fatigue properties of laser welded dual-phase steel joints. *Procedia Engineering*, 2(1) :835–843, 2010.
- [21] N. Farabi, D. L. Chen, J. Li, Y. Zhou, and S. J. Dong. Microstructure and mechanical properties of laser welded DP600 steel joints. *Materials Science and Engineering : A*, 527(4 5) :1215–1222, February 2010.
- [22] N. Farabi, D. L. Chen, and Y. Zhou. Microstructure and mechanical properties of laser welded dissimilar DP600/DP980 dual-phase steel joints. *Journal of Alloys and Compounds*, 509(3) :982–989, January 2011.
- [23] C. Dharmendra, K.P. Rao, J. Wilden, and S. Reich. Study on laser welding-brazing of zinc coated steel to aluminum alloy with a zinc based filler. *Materials Science and Engineering : A*, 528(3) :1497–1503, 2011.
- [24] Mingsheng Xia, Elliot Biro, Zhiling Tian, and Y. Norman Zhou. Effects of heat input and martensite on HAZ softening in laser welding of dual phase steels. *ISIJ International*, 48(6) :809–814, 2008.
- [25] X. Li, S. Lawson, Y. Zhou, and F. Goodwin. Novel technique for laser lap welding of zinc coated sheet steels. *Journal of Laser Applications*, 19(4) :259–264, 2007.
- [26] H. Tresca. *Comptes Rendus Acad. Sci. Paris*, 59, 1864.
- [27] H. Tresca. *Comptes Rendus Acad. Sci. Paris*, 64, 1867.
- [28] R Von Mises. *Göttinger nachrichten. math.-phys*, 1913.
- [29] R. Hill. A variational principle of maximum plastic work in classical plasticity. *The Quarterly Journal of Mechanics and Applied Mathematics*, 1(1) :18–28, 1948.
- [30] R Hill. A theory of the yielding and plastic flow of anisotropic metals. *Proceedings of the Royal Society of London*, 193(1033) :281–297, 1948.

- [31] L. Bourne and R. Hill. LX. On the correlation of the directional properties of boiled shee in tension and cupping tests. *The London, Edinburgh, and Dublin Philosophical Magazine and Journal of Science*, 41(318) :671–681, July 1950.
- [32] R. Hill. Theoretical plasticity of textured aggregates. In *Mathematical Proceedings of the Cambridge Philosophical Society*, volume 85, pages 179–191. Cambridge Univ Press, 1979.
- [33] R. Hill. Constitutive modelling of orthotropic plasticity in sheet metals. *Journal of the Mechanics and Physics of Solids*, 38(3) :405–417, 1990.
- [34] Zheng Lin. *Cailiao Tanxing Changshu Zhi Xintan (The new development of elastic constants)*. Kexue Chuban She (Science Press), 2011.
- [35] H Hibbitt, B Karlsson, and P Sorensen. *Abaqus analysis user's manual version 6.10*. Dassault Systèmes Simulia Corp. : Providence, RI, USA, 2011.
- [36] Surajit Kumar Paul. Predicting the flow behavior of metals under different strain rate and temperature through phenomenological modeling. *Computational Materials Science*, 65 :91–99, 2012.
- [37] Frank J. Zerilli and Ronald W. Armstrong. Dislocation-mechanics-based constitutive relations for material dynamics calculations. *Journal of Applied Physics*, 61(5) :1816–, 1987.
- [38] G. Rr Cowper and Paul Southworth Symonds. Strain-hardening and strain-rate effects in the impact loading of cantilever beams. *DTIC Document*, pages –, 1957.
- [39] Gordon R John and William H Cook. A constitutive model and data for metals subjected to large strains, high strain rates and high temperatures. *Proceedings of the 7th International Symposium on Ballistics*, 21 :541–547, 1983.
- [40] Han Zhao. A constitutive model for metals over a large range of strain rates identification for mild-steel and aluminium sheets. *Materials Science and Engineering : A*, 230(1-2) :95–99, 1997.
- [41] Akhtar S Khan and Riqiang Liang. Behaviors of three bcc metal over a wide range of strain rates and temperatures : experiments and modeling. *International Journal of Plasticity*, 15(10) :1089–1109, 1999.
- [42] A Gavras. Formulation of a new constitutive equation available simultaneously for static and dynamic loadings. *DYMAT-International Conference on the Mechanical and Physical Behaviour of Materials under Dynamic Loading*, 2 :1239–1244, 2009.
- [43] Adinel Gavras. Constitutive equation for description of metallic materials behavior during static and dynamic loadings taking into account important gradients of plastic deformation. *Key Engineering Materials*, 504 :697–702, 2012.
- [44] Adinel Gavras, Florina Bucur, Adrian Rotariu, and Sorin Cananau. Analysis of metallic materials behavior during severe loadings using a fe modeling of the shpb test based on a numerical calibration of elastic strains with respect to the raw measurements and on the inverse analysis principle. *Key Engineering Materials*, 554 :1133–1146, 2013.

- [45] A Gavrus, P Caestecker, E Ragneau, and B Davoodi. Analysis of the dynamic SHPB test using the finite element simulation. *Journal de Physique IV (Proceedings)*, 110 :353–358, 2003.
- [46] Adinel Gavrus. Identification automatique des parametres rheologiques par analyse inverse. PhD thesis, Ecole Nationale Superieure des Mines de Paris, France, 1996.
- [47] Ji Hyun Sung, Ji Hoon Kim, and RH Wagoner. A plastic constitutive equation incorporating strain, strain-rate, and temperature. *International Journal of Plasticity*, 26(12) :1746–1771, 2010.
- [48] Dipti Samantaray, Sumantra Mandal, and A.K. Bhaduri. Constitutive analysis to predict high-temperature flow stress in modified 9Cr-1Mo (p91) steel. *Materials & Design*, 31(2) :981–984, 2010.
- [49] M. M. Hutchison. The temperature dependence of the yield stress of polycrystalline iron. *Philosophical Magazine*, 8(85) :121–127, 1963.
- [50] Akhtar S. Khan, Yeong Sung Suh, and Rehan Kazmi. Quasi-static and dynamic loading responses and constitutive modeling of titanium alloys. *International Journal of Plasticity*, 20(12) :2233–2248, 2004.
- [51] Siying Chen, Chenguang Huang, Chunkui Wang, and Zhuping Duan. Mechanical properties and constitutive relationships of 30CrMnSi steel heated at high rate. *Materials Science and Engineering : A*, 483-484 :105–108, 2008.
- [52] Frederick Harwood Norton. The creep of steel at high temperatures. Number 35. McGraw-Hill Book Company, Incorporated, 1929.
- [53] Kazutoshi Ohashi, Hiroshi Utsunomiya, and Ryo Matsumoto. Evaluation of r-value of steels using vickers hardness test. *Journal of Physics : Conference Series*, 379 :012045, 2012.
- [54] M Arminjon and B Bacroix. On plastic potentials for anisotropic metals and their derivation from the texture function. *Acta Mechanica*, 88(3-4) :219–243, 1991.
- [55] W Nasri, A Gavrus, A Kouadri-David, and K Sai. Experimental characterization and numerical modeling of the three-dimensional anisotropic behavior of a thick sheet aluminum alloy AA2024-T351 using multi-scale approaches. *High Performance and Optimum Design of Structures and Materials II*, 166 :163, 2016.
- [56] E Voce. A practical strain-hardening function. *Metallurgia*, 51(307) :219–226, 1955.
- [57] Ju Chen, Ben Young, and Brian Uy. Behavior of high strength structural steel at elevated temperatures. *Journal of structural engineering*, 132(12) :1948–1954, 2006.
- [58] Bülent Aydemir, Havva Kazdal Zeytin, Gökhan Güven, and Aygun Güngör. Investigation of mechanical properties of DP600 steels at elevated temperatures. In *ISITES2014*. Intech, 2014.
- [59] Hibbitt, Karlsson, and Sorensen. *ABAQUS : Theory Manual*, volume 2. Hibbitt, Karlsson & Sorensen, 1997.

- [60] Michael T Hutchings, Philip J Withers, Thomas M Holden, and Torben Lorentzen. Introduction to the characterization of residual stress by neutron diffraction. CRC press, 2005.
- [61] K Pawlik and P Ozga. LaboTex : the texture analysis software. Göttinger Arbeiten zur Geologie und Paläontologie, SB4, 1999.
- [62] P Staron, M Kocak, S Williams, and A Wescott. Residual stress in friction stir-welded al sheets. *Physica B : Condensed Matter*, 350(1) :E491–E493, 2004.
- [63] S. M. Ulam and J. von Neumann. Random ergodic thorems. *Bull. Amer. Math*, 51 :660, 1945.
- [64] John Conway. The game of life. *Scientific American*, 223(4) :4, 1970.
- [65] Stephen Wolfram. A new kind of science, volume 5. Wolfram media Champaign, 2002.
- [66] M. Rappaz and Ch. A. Gandin. Probabilistic modelling of microstructure formation in solidification processes. *Acta Metallurgica et Materialia*, 41(2) :345–360, 1993.
- [67] Xiaohong Zhan, Yanhong Wei, and Zhibo Dong. Cellular automaton simulation of grain growth with different orientation angles during solidification process. *Journal of Materials Processing Technology*, 208(1–3) :1–8, November 2008.
- [68] Xiao-Hong Zhan, Zhi-Bo Dong, Yan-Hong Wei, and Yong Wang. Simulation of columnar dendrite grain growth in weld pool of Ni-Cr binary alloy. *The Chinese Journal of Nonferrous Metals*, 19(8) :1431–1436, 2009.
- [69] L. Nastac. Numerical modeling of solidification morphologies and segregation patterns in cast dendritic alloys. *Acta Materialia*, 47(17) :4253–4262, 1999.
- [70] W. Wang, P. D. Lee, and M. McLean. A model of solidification microstructures in nickel-based superalloys : predicting primary dendrite spacing selection. *Acta Materialia*, 51(10) :2971–2987, 2003.
- [71] Dieter Radaj. Welding residual stresses and distortion. Calculation and measurement, DVS-Verlag, Dusseldorf, 2003.
- [72] X. H. Zhan, Z. B. Dong, Y. H. Wei, and Y. L. Xu. Dendritic grain growth simulation in weld molten pool based on CA-FD model. *Crystal Research and Technology*, 43(3) :253–259, 2008.
- [73] A Tiziani, P Ferro, R Cervo, and M Durante. Effects of different welding technologies on metallurgical anf mechanical properties of dp600 steel welded joints. *La Metallurgia Italiana*, 1(1), 2011.
- [74] Xin Lin, Lei Wei, Meng Wang, and Wei Dong Huang. A cellular automaton model with the lower mesh-induced anisotropy for dendritic solidification of pure substance. *Materials Science Forum*, 654-656 :1528–1531, 2010.
- [75] Y. H. Wei, X. H. Zhan, Z. B. Dong, and L. Yu. Numerical simulation of columnar dendritic grain growth during weld solidification process. *Science and Technology of Welding and Joining*, 12(2) :138–146, 2007.

- [76] M. Marya and X. Q. Gayden. Development of requirements for resistance spot welding dual-phase (dp600) steels part 1—the causes of interfacial fracture. *Welding Journal*, 84(11) :172–182, 2005.
- [77] Chansopheak Seang. Evaluation numérique des contraintes résiduelles appliquée à l'acier DP600 soudé par laser de haute puissance Nd : YAG. PhD thesis, Rennes, INSA, 2013.
- [78] F Ozturk, S Toros, and S Kilic. Tensile and spring-back behavior of DP600 advanced high strength steel at warm temperatures. *Journal of Iron and Steel Research, International*, 16(6) :41–46, 2009.
- [79] Danyang Dong, Yang Liu, Yuling Yang, Jinfeng Li, Min Ma, and Tao Jiang. Microstructure and dynamic tensile behavior of DP600 dual phase steel joint by laser welding. *Materials Science and Engineering : A*, 594 :17–25, January 2014.
- [80] Y Y Zhao, Y S Zhang, and W Hu. Effect of welding speed on microstructure, hardness and tensile properties in laser welding of advanced high strength steel. *Science and Technology of Welding and Joining*, 18(7) :581–590, October 2013.
- [81] Sudook A. Kim and Ward L. Johnson. Elastic constants and internal friction of martensitic steel, ferritic-pearlitic steel, and α -iron. *Materials Science and Engineering : A*, 452-453 :633–639, 2007.

AVIS DU JURY SUR LA REPRODUCTION DE LA THESE SOUTENUE

Titre de la thèse:

Étude numérique et expérimentale des contraintes résiduelles générées lors du soudage laser sur des plaques d'acier dual phase DP600

Nom Prénom de l'auteur : LIU SHIBO

Membres du jury :

- Madame KOUADRI-DAVID Afia
- Monsieur MANACH Pierre-Yves
- Monsieur GAVRUS Adinel
- Monsieur RAZAFIMAHERY Fulgence
- Monsieur BARRALLIER Laurent
- Madame FAVIER Véronique
- Monsieur GERMAIN Guenael
- Monsieur NISTOR Ionel

Président du jury : *Madame FAVIER Véronique*

Date de la soutenance : 08 Juin 2017

Reproduction de la these soutenue

~~Thèse pouvant être reproduite en l'état~~

Thèse pouvant être reproduite après corrections suggérées

Fait à Rennes, le 08 Juin 2017

Signature du président de jury



Le Directeur,

M'hamed DRISSI



Résumé

Le procédé de soudage laser est largement utilisé dans les travaux d'assemblage, en particulier, dans le domaine de l'industrie automobile. L'acier dual phase DP600 est un acier à haute résistance qui permet de réduire le poids de l'automobile dans le cadre de l'allègement des structures. Notre travail s'est essentiellement basé sur l'évaluation des contraintes résiduelles générées dans l'acier DP600 lors du soudage par laser. Deux approches ont été réalisées. L'approche expérimentale a été réalisée à l'aide de méthodes de rayon X et par neutrons pour calculer les contraintes résiduelles. L'approche de simulation a été réalisée par couplage de différentes formulations numériques.

Numériquement, le formalisme de la mécanique continue a été utilisé par des simulations par éléments finis (FEM) pour analyser et évaluer les contraintes résiduelles. Sur la base de tests de traction expérimentaux, le modèle constitutif élasto-thermo-plastique de l'acier DP600 a été identifié. L'érouissage du matériau a été étudié par la loi de Ludwik et de Voce. A partir de résultats expérimentaux, un modèle a été proposé et les résultats analysés en utilisant une loi de mélange martensite (érouissage Ludwik) et ferrite (adoucissement de Voce). De même, nous avons étudié la sensibilité à la température en utilisant plusieurs modèles : Johnson-Cook, Khan, Chen. A partir de cette étude, nous avons proposé un modèle de sensibilité à la température. Enfin, un modèle de sensibilité à la déformation plastique, à la vitesse de déformation issu des travaux d'A. Gavras et un modèle d'anisotropie planaire défini par la théorie de Hill ont été ajoutés.

Une méthode d'automate cellulaire (CA) 2D a été programmée pour simuler l'évolution de la microstructure lors de la salification liée au processus de soudage laser. Dans ce modèle, les phénomènes de nucléation avec prise en compte de l'orientation de la croissance, de la concentration et de la vitesse de croissance à l'interface solide/liquide, l'anisotropie de la tension de surface, de la diffusion, ainsi que la fraction des phases en présence ont été pris en compte. De plus, les équations de conservation ont été étudiées en détail et analysés. Les résultats ainsi que le champ de température issu du modèle FEM ont été importés dans le modèle CA. En comparant la simulation et les résultats expérimentaux, de bonnes concordances ont été trouvées.

Par la suite, nous avons réalisés un couplage des deux modèles CA et FEM. Concernant le procédé laser, les résultats du modèle par éléments finis ont été analysés. La géométrie de l'échantillon, la source de chaleur, les conditions aux limites, le comportement thermo-mécanique de l'acier dual phase DP600 telles que la conductivité, la densité, la chaleur spécifique, l'expansion, l'élasticité et la plasticité sont introduites. Les modèles d'analyse du terme d'érouissage, de la sensibilité à la vitesse de déformation, de la sensibilité à la température, de l'anisotropie plastique et de l'anisotropie élastique ont été simulés. Les fractions volumiques concernant la nature des deux phases en présence ont été également étudiées.

Les résultats numériques finaux les contraintes résiduelles ont été étudiées. Les comparaisons avec des mesures expérimentales ont montré à la fois quels phénomènes étudiés sont prépondérants et les effets moins influents sur l'évaluation des contraintes résiduelles. Les résultats les plus probants ont montré des bonnes convergences entre l'approche numérique et expérimentale. Ces résultats confortent la robustesse du modèle numérique développé.

Mots-clés : Soudage Laser, DP600, Contraintes Résiduelles, Automate Cellulaire, Erouissage, Sensibilité à la Température, Sensibilité à la vitesse de déformation, Anisotropie, Loi de mélange dual-phase

Abstract

The laser welding process is widely used in assembly work, particularly in the field of the automobile industry. The dual phase DP600 steel is a high-strength steel which reduces the weight of the automobile through lightening the structures. Our work was mainly based on the evaluation of the residual stresses generated in the DP600 steel during laser welding. Two approaches have been developed. The experimental approach was carried out using X-ray and neutron methods to calculate the residual stresses. The simulation approach was realized by coupling different numerical formulations.

Numerically, the theory of continuous mechanics has been used by finite element simulations (FEM) to analyze and evaluate residual stresses. Based on experimental tensile tests, the elasto-thermo-plastic constitutive model of DP600 steel was identified. The material hardening was studied by the law of Ludwik and of Voce. From experimental results, a model has been proposed and the results are analyzed by using a mixing law between martensite (Ludwik hardening) and ferrite (Voce softening). Moreover, we have studied temperature sensitivity using several models : Johnson-Cook, Khan, Chen. From this study, we proposed a model of temperature sensitivity. Finally, a model of sensitivity of plastic strain and of strain rate according to the work of A. Gavras and a planar anisotropy model defined by Hill theory were added.

A 2D Cellular Automaton (CA) method has been programmed to simulate the evolution of the microstructure during the laser welding process. In this model, the nucleation phenomena, the orientation of the growth, the concentration and the growth rate at the solid / liquid interface, the anisotropy of the surface tension, the diffusion as well as the fraction of the phases involved have been taken into account. In addition, conservation equations were studied in detail and analyzed. The results of the temperature field from the FEM model were imported into the CA model. By comparing the simulation and the experimental results, good concordances were found.

Subsequently, we performed a coupling of the two models CA and FEM. The results of the finite element model were analyzed for the laser process. Sample geometry, heat source, boundary conditions, thermo-mechanical behavior of dual phase DP600 steel such as conductivity, density, specific heat, expansion, elasticity and plasticity are introduced. The models analyzing the term of hardening, the strain rate sensitivity, the temperature sensitivity, the plastic anisotropy and the elastic orthotropic anisotropy were simulated. The voluminal fractions concerning the nature of the two phases were also studied.

The final numerical results of the residual stresses were studied. Comparisons with experimental measurements showed that some influence on residual stresses are preponderant while other influences are less important. The most convincing results showed good convergence between the numerical and experimental approach. These results confirm the validation of the developed numerical model.

Keywords : Laser Welding, DP600, Residual Stress, Cellular Automaton, Hardening, Temperature sensitivity, Strain Rate Sensitivity, Anisotropy, Mixture dual-phase law.